UNIVERSITY OF STELLENBOSCH

A critical appraisal of existing models for nonlinear finite element analysis of reinforced concrete response.

Charl de Jager

Thesis presented in partial fulfilment of the requirements for the degree of Master of Science in Engineering.

Professor GPAG van Zijl

Department of Structural Engineering
University of Stellenbosch
March 2011

Declaration

I, the undersigned, hereby declare that the following work contained within this thesis is my own, original work except where specifically acknowledged in the text; and that I have never previously submitted it in its entirety or in part in order to obtain any other qualification.

 Date: March 2012

Abstract

This study entails the appraisal of the constitutive models available for the non linear finite element analysis of reinforced concrete, using the DIANA finite element package and following generally accepted guidelines for non linear finite element analyses. The constitutive models considered are plasticity and total strain based (fixed and rotating crack) models. The appraisal consists of the analysis of various experiments performed on reinforced concrete beams that are governed by compressive, shear and tensile dominated failures. The investigation is not limited to the accuracy of the results obtained using these models but also of the consistency of the results obtained with regard to various mesh types and sizes, as well as a study of the individual influence of several material parameters. The intention of the study was to provide the reader with an indication of the performance capacity (accuracy and consistency) of the available constitutive models, where the notion of the use of the results obtained from non linear finite element analyses for design purposes is considered.

The results obtained were varied. The models performed reasonably well in the compressive and tension dominated studies, with the importance of accurate material parameters being emphasized especially for the more advanced cementitious materials investigated. The total strain rotating crack model also showed a proclivity of simulating incorrect failure modes as well as exhibiting reluctance towards stress redistribution. All models used for the shear dominated study yielded mostly inaccurate and inconsistent results, but it was found that the four node quadrilateral element with selective reduced integration performed the best. The plasticity model did not capture shear failure well, and convergence was often not attained. The constant shear retention factor of the total strain fixed crack model was found to yield more detailed response curves for the smaller mesh sizes. The results of the tension dominated beams inspired more confidence in the models as quite accurate values were attained, especially by the plasticity model used.

The ability of the available models to simulate realistic structural behaviour under various failure modes is very limited, as is evident from the results obtained. The development of a more advanced and robust model is required, which can provide consistently accurate results and failure modes, and even ‘anticipate’ potential failure modes not considered by the user.

Acknowledgements

I would like to acknowledge the help and contribution of my supervisor, Professor GPAG Van Zijl, for his patience and expertise as well as imparting unto me some of his significant knowledge.

I would also like to thank the German Academic Exchange Service (DAAD) for their financial backing during the duration of this study.

The overwhelming support from my family throughout my academic career is also sincerely appreciated.

Table of Contents

List of Tables

List of Figures

Introduction

As has been determined by our past and the history of engineering, we find ourselves looking towards a future of engineering governed by and directed towards practice that would least effect the environment. We are no longer in a position to merely adapt our environment to suit our needs, and a change in engineering practice is necessary. In the field of structural engineering, many advanced cementitious materials have been developed with superior mechanical properties, the exploitation and use of which could potentially reduce construction costs by reducing the amount of material needed, increase the durability of structures and thus also ultimately lower the cost to the environment. However, the most important factor when considering the design and construction of structures will always be the safety against failure. Thus a design which maximizes structural safety and minimizes environmental impact is the new direction of structural engineering.

This study investigates a step in this direction, where the use of results based on non linear finite element analysis in design to exploit the properties advanced cementitious materials is investigated. In using non linear mechanics to computationally model reinforced concrete structures, a more precise description of reality can be attained due to the non linear nature of reinforced concrete. This accurate description of reality can then allow the designer to achieve the balance between maximizing structural safety while minimizing environmental impact. This study is mostly concerned with the question of how accurately and how consistently accurately can such non linear mathematical descriptions describe realistic reinforced concrete response in a computational framework.

Scope and Objectives

This study involves the appraisal of the non linear constitutive models available for implementation in non linear finite element analyses in order to establish whether reinforced concrete response can in fact be accurately simulated, using one of the most advanced finite element software packages available (DIANA (2009)) and following guidelines for non linear finite element analyses as

suggested by Hendriks et al. (2009). Various other aspects such as the influence of specific material parameters inherent in the constitutive models are considered. The finite element mesh type and size influence is also investigated as well as the compatibility between the constitutive models and mesh types.

Various previously performed experimental studies are studied, which involve the testing of reinforced concrete beams designed to fail in compression, shear and tension. The appraisal consists of performing non linear finite element analyses on these beam specimens using either plasticity or total strain based constitutive relations, as well as various mesh sizes and types for the finite element model and investigating the reasons for the responses attained. The intention being to ascertain whether the response of the reinforced concrete beams can be accurately and consistently (across mesh types and sizes) simulated computationally, and thus establish whether these models can be used for design purposes.

Firstly, the reader will be familiarized with some of the aspects of non linear finite element analyses, including a discussion about the incorporation of physically non linear behaviour in the finite element method and the solutions thereof. The constitutive relations used in this study are then described and discussed giving some insight into the mathematical formulations of these theories. Finally the analyses of each of the failure types are discussed individually in three parts, with a background to the experimental work provided, as well as a discussion of the procedures and parameters used, and results obtained for the analyses conducted in this study.

A. Literature Review

A.1 Structure of Nonlinear Finite Element Programs

The finite element method is most commonly implemented in software using the pure displacement version of the method, which has been shown to be the most convenient and robust spatial discretization method for several applications of non-linear constitutive relations. Inherently the formulation of the displacement based finite element method is relatively simple and thus allows for easy implementation of usually complex non-linear constitutive relations. There are certain cases where the displacement version of the method fails to yield accurate results where other hybrid methods may need to be resorted to, which could in turn increase the risk of improper element behaviour especially when considering physical non linearities where the possibility of spurious kinematic modes occurring in elements is increased. Therefore, for its ease of implementation and avoiding the potential of spurious kinematic modes occurring in elements, the displacement based version of the finite element method is often preferred especially in analyses where physical non linearities are involved (such as damage or plasticity). The pure displacement version of the method will be briefly discussed further to provide the reader with a quick review of the method as well as a basic understanding of the backbone of DIANA.

A.2 Equilibrium and virtual work

An elegant derivation of the equilibrium equations involves considering the entire equilibrium stress state of a body. If the tractions on the surface of the body are collected in a vector $\boldsymbol{t}$ and the gravity force of the body in a vector $\boldsymbol{g}$, then equilibrium of the body would require the following

$$\int_S \boldsymbol{t}.\,dS + \int_V \rho\,\boldsymbol{g}.\,dV = 0 \qquad \text{(A.2.1)}$$

Considering the relationship between the stress tensor ($\boldsymbol{\Sigma}$) and the traction vector ($\boldsymbol{t}$) as established in continuum mechanics ($\boldsymbol{\Sigma n = t}$), the equilibrium equation can be changed to

$$\int_S \boldsymbol{\Sigma n}.\, dS + \int_V \rho\, \boldsymbol{g}.\, dV = 0 \tag{A.2.2}$$

with n being the outward unit vector normal to the boundary of the body and the symmetrical Cauchy stress tensor being

$$\boldsymbol{\Sigma} = \begin{bmatrix} \sigma_{xx} & \sigma_{xy} & \sigma_{zx} \\ \sigma_{xy} & \sigma_{yy} & \sigma_{yz} \\ \sigma_{zx} & \sigma_{yz} & \sigma_{zz} \end{bmatrix} \tag{A.2.3}$$

Gauss's divergence theorem can now be applied to the above equation. The theorem allows for a surface integral to be changed into a volume integral:

$$\int_V div\, \boldsymbol{v}.\, dV = \int_S \boldsymbol{n^T}\, \boldsymbol{v}.\, dS \tag{A.2.4}$$

with $\boldsymbol{n}$ the outward normal unit vector and div the divergence operator:

$$div\, \boldsymbol{v} = \frac{dv_1}{dx_1} + \frac{dv_2}{dx_2} + \frac{dv_3}{dx_3} \tag{A.2.5}$$

Now applying this theorem to eqn. (A.2.2), one obtains

$$\int_V (div\, \boldsymbol{\sigma} + \rho \boldsymbol{g}).\, dV = 0 \tag{A.2.6}$$

This must hold locally for small volumes of the body for it to hold globally, thus:

$$div\, \boldsymbol{\sigma} + \rho \boldsymbol{g} = \boldsymbol{0} \tag{A.2.7}$$

with $\boldsymbol{\sigma}$ being the stress tensor in vector form: $\boldsymbol{\sigma^T} = \{\sigma_{xx}, \sigma_{yy}, \sigma_{zz}, \sigma_{xy}, \sigma_{yz}, \sigma_{zx}\}$ - the six independent components of the symmetrical stress tensor. Thus if g_x, g_y, g_z are the components of $\boldsymbol{g}$, eqn. (A.2.7) can be expressed in component form as:

$$\begin{aligned}
\frac{d\sigma_{xx}}{dx} + \frac{d\sigma_{xy}}{dy} + \frac{d\sigma_{zx}}{dz} + \rho g_x = 0 \\
\frac{d\sigma_{xy}}{dx} + \frac{d\sigma_{yy}}{dy} + \frac{d\sigma_{yz}}{dz} + \rho g_y = 0 \\
\frac{d\sigma_{zx}}{dx} + \frac{d\sigma_{yz}}{dy} + \frac{d\sigma_{zz}}{dz} + \rho g_z = 0
\end{aligned} \tag{A.2.8}$$

To express the above equations in a compact matrix-vector format, the operator matrix $\mathbf{L}$ is introduced,

$$\mathbf{L^T} = \begin{bmatrix} \frac{d}{dx} & 0 & 0 & \frac{d}{dy} & 0 & \frac{d}{dz} \\ 0 & \frac{d}{dy} & 0 & \frac{d}{dx} & \frac{d}{dz} & 0 \\ 0 & 0 & \frac{d}{dz} & 0 & \frac{d}{dy} & \frac{d}{dx} \end{bmatrix} \tag{A.2.9}$$

and with the stress tensor in vector form as described before, the eqns. (A.2.8) become:

$$\mathbf{L^T}\boldsymbol{\sigma} + \boldsymbol{\rho g} = \mathbf{0} \tag{A.2.10}$$

The next step is to get this equation into the 'weak format' which is done by multiplying it by a virtual displacement field $\delta\boldsymbol{u}$, where $\boldsymbol{u^T} = (u_x, u_y, u_z)$ and integrating the function over the entire volume $\boldsymbol{V}$ occupied by the body.

$$\int_V \delta\boldsymbol{u^T}\,[\mathbf{L^T}\boldsymbol{\sigma} + \boldsymbol{\rho g}].\,dV = 0 \tag{A.2.11}$$

The divergence theorem is again applied to this formula and results in

$$\int_V (\mathbf{L}\delta\boldsymbol{u})^T\,\boldsymbol{\sigma}.\,dV = \int_V \boldsymbol{\rho}\delta\boldsymbol{u^T}\boldsymbol{g}\,.\,dV + \int_S \delta\boldsymbol{u^T}\boldsymbol{t}.\,dS \tag{A.2.12}$$

with the assumed boundary conditions being

$$\boldsymbol{\Sigma n} = \boldsymbol{t}\ or\ \boldsymbol{u} = \boldsymbol{u_p} \tag{A.2.13}$$

which are prescribed on the complementary parts of the surface of the body S.

Equation (A.2.12) represents the weak form of the equilibrium equations and in its derivation, no assumptions have yet been made regarding the material behaviour or the displacements, thus the set of equations are valid for both linear and non-linear material behaviour. Eqn. (A.2.12) can be simply expressed as:

$$\delta W_{int} = \delta W_{ext} \tag{A.2.14}$$

with

$$\delta W_{int} = \int_V (\mathbf{L}\delta \boldsymbol{u})^{\boldsymbol{T}} \boldsymbol{\sigma}. dV \tag{A.2.15}$$

describing the internal virtual work of the internal stresses in the body and,

$$\delta W_{ext} = \int_V \boldsymbol{\rho}\delta \boldsymbol{u}^{\boldsymbol{T}} \boldsymbol{g}\, . dV + \int_S \delta \boldsymbol{u}^{\boldsymbol{T}} \boldsymbol{t}. dS \tag{A.2.16}$$

which describes the external virtual work on the body - as a result of the gravity force and tractions respectively.

A.2.1 Spatial Discretization by Finite Elements

A displacement based formulation of the FEM will be briefly discussed as stated before. In this formulation, the displacement degrees of freedom are the fundamental unknowns within the system. The continuous displacement field $\boldsymbol{u}$ can be approximated by the interpolation of the nodal displacement vectors throughout the body. The nodal displacement vectors for an 'n-noded' element are taken as $\boldsymbol{a_i}$ with the components (a_{ix}, a_{iy}, a_{iz}), being the displacements at node i in the directions of the spatial coordinate system x, y, z. The continuous displacement field $\boldsymbol{u}$ can then be approximated per element as

$$\boldsymbol{u} = \sum_{i=1}^{n} \hbar_i(\xi, \eta, \zeta)\boldsymbol{a}_i \tag{A.2.17}$$

where $\hbar_i(\xi, \eta, \zeta)$ are the interpolation functions of the n-noded element under consideration expressed in terms of the normalized isoparametric spatial coordinate system (ξ, η, ζ).

Using the vector expression $\boldsymbol{a_e}$ which collects all the nodal displacement vectors of the element, $\boldsymbol{a_i}$ and thus containing all the displacement degrees of freedom as follows:

$$\boldsymbol{a_e} = \begin{bmatrix} \boldsymbol{a_1} \\ \boldsymbol{a_2} \\ \boldsymbol{a_3} \\ \vdots \\ \boldsymbol{a_n} \end{bmatrix} \tag{A.2.18}$$

and by also introducing the matrix $\mathbf{H}$ with dimensions 3x3n

$$\mathbf{H} = \begin{bmatrix} \boldsymbol{h}_1 & 0 & 0 & \boldsymbol{h}_2 & 0 & 0 & \dots & \boldsymbol{h}_n & 0 & 0 \\ 0 & \boldsymbol{h}_1 & 0 & 0 & \boldsymbol{h}_2 & 0 & \dots & 0 & \boldsymbol{h}_n & 0 \\ 0 & 0 & \boldsymbol{h}_1 & 0 & 0 & \boldsymbol{h}_2 & \dots & 0 & 0 & \boldsymbol{h}_n \end{bmatrix} \tag{A.2.19}$$

The interpolation of the displacement degrees of freedom throughout the element (eqn. (A.2.17)) can be expressed in the more convenient and compact form of:

$$\boldsymbol{u} = \mathbf{H}\boldsymbol{a_e} \tag{A.2.20}$$

The displacements contained in the element specific vector $\boldsymbol{a_e}$ can be related to the global displacement vector by using the topology matrix $\boldsymbol{Z_e}$.

$$\boldsymbol{a_e} = \boldsymbol{Z_e}\boldsymbol{a} \tag{A.2.21}$$

Using the eqns. (A.2.20) and (A.2.21) the weak form of the equilibrium equations, eqn. (A.2.12) can be rewritten as:

$$\sum_{e=1}^{NEL} \int_{V_e} (\mathbf{L}\mathbf{H}\boldsymbol{Z_e}\delta\boldsymbol{a})^T \boldsymbol{\sigma}.\, dV = \sum_{e=1}^{NEL} \int_{V} \boldsymbol{\rho}(\mathbf{H}\boldsymbol{Z_e}\delta\boldsymbol{a})^T \boldsymbol{g}\,.\, dV + \sum_{e=1}^{NEL} \int_{S} (\mathbf{H}\boldsymbol{Z_e}\delta\boldsymbol{a})^T \boldsymbol{t}.\, dS \tag{A.2.22}$$

where the integration is done throughout the entire volume V of each of the elements within the total number NEL of elements in the mesh. The nodal virtual displacements $\boldsymbol{\delta a}$ are independent of the spatial coordinate system and can thus be taken out of the integral expressions as well as the summation expressions. The topology matrices differ for each element but are also independent of the spatial coordinate system, and can thus also be taken out of the integral

expressions but still remain a part of the summations. These manipulations result in:

$$\delta \boldsymbol{a}^{T} \sum_{e=1}^{NEL} \boldsymbol{Z_e}^{T} \int_{V_e} (\mathbf{LH})^{T} \boldsymbol{\sigma} . dV = \delta \boldsymbol{a}^{T} \sum_{e=1}^{NEL} \boldsymbol{Z_e}^{T} \int_{V} \boldsymbol{\rho} \mathbf{H}^{\mathbf{T}} \boldsymbol{g} . dV + \delta \boldsymbol{a}^{T} \sum_{e=1}^{NEL} \boldsymbol{Z_e}^{T} \int_{S} \mathbf{H}^{\mathbf{T}} \boldsymbol{t} . dS \tag{A.2.23}$$

Considering then that the above equation must be valid for all virtual displacements, one attains:

$$\sum_{e=1}^{NEL} \boldsymbol{Z_e}^{T} \int_{V_e} (\mathbf{LH})^{T} \boldsymbol{\sigma} . dV = \sum_{e=1}^{NEL} \boldsymbol{Z_e}^{T} \int_{V} \boldsymbol{\rho} \mathbf{H}^{T} \boldsymbol{g} . dV + \sum_{e=1}^{NEL} \boldsymbol{Z_e}^{T} \int_{S} \mathbf{H}^{T} \boldsymbol{t} . dS \tag{A.2.24}$$

This can be expressed more succinctly as:

$$\boldsymbol{f}_{int} = \boldsymbol{f}_{ext} \tag{A.2.25}$$

which is essentially the equilibrium condition between the forces resulting from the stresses within the body, the internal force vector:

$$\boldsymbol{f}_{int} = \delta \boldsymbol{a}^{T} \sum_{e=1}^{NEL} \boldsymbol{Z_e}^{T} \int_{V_e} (\mathbf{LH})^{T} \boldsymbol{\sigma} . dV \tag{A.2.26}$$

and the forces caused by the external actions on the body, the external force vector:

$$\boldsymbol{f}_{ext} = \delta \boldsymbol{a}^{T} \sum_{e=1}^{NEL} \boldsymbol{Z_e}^{T} \int_{V} \boldsymbol{\rho} \mathbf{H}^{T} \boldsymbol{g} . dV + \delta \boldsymbol{a}^{T} \sum_{e=1}^{NEL} \boldsymbol{Z_e}^{T} \int_{S} \mathbf{H}^{T} \boldsymbol{t} . dS \tag{A.2.27}$$

To simplify this expression, the **LH** matrix multiplication of eqn. (A.2.26) is replaced by the matrix **B** (**B = LH**). Then equation (A.2.26) becomes:

$$\boldsymbol{f}_{int} = \sum_{e=1}^{NEL} \boldsymbol{Z_e}^{T} \int_{V} \mathbf{B}^{T} \boldsymbol{\sigma} . dV \tag{A.2.28}$$

This is merely a statement of the equilibrium between the external forces acting on the body and the internal forces caused by the stresses within the body. Calculation of the internal and external force vectors entails the evaluation of

integrals over the domain of the element considered. These integrals can become very complex, especially when high order interpolation functions or complex geometries are used. Thus analytical integration of these integrals is often difficult. This is especially the case when material non linearity is considered, where the tangential material stiffness variation over the domain of the element is not known a priori – thus the response of the material cannot be established upon attempting to solve the system. For these reasons and the scale of the computations involved, numerical integration is employed with various numerical integration techniques available.

A.2.2 Solution Techniques

A.2.2.1 Incremental Iterative solution procedures

The set of equations that arise from trying to calculate a displacement vector that yields a state of equilibrium between the internal and external force vectors, are nonlinear when considering the discretization of a physically nonlinear continuum model (where the displacements can become dependent on previous displacements such as in plasticity). Thus, to solve this system of equations, an iterative procedure is required. Furthermore, these systems are solved using a combination of spatial discretization (using finite elements) and 'time' discretization (using increments). The concept of 'time' is used for the sake of discussion (not physical time as governs creep processes etc) as the relationship governing the equilibrium of the system (eqn. (A.2.28)) is a static process. This combination of iteration performed at various increments is termed an incremental-iterative solution (DIANA, 2009).

The internal force vector can depend nonlinearly on the displacements, as well as on the history of the displacements as is the case for a path dependant material. Nonlinearity can also occur when the external force vector is dependent on the displacement, as is the case in geometrical nonlinearities. Thus eqn. (A.2.25) becomes (DIANA, 2009):

$$\boldsymbol{f}\,(\mathbf{u}, \mathbf{history})_{int} = \boldsymbol{f}_{ext}(\mathbf{u}) \tag{A.2.29}$$

This system of equations is already spatially discretized, and in order to perform a numerical solution, it needs to be discretized in time as well, with time only describing a sequence of events (unless time dependant systems are considered

of course, in which the time referred to will have a physical meaning). At a time the displacement $\boldsymbol{u^t}$ is known and a solution $\boldsymbol{u^{t+\Delta t}}$ is sought after for which the relation in eqn. (A.2.29) is satisfied. Only the displacements at the start and end of this time increment are known, and the internal force vector is calculated from the state at time t as well as the time and displacement increments (Δt and Δu respectively). Considering only one increment, the situation at the start of the increment and the time increment are fixed – thus the equilibrium equation within that increment will only depend on $\boldsymbol{\Delta u}$. The nonlinear system can then be written as:

$$\boldsymbol{u}^{t+\Delta t} = \boldsymbol{u}^{t} + \boldsymbol{\Delta u} \tag{A.2.30}$$

With the intention being finding $\boldsymbol{\Delta u}$ for that time step. An expression for the out of balance force vector can then be obtained for the increment, which must equal 0 for complete equilibrium:

$$\mathrm{g}(\boldsymbol{\Delta u}) = \boldsymbol{f}_{ext}(\boldsymbol{\Delta u}) - \boldsymbol{f}_{int}(\boldsymbol{\Delta u}) = 0 \tag{A.2.31}$$

A.2.2.2 Iterative Procedures

Most iteration processes follow the same general procedure. The total incremental displacement Δu is changed iteratively through iterative increments, $\boldsymbol{\delta u}$, until a satisfactory point of equilibrium is reached (when g of eqn. (A.2.31) is small enough). Thus the incremental displacements for iteration $i+1$ are calculated as follows:

$$\boldsymbol{\Delta u}_{i+1} = \boldsymbol{\Delta u}_{i} + \boldsymbol{\delta u}_{i+1} \tag{A.2.32}$$

The various iteration procedures available differ mainly by the way in which $\boldsymbol{\delta}\mathbf{u}$ is calculated. The displacement vector and force vector are related through the stiffness matrix K, and the following direct approach can be used to determine the iterative increments:

$$\boldsymbol{\delta u}_{i} = \mathbf{K}_{i}^{-1}\mathbf{g}_{\boldsymbol{i}} \tag{A.2.33}$$

Where $\mathbf{K}_i$ is the stiffness matrix at iteration i and $\mathbf{g}_i$ is the out of balance force vector at the beginning of iteration i, which yields a set of linear equations that can be solved at every iteration. The two main iterative processes used in this study will be briefly discussed.

A.2.2.2.1 NEWTON RAPHSON

The regular Newton-Raphson iteration method uses eqn. (A.2.33) to determine the iterative increment of the displacement vector. In this method, the tangential stiffness of the structure represents the stiffness matrix at that increment as follows:

$$\mathbf{K}_i = \frac{\partial \mathrm{g}}{\partial \Delta \boldsymbol{u}} \tag{A.2.34}$$

This relation for the stiffness matrix is evaluated at each iteration, thus the prediction for the iterative increment of the displacement vector depends on the previously predicted situation, even though that situation may not be the equilibrium state (DIANA, 2009). The iteration procedure is shown in Figure A.2-1- Regular Newton Raphson iteration method ., where the value of $\delta\mathbf{u}_1$ value depends on g_1, which is the residual force vector as obtained from the previous iteration.

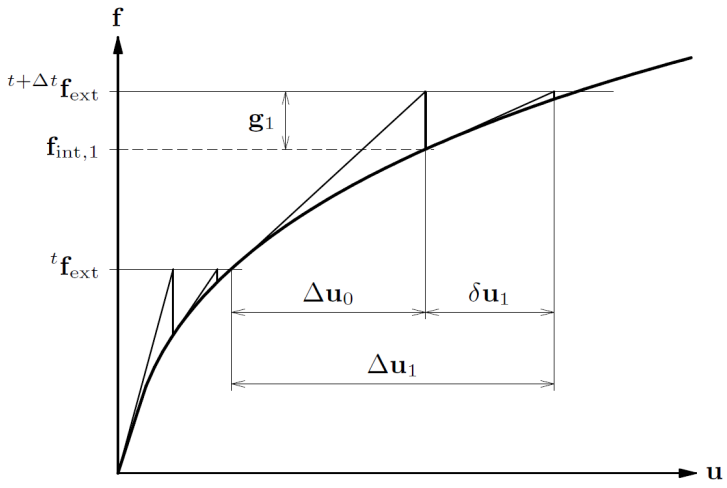

Figure A.2-1- Regular Newton Raphson iteration method (DIANA, 2009).

A.2.2.2.2 SECANT

Secant methods achieve better approximations of the solution through using information of the previous out of balance forces and solution vectors during the increment. A new stiffness matrix does not need to be calculated at the start of every iteration, as is the case with the Regular Newton Raphson method but the stiffness is rather determined from the known positions on the path of equilibrium, thus slight alterations are made to the initial tangential stiffness matrix with which to find solution. Considering the change in the out of balance force vector between iterations that corresponds with the iterative displacement vector $\delta\mathbf{u}_i$, the secant relation is:

$$\mathbf{K}_{i+1}\delta\mathbf{u}_i = \delta \mathrm{g}_i \tag{A.2.35}$$

Using a matrix $\mathbf{K}_i$ that satisfies eqn. (A.2.35), the iterative increment of the displacement field for the next iteration can be calculated from eqn. (A.2.33).

The secant method used in this study is the BFGS (Broyden-Fletcher-Goldfarb-Shanno) method. It can be shown that the following matrix yields a solution for eqn.(A.2.35):

$$\mathbf{K}_{i+1} = \mathbf{K}_i + \frac{(\delta \mathrm{g}_i - \mathbf{K}_i\delta\mathbf{u_i})\mathbf{c^T} + \mathbf{c}(\delta \mathrm{g}_i - \mathbf{K}_i\delta\mathbf{u_i})^T}{\mathbf{c^T}\delta\mathbf{u_i}} - \frac{(\delta \mathrm{g}_i - \mathbf{K}_i\delta\mathbf{u_i})^T\delta\mathbf{u_i}\mathbf{cc^T}}{(\mathbf{c^T}\delta\mathbf{u_i})^2} \tag{A.2.36}$$

where c is an arbitrary vector. The following relation was then established by BFGS for the inverse secant stiffness, which is directly obtained from the inverse of the secant stiffness matrix from the previous iteration and the so-called update vectors:

$$\mathbf{K}_{\mathbf{i+1}}^{\mathbf{-1}} = \left(\mathbf{I} + \frac{\delta\mathbf{u}_i\delta\mathbf{g}_i^T}{\delta\mathbf{u}_i^T\delta\mathbf{g}_i}\right)\mathbf{K}_i^{-1}\left(\mathbf{I} - \frac{\delta\mathbf{g}_i\delta\mathbf{u}_i^T}{\delta\mathbf{u}_i^T\delta\mathbf{g}_i}\right) + \frac{\delta\mathbf{u}_i\delta\mathbf{u}_i^T}{\delta\mathbf{u}_i^T\delta\mathbf{g}_i} \tag{A.2.37}$$

This expression is then substituted into eqn. (A.2.35) to calculate the iterative increment of the displacement field, with the inverse secant stiffness matrix never needing to be calculated explicitly. Through successive application of the relation in (A.2.37), the inverse secant stiffness's can be calculated for each iteration based on the initial secant stiffness used at the start of the increment, K_o, by adjusting it with the appropriate 'update vectors'. Thus with every iteration

the applicable update vectors need to be stored, which depend on the number of degrees of freedom in the system. This Secant procedure is illustrated in Figure A.2-2, and it can be seen that a better approximation of the solution can be obtained per increment when compared to the Regular Newton Raphson method.

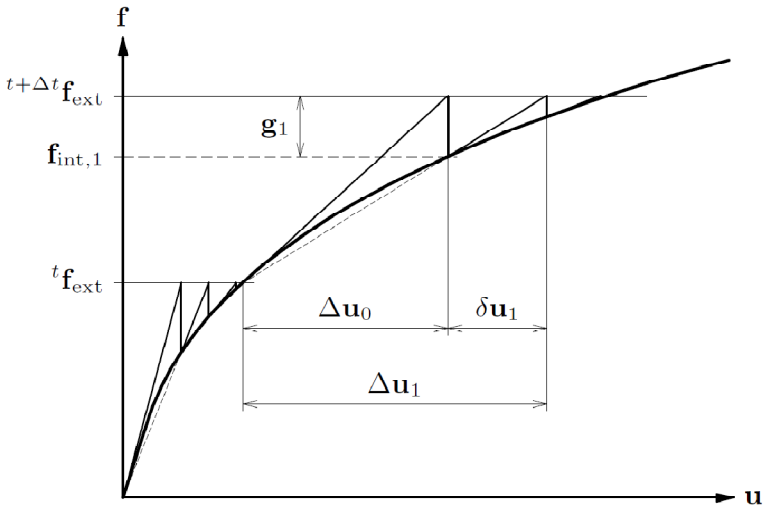

Figure A.2-2 - The Secant iteration method (DIANA, 2009).

A.2.2.2.3 CONVERGENCE CRITERIA

The two types of convergence criteria used in this study are the force and energy tolerance criteria. These criteria need to be met (either individually or simultaneously) in order for a satisfactory point on the path of structural response to obtained, which is a sufficient approximation to the equilibrium path.

The force convergence criterion determines the Euclidian norm of the vector g - the out of balance force vector. The force norm at the end of the current iteration is checked against the force norm of the initial out of balance force norm. The ratio of these two norms is calculated as follows (DIANA, 2009):

$$Force\ norm\ Ratio = \frac{\sqrt{\mathbf{g_i^T g_i}}}{\sqrt{\mathbf{g_0^T g_0}}} \tag{A.2.38}$$

The energy based convergence criteria is based on the calculation of the energy norms between iterations, using values for the internal forces and relative incremental displacements. These relationships are shown in Figure A.2-3.

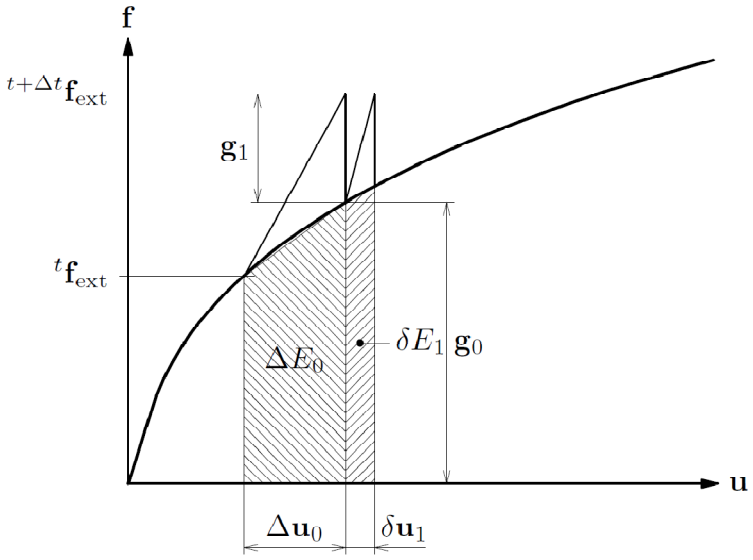

Figure A.2-3 - Values used to calculate energy norm (DIANA, 2009).

The energy norm ratio is determined by the following, to check convergence:

$$Energy\ norm\ ratio = \left| \frac{\delta \mathbf{u}_i^T (\mathbf{f}_{int,i+1} + \mathbf{f}_{int,i})}{\Delta \mathbf{u}_0^T (\mathbf{f}_{int,i+1} + \mathbf{f}_{int,i})} \right| \tag{A.2.39}$$

A.2.2.3 Incremental Procedures

The final requirement in an incremental-iterative solution of a nonlinear system is an incremental procedure, within which the previously discussed iteration procedures are applied until the convergence criteria is met for that increment.

A.2.2.3.1 DISPLACEMENT CONTROL

All analyses in this study were conducted through applying displacement increments to the system. External loading is applied to the structure through prescribing specific displacements to certain degrees of freedom, this is essentially displacement control. Another incremental procedure, force control, consists of prescribing force increments directly to certain degrees of freedom. However, load controlled analyses may 'miss' the peak of the structural response along with the post peak response, if the load increments are not carefully chosen. Displacement control can easily pass the peak of the response as well as effectively capture the post peak behavior. This is shown in Figure A.2-4 for a simple response curve, where the load control procedure (left) will not result in convergence at the peak or capture post peak response if the step sizes are

specified explicitly as they are. The displacement control procedure (right) does not encounter this problem.

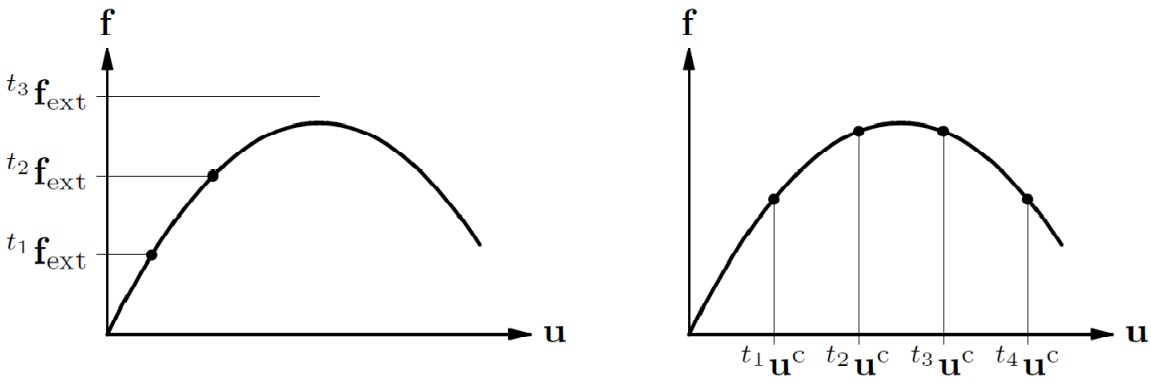

Figure A.2-4 - Load and displacement control (DIANA, 2009).

A.3 Constitutive models

The numerical constitutive modelling of reinforced and plain concrete started in the 1960's with the introduction of discrete and smeared crack models, with cracking being the main cause of nonlinearity in concrete. In general, the smeared cracking approach was the best received and gained much popularity, with significant research efforts geared in this direction (de Borst, 2001). Approaches based on mathematical plasticity theories have also been adopted to model the inelastic nature of concrete. The quasi-brittle nature of concrete results in several difficulties in formulating a plasticity framework to adequately describe the different response of concrete when subjected to tension or compression. Several Plasticity models incorporating multiple yield surfaces to describe the different tensile and compressive capacity of concrete as well as the potential anisotropic nature thereof have been proposed. One of these, as proposed by Lourenco et al. (Lourenco, et al., 1997), employs a multi-surface approach based on a Rankine-type yield surface to model tensile behaviour, combined with a Hill-type yield surface to model compressive behaviour under plane stress conditions.

The constitutive models considered within this study as available for implementation in DIANA Finite Element Software are the Total Strain Crack Models (Fixed and Rotating cracks, based on smeared cracking concepts) and

the Rankine-Hill plasticity models for the modelling of the reinforced concrete beams, as well as the adapted Rankine-Hill plasticity models for the modelling of SHCC. The underlying theory behind these constitutive models will be discussed.

A.3.1 Total Strain Crack Models

These crack models are based on the 'total strain' concept, in which an injective relation (or one to one relation) between the stress (σ) and the total strain (ε) is assumed, and where the total strain field is taken as being a combination of the concrete strain and the cracking strain (de Borst, et al., 2002):

$$\dot{\varepsilon} = \dot{\varepsilon}^{co} + \dot{\varepsilon}^{cr} \tag{A.3.1}$$

This affords the advantage of the constitutive behaviour of the concrete to be modelled separately from the behaviour at the crack interface (Rots, et al., 1985).

These models have been shown to work well in several applications, but their drawbacks include their inability to model other nonlinear phenomena that may be encountered in reinforced concrete analyses (such as shrinkage, thermal effects, creep) in conjunction with cracking, unless the total strain's constituents (eqn. (A.3.1)) are themselves further decomposed to incorporate additional strain rates (de Borst, 2001). Thus the models are appropriate for Serviceability Limit State and Ultimate Limit State analyses which are largely governed by crushing or cracking of the cementitious materials, due to the assumption of the injective relation between stress and strain (DIANA, 2009).

A.3.1.1 Smeared Cracking (Fixed and Rotating Crack models)

As previously stated, smeared cracking approaches are more popular and have largely replaced discrete crack models. Discrete crack models were formulated on the basis that cracking was assumed to occur when the tensile nodal force normal to the mesh element boundary exceeded the maximum tensile capacity of the material New degrees of freed were then added to the Finite Element model at the location of this node, and the crack was represented by the establishment of a geometrical discontinuity between the 'new' and 'old' nodes. This meant that the formations of cracks in the Finite Element model were

dependant on the mesh element boundary locations, and that the topology of the entire system would change upon each crack formation as new degrees of freedom are added (de Borst, et al., 2002).

Attempts such as re-meshing techniques were made to rectify these drawbacks. Re-meshing consisted of using linear elastic fracture mechanics techniques to establish where and in what direction cracks will form and propagate. Once established, a new mesh is created in which the crack's formation or propagation is included and the topology of the system could be maintained. Such techniques as well as others still proved to be too computationally expensive compared to models based on the smeared cracking concept, in which a cracked solid is assumed to be a continuum in which the concepts of stress and strain are still valid. The cracking of the material can then be represented by a stress strain relationship, with the initiation of cracking leading to the replacement of the initial isotropic stress strain relation by an orthotropic stress strain relation. Thus the original topology of the system is preserved, proving more efficient than discrete crack models (de Borst, et al., 2002).

A discussion of the Total Strain crack models is not complete without first addressing some of the elementary smeared cracking concepts. Quasi-brittle materials such as concrete can be satisfactorily modelled as isotropic, linear elastic materials before inelastic material behaviour is encountered (usually cracking of the material). Thus, the following two-dimensional stress state would be expected (de Borst, 2001):

$$\begin{bmatrix}\sigma_{xx}\\ \sigma_{yy}\\ \sigma_{xy}\end{bmatrix} = \frac{E}{1-v^2}\begin{bmatrix}1 & v & 0\\ v & 1 & 0\\ 0 & 0 & 0.5(1-v)\end{bmatrix}\begin{bmatrix}\varepsilon_{xx}\\ \varepsilon_{yy}\\ \gamma_{xy}\end{bmatrix} \quad \text{(A.3.2)}$$

Once the combination of principal stresses exceed some pre-established tension cut-off criterion, the isotropic material law is replaced by an orthotropic one, with a crack being formed in a direction perpendicular to the direction of the maximum principal stress. At this sampling point the stress, strain and history variables (that represent the damage or rather the loading or unloading situation in the material) are checked and monitored. The axes of orthotropy (n and s axes) are positioned perpendicular to the crack direction, with the n direction defined normal to the crack (mode I cracking, Figure A.3-1) and the s direction tangential

to the crack plane (mode II cracking, Figure A.3-1). See Figure A.3-2 for the orthotropic material axis orientation.

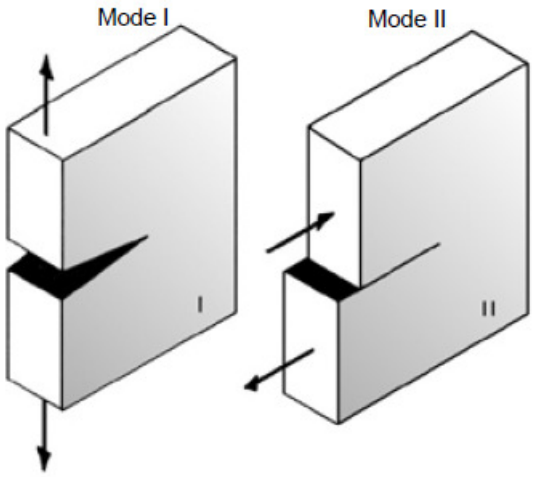

Figure A.3-1 - Mode I and Mode II cracking (Van Zijl, 2010).

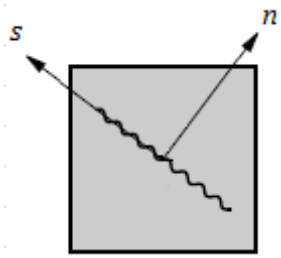

Figure A.3-2 - Orientation of the newly formed Orthotropic Material Axes (DIANA, 2009).

The orthotropic material law at a sampling point as in Figure A.3-2 can, quite simply, be defined by (Rashid, 1968):

$$\begin{bmatrix}\sigma_{nn}\\ \sigma_{ss}\\ \sigma_{ns}\end{bmatrix} = \begin{bmatrix}0 & 0 & 0\\ 0 & E & 0\\ 0 & 0 & 0\end{bmatrix}\begin{bmatrix}\varepsilon_{nn}\\ \varepsilon_{ss}\\ \gamma_{ns}\end{bmatrix} \tag{A.3.3}$$

It is clear that in eqn. (A.3.3) both the shear and normal stiffness across the crack are set to 0. Thus Poisson's ratio is eliminated from the relation and any influence of lateral expansion or contraction is removed.

Considering a plane stress situation, where $\boldsymbol{\sigma_{ns}} = \{\sigma_{nn}, \sigma_{ss}, \sigma_{ns}\}^T$ and $\boldsymbol{\varepsilon_{ns}} = \{\varepsilon_{nn}, \varepsilon_{ss}, \gamma_{ns}\}^T$ and the coefficient matrix of eqn. (A.3.25) being the secant

stiffness matrix ($\mathbf{D}_{ns}^{s}$), the orthotropic material law in the n, s coordinate system becomes (the orthotropic elastic stiffness relation) (de Borst, 2001):

$$\boldsymbol{\sigma}_{ns} = \mathbf{D}_{ns}^{s}\,\boldsymbol{\varepsilon}_{ns} \tag{A.3.4}$$

Introducing the angle φ to represent the angle between the crack (n axis) and the global x axis, the relation between the strain and stress vectors defined relative to the orthotropic axis system can be defined in the global (x, y coordinate system) as follows (using the standard transformation matrices $\mathbf{T}_{\varepsilon}$ and $\mathbf{T}_{\sigma}$) (de Borst, et al., 2002):

$$\boldsymbol{\varepsilon}_{ns} = \mathbf{T}_{\varepsilon}(\varphi)\boldsymbol{\varepsilon}_{xy} \tag{A.3.5}$$

and

$$\boldsymbol{\sigma}_{ns} = \mathbf{T}_{\sigma}(\varphi)\boldsymbol{\sigma}_{xy} \tag{A.3.6}$$

The orthotropic stiffness relation of eqn. (A.3.26) can then be transformed into a stiffness relation in the global coordinate system (de Borst, 2001):

$$\boldsymbol{\sigma}_{xy} = \mathbf{T}_{\sigma}^{-1}(\varphi)\mathbf{D}_{ns}^{s}\mathbf{T}_{\varepsilon}(\varphi)\boldsymbol{\varepsilon}_{xy} \tag{A.3.7}$$

This expression, for the case that the angle φ is fixed once the limits of the tensile criterion are exceeded, or upon crack initiation, is known as the fixed smeared-crack model (de Borst, 2001).

Due to ill-conditioning (where a small change in the coefficient matrix may significantly influence the solution) of eqn.(A.3.3) some convergence difficulties may be encountered when using this model. Researchers have also found that physically unrealistic cracking behaviour may also occur (Suidan, et al., 1973). Thus an additional reduced shear modulus term βG, $0 \leq \beta \leq 1$, was added to the formulation (de Borst, 2001):

$$\mathbf{D}_{ns}^{s} = \begin{bmatrix} 0 & 0 & 0 \\ 0 & E & 0 \\ 0 & 0 & \beta G \end{bmatrix} \tag{A.3.8}$$

Using this 'shear retention factor' β doesn't only reduce numerical problems but also enhances the models physical representation of reality, where the retention

of some shear stiffness at the crack interface can be considered as the numerical representation of aggregate interlock. Often a constant value for β is adopted by researchers (commonly $\beta = 0.2$ is used) but sometimes β is related to the crack strain (Kolmar, et al., 1984), which is more realistic considering that the mode II stress transfer capacity of a crack would decrease as the crack opens (de Borst, et al., 2002).

Numerical difficulties may also arise due to the stiffness normal to the crack in eqn. (A.3.8) being equal to zero, thus a sudden drop of the tensile stress at the sampling point to zero once the crack is initiated. Experiments have shown that concrete is not a perfectly brittle material and that it actually possesses some residual tensile load carrying capability once the ultimate tensile strength has been exceeded. These observations have led to the inclusion of tension softening models where a descending branch was introduced to represent the gradual decrease of tensile strength of the concrete as the crack strain increases. Hillerborg et al. (1976) proposed a Fictitious Crack Model for discrete crack models, which ensured that the release of energy due to the tensile softening of the material was mesh independent upon crack propagation. This concept was adapted to suit smeared crack modelling by Bazant and Oh (1983) (See Section A.3.1.2 on page 22), who developed the Crack Band Model, where the fracture energy G_f as introduced by Hilleborg, is 'smeared out' over a mesh area where the crack localises (de Borst, et al., 2002). This adaptation can be incorporated in the smeared cracking context by introducing a normal reduction factor μ in the secant stiffness matrix (de Borst, 2001):

$$\mathbf{D}_{\boldsymbol{ns}}^{\boldsymbol{s}} = \begin{bmatrix} \mu E & 0 & 0 \\ 0 & E & 0 \\ 0 & 0 & \beta G \end{bmatrix} \tag{A.3.9}$$

This normal reduction factor can be defined as a function of the strain normal to the crack $\mu = \mu(\varepsilon_{nn})$. Finally Poisson coupling after crack formation is added, which results in a relation incorporating mode II shear retention and mode I crack band formulation of Bazant and Oh (1983) in the secant stiffness matrix:

$$\mathbf{D}_{\boldsymbol{ns}}^{\boldsymbol{s}} = \begin{bmatrix} \frac{\mu E}{1-v^2\mu} & \frac{v\mu E}{1-v^2\mu} & 0 \\ \frac{v\mu E}{1-v^2\mu} & \frac{E}{1-v^2\mu} & 0 \\ 0 & 0 & \beta G \end{bmatrix} \tag{A.3.10}$$

The defining feature of this fixed single crack model formulation is the inclusion of the shear retention factor, β, for the cracked plane – which is fixed upon the tension cut-off criterion being exceeded. The shear retention across the crack face causes a build of shear stress across the plane, which, in conjunction with a softening model for the stresses normal to the plane, will cause a new principal stress direction not aligned with the incipient crack direction, which then may result in the tension cut-off criterion to be violated in this newly formed principal direction. To overcome this problem, the Rotating Crack concept was introduced, originally by Cope et al. (1980). The Rotating Crack model is similar to the total-strain elasticity based fixed crack model, with the point of departure being at eqn. (A.3.7), where the angle φ is no longer a constant and fixed value established upon incipient cracking, but which now rather continuously changes as the stresses are revaluated. A term representing the shear stiffness across the cracking plane (βG) is no longer required, as the major principal stress direction is aligned with the normal to the crack plane throughout the cracking process. Thus the local n, s coordinate system (Figure A.3-2) is coaxial with the principal stress directions as cracking occurs, therefore the shear stress on the crack plane, σ_{ns}, is always zero (as is the nature of the principal stress tensor). The shear strain γ_{ns} also equals zero as it is rotated continuously about the same angle φ, thus it is meaningless to incorporate a shear stiffness term in the secant stiffness matrix in the n, s coordinate system. The shear stiffness is implicitly taken into account through the incessant rotation of the principal stress axes. Thus the Rotating Crack model eliminates the need for a feasible shear retention factor or function - which is innately difficult to determine – as well as the possibility that the tension cut-off criterion is violated by a principal stress tensor in a direction different to that of the first crack (de Borst, et al., 2002). The rotating crack model has been found to yield results with a lower limit failure load when compared to the fixed crack model (DIANA, 2009). This has been attributed to the fact that the rotating crack model is not affected by spurious stress-locking which occurs in the fixed crack model. This stress-locking results

in an overestimation of the failure load due to the significant rotation of stresses after the formation of the crack (Rots, 1988) – thus the tensile failure criterion may actually be exceeded in the new principal stress directions .

A.3.1.2 Softening and Fracture Energy concepts

As was previously elucidated, concrete is not a perfectly brittle material and tensile ductility has been experimentally observed. The softening relations are incorporated in the formulation of the smeared crack models as seen in eqn. (A.3.9) by introduction of the parameter μ - the normal stress reduction factor. This parameter can be determined from a simple tensile test (for tensile softening modeling) but implementation of these experimentally established values in FEM analyses have yielded results which are not mesh independent (Bazant, 1976). Thus a material parameter termed the fracture energy (G_f) was introduced to overcome this problem. This fracture energy is defined as the 'amount of energy that is required to create one unit area of a continuous crack', and is the primary parameter that governs crack propagation (de Borst, 2001).

A.3.1.2.1 TENSILE SOFTENING

Tensile softening refers to the gradual reduction in the tensile load carrying capacity of a material due to its innate ductility. These softening models attempt to emulate the physical fracture process of cracking, being the principal fracture process in concrete. Upon cracking, a small region in front of the crack tip develops in which many micro-cracks form and combine. This region is commonly termed the 'fracture process zone'. If this fracture process zone is small enough when compared with the overall structural dimensions, the assumption of linear elastic fracture mechanics still holds. However, as it develops and grows the cohesive forces (responsible for the crack formation and combination) in the fracture process zone need to be accounted for, and the need arises for the use of 'cohesive zone models'. In these models, the degrading mechanisms ahead of the crack tip are monitored along a discrete line ahead of the crack tip, along which a stress-separation diagram ($\sigma - w \; or \; \sigma - \varepsilon$) reflects the softening effects within the fracture process zone. See Figure A.3-3 for an illustration of the crack tip and cohesive zone, where the many micro cracks and fracture mechanisms ahead of the crack tip are taken as acting along the discrete line of the cohesive zone (de Borst, 2001).

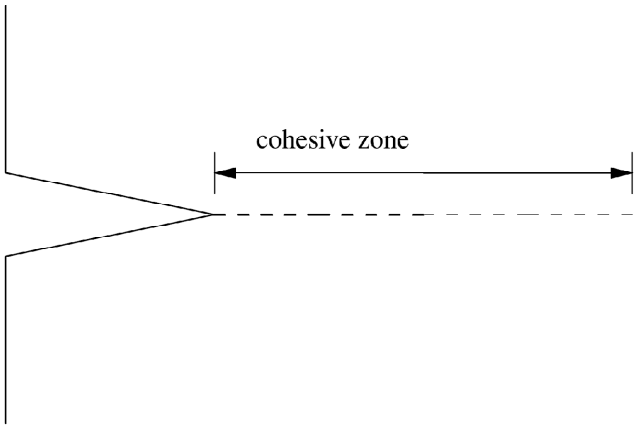

Figure A.3-3 - Cohesive Zone and crack tip (de Borst, 2001).

Not only is the shape of the stress-separation law dependant on the material but also the area beneath the curve, which represents the fracture energy, G_f. The fracture energy (mode I) is formally defined as follows (de Borst, 2001), (Rots, et al., 1985) :

$$G_f = \int \sigma_{nn}\, dw \tag{A.3.11}$$

where σ_{nn} and w are the stress and displacement (crack mouth opening displacement) across the fracture process zone respectively. w is therefore the sum of all the opening displacements of all the micro cracks in the fracture process zone. Refer to Figure A.3-4 b) which illustrates this relationship.

Hillerborg's (1976) fictitious crack model for concrete was developed for quasi-brittle materials which ensured a mesh independent release of fracture energy during crack propagation. This concept was then adapted to fit the framework of smeared formulations by Bazant and Oh (1983), who formulated the crack band model. In this formulation the fracture energy is assumed to be 'smeared out' over a width of area in the mesh in which the crack localizes, termed the crack band width h (See Figure A.3-4 a)). Thus w is represented as being the crack strain which is accumulated across this crack band width over which the cracks are 'smeared' (Rots, et al., 1985):

$$w = \int_h \varepsilon_{nn}^{cr}(x)dx \tag{A.3.12}$$

Combining eqns. (A.3.11) and (A.3.12) leads to (de Borst, 2001):

$$G_f = \int \int \sigma_{nn}\, d\varepsilon_{nn}^{cr}(x)dx \tag{A.3.13}$$

With x being the spatial variable orthogonal to the crack direction and ε_{nn}^{cr} being mode I cracking strain. It is then assumed that the micro cracks are distributed uniformly over the bandwidth h in the area where the strain has localized, resulting in (Rots, et al., 1985):

$$w = h\varepsilon_{nn}^{cr} \tag{A.3.14}$$

Thus eqn. (A.3.11), with $dw = hd\varepsilon_{nn}^{cr}$, becomes:

$$G_f = hg_f \tag{A.3.15}$$

where g_f is the energy dissipated per unit area of fully damaged material:

$$g_f = \int \sigma_{nn}\, d\varepsilon_{nn}^{cr} \tag{A.3.16}$$

See Figure A.3-4 a) for a diagrammatic representation of the above formulation.

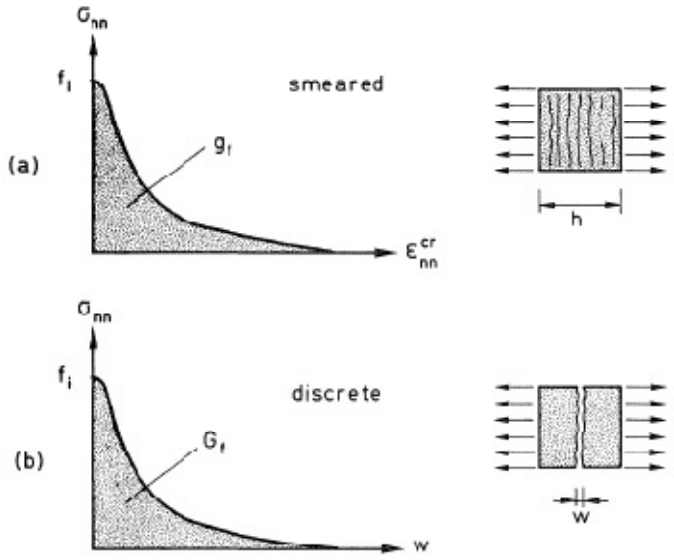

Figure A.3-4 - Smeared cracking concepts (Rots, et al., 1985).
a) Tensile Stress vs. Cracking Strain (Smeared approach)
b) Tensile Stress vs. Crack mouth opening displacement (Discrete approach).

Now assuming a uniform strain distribution, and performing the integral of eqn. (A.3.24) for the case of a linear softening diagram, the following expression is obtained for the ultimate strain at which the tensile strength is depleted (de Borst, 2001):

$$\kappa_u = \frac{2G_f}{f_t h} \tag{A.3.17}$$

Which is related to the mesh element size and the tensile fracture energy, ensuring the ultimate strain is attained and fracture energy is dissipated over the mesh element size where the localization occurs. For the case of a one dimensional bar divided into m linearly interpolated elements and of length L, with $h=L/m$ a softening modulus S can be obtained as:

$$S = -\frac{Lf_t^2}{2mG_f - Lf_t^2/E} \tag{A.3.18}$$

It is clear that this softening modulus is proportional to the overall structural size and inversely proportional to the number of elements.

When one of the elements in the bar's discretization is given a slightly lower tensile strength than the others (to ensure localization), the following expression can be obtained for the average strain in the bar beyond the ultimate tensile load:

$$\bar{\varepsilon} = \frac{\sigma}{E} + \frac{2G_f(f_t - \sigma)}{Lf_t^2} \tag{A.3.19}$$

It is evident that the inclusion of the fracture energy in the formulation has made the stress vs. average strain curve, and thus the load vs. displacement curve, not depend on the refinement of the mesh (de Borst, 2001).

Extending this to 2 and 3 dimensional examples does not lead to the global load displacement response being entirely independent of the mesh size as in the previous one dimensional situation. This can mainly attributed to the difficulty involved in determining the crack bandwidth h. This is especially the case when the crack propagation takes place in directions that intersect the mesh lines. It is usually assumed that the fracture energy is distributed over a width which is related to the area of a mesh element (A_e) (Feenstra, 1993):

$$w = \alpha\sqrt{A_e} = \alpha\sqrt{\sum_{i=1}^{NINT} \gamma_i det\mathbf{J_i}} \tag{A.3.20}$$

where α is a modification factor that depends on the integration scheme and element type, γ_i are the weight factors for the integration scheme and $\mathbf{J_i}$ the Jacobian matrix of the transformation from the isoparametric coordinate system to the global coordinate system for integration i.

A.3.1.2.2 COMPRESSIVE SOFTENING

A similar approach is applied to model the compressive softening of concrete to ensure the dependence of the model on the discretization of the finite element mesh is eliminated. It has been suggested that compressive behavior be modeled using compressive softening models which incorporate a dependence on compressive fracture energy (G_c), in a similar manner to the crack band models for modeling tensile behavior (Feenstra, 1993). Figure A.3-5 illustrates a fracture energy based compression curve with κ_c denoting the internal damage variable and f_c the ultimate compressive strength (de Borst, 2001).

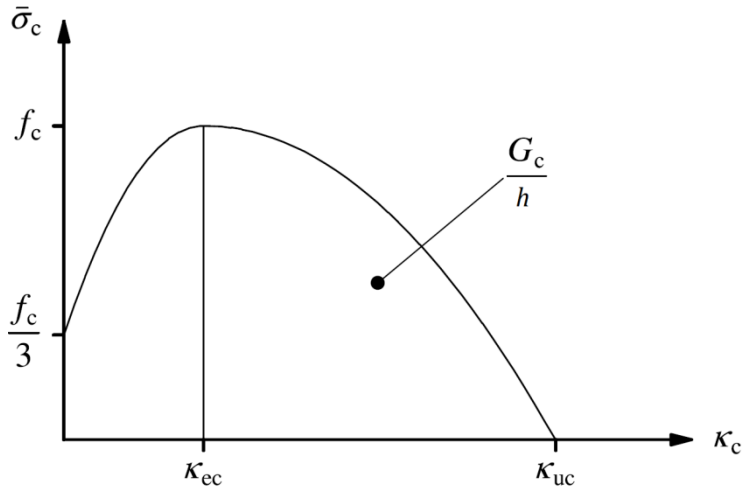

Figure A.3-5 - Fracture Energy based stress-strain compression curve (de Borst, 2001).

The following equations governing this compressive behavior (for the simple parabolic relationship considered) are (de Borst, 2001):

$$\bar{\sigma}_c(\kappa_c) = \begin{cases} \frac{f_c}{3}\left(1 + 4\frac{\kappa_c}{\kappa_{cc}} - 2\frac{\kappa_c^2}{\kappa_{ec}^2}\right) & if \quad \kappa_c < \kappa_{ec} \\ f_c\left(1 - \frac{(\kappa_c - \kappa_{ec})^2}{(\kappa_{uc} - \kappa_{ec})^2}\right) & if \quad \kappa_{ec} \leq \kappa_c < \kappa_{uc} \end{cases} \tag{A.3.21}$$

The maximum compressive stress f_c is attained at an equivalent strain of κ_{ec}, which does not depend on the mesh size or fracture energy (as these parameters are included only in the softening phase):

$$\kappa_{ec} = \frac{4}{3}\frac{f_c}{E_c} \tag{A.3.22}$$

The ultimate compressive strain, however, is related to the mesh size and the compressive fracture energy (similar to the crack band model's dependence of ultimate tensile strain on tensile fracture energy and mesh size to model the materials ductility) as follows (de Borst, 2001):

$$\kappa_{ec} = \frac{3G_c}{2hf_c} \tag{A.3.23}$$

A.3.1.3 TENSILE BEHAVIOR

Several approaches are available to model the tensile behaviour of reinforced concrete when using the total strain crack model. Fracture energy based formulations representing tensile behaviour are available for implementation in DIANA. The user may also implement tensile softening relations which are not directly dependant on the fracture energy such as a linear relation, multi linear relation or brittle behaviour. In these relations certain values for stress and strain need to be specified. The various tensile softening curves are summarised in Figure A.3-6 (DIANA, 2009). Note the fracture energies of graphs d) e) and f) should be defined as the area under the graph of the stress strain response after the tensile strength is reached, being the inelastic work available for crack propagation, thus existing in the domain defined by ε_p, with $\varepsilon_t \leq \varepsilon_p \leq \varepsilon_{ult}$.

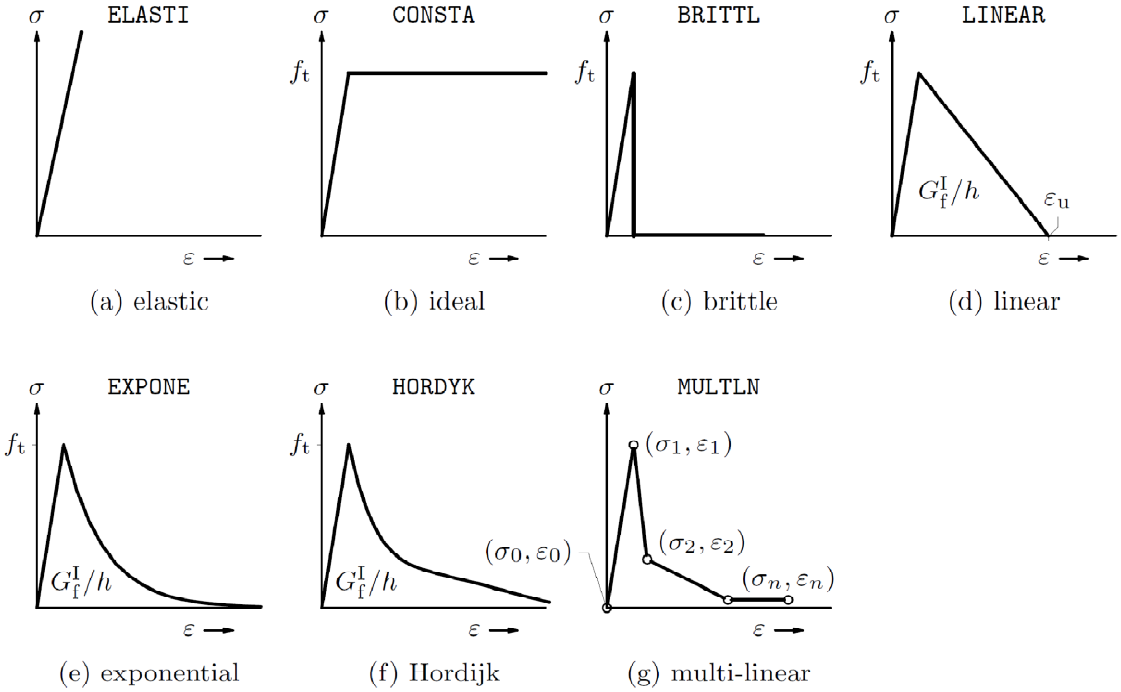

Figure A.3-6 - Predefined Tension Curves available for implementation in (DIANA, 2009).

A.3.1.4 SHEAR BEHAVIOR

Modelling of the shear behaviour is only required if implementing the fixed crack concept where the shear stiffness is reduced after cracking. A constant shear stiffness reduction may be modelled in DIANA, utilizing a specified shear retention factor β, with $0 \leq \beta \leq 1$. Implementing a variable shear retention

factor is also possible, through implementing it as a function of either shear stress or shear strain (DIANA, 2009).

A.3.1.5 Compressive Behavior

Various models are also available for modelling the compressive behaviour of concrete, and are shown in Figure A.3-7. These are based on either fracture energy or on known stress-strain points on the response path as established from compressive testing.

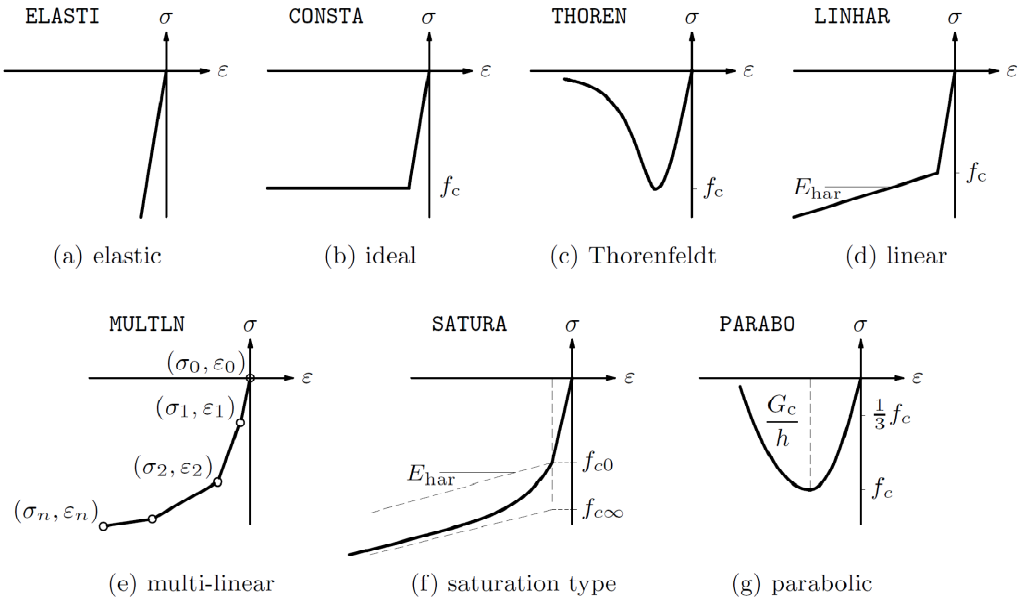

Figure A.3-7 - Predefined Compression Curves available for implementation in DIANA (DIANA, 2009).

A.3.2 PLASTICITY

When considering elastic and plastic behaviour of materials, the key observation is that permanent deformations do not occur when considering elastic material behaviour, but such permanent and irreversible deformations can occur in plastic material behaviour. Generally, when small strains are considered, the inclusion of the permanent deformations in the mathematical framework of plasticity models is done by the decomposition of the strain into an elastic and plastic (irreversible) part, as follows (de Borst, et al., 2002):

$$\varepsilon = \epsilon_e + \varepsilon_p \tag{A.3.24}$$

Before discussing the specific plasticity model used in this study, a brief overview of some of the concepts inherent in the mathematical framework of plasticity model formulations will be discussed in a simple form, to elucidate the processes by which these relations are governed and how they are implemented numerically to conform to the nature of the Finite Element Method.

A.3.2.1 SIMPLE SLIP MODEL (COULOMB FRICTION)

The relatively complex plasticity concepts are best explained with a formulation of plasticity theory based on a simple spring sliding system as shown in Figure A.3-8.

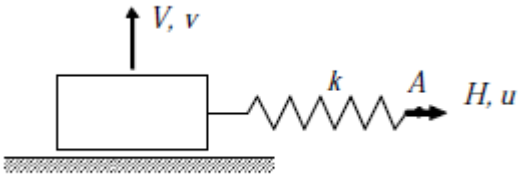

Figure A.3-8 - Simple two degree of freedom spring-sliding system (de Borst, et al., 2002).

Initially, the displacement of point A is entirely due to the deformation in the spring, due to the friction between the block and the floor preventing the sliding of the block. The block will thus only start sliding once the maximum shear force due to the friction is overcome. Once this occurs, the total horizontal displacement of point A will be due to both the sliding of the block as well as the deformation in the spring. With u denoting the horizontal displacement of point A and using the superscripts e and p to denote the contributions from the spring's

deformation and the sliding of the block respectively, the total displacement of point A (after sliding has started) can thus be expressed by the following (de Borst, et al., 2002):

$$u = u^e + u^p \tag{A.3.25}$$

The first component of this equation is usually referred to as the elastic component, due to the fact that once the force on the spring is removed, the deformation in the spring is recovered. However, the second component of the equation is that due to the movement of the block, a displacement which is not recoverable upon removal of the force and is thus named inelastic or permanent deformation (de Borst, et al., 2002).

If the surface between the block and the floor is slightly rough, any horizontal movement of the block will also cause vertical movement of the block. The plastic component of the vertical displacement will be denoted by v^p. Thus the plastic displacement components for the body can then be collected in a vector $\mathbf{u^p}$ (de Borst, et al., 2002):

$$\mathbf{u^p} = [u^p,\ v^p]^T \tag{A.3.26}$$

The elastic deformation components can also be collected into a vector $\mathbf{u^e}$**:**

$$\mathbf{u^e} = [u^e,\ v^e]^T \tag{A.3.27}$$

Thus eqn. (A.3.25) can be expanded to include the vertical displacements:

$$\mathbf{u} = \mathbf{u^e} + \mathbf{u^p} \tag{A.3.28}$$

An important difference between these two deformations, the elastic (spring deformations) and plastic or inelastic (the sliding deformations), is that there only exists a unique relationship between the elastic deformation and the applied force H (de Borst, et al., 2002):

$$H = ku^e \tag{A.3.29}$$

where k is the spring constant. It is evident that if the force H were to be reduced to zero after having had some non-zero value, the elastic displacement u^e would also reduce to zero (recovered deformation). No such unique relationship can be

established between the force and the inelastic deformation, as the inelastic deformation cannot be expressed in terms of an instantaneous value of the applied force as in eqn. (A.3.29). However, the velocity of the inelastic deformation during the plastic deformation phase (sliding of the block) can be determined. Now it is assumed that the relationship between the vertical plastic deformation velocity $\dot{v}^p$ and the horizontal plastic deformation $\dot{u}^p$ velocity is controlled by a new parameter ψ, called the dilatancy angle, as follows (de Borst, et al., 2002):

$$tan\psi = \frac{\dot{v}^p}{\dot{u}^p} \tag{A.3.30}$$

With this relationship established, the direction of the plastic flow can be fully determined by introducing the factor $\dot{\lambda}$ (de Borst, et al., 2002):

$$\dot{\mathbf{u}}^{\mathbf{p}} = \dot{\lambda}\mathbf{m} \tag{A.3.31}$$

where the factor $\dot{\lambda}$ can be established from the prerequisite that during plastic flow, the force remains bounded, and with:

$$\mathbf{m} = \begin{bmatrix} 1 \\ tan\,\psi \end{bmatrix} \tag{A.3.32}$$

This is called the flow theory of plasticity and is the most ubiquitous theory in plasticity literature. The transition between plastic and elastic stress states can be defined in a simple manner even for multi-dimensional stress states, which is not the case for the so-called deformation theories of plasticity where the plastic strain and not the strain rate is related to instantaneous values of the stresses (in this simple case the force) (de Borst, et al., 2002).

The force vector $\mathbf{f}$ is now defined in a similar manner to the displacement vector:

$$\mathbf{f} = [H, V]^T \tag{A.3.33}$$

Thus the elastic displacement vector can be related to the force vector by multiplication with the elastic stiffness matrix $\mathbf{D^e}$:

$$\mathbf{f} = \mathbf{D^e u^e} \tag{A.3.34}$$

with $\mathbf{D^e}$ defined as follows:

$$\mathbf{D^e} = \begin{bmatrix} k & 0 \\ 0 & 0 \end{bmatrix} \tag{A.3.35}$$

Next the deformation decomposition (A.3.28) is differentiated:

$$\dot{\mathbf{u}} = \dot{\mathbf{u}}^{\mathbf{e}} + \dot{\mathbf{u}}^{\mathbf{p}} \tag{A.3.36}$$

as well as the elastic force displacement relation for the spring:

$$\dot{\mathbf{f}} = \mathbf{D^e}\dot{\mathbf{u}}^{\mathbf{e}} \tag{A.3.37}$$

These two equations are then combined and using the definition established for the direction of the plastic velocity one obtains (de Borst, et al., 2002):

$$\dot{\mathbf{f}} = \mathbf{D^e}[\dot{\mathbf{u}} - \dot{\lambda}\mathbf{m}] \tag{A.3.38}$$

The onset of plastic deformations has thus far been vaguely described as being the instant once the maximum shear force between the block and the floor has been overcome. However a more mathematically sound description is required to describe the borderline between the purely elastic deformations and the onset of plastic deformations. The simplest assumption is that sliding takes place once the Coulomb friction, along with some adhesion coefficient, is overcome described by (de Borst, et al., 2002):

$$H + V\tan\phi - c = 0 \tag{A.3.39}$$

with the variables ϕ and c being the friction angle and adhesion coefficient respectively. The second term would contribute negatively due to $V < 0$. Eqn. (A.3.39) is known as the yield function, and bounds the maximum value of the horizontal stress, in this case the maximum permissible force. The extension of this yield function described in terms of forces as in eqn. (A.3.39) to some continuum problem is performed by expressing it in terms of stresses and strains. Thus in a higher dimensional continuum problem, a yield surface can be described as “a function that defines the hyper surface in the n-dimensional stress space which separates permissible form non-permissible stress states” (de Borst, et al., 2002). If the stresses on the body coincide with a stress point within this yield function or surface, the associated deformations are solely

elastic and plastic deformations only occur when the stress point is this the yield surface. Note that, for this simple system, forces and displacements are used to more effectively describe plasticity concepts, whereas the extension of the theory to a continuum would instead entail the use of stresses and strains in the formulations. Exclusively, elastic deformations would take place if:

$$H + V\tan\phi - c < 0 \tag{A.3.40}$$

A situation where

$$H + V\tan\phi - c > 0 \tag{A.3.41}$$

is physically impossible, as the maximum horizontal force is limited by the restriction imposed by eqn. (A.3.39). Upon assuming ϕ and c are constants and deriving eqn. (A.3.39) yields (de Borst, et al., 2002):

$$\dot{H} + \dot{V}\tan\phi = 0 \tag{A.3.42}$$

which can be written symbolically, utilizing the vector $\mathbf{n}$**:**

$$\mathbf{n} = \begin{bmatrix} 1 \\ \tan\phi \end{bmatrix} \tag{A.3.43}$$

resulting in:

$$\mathbf{n^T}\dot{\mathbf{f}} = 0 \tag{A.3.44}$$

Now to obtain an expression for the factor $\dot{\lambda}$, eqn. (A.3.38) is pre-multiplied with $\mathbf{n^T}$ knowing that eqn. (A.3.44) must hold during plastic flow, giving the following (de Borst, et al., 2002):

$$\dot{\lambda} = \frac{\mathbf{n^T D^e \dot{u}}}{\mathbf{n^T D^e m}} \tag{A.3.45}$$

which can be substituted directly into eqn. (A.3.38) to obtain a direct relation between the rate of force vector $\dot{\mathbf{f}}$ and the velocity vector $\dot{\mathbf{u}}$ (de Borst, et al., 2002):

$$\dot{\mathbf{f}} = \left[\mathbf{D}^{\mathbf{e}} - \frac{\mathbf{D}^{\mathbf{e}}\mathbf{m}\mathbf{n}^{\mathbf{T}}\mathbf{D}^{\mathbf{e}}}{\mathbf{n}^{\mathbf{T}}\mathbf{D}^{\mathbf{e}}\mathbf{m}}\right]\dot{\mathbf{u}} \tag{A.3.46}$$

Generally the incremental equations of eqn. (A.3.46) are non-symmetric as the vectors $\mathbf{m}$ and $\mathbf{n}$ are not equal due to $\phi \neq \psi$. A direct relation between force (stress) and displacement (strain) cannot be established by this flow theory of plasticity, only a relation between the force rate (stress rate) and the velocity (strain rate). Important to mention is the fact that once the condition for plastic flow (as represented by eqn. (A.3.39)) is no longer satisfied, purely elastic behaviour is then once again observed. Thus unloading in a plasticity based system is solely an elastic process, which also holds for reloading provided the conditions of the inequality of eqn. (A.3.40) are met. This process is shown in Figure A.3-9 (de Borst, et al., 2002).

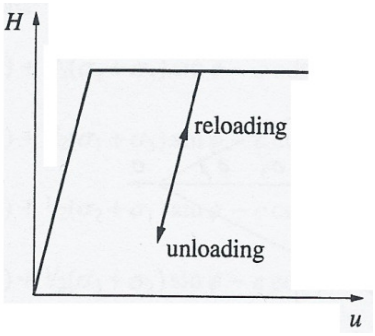

Figure A.3-9 - Loading, unloading, reloading concepts for simple plasticity model (de Borst, et al., 2002).

Extending this simple model to a continua where the yield conditions are described in terms of stresses (a specific example of which is used in this study will be discussed further at a later stage), it is convenient to introduce the more abstract concept of a yield function which bounds all the possible stress states (de Borst, et al., 2002):

$$f(\boldsymbol{\sigma}) \leq 0 \tag{A.3.47}$$

where the equality sign accounts for stress states on the yield surface (or contour depending on the dimensional space the yield function exists in) and the inequality sign accounts for the stress states within the yield function, thus those causing purely elastic deformations.

A.3.2.2 The Flow Rule

In order to obtain plastic deformations the stress point must not merely be on the yield surface, but must actually remain there for a short while. Thus plastic straining will only occur if the following two conditions are met simultaneously (de Borst, et al., 2002):

$$f = 0 \tag{A.3.48}$$

$$\dot{f} = 0 \tag{A.3.49}$$

The second of these conditions is usually referred to as Prager's consistency condition and denotes that the yield condition needs to be satisfied for a least some small time increment for plastic flow to occur (de Borst, et al., 2002).

The yield function still only bounds the elastic domain, in which an expression between the stress and strain (only elastic) can be obtained upon the onset of plastic flow when eqs. (A.3.48) and (A.3.49) are satisfied (de Borst, et al., 2002)**:**

$$\boldsymbol{\sigma} = \mathbf{D^e}\boldsymbol{\varepsilon^e} \tag{A.3.50}$$

where $\mathbf{D^e}$ is the continuum elastic stiffness matrix. The remainder of the strain is the plastic strain, which is obtained by subtraction of the elastic strain from the total strain:

$$\boldsymbol{\varepsilon_p} = \boldsymbol{\varepsilon} - \boldsymbol{\epsilon_e} \tag{A.3.51}$$

Combination of eqns. (A.3.50) and (A.3.51) yields (de Borst, et al., 2002):

$$\boldsymbol{\sigma} = \mathbf{D^e}(\boldsymbol{\varepsilon} - \boldsymbol{\varepsilon^p}) \tag{A.3.52}$$

In a three dimensional situation, eqn. (A.3.52) contains six equations and twelve unknowns (six from the stress vector $\boldsymbol{\sigma}$ and another six from the plastic strain vector $\boldsymbol{\varepsilon^p}$). The overall strain vector $\boldsymbol{\varepsilon}$ is known and can be obtained directly from the displacement field. Five of the six missing equations need to be supplied by measurements, where the remaining equation can be obtained from the consistency requirement eqn. (A.3.49). Considering the equation that results from the mathematical structure of the plasticity theory, we now express the plastic strain rate as follows to obtain the flow rule (de Borst, et al., 2002):

$$\dot{\boldsymbol{\varepsilon}}^{\mathbf{p}} = \dot{\lambda}\mathbf{m} \tag{A.3.53}$$

In equation (A.3.53) $\dot{\lambda}$ is the magnitude of the plastic flow, and $\mathbf{m}$ describes the direction of plastic flow. Considering that the yield function f has up to now been considered as only a function of the stress tensor, $f = f(\boldsymbol{\sigma})$, the consistency condition of eqn. (A.3.49) can be expressed as:

$$\mathbf{n}^{\mathbf{T}}\dot{\boldsymbol{\sigma}} = 0 \tag{A.3.54}$$

where $\mathbf{n}$ is the gradient vector of the yield function at the current stress point under consideration, see Figure A.3-10.

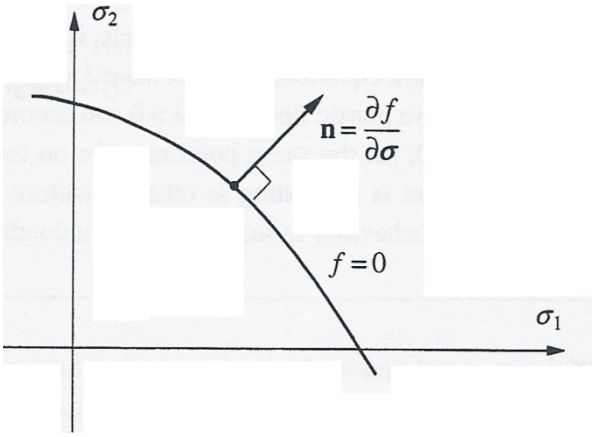

Figure A.3-10 - Gradient Vector n, normal to the yield surface (de Borst, et al., 2002)

$$\mathbf{n} = \frac{\partial f}{\partial \boldsymbol{\sigma}} \tag{A.3.55}$$

Now, similar to what was done in the simple sliding block example, eqn. (A.3.52) is derived with respect to virtual time, and the eqs. (A.3.53) and (A.3.54) are substituted into the result to obtain the following expression for the amount of plastic flow (de Borst, et al., 2002):

$$\dot{\lambda} = \frac{\mathbf{n}^{\mathbf{T}}\mathbf{D}^{\mathbf{e}}\dot{\boldsymbol{\varepsilon}}}{\mathbf{n}^{\mathbf{T}}\mathbf{D}^{\mathbf{e}}\mathbf{m}} \tag{A.3.56}$$

Now the relation between stress rate and strain rate is obtainable (as was done for the simple slip model between force rate and velocity, cf. eqn. (A.3.36).

$$\dot{\boldsymbol{\sigma}} = \left[\mathbf{D^e} - \frac{\mathbf{D^e m n^T D^e}}{\mathbf{n^T D^e m}}\right]\dot{\boldsymbol{\varepsilon}} \tag{A.3.57}$$

The vector $\mathbf{m}$, the plastic flow direction, needs to be established experimentally, or some initial assumption can be made regarding the flow direction which can then later be verified. Ideal plastic material behaviour results in what is referred to as associated plasticity, which occurs when the plastic flow direction, $\mathbf{m}$ is a scalar multiple of the gradient vector of the yield function, $\mathbf{n}$. Thus the plastic flow direction is also orthogonal (or normal, referred to as the 'normality rule') to the yield surface. Thus the following holds for an 'associated plasticity' flow rule (de Borst, et al., 2002):

$$\mathbf{m} = \mu\mathbf{n} \tag{A.3.58}$$

$$\dot{\boldsymbol{\varepsilon}}^{\mathbf{p}} = \dot{\lambda}\mathbf{n} \tag{A.3.59}$$

However, flow rules that do not adhere to the condition of eqn. (A.3.58) are called 'non-associated' flow rules and thus do not obey the normality rule. A subclass of these rules, which covers the majority of such applications, is defined such that a function of the stresses, g (termed the plastic potential function) exists in such a way that (de Borst, et al., 2002):

$$\mathbf{m} = \frac{\partial g}{\partial \boldsymbol{\sigma}} \tag{A.3.60}$$

Thus the plastic flow direction is orthogonal to the surface described by the equation $g=0$.

Therefore a non associated flow rule, where the strain development commences in a direction perpendicular to the plastic potential surface (the stress derivative of the plastic potential functions) can be expressed by combining eqns. (A.3.53) and (A.3.60) (de Borst, et al., 2002):

$$\dot{\boldsymbol{\varepsilon}}^{\mathbf{p}} = \dot{\lambda}\frac{\partial g}{\partial \boldsymbol{\sigma}} \tag{A.3.61}$$

It is evident that non-associated flow rules ($\mathbf{m}\neq\mu\mathbf{n}$) will result in a non-symmetric tangential operator when considering the relation between stress rate and strain rate as in eqn. (A.3.57), whereas associated flow rules ($\mathbf{m}=\mu\mathbf{n}$) yield a symmetric

tangential operator and thus numerical stability is often more easily attained when solving such a system.

So far, it has been assumed that the yield function solely depends on the stress tensor, $\boldsymbol{\sigma}$. However, considering the simple sliding block model, it is conceivable that as the horizontal force overcomes the friction force, the adhesion between the block and the floor would reduce with time, thus the friction coefficient can be expressed as a descending function that depends on the total amount of sliding the block has undergone (thus depends on the previous loading history). In early applications of Finite Element Analysis to the structural mechanics of quasi brittle materials (such as concrete), an abrupt drop to zero stress level upon the attainment of the tensile and compressive strength of the material, was assumed. However, these assumptions were shown to be erroneous due to the results obtained from carefully conducted experiments which showed that a descending branch on the force-displacement results was observed, termed the 'softening' of the material, where the 'hardening' would be represented by the inelastic ascending slope of the results. Yield functions have therefore been adapted in some cases to incorporate parameters that deem the entire function dependant on the strain history of the system. The simplest extension of the yield function beyond the realms of ideal plasticity as has been discussed until now is to include the dependence of the yield function on a scalar measure of the plastic strain tensor as follows (de Borst, et al., 2002):

$$f = f\left(\boldsymbol{\sigma}, \kappa\right) \tag{A.3.62}$$

The yield function of eqn. (A.3.62) depends on stress tensor as well as the scalar value κ, the hardening parameter, which is dependent on the strain history. However, various options are available to express the dependence of the yield function on the strain history. Typically these entail the hardening parameters being dependant on the invariants of the plastic strain tensor, or possibly on the dissipated plastic work; or even functions of either the invariants of the plastic strain tensor or dissipated plastic work may be used instead of merely a scalar value. Commonly, two choices for the formulation of hardening parameter are used, namely the work hardening or strain hardening hypotheses. These hypotheses result in a scalar value for κ, meaning that the yield surface can only expand or shrink and not translate or rotate in the stress space considered. Due

to this these hardening hypotheses are often referred to as isotropic hardening, where the shrinking of the yield surface is described as isotropic softening (de Borst, et al., 2002). Figure A.3-11 illustrates the isotropic hardening of a yield surface. Elastic loading occurs within the yield surface along path OA until the initial yield surface is encountered. The plastic stress increment AB then occurs upon further loading of the material and causes isotropic hardening or uniform expansion of the yield surface which now encapsulates the new stress space shown as the subsequent yield surface. Any unloading that may now occur within this subsequent yield surface, such as path BA, will be elastic as well as any reloading such as path OC (Pedersen, et al., 1996).

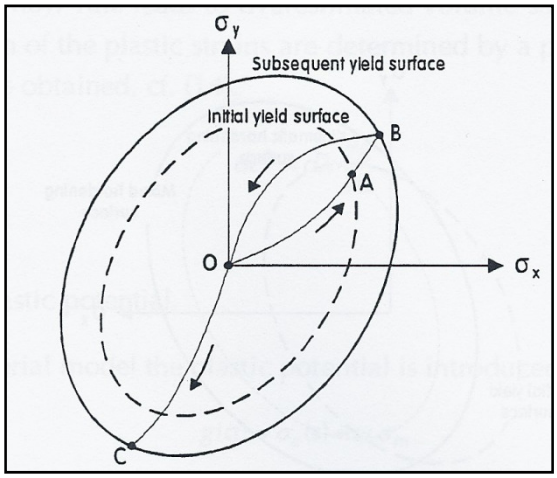

Figure A.3-11 - Isotropic hardening (Pedersen, et al., 1996).

There are, however, models to describe the translation of the yield surface which are termed kinematic hardening models. For these instances, a scalar representation of hardening no longer suffices, and a tensor description is required to describe the movement of the origin of the yield surface in the stress space (de Borst, et al., 2002). These kinematic hardening models were formed due to the observed Bauschinger effect, where the plastic deformation in one material direction led to a proportional decrease in the elastic capacity of the opposite direction. This can be seen in Figure A.3-12. The plastic deformation caused by the plastic stress increment of path AB, has cause the yield surface to translate in the stress space in the direction of this maximum principal stress increment. The subsequent yield surface now restricts the elastic range that reloading along path OC is able to undergo, hence its elastic capacity in this direction has been diminished (Pedersen, et al., 1996).

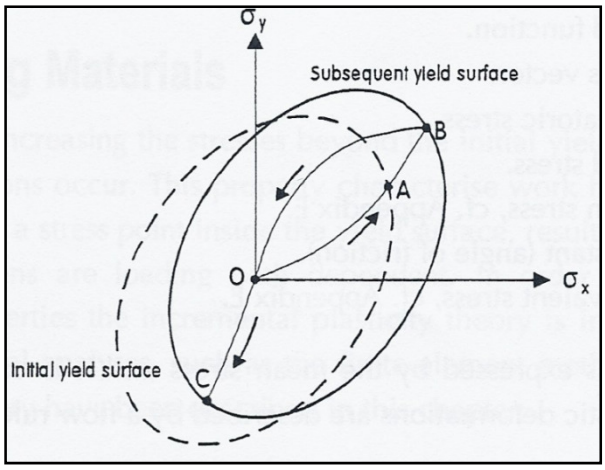

Figure A.3-12 - Kinematic hardening (Pedersen, et al., 1996).

The inclusion of hardening functions further complicates the solution process as more terms are gathered in the consistent tangential matrix of eqn. (A.3.57), especially when considering non associated plasticity where the tangential operator is non-symmetric. Due to this, as well as the fact that fundamentally the flow rule of plasticity yields a relationship between the stress rate and the strain rate, the obtainment of accurate results through the necessary integration can become very complex, especially once multi-dimensional stress states are considered. Thus techniques such as the Euler backward method and return mapping are employed by any competent software programs available for the implementation of such plasticity theories, the intricacies of which will not be discussed here (de Borst, et al., 2002).

A.3.2.3 Rankine Hill Plasticity Model

Along with the Total Strain crack models as previously discussed the anisotropic Rankine Hill plasticity model will also be employed to model the constitutive relations of the concrete specimens under consideration. This is a multi-surface model, meaning two yield surfaces are considered for tensile and compressive behaviour, according to the models established by Rankine and Hill respectively. Thus yielding will occur if the stresses satisfy the general yield criterion:

$$f\left(\boldsymbol{\sigma}, \bar{\sigma}(\kappa)\right) = 0 \tag{A.3.63}$$

where $\bar{\sigma}(\kappa)$ is the hardening/ softening law (function of the scalar hardening parameter(κ) expressing the amount of plastic straining that has occurred) . The

elastic domain is thus defined by the two yield surfaces (according to Rankine and Hill), with the functions $f_i < 0$ defining the 'composite' yield surface (Lourenco, et al., 1997). The composite yield surface exists in a 3 dimensional stress space, defined by the stress axes σ_x, σ_y and τ_{xy} of The combined yield surface is shown in Figure A.3-13, with iso-shear stress lines indicating 'depth':

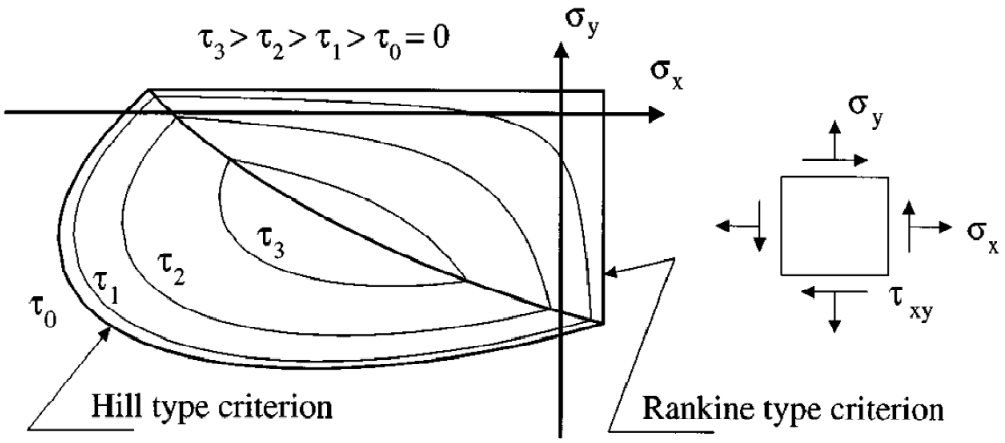

Figure A.3-13 - Combined Rankine-Hill yield surface, (Lourenco, et al., 1997)

For this composite yield surface, corners exist at the point of intersection of the two yield surfaces. This complication is overcome through using Koiter's generalization, in which the total plastic strain rate vector ($\dot{\boldsymbol{\varepsilon}}^{\mathbf{p}}$) in the corner is acquired by combining the plastic strain rate vectors of the intersecting yield surfaces in a linear manner as follows (Koiter, 1953):

$$\dot{\boldsymbol{\varepsilon}}^{\mathbf{p}} = \dot{\boldsymbol{\varepsilon}}_{\mathbf{1}}^{\mathbf{p}} + \dot{\boldsymbol{\varepsilon}}_{\mathbf{2}}^{\mathbf{p}} = \dot{\lambda}_1 \frac{\partial g_1}{\partial \boldsymbol{\sigma}} + \dot{\lambda}_2 \frac{\partial g_2}{\partial \boldsymbol{\sigma}} \tag{A.3.64}$$

The yield surfaces are assumed to be uncoupled as they represent the different failure mechanisms, tension and compression failure. Tension failure is considered as a localised fracture process (such as cracking of the material) whereas compressive failure is considered as more of a distributed fracture process (crushing of the material) (Lourenco, et al., 1997).

As was the case for Prager's consistency equation for plastic flow (cf. eqs. (A.3.48), (A.3.49)), Kuhn-Tucker's loading-unloading conditions are used in the Rankine-Hill model formulation to describe the onset and continuation of plastic

flow, and the subsequent return to elastic deformation. These conditions are described in the following three equations:

$$f \leq 0 \ , \qquad \dot{\lambda} \geq 0 \ , \qquad f\dot{\lambda} = 0 \tag{A.3.65}$$

Evidently, if a stress point is elastic, $f < 0$ and due to the third condition $\dot{\lambda} = 0$, thus no plastic flow. However, when plastic flow occurs, $\dot{\lambda} > 0$ and $f = 0$ must hold, then the stress point must be on the yield surface, all of which adheres to the formulation of the plasticity theory thus far (de Borst, et al., 2002).

A.3.2.3.1 THE RANKINE TYPE CRITERION

The Rankine yield criterion is expressed in terms of a single function of the first principal stress and a stress function $\bar{\sigma}_t(\kappa)$ (which describes the softening behavior) as follows:

$$f_1 = \frac{\sigma_x + \sigma_y}{2} + \sqrt{(\frac{\sigma_x - \sigma_y}{2})^2 + {\tau_{xy}}^2} - \bar{\sigma}_t(\kappa_t) \tag{A.3.66}$$

where κ_t is a scalar value controlling the amount of softening. As quasi-brittle materials, such as concrete, can be loaded to their maximum tensile strength even if damage has occurred in the direction perpendicular to the loading, an assumption of isotropic softening is not valid (where softening will occur equally in both directions due to the shrinking of the yield surface). Thus kinematic softening models should be used to describe such behavior by translation of the yield surface in the direction of the first principal stress (to express the softening in this direction, and not also show softening in the orthogonal material direction) (Feenstra, et al., 1995). Another consideration for isotropic softening models, is that if the softening in a certain direction of the material is completed, and subsequent loading is commenced in an orthogonal direction, the material response in this direction is ideally plastic, as the available fracture energy (inelastic work available for crack propagation) has been dissipated in the formation of the first crack. The use of two independent softening parameters can be considered to solve this problem, as each would separately control the appropriate shifting of the yield surface. Such a formulation, however, can result in numerical difficulties and be computationally expensive upon large scale implementation, thus a compromise has been developed (Lourenco, et al., 1997).

The dominating failure processes governing this multi-surface plasticity model are tensile and compressive failure. Tensile failure is represented by strain localization or cracking which is represented in the Rankine-Hill plasticity model by a fracture energy approach. The approach is similar to that more elaborately discussed in Section A.3.1.2.1 for the softening in the Total Strain models. This cracking of the material is seen as a dissipation of energy at the crack zone. A parameter termed fracture energy (G_f) is used to represent the amount of inelastic work available in the material. It is assumed that this fracture energy is uniformly dissipated in a representative area of the structure termed the equivalent length (h). Thus the cracking that occurs at the physical level is numerically modeled as a dissipation of the available fracture energy over this equivalent length of the model, thus reducing the tensile capacity (tensile softening) of the structure at this damaged zone (which is still considered to be a continuum). With this approach, the scalar κ can represent the localized damage, which is related to the released energy per unit cracked area (G_f) by the equivalent length, h. A similar concept is introduced to numerically describe compressive failure (crushing), through using compressive fracture energy (G_c) as is discussed later. This is not a widely accepted notion but has its use has shown to obtain mesh objective results (Lourenco, et al., 1997).

The equivalent length, h, over which the fracture energy is dissipated, is calculated in a such a way that it correlates to a representative dimension of the size of the mesh so that the results obtained are independent of the mesh refinement. It thus depends on the element size, type, shape and the problem under consideration (Lourenco, et al., 1997). In the Rankine-Hill formulation, the equivalent length is dependent on the area of the element (Feenstra, 1993):

$$h = \alpha_h \sqrt{A_e} = \alpha_h \left(\sum_{\xi=1}^{n_\xi} \sum_{\eta=1}^{n_\eta} \det(J) w_\xi w_\eta \right)^{\frac{1}{2}} \tag{A.3.67}$$

where α_h is a modification factor which equals 1 for quadratic elements and $\sqrt{2}$ for linear elements. w_ξ and w_η are the weight factors appropriate for Gaussian integration on the normalized element in the coordinate system defined by ξ and η.

The inelastic work ($g_{f/c}$) is then defined as the area under the stress strain diagram obtained for uniaxial loading, given by the following integral:

$$g_{f/c} = \int \boldsymbol{\sigma}^{\mathbf{T}} d\varepsilon^{p} \tag{A.3.68}$$

Then, based on the assumption that this inelastic work is evenly distributed over the equivalent length of the mesh, the following relation is obtained between the fracture energy ($G_{f/c}$), inelastic work ($g_{f/c}$) and the equivalent length (h):

$$g_{f/c} = \frac{G_{f/c}}{h} \tag{A.3.69}$$

Thus the material model is now related to this fracture energy which has to be dissipated due to the permanent deformations (irreversible damage) in the material (Lourenco, et al., 1997).

As previously discussed, a single scalar value, κ, is used in this formulation to control the softening in the Rankine criterion. This scalar value measures the amount of softening (thus represents the strain history) in the direction of the two material axes simultaneously, and not separately as would be more ideal but computationally more expensive. Thus the compromise is the incorporation of two different fracture energies for each material direction to express material anisotropy, so that the loading in a direction perpendicular to a fully developed crack will no longer lead to ideally plastic deformation as the fracture energy for this new direction is still available for dissipation. Thus the Rankine expression as in eqn. (A.3.66) is reformulated as follows to explicitly include softening in each material direction:

$$f_1 = \frac{(\sigma_x - \bar{\sigma}_t(\kappa_t)) + (\sigma_y - \bar{\sigma}_t(\kappa_t))}{2} + \sqrt{\left(\frac{(\sigma_x - \bar{\sigma}_t(\kappa_t)) - (\sigma_y - \bar{\sigma}_t(\kappa_t))}{2}\right)^2 + {\tau_{xy}}^2} \tag{A.3.70}$$

Modifying this expression to create a Rankine-type yield condition for an orthotropic material is done by incorporating different yield values along the x and y axes as below:

$$f_1 = \frac{(\sigma_x - \bar{\sigma}_{tx}(\kappa_t)) + (\sigma_y - \bar{\sigma}_{ty}(\kappa_t))}{2} + \sqrt{\left(\frac{(\sigma_x - \bar{\sigma}_{tx}(\kappa_t)) - (\sigma_y - \bar{\sigma}_{ty}(\kappa_t))}{2}\right)^2 + \alpha{\tau_{xy}}^2} \tag{A.3.71}$$

where the parameter α is introduced to control the contribution of the shear stress to failure:

$$\alpha = \frac{f_{tx} f_{ty}}{{\tau_{u,t}}^2} \tag{A.3.72}$$

where f_{tx} and f_{ty} are the tensile strength in the x and y directions and $\tau_{u,t}$ is shear strength corresponding to zero normal stress. Normally α has a value of one. These parameters are illustrated by the Rankine yield surface as depicted in Figure A.3-14.

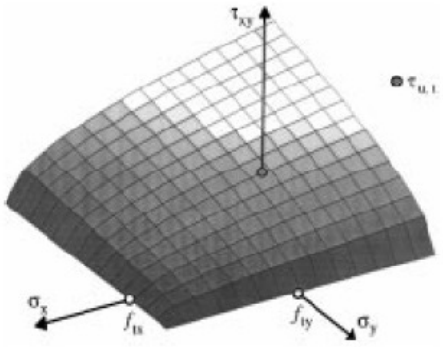

Figure A.3-14 - Rankine type Criterion for Orthotropic material (Lourenco, et al., 1997).

For convenience sake, the material axes are assumed to coincide with the physical coordinate system, thus eqn. (A.3.71) can be expressed as follows in matrix format:

$$f_1 = \left(\frac{1}{2}\boldsymbol{\xi}^{\mathbf{T}}\mathbf{P}_{\mathbf{T}}\boldsymbol{\xi}\right)^{1/2} + \frac{1}{2}\boldsymbol{\pi}^{\mathbf{T}}\boldsymbol{\xi} \tag{A.3.73}$$

where $\mathbf{P_T}$, the projection matrix: and $\boldsymbol{\pi}$ the projection vector are:

$$\mathbf{P_T} = \begin{bmatrix} \frac{1}{2} & -\frac{1}{2} & 0 \\ -\frac{1}{2} & \frac{1}{2} & 0 \\ 0 & 0 & 2\alpha \end{bmatrix} \quad \text{and} \quad \boldsymbol{\pi} = \begin{bmatrix} 1 \\ 1 \\ 0 \end{bmatrix} \tag{A.3.74}$$

and the reduced stress vector $\boldsymbol{\xi}$:

$$\boldsymbol{\xi} = \boldsymbol{\sigma} - \boldsymbol{\eta} \tag{A.3.75}$$

and finally where the stress vector and stress softening vector are defined by:

$$\boldsymbol{\sigma} = [\sigma_x \quad \sigma_y \quad \tau_{xy}]^T \tag{A.3.76}$$

$$\boldsymbol{\eta} = [\bar{\sigma}_{tx}(\kappa_t) \quad \bar{\sigma}_{ty}(\kappa_t) \quad 0]^T \tag{A.3.77}$$

Exponential tensile softening is assumed in the orthogonal directions with the different fracture energies (G_{fx} and G_{fy}) in each direction and for each yield value:

$$\bar{\sigma}_{tx} = f_{tx} \exp\left(-\frac{hf_{tx}}{G_{fx}}\kappa_t\right) \quad , \quad \bar{\sigma}_{ty} = f_{ty} \exp\left(-\frac{hf_{ty}}{G_{fy}}\kappa_t\right) \tag{A.3.78}$$

The notion of fracture energy and energy based softening derivation is deemed invalid if snap back behavior (at the constitutive level) is allowed to occur due to the element size being too large. The equivalent length h is therefore limited to prevent this from happening:

$$h \leq \frac{G_{fy}E_i}{f_{ti}^{\,2}} \tag{A.3.79}$$

with the subscript i denoting the axes and E_i the Young's modulus.

Regularization of energy dissipation is also achieved by the addition of crack rate dependence in the softening regime of the model, as suggested by Van Zijl (2001). This includes the introduction of a parameter termed the cracking viscosity, m ($\frac{Nmm}{s^2}$), which governs the rate of cracking stress development and is determined by inverse analysis. The one parameter viscous cracking model is expressed in each direction as:

$$\sigma_{t,x} = \left(f_{t,x} + m_x\dot{\kappa}\right)\exp\left(-\frac{f_{t,x}}{g_{fx}}\kappa\right) and\ \sigma_{t,y} = \left(f_{t,y} + m_y\dot{\kappa}\right)\exp\left(-\frac{f_{t,y}}{g_{fy}}\kappa\right) \tag{A.3.80}$$

A non-associated flow rule is considered (where the yield function does not equal the potential function, $f \neq g$). The plastic potential function g_1 is taken as

$$g_1 = \left(\frac{1}{2}\boldsymbol{\xi}^T\mathbf{P_g}\boldsymbol{\xi}\right)^{1/2} + \frac{1}{2}\boldsymbol{\pi}^T\boldsymbol{\xi} \tag{A.3.81}$$

where the projection matrix $\mathbf{P_g}$ corresponds to the Rankine plastic flow as originally considered and is expressed as:

$$\mathbf{P_g} = \begin{bmatrix} \frac{1}{2} & -\frac{1}{2} & 0 \\ -\frac{1}{2} & \frac{1}{2} & 0 \\ 0 & 0 & 2 \end{bmatrix} \tag{A.3.82}$$

Note that the only difference between the projection matrices of eqns. (A.3.74) and (A.3.82) is the inclusion of α in eqn. (A.3.74). Thus, for $\alpha = 1$, the Rankine type yield function adopts an associative flow rule.

All that remains to develop the Rankine type yield criterion formulation is some softening hypothesis to express the scalar hardening parameter κ, which is done by incorporating the maximum principal plastic strain $\dot{\varepsilon_1}^p$. The rate of hardening is expressed as:

$$\dot{\kappa}_t = \dot{\varepsilon_1}^p = \frac{\dot{\varepsilon_x}^p + \dot{\varepsilon_y}^p}{2} + \frac{1}{2}\sqrt{(\dot{\varepsilon_x}^p - \dot{\varepsilon_y}^p)^2 + (\dot{\gamma}_{xy}^P)^2} \tag{A.3.83}$$

This is restated in matrix form as:

$$\dot{\kappa}_t = \dot{\varepsilon_1}^{\mathrm{p}} = (\frac{1}{2}(\dot{\boldsymbol{\varepsilon}}^{\mathbf{p}})^T \mathbf{Q} \dot{\boldsymbol{\varepsilon}}^{\mathbf{p}})^{1/2} + \frac{1}{2}\pi^T \dot{\boldsymbol{\varepsilon}}^{\mathbf{p}} \tag{A.3.84}$$

with

$$\mathbf{Q} = \begin{bmatrix} \frac{1}{2} & -\frac{1}{2} & 0 \\ -\frac{1}{2} & \frac{1}{2} & 0 \\ 0 & 0 & \frac{1}{2} \end{bmatrix} \tag{A.3.85}$$

Recalling that $\dot{\boldsymbol{\varepsilon}}_{\mathbf{1}}^{\mathbf{p}} = \dot{\lambda}_1 \frac{\partial g_1}{\partial \boldsymbol{\sigma}}$ it is evident that eqn. (A.3.84) can reduce to the following simple expression (where the subscripts t and 1 refer to tension and yield surface 1, both of which are the Rankine type criterion):

$$\dot{\kappa}_t = \dot{\lambda}_t \tag{A.3.86}$$

A.3.2.3.2 THE HILL TYPE CRITERION

The simplest compressive yield surface which allows for different compressive strengths (f_{cx} , f_{cy}) in the two material directions considered is a rotated and centered ellipsoid, existing in a space defined fully by the plane stress parameters ($\sigma_x, \sigma_y, \tau_{xy}$). This yield surface is shown in Figure A.3-15.

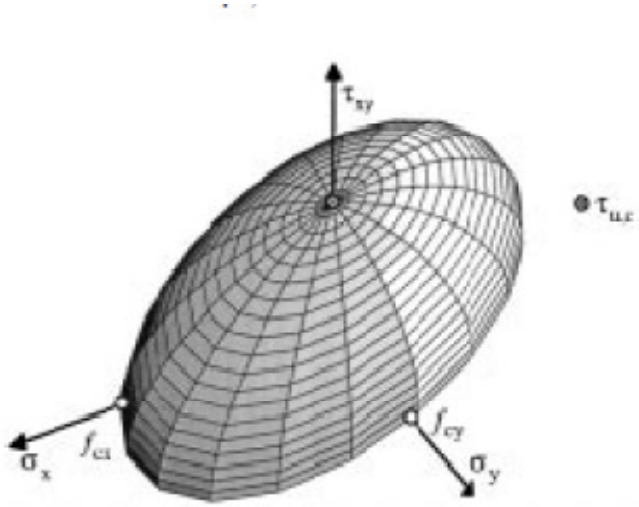

Figure A.3-15 - The Hill-Type Yield Criterion (Lourenco, et al., 1997).

The function that defines this yield surface is:

$$f_2 = A\sigma_x^2 + B\sigma_x\sigma_y + C\sigma_x^2 + D\tau_{xy}^2 - 1 = 0 \tag{A.3.87}$$

In which A, B, C and D are material parameters. Once again, the description of the yield surface in matrix form allows for more convenient numerical implementation. Additional material parameters, β and γ , are introduced which describe the yield surface shape. β controls the relation between the normal stress components of the surface, thus controls the rotation of the ellipsoid about the shear stress axis. Additional experiments such as a biaxial compression tests (with a one to one stress ratio to obtain $f_{45°}$) need to be performed to obtain accurate values for β, which is calculated by:

$$\beta = \left[\frac{1}{f_{45°}^2} - \frac{1}{f_{cx}^2} - \frac{1}{f_{cy}^2}\right] f_{cx} f_{cy} \tag{A.3.88}$$

γ controls the contribution of the shear stress to compressive failure, and is calculated by:

$$\gamma = \frac{f_{cx} f_{cy}}{\tau_{u,c}^2} \tag{A.3.89}$$

Expressions for the parameters A, B, C and D can now be found with the aid of these new parameters and by the following relations:

$$A = \frac{1}{(\bar{\sigma}_{cx}(\kappa_c))^2} \ , B = \frac{\beta}{(\bar{\sigma}_{cx}(\kappa_c)\bar{\sigma}_{cy}(\kappa_c))} \tag{A.3.90}$$

$$C = \frac{1}{(\bar{\sigma}_{cy}(\kappa_c))^2} \ , D = \frac{\gamma}{(\bar{\sigma}_{cx}(\kappa_c)\bar{\sigma}_{cy}(\kappa_c))}$$

where $\bar{\sigma}_{cx}$ and $\bar{\sigma}_{cy}$ are the yield values in the x and y directions, and the parameter κ_c controls the softening or hardening in behaviour in the material. The yield surface can now be expressed in convenient matrix form as:

$$f_2 = \left(\frac{1}{2}\boldsymbol{\sigma}^{\mathbf{T}}\mathbf{P_c}\boldsymbol{\sigma}\right)^{1/2} - \bar{\sigma}_c(\kappa_c) \tag{A.3.91}$$

with the projection matrix $\mathbf{P_c}$ being:

$$\mathbf{P_c} = \begin{bmatrix} 2\frac{\bar{\sigma}_{cy}(\kappa_c)}{\bar{\sigma}_{cx}(\kappa_c)} & \beta & 0 \\ \beta & 2\frac{\bar{\sigma}_{cx}(\kappa_c)}{\bar{\sigma}_{cy}(\kappa_c)} & 0 \\ 0 & 0 & 2\gamma \end{bmatrix} \tag{A.3.92}$$

and $\bar{\sigma}_c$ being:

$$\bar{\sigma}_c = \sqrt{\bar{\sigma}_{cx}\bar{\sigma}_{cy}} \tag{A.3.93}$$

The inelastic law that governs the material behaviour consists of parabolic hardening and subsequent parabolic and exponential softening in both material directions, distinguished by different compressive fracture energies in each direction ($G_{fc,x}$ and $G_{fc,y}$). This law is illustrated in Figure A.3-16, showing the hardening, softening and the residual plateau of plastic behaviour, as well as the associated functions describing these responses.

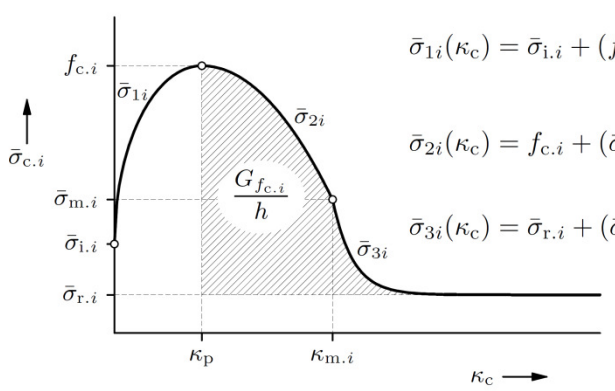

$$\bar{\sigma}_{1i}(\kappa_c) = \bar{\sigma}_{i.i} + (f_{c.i} - \bar{\sigma}_{i.i})\sqrt{\frac{2\kappa_c}{\kappa_p} - \frac{\kappa_c^2}{\kappa_p^2}}$$

$$\bar{\sigma}_{2i}(\kappa_c) = f_{c.i} + (\bar{\sigma}_{m.i} - f_{c.i})\left(\frac{\kappa_c - \kappa_p}{\kappa_{m.i} - \kappa_p}\right)^2$$

$$\bar{\sigma}_{3i}(\kappa_c) = \bar{\sigma}_{r.i} + (\bar{\sigma}_{m.i} - \bar{\sigma}_{r.i})\exp\left(2\left(\frac{\bar{\sigma}_{m.i} - f_{c.i}}{\kappa_{m.i} - \kappa_p}\right)\left(\frac{\kappa_c - \kappa_{m.i}}{\bar{\sigma}_{m.i} - \bar{\sigma}_{r.i}}\right)\right)$$

Figure A.3-16 - Compressive Plasticity Law (DIANA, 2009).

Isotropic hardening is assumed in both material directions (thus the peak compressive strength is simultaneously reached in each direction) and anisotropic behaviour is incorporated upon the compressive softening of the material where the fracture energies available for dissipation in each material direction differ (anisotropic softening). The residual plateau of compressive strength is assumed for simpler computer implementation, avoiding the degeneration of the compressive stresses into a tensile state as well as degeneration to some defined point, which could cause numerical difficulties. The stress values (as in Figure A.3-16 and used in the accompanying equations) associated with the compressive law are all related to the maximum compressive stress f_{ci} : $\bar{\sigma}_{ii} = \frac{1}{3}f_{ci}$, $\bar{\sigma}_{mi} = \frac{1}{2}f_{ci}$ and $\bar{\sigma}_{ri} = \frac{1}{10}f_{ci}$. The equivalent plastic strain κ_p is considered as another material parameter and corresponds to the maximum compressive stress, f_{ci}. The parameter κ_{mi} is calculated as follows to ensure that the energy dissipation is independent of the mesh (using a fracture energy approach as discussed previously):

$$\kappa_{mi} = \frac{75}{67}\frac{G_{fci}}{h\, f_{ci}} + \kappa_p \tag{A.3.94}$$

and to ensure 'snap-back' behaviour does not occur at this constitutive level, the following restriction is imposed:

$$\kappa_{mi} \geq \frac{f_{ci}}{E_i} + \kappa_p \tag{A.3.95}$$

Finally the equivalent plastic strain rate is governed by an associated flow rule ($f = g$) and a work-hardening rule to yield:

$$\dot{\kappa}_c = \frac{1}{\bar{\sigma}_c}\sigma^T \dot{\varepsilon}^P = \dot{\lambda}_c \tag{A.3.96}$$

A.3.2.4 Constitutive modeling of Strain Hardening Cement Composites (SHCC)

The constitutive model used for the analysis of the SHCC beams in this analysis is that proposed by Van Zijl (2000), which has also been implemented as a user subroutine for use with DIANA. The modeling of SHCC materials that effectively capture realistic behavior of the material can prove to be quite complex. Of particular consideration is the rate dependant nature of the tensile strength development of the material, as is evident in Figure A.3-17 which illustrates the results of tensile test specimens loaded at various rates. It is clear that the first cracking and ultimate tensile strength of the material as well as its ductility increase with increasing loading rate (Van Zijl, 2009).

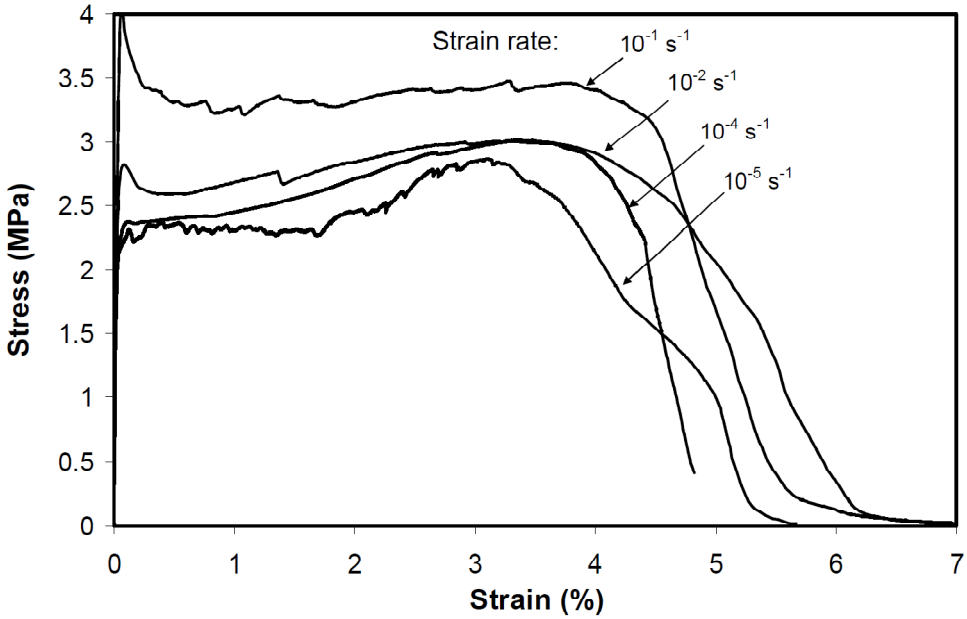

Figure A.3-17 - Stress Strain Response of Uniaxial Tensile tests on SHCC Dumbbell Specimens (Van Zijl, 2009).

The time dependence of SHCC is not limited to the loading rate applied to it, but also extends to higher creep fracture values at higher loading rates. This aspect is incorporated in the formulation, but is not of concern in this study. The

computational model developed by Van Zijl (2009) is based in a computational plasticity framework. It is a multi-surface, rate-dependant anisotropic, continuum plasticity model.

The multi-surface model is a combination of two Rankine-type yield surfaces for tension and compression, as shown in Figure A.3-18 (with iso-shear stress lines, $\tau_3 > \tau_2 > \tau_1$). This multi-surface model has been modified to include rate dependence (Van Zijl, 2009) .

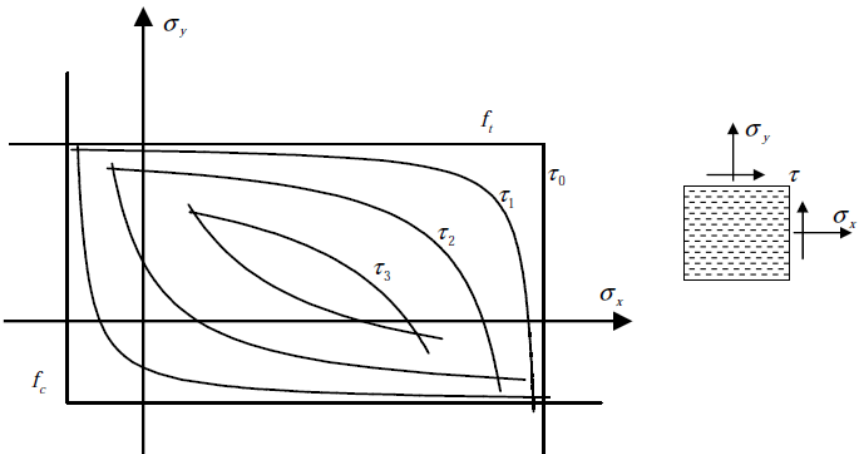

Figure A.3-18 - Multi-surface Yield function for SHCC model, (Van Zijl, 2009)

The plane stress formulation of the model will be briefly discussed, and the similarities in its formulation with that of the Rankine-type criterion from the Rankine-Hill plasticity model formulation (cf. Section A.3.2.3.1) will be repeated for convenience.

The stress rate vector for the SHCC model is given by (Van Zijl, 2009):

$$\dot{\boldsymbol{\sigma}} = \mathbf{D}^{\mathbf{ve}}\dot{\boldsymbol{\varepsilon}}^{\mathbf{ve}} + \boldsymbol{\Sigma} = \mathbf{D}^{\mathbf{ve}}(\dot{\boldsymbol{\varepsilon}} - \dot{\boldsymbol{\varepsilon}}^{\mathbf{p}} - \dot{\boldsymbol{\varepsilon}}^{\mathbf{0}}) + \boldsymbol{\Sigma} \qquad \text{(A.3.97)}$$

where $\mathbf{D}^{\mathbf{ve}}$ is the time dependent stiffness modulus. $\dot{\boldsymbol{\varepsilon}}^{\mathbf{ve}}$ is the visco-elastic strain vector which is decomposed into $\dot{\boldsymbol{\varepsilon}}^{\mathbf{0}}$ the initial strain vector (to incorporate shrinkage or thermal strains) and $\boldsymbol{\Sigma}$ is a viscous stress vector which takes the stress history into account (to incorporate creep in the model). The plastic strain rate is included only once the resistance of the material is exceeded and is expressed as proportional to the stress derivative of the plastic potential function, yielding the following non-associated flow rule (cf. eqn. (A.3.61)):

$$\dot{\boldsymbol{\varepsilon}}^{p} = \dot{\lambda}\frac{\partial g}{\partial \boldsymbol{\sigma}} \tag{A.3.98}$$

A schematic representation of the model can be seen in Figure A.3-19. The visco-elastic stiffness is calculated from the combination of the dashpot viscosities and spring stiffness's in the Maxwell chain component of the model, to represent the 'bulk creep' stiffness. The initial strains from thermal or shrinkage effects can also be incorporated, but of import for this study is the time-dependant cracking component of this model.

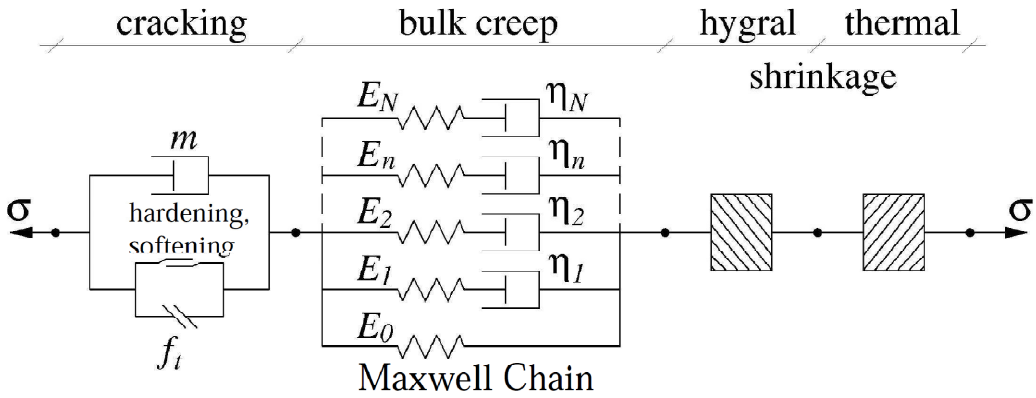

Figure A.3-19 - Diagram of the unified SHCC material model (Van Zijl, 2009).

A.3.2.4.1 LIMIT STATE FUNCTIONS FOR TENSION AND COMPRESSION

The Rankine-type yield function (Lourenco, et al., 1997) is implemented for modeling the tensile response of the material (cf. Section A.3.2.3.1 and eqn. (A.3.71)). This maximum principal stress based criterion is repeated below:

$$f_t = \frac{(\sigma_x - \bar{\sigma}_{tx}(\kappa_t)) + (\sigma_y - \bar{\sigma}_{ty}(\kappa_t))}{2} + \sqrt{\left(\frac{(\sigma_x - \bar{\sigma}_{tx}(\kappa_t)) - (\sigma_y - \bar{\sigma}_{ty}(\kappa_t))}{2}\right)^2 + \alpha {\tau_{xy}}^2} \tag{A.3.99}$$

An associated flow rule is adopted in tension if the parameter α in eqn. (A.3.99) (which represents the shear stress contribution to failure) is set equal to 1, thus the plastic potential function will equal the yield function:

$$g = f|_{\alpha=1} \tag{A.3.100}$$

The tensile stress–plastic (equivalent) strain relations are illustrated in Figure A.3-20 for both material directions, where the initial tensile strain hardening, followed by exponential softening, is characteristic of SHCC (cf. Figure A.3-17).

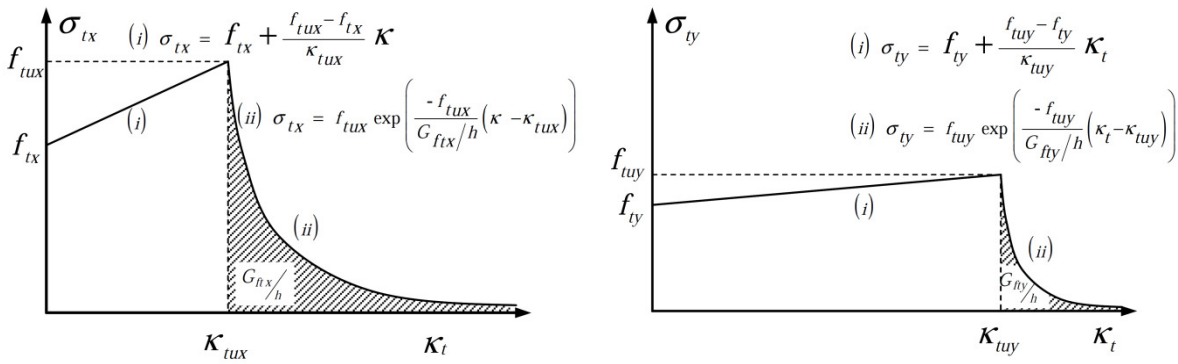

Figure A.3-20 - Tensile stress-plastic strain relations for axes of Anisotropy (Van Zijl, 2009).

Anisotropy of the material is incorporated in the model by the different material parameters and separate stress-plastic strain relations used in orthogonal directions, hence the two figures for the two axes of anisotropy in Figure A.3-20 (Van Zijl, 2009).

Hardening and softening in tension is controlled by the equivalent tensile strain parameter κ_t, which is related to the maximum (tensile) principal plastic strain, as is considered adequate for SHCC modelling - cf. eqn. (A.3.83), repeated below:

$$\dot{\kappa}_t = \dot{\varepsilon}_1^{\,p} = \frac{\dot{\varepsilon}_x^{\,p} + \dot{\varepsilon}_y^{\,p}}{2} + \frac{1}{2}\sqrt{(\dot{\varepsilon}_x^{\,p} - \dot{\varepsilon}_y^{\,p})^2 + (\dot{\gamma}_{xy}^{P})^2} \qquad \text{(A.3.101)}$$

It can be shown further, through use of eqns. (A.3.98) and (A.3.101), that (Van Zijl, 2009):

$$\dot{\kappa}_t = \dot{\lambda} \qquad \text{(A.3.102)}$$

A Rankine-type criterion is also implemented for modelling the compressive response of the material based on the minimum (compressive) principal stresses:

$$f_c = -\frac{(\sigma_x - \bar{\sigma}_{cx}(\kappa_c)) + (\sigma_y - \bar{\sigma}_{cy}(\kappa_c))}{2} + \sqrt{\left(\frac{(\sigma_x - \bar{\sigma}_{cx}(\kappa_c)) - (\sigma_y - \bar{\sigma}_{cy}(\kappa_c))}{2}\right)^2 + \alpha {\tau_{xy}}^2} \quad \text{(A.3.103)}$$

The compressive stress – plastic (equivalent) strain relations are shown in Figure A.3-21, and are controlled by the same functions as the tensile relations with the pertinent compression parameters used instead. As in the tensile regime, linear strain hardening is followed by exponential strain softening.

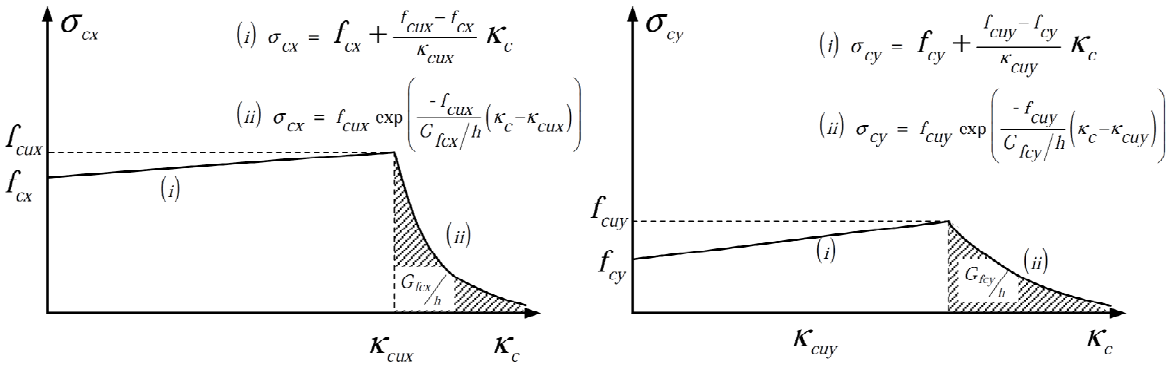

Figure A.3-21 - Compressive Stress-Plastic strain relations for axes of Anisotropy (Van Zijl, 2009).

The hardening-softening is controlled by the equivalent compressive strain (κ_c) which is related to the minimum (compressive) principal plastic strain as follows:

$$\dot{\kappa}_c = -\dot{\varepsilon_2}^p = -\frac{\dot{\varepsilon_x}^p + \dot{\varepsilon_y}^p}{2} + \frac{1}{2}\sqrt{(\dot{\varepsilon_x}^p - \dot{\varepsilon_y}^p)^2 + (\dot{\gamma}_{xy}^P)^2} \quad \text{(A.3.104)}$$

The plastic strain rate development at the intersection of the two Rankine-type yield surfaces representing the potential function is defined according to Koiter's (1953) generalization:

$$\dot{\boldsymbol{\varepsilon}}^{\mathbf{p}} = \dot{\boldsymbol{\varepsilon}}_{\mathbf{1}}^{\mathbf{p}} + \dot{\boldsymbol{\varepsilon}}_{\mathbf{2}}^{\mathbf{p}} = \dot{\lambda}_1 \frac{\partial g_1}{\partial \boldsymbol{\sigma}} + \dot{\lambda}_2 \frac{\partial g_2}{\partial \boldsymbol{\sigma}} \quad \text{(A.3.105)}$$

A.3.2.4.2 CRACKING RATE DEPENDENCE

The time dependence of SHCC has been attributed to two sources: that of creep and crack mouth opening rate when subjected to tension. SHCC's mechanical response is highly rate dependent as was shown in Figure A.3-17 for the tensile response. This dependence is accounted for in a computational framework by incorporating cracking rate dependence parameters in the material model (Wu,

et al., 1993), (Van Zijl, et al., 2001). Thus the resistance to cracking of the material is enhanced as the loading rate increases. In tension, the flow rule of eqn. (A.3.98) can be thought of as the average cracking strain $\dot{\boldsymbol{\varepsilon}}^{cr}$ resulting in:

$$\dot{\boldsymbol{\varepsilon}}^{p} = \dot{\boldsymbol{\varepsilon}}^{cr} = \frac{\dot{w}}{l_b}\frac{\partial g}{\partial \boldsymbol{\sigma}} \tag{A.3.106}$$

with w being the crack opening displacement which is taken as being uniformly distributed across the fracture process zone which has a width of l_b. It is evident from inspection of eqs. (A.3.98), (A.3.101) and (A.3.106) that the equivalent tensile strain parameter is given by:

$$\kappa_t = \frac{w}{l_b} \tag{A.3.107}$$

The increased cracking resistance due to increase in loading rate was introduce by Wu and Bazant (1993) through postulating that a time effect other than that of the 'bulk creep' acts over the fracture process zone in materials that are brittle. The following equation was then derived in order to express the crack opening rate and its dependence on the loading rate (Van Zijl, 2009):

$$\dot{w} = \dot{w}_r sinh\left[\frac{\sigma - \sigma_t(w)}{c_1[\sigma_t(w) + c_2 f_t]}\right] \tag{A.3.108}$$

where $\dot{w}_r$ is the reference crack opening rate and remains constant. Combining eqns. (A.3.106) and (A.3.108), the new crack rate dependent tensile stress-equivalent strain equations for hardening and softening of Figure A.3-20 can be obtained as follows:

$$\sigma_{ti} = \left(f_{ti} + \frac{f_{tui} - f_{ti}}{\kappa_{tui}}\kappa_t\right)\left[1 + c_1 \sinh^{-1}\left(\frac{\dot{\kappa}_t}{\dot{\kappa}_r}\right)\right] + c_1 c_2 f_{tui} \sinh^{-1}\left(\frac{\dot{\kappa}_t}{\dot{\kappa}_r}\right) \tag{A.3.109}$$

$$\sigma_{ti} = f_{tui} exp\left(\frac{-f_{tui}}{G_{fti}/l_b}(\kappa_t - \kappa_{tui})\right)\left[1 + c_1 \sinh^{-1}\left(\frac{\dot{\kappa}_t}{\dot{\kappa}_r}\right)\right] + c_1 c_2 f_{tui} \sinh^{-1}\left(\frac{\dot{\kappa}_t}{\dot{\kappa}_r}\right) \tag{A.3.110}$$

where the subscript i refers to the x and y material axes. Eqn. (A.3.109) applies for the domain $\kappa_t \leq \kappa_{tui}$, and eqn. (A.3.110) for the domain $\kappa_t > \kappa_{tui}$. It is worthwhile noting that the length of the fracture process zone, l_b, is not

equivalent to the representative finite element mesh size h where localization was assumed to occur previously (cf. Section, A.3.2.3.1) and may instead span across a number of mesh elements. c_2 is merely a small offset value with the purpose of avoiding the potential singularity of eqn. (A.3.108). The reference strain rate $\dot{\kappa}_r$ is the strain rate that is low enough to ensure that the tensile stress values (from eqns. (A.3.109) and (A.3.110)) are rate independent. Finally the third parameter in this so called three parameter modelc_1 can be calculated from experimental tensile test data conducted at various loading rates.

It has been shown that this three parameter model yields mesh dependant results, which has been attributed to the presence of the inverse hyperbolic trig operator present in the formulation. The model exhibits a large damping response in post peak behavior if the reference rate $\dot{\kappa}_r$ is very small or the value of the $\frac{\dot{\kappa}_t}{\dot{\kappa}_r}$ is too large (Van Zijl, 2000).

An alternative to the above mentioned three parameter model of Wu and Bazant (1993) is a one parameter model suggested by Van Zijl (2000) for cementitious materials. This has been adapted in a manner appropriate for SHCC constitutive modeling as follows (Van Zijl, 2009):

$$\sigma_{ti} = f_{ti} + \frac{(f_{tui} + m_i\dot{\kappa}_t) - f_{ti}}{\kappa_{tui}}\kappa_t \tag{A.3.111}$$

$$\sigma_{ti} = \left(1 + \frac{m_i\dot{\kappa}_t}{f_{tui}}\right) f_{tui} exp\left(\frac{-f_{tui}}{G_{fti}/l_b}(\kappa_t - \kappa_{tui})\right) \tag{A.3.112}$$

The parameter m_i represents the different cracking viscosities in each material direction.

A.4 Modeling of Reinforced concrete

The main underlying assumption adopted in most FES packages to incorporate steel reinforcement in analyses is that there exists a perfect bond between the concrete and the reinforcement. Thus the reinforcement and the concrete within which it is embedded are both subjected to the same displacements. This

assumption holds well for cases where linear elastic behavior is observed, but problems arise upon the onset of nonlinearities such as cracking, where assumptions regarding the concrete-reinforcement interaction are governed by either tension stiffening or tension softening models. Tension softening models for concrete are as discussed previously within this document, where concrete reaches some maximum tensile stress which is followed by a gradual decrease in tensile load carrying capacity with increasing strain – with the gradual decrease in capacity being attributed to the 'ductility' or non brittle nature of concrete. Tension stiffening models are only applicable for reinforced concrete structures, where there is also a gradual decrease in tensile load carrying capacity upon cracking but this decrease is attributed to the residual resistance afforded by the concrete parts of the structure in between the cracks, which are still in contact with the reinforcement.

The use of the assumption of perfect bond for reinforcement modeling can prove insufficient when matters concerning cracking and crack spacing are of greatest importance in the analyses, due to the influence of the reinforcement on these factors. Thus in such analyses, pull out of the bars can be modeled, using interface elements to model the concrete-reinforcement interaction. This introduces new complexities though, considering the additional elements and degrees of freedom introduced as well as the fact that these elements incessantly need to be aligned with the reinforcement elements throughout the analysis.

The inclusion of embedded reinforcements in the FEM formulation causes there being two contributions (from the concrete and the reinforcement) to the internal virtual work considered. It is then possible to establish a separate stress strain relationship for the reinforcement which is independent to that of the concrete's relation. It can then be shown mathematically that the concrete and reinforcement element are controlled by the same displacement field but under different numerical integration rules each with their own integration points.

Reinforcement elements embedded in plane stress elements are available for implementation in DIANA and will be used in this study. The strains in the reinforcement are established from the displacement in the 'mother' elements with the assumption of a perfect bond. Unfortunately, thus far a bond-slip model

is only available for use with reinforcement elements embedded in solid (3D) elements.

B. Analytical Investigation

Plane stress analyses were conducted on reinforced concrete beams under flexural loading conditions. Three separate experimental programs were analyzed using DIANA Finite Element Software (2009), in each of which different failure mechanisms governed – compressive, tensile and shear dominated failure mechanisms. Various aspects which govern the results obtained from NLFEA's were considered, such as the mesh element type and size, as well as the constitutive laws (Total Strain and Plasticity models) to be used to model the concrete behavior. Various other parameters were also considered and their influences on the outcome of the NLFEA's were investigated, and will be elucidated.

Considering the notion of this project being geared towards an aid in the development of reliability based design guidelines based on the results of NLFEA's, the end designer or analyst was kept in mind throughout. Thus the ease of implementation of the NLFEA when considering the goal of obtaining results that correspond to the experimental results was important, and as such relatively simple modeling approaches were adopted and the procedures and guidelines as provided in "Guidelines for Non- linear Finite Element Analysis of Concrete Structures" (Hendriks, et al., 2009) were followed - as such documentation would be available for the hypothetical designer. In establishing how well and with what amount of ease the reality of the various failure mechanisms can be captured through the use of one of the preeminent Finite Element Software packages available to date following generally accepted guidelines, one can deduce whether the notion of establishing design codes on the results of these analyses is warranted. More importantly, additional modifications and enhancements may be required to make such a new code development feasible for the average, less than experienced final designer, as well as identify any simplifications/modifications that could be introduced for large scale (regarding structural size) implementation.

The outcomes of the various NLFEA's are later compared to the experimental results, with the following Section providing insight into the various case studies as well as the modeling procedures adopted.

B.1 General Modeling Approach

B.1.1 Nomenclature

A number of analyses were conducted, dominated by various failure modes, comprised of various element types and sizes as well as controlled by various material models. Thus, to ease distinguishing between them, the following naming convention was adopted, shown in Figure B.1-1:

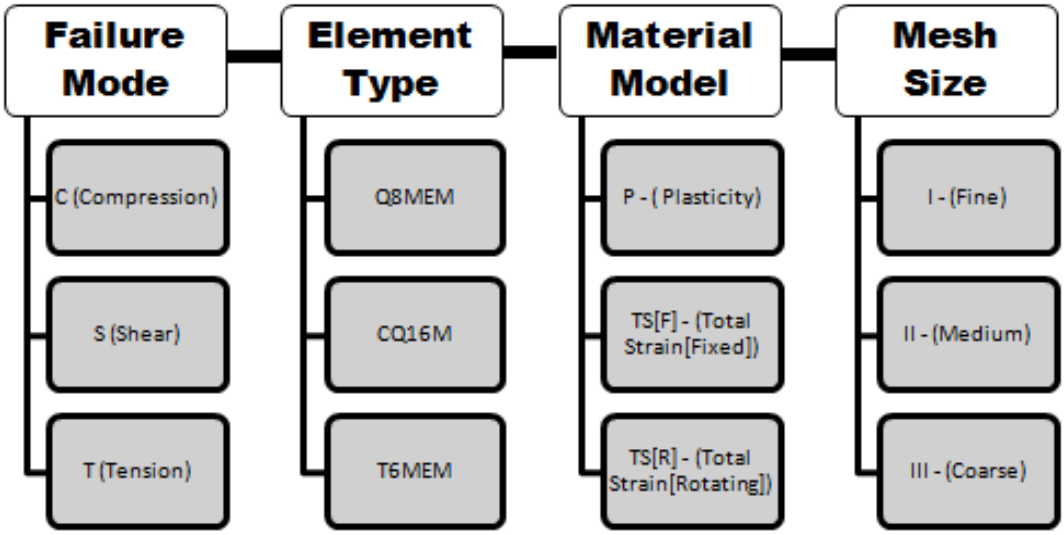

Figure B.1-1 - Naming Convention for Analyses.

The symbols in the grey boxes in Figure B.1-1 are combined in the order indicated by the white boxes and separated by hyphens. Thus the Compression dominated (C), linearly interpolated quadrilateral element type (Q8MEM), using a Total Strain fixed crack model (TS[F]) with a coarse mesh (III) analysis has the code C-Q8MEM-TS[F]-III.

B.1.2 Material Reference Parameters

The various material reference parameters used in the analyses were mostly based on values obtained from uniaxial compressive or tensile tests, using the suggested expressions for compressive and tensile behavior as suggested by Hendriks et al. (2009). The other material parameters based on the concrete mean compressive strength through relationships established in the Model Code (1990) as are the suggested values when considering Ultimate Limit State

design criteria (Hendriks, et al., 2009), were used in the analyses if no other information was available or attainable.

The material parameters for the reinforcing steel were obtained from tensile test data if provided by the various authors, otherwise standard values for reinforcing steel were assumed where appropriate.

B.1.3 Element Types

Plane stress analyses were performed on all the reinforced concrete beams investigated, using the following plane stress elements available for use in DIANA.

B.1.3.1 Q8MEM

The Q8MEM plane stress elements (Figure B.1-2) are 4-node, linearly interpolated isoparamertic quadrilateral membrane elements with 8 degrees of freedom (2 displacement degrees of freedom at each node) (DIANA, 2009).

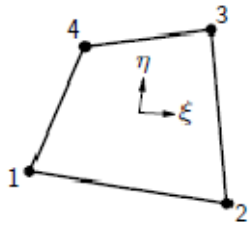

Figure B.1-2 - Q8MEM element (DIANA, 2009).

Full Gaussian integration is applied on the element, with a 2x2 integration scheme by default. The linearly interpolated quadrilaterals have the default property of having a reduced integration scheme applied to the shear stiffness terms of the element stiffness matrix in the FEM formulation, to enable enhanced behavior in shear when subjected to flexure. This selective reduced integration (the option CSHEAR in DIANA) may become unstable in non-linear analyses, and its influence is considered in the analyses (DIANA, 2009). This constant shear option yields the shear strain γ_{xy} to be constant throughout the element area. Overall reduced integration is impossible to apply to avoid the occurrence of any spurious kinematic modes.

B.1.3.2 CQ16M

The CQ16M plane stress elements are 8-node quadratically interpolated isoparamertic quadrilateral membrane elements with 16 degrees of freedom (2 displacement degrees of freedom at each node) (DIANA, 2009).

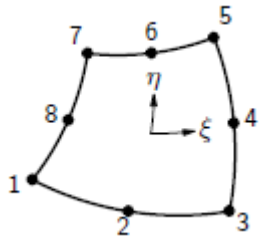

Figure B.1-3 - CQ16M Plane stress Element (DIANA, 2009).

This element type is explicitly suggested for use in NLFEA's by Hendriks et al. (2009) for analyzing beams, due to their proclivity of more accurately describing the displacement field through describing more complex deformation modes, as well as their capacity in describing complex failure such as shear failure (Hendriks, et al., 2009). Full (3x3) Gaussian integration was applied to these elements in all analyses considered.

B.1.3.3 T6MEM

The T6MEM plane stress elements are 3-node linearly interpolated isoparametric triangular elements based on area integration (DIANA, 2009). 3 Point area integration was applied over the elements, to avoid zero energy deformation modes.

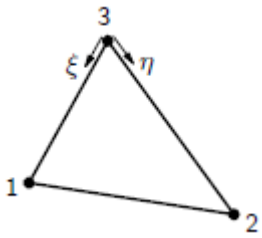

Figure B.1-4 - T6MEM Plane stress element (DIANA, 2009).

These elements were used to generate mesh consisting of cross-diagonal triangles (See Figure B.1-5), as was seen to behave well under situations where volumetric locking occurs (Nagtegaal, et al., 1974).

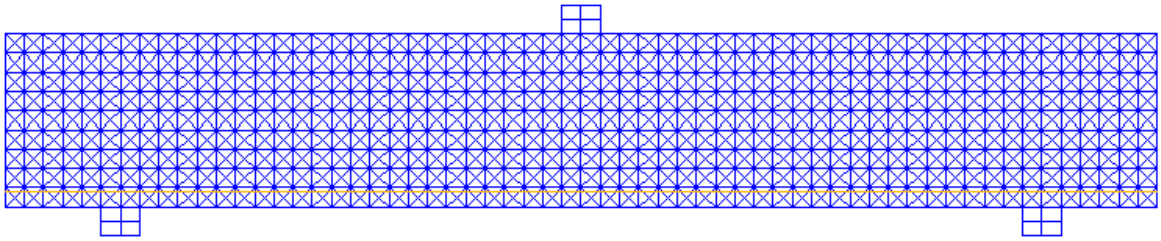

Figure B.1-5 - Cross-diagonal mesh.

The purpose of this was to investigate whether the potential problem of volumetric locking due to the discord between the kinematic constraints imposed on the element's volume change due to the materials plastic yield criterion and the elements degrees of freedom's velocity field could be avoided. In using such a cross-diagonal triangle mesh more displacement degrees of freedom are present within the quadrilateral formed by the triangles, enabling the kinematic constraint equations to be solved for non trivial values of the velocity field.

B.1.4 Boundary Conditions and Tyings

All reinforced concrete beams were tested under simply supported conditions. The relevant loading/bearing plates were incorporated in the FEM models to ensure distribution of the forces throughout the mesh and avoid local crushing of the concrete. All the loading/ bearing platens were assumed to be steel, to ensure an effective distribution of forces through the mesh at the supports.

The area of contact between the steel plates and concrete beams was modeled as simply as possible. It was assumed that the coincident nodes at the points of contact shared vertical degrees of freedom. Meshing was done in a manner to ensure nodes were available at the centre points of the plates as well as the correct corresponding position on the beam mesh. At these centre nodes, the coincident nodes on the beam and plates were related by sharing horizontal degrees of freedom. The simple relation was assumed to avoid difficulties inherent in establishing parameters to describe interface behavior, as well as the consideration of the ease of implementation for the end user (albeit that the tests are not necessarily representative of realistic design structures encountered in practice). There was also no mention in any of the studies investigated of any slipping occurring at the supports, thus the friction afforded by the beam-plate interaction was assumed to be significant, and thus justifying the modeling approach.

B.1.5 Localization Technique

All meshes in the FEM models were symmetric about the vertical axis. Thus there existed an even number of mesh columns at each support position. This meant that the constant stress field to which the beams would be exposed (due to the symmetric loading and supports) would lead to the straining of these columns to be equal. Therefore localization is not possible and therefore too softening will be applied simultaneously over elements in these columns. With the representative length (h) over which the fracture energy is dissipated being proportional to the size of *one* element, the fracture energy for one element would be available for dissipation over both the elements at the area of maximum stress encountered in the constant stress region (directly beneath the loading plate in the 3 point bending problems and between the loading plates for the 4 point bending problems). Thus the fracture process zone is too large for the available energy simply due to the geometry definition and consequently mesh placement and localization cannot occur. To ensure localization takes place, a column of elements in the constant stress regions has been weakened to ensure the available fracture energy is dissipated over the appropriate representative area and to ensure numerical stability upon the first nonlinearities encountered in the analyses. The weaker column of elements was taken as having material properties that are equal to 95% of the original element material parameters. The inclusion of this asymmetry in the model is shown in Figure B.1-6, a colour coded illustration of the different materials in the model, showing the localization zone

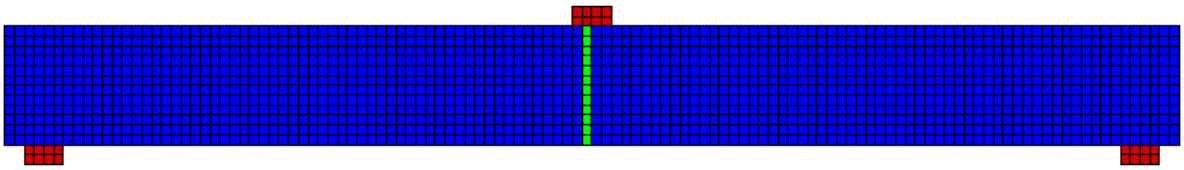

Figure B.1-6 - Induced localization zone to ensure numerical stability.

B.2 Compression Dominated Case Study

B.2.1 Introduction

The compression dominated study considered is that of Pedersen et al. (1996), which formed part of a round robin analysis conducted by Van Mier and Ulfkjaer (2000). The experimental and numerical investigations of Pedersen et al. (1996) were concerned with over reinforced concrete beams of various sizes and concrete types that were designed to fail in compression. A main purpose of the study was to investigate the influence of constitutive compressive numerical modeling based on uniaxial compressive test results, in which either high or low friction boundary conditions had been applied. Thus physical beam experiments were compared to numerical analyses (from two different software packages) in which the results from the different uniaxial compressive testing techniques (using either high or low friction loading platens) were implemented, to establish which technique is more suitable for constitutive modeling purposes and more closely resembles realistic structural compressive response. Various authors contributed to the round robin study in the form of numerical modeling of the beams, and some of their contributions will also be shown and discussed.

B.2.2 Experimental Setup and Results

The experimental work was performed at Aalborg University by Pedersen et al. (1996). The experiments consisted of 4 point bending tests on over reinforced specimens cast using various cementitious materials; namely: NSC (Normal Strength Concrete), HSC (High Strength Concrete) and FRHSC (Fibre Reinforced High Strength Concrete). Two test series were conducted, for small and large beams. The large beam testing was only done on a NSC beam. The test series details are given in Table B.2-1. 3 beam specimens for each concrete type and beam size were cast and tested.

BEAM TYPE	Series I	Series II
Length (m)	3.8	7.5
Clear Span (m)	3.6	7.2
Width (m)	100	200
Height (m)	200	400
As	8 stranded wires	9 Ks550s (20mm)
As'	2 Ks550 (20mm)	2 Ks550 (20mm)
Shear reinforcement	Ks550s (6mm) @100mm c/c	Ks550s (6mm) @200mm c/c
Concrete type	NSC/HSC/FRHSC	NSC

Table B.2-1 - Test series for Compression Dominated experiments

The 4 point bending test setup is shown for the simply supported beams in Figure B.2-1, for both test Series.

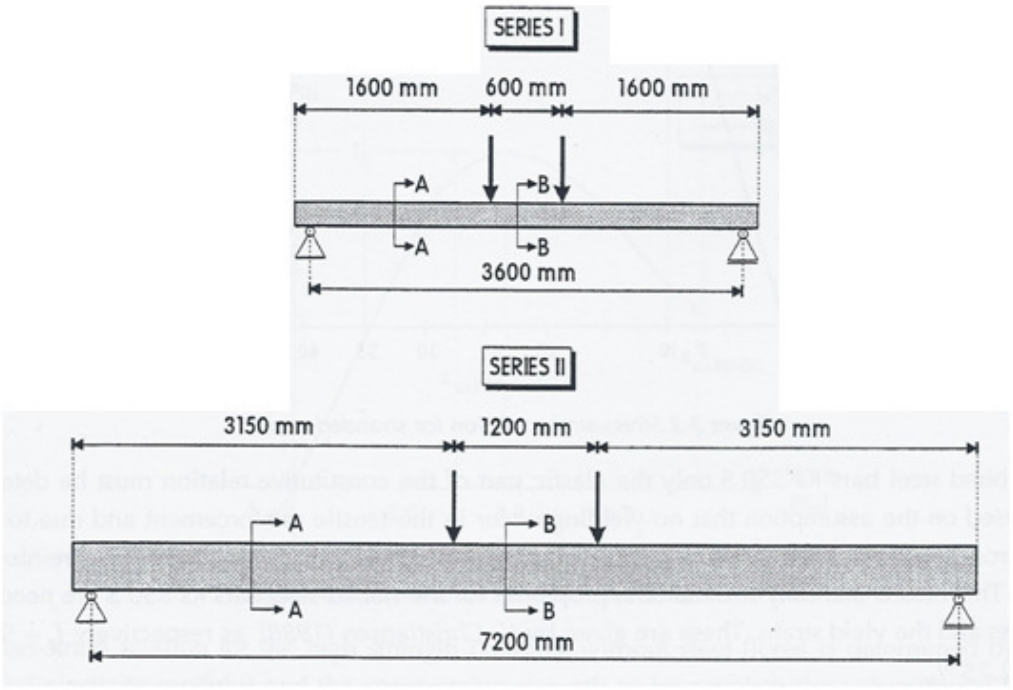

Figure B.2-1 - 4 Point Bending test setup (Pedersen, et al., 1996).

All beams were designed to fail in compression, with the Series I beams reinforced with stranded wires and the large beam with conventional steel reinforcing. Reinforcement was provided in the top of the beam, to facilitate stirrup placement, but was not present along the portion of the beam between

the loading plates where concrete crushing was desired. Refer to Appendix A for drawings of the test beams and reinforcement detailing.

The load (kN) vs. displacement (mm) results at midspan are shown for the various beams in the following Figures.

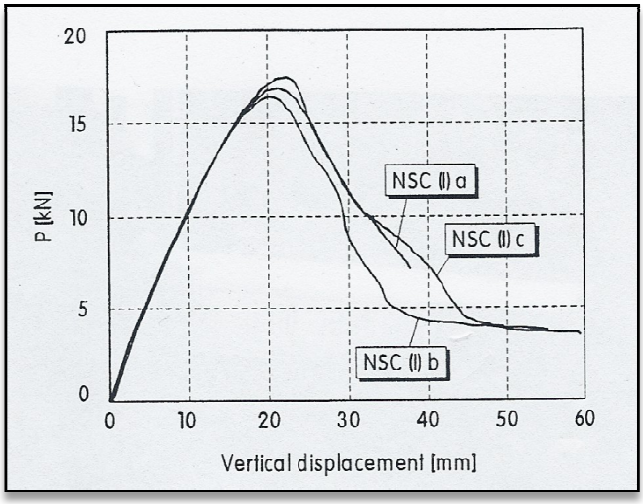

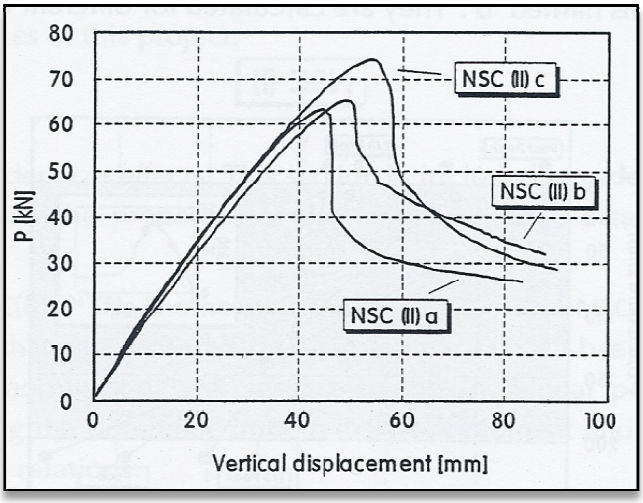

Figure B.2-2 - Results for NSC beams, series I and II (Pedersen, et al., 1996).

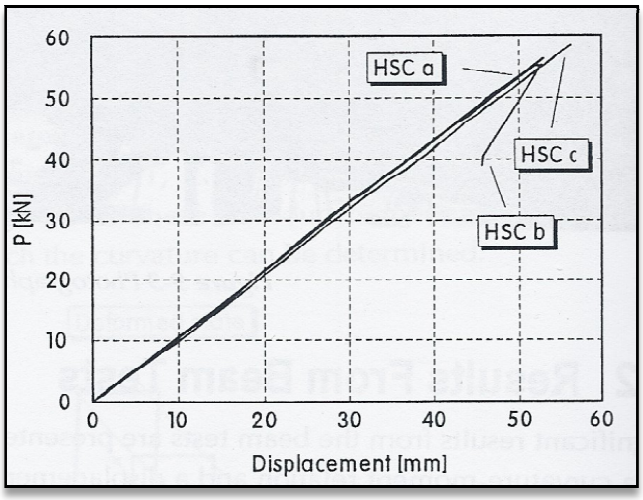

Figure B.2-4 - Results for HSC beams (Pedersen, et al., 1996).

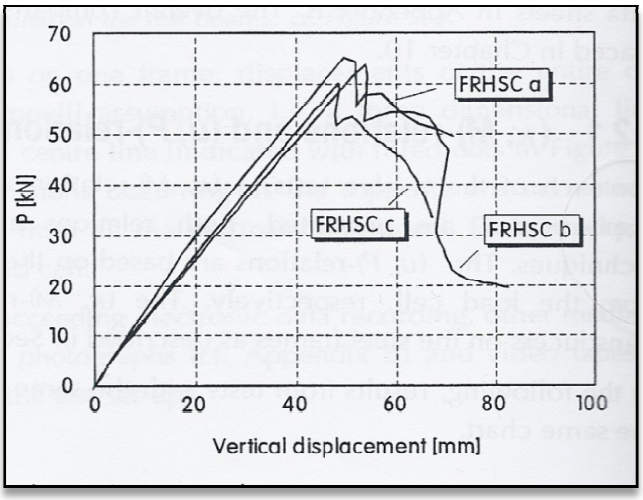

Figure B.2-3 - Results for FRHSC beams (Pedersen, et al., 1996)

The NSC (Figure B.2-2) and FRHSC (Figure B.2-3) beams clearly showed a more ductile response than the HSC beams (Figure B.2-4). The HSC beams were observed to exhibit very brittle and sudden failure, typical of the nature of the material and the sudden release of energy upon localization. Snap through

behavior was observed at peak load in the FRHSC beams, causing the load jump in Figure B.2-3. All beams were found to fail in compression, through spalling at the top of the beams in the compressive zone.

B.2.3 Numerical Analyses and Results

Two numerical analyses were conducted by Pedersen et al. (1996) on the over reinforced beams. Two different software programs were used, one called BEAM and another called FEMLAB, which is based on the FEM. The reference parameters used were as obtained by uniaxial compressive or tensile tests. BEAM was used to compare the constitutive relations for compression by implementing the compressive test results obtained for high and low friction platen tests. The analysis in FEMLAB implemented only the constitutive compressive relation obtained for the low friction uniaxial compressive stress for NSC. The compressive constitutive relations in Figure B.2-5 were implemented by Pedersen et al. (1996), due to the smooth curves and ample post peak data available (results are shown for the high friction and low friction boundary conditions) (Pedersen, et al., 1996):

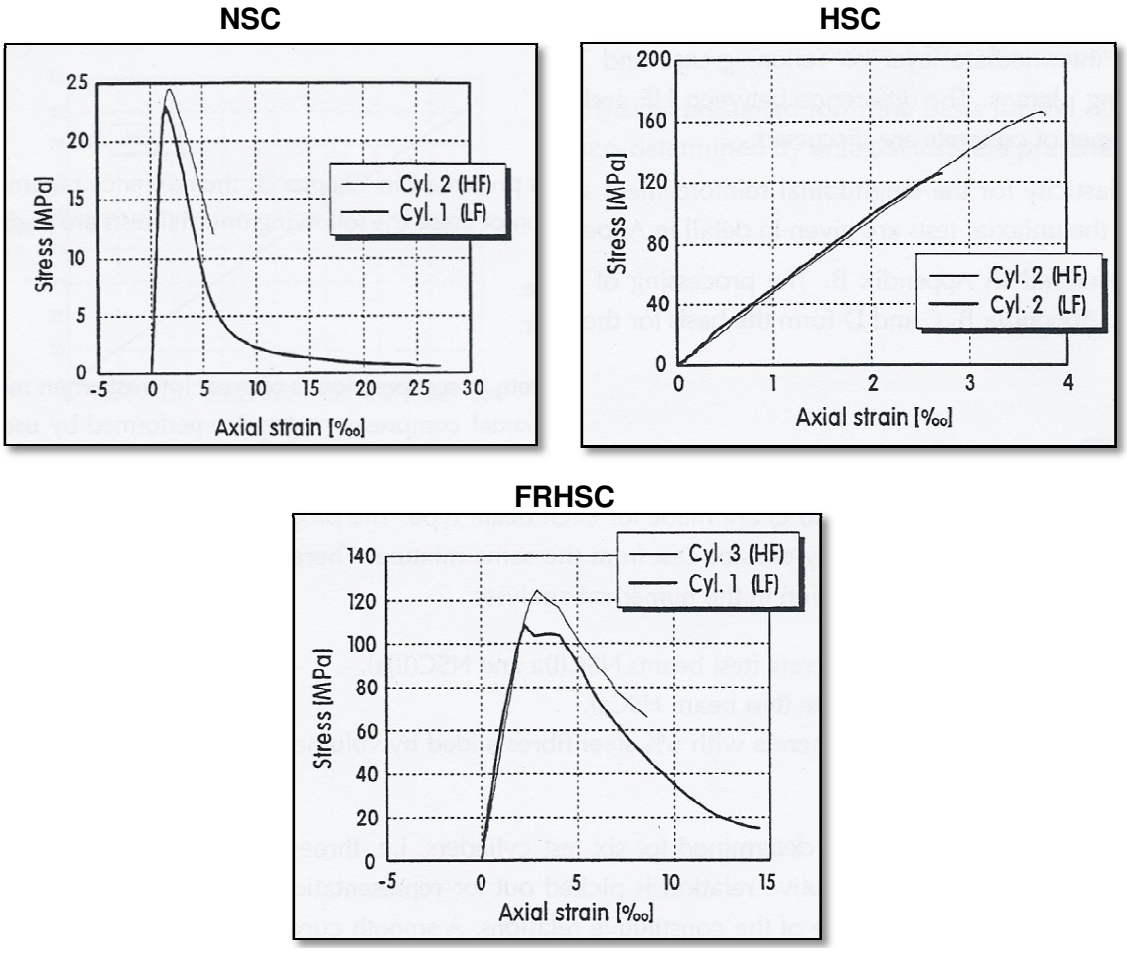

Figure B.2-5 - Compressive Constitutive Relations used in Analyses by Pedersen et al. (1996).

It is evident that the FRHSC is superior in terms of ductility, where the NSC tests also exhibit some ductility which is accommodated by the relatively low stresses it had absorbed to attain maximum compressive stress. The HSC shows a brittle response due to the large amount of energy released upon softening.

The tensile reinforcing for the Series I beams consisted of stranded wires, the Young's modulus of which was taken as 1.97×10^5 MPa and which was considered to not yield. The reinforcing steel bars used in the experiments (in Series I and II) were Ks550 s bars and the reference parameters for these were obtained from uniaxial tensile tests, the results of which are shown in Figure B.2-6. The Young's modulus was taken as 2.22×10^5 MPa (Pedersen, et al., 1996):

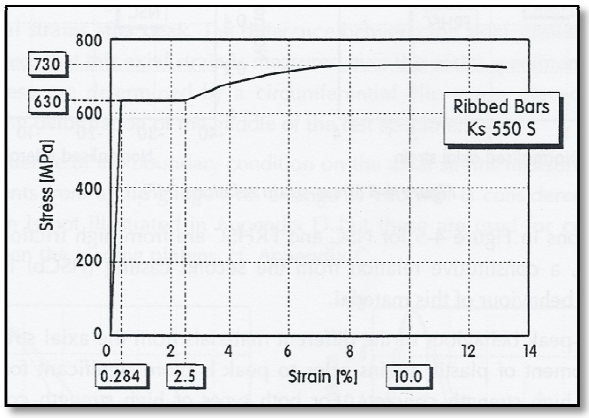

Figure B.2-6 - Uniaxial tensile test results for reinforcement (Pedersen, et al., 1996).

The results obtained using the design tool BEAM developed for the study by Pedersen et al. (1996) are shown in Figure B.2-7 for the high friction and low friction constitutive laws. The program is based on the Bernoulli assumption, being that plane cross sections remain plane. It also assumes that there are no plastic deformations. For more information on the program structure, assumptions, algorithms etc. kindly refer to Pedersen et al. (1996).

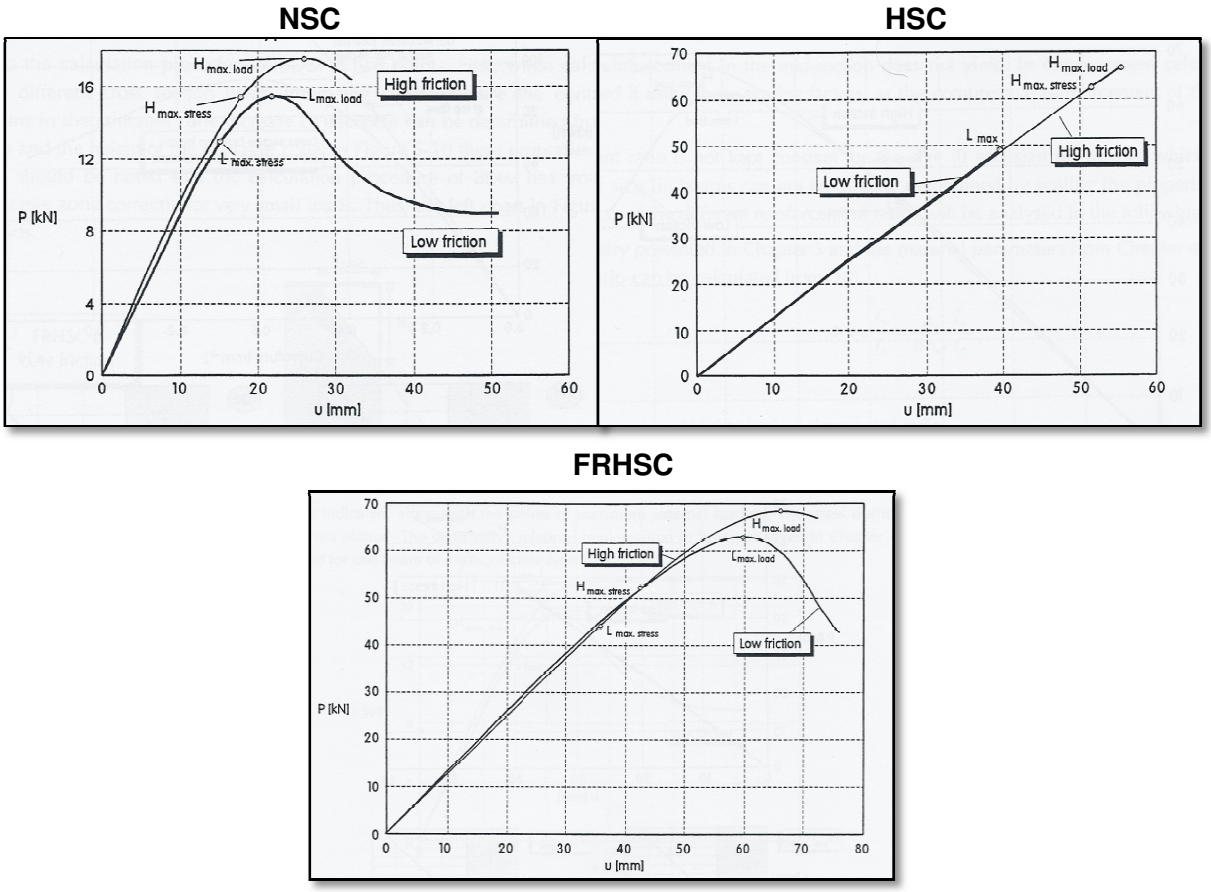

Figure B.2-7 - Results obtained using BEAM program (Pedersen, et al., 1996)

A non linear finite element analysis was carried out on the small NSC beam specimens using the program FEMLAB, which supplied a more detailed description of the mechanics of the structures, but further complexities arise such as obtaining and implementing appropriate plasticity models that more accurately describe material behaviour. Refer to Pedersen et al. (1996) for a more detailed description of FEMLAB.

Symmetry was used in the finite element model, and only NSC beams from series I were analyzed, using the constitutive relations obtained from uniaxial compression tests with low friction platens. The finite element model implemented in this program is illustrated in Figure B.2-8.

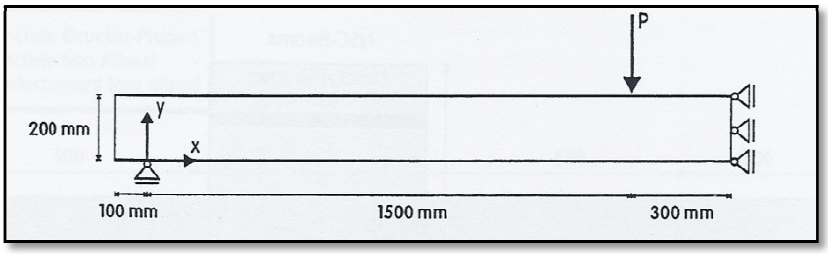

Figure B.2-8 - Model used in FEMLAB (Pedersen, et al., 1996)

A plane stress analysis was conducted. The reinforcement was modelled in layers by finding the equivalent area of reinforcement which contributes to the stiffness of the cross section, as shown in Figure B.2-9.

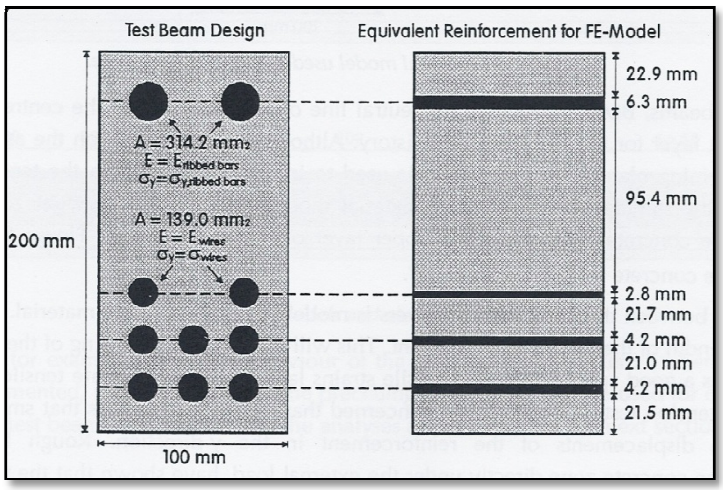

Figure B.2-9 - Equivalent Plane Stress Model (Pedersen, et al., 1996)

The concrete was modelled using a Drucker-Prager material model. However, a tension cut off for the material was required. Thus it was decided to introduce this tension cut off in the concrete model by modelling the concrete as an orthotropic material. Based on the BEAM analysis, a neutral line of strain was found to be close to the upper layer of tension reinforcement, for the entire period of loading. Thus the Drucker-Prager model was applied to the concrete above this reinforcement layer. The concrete below this layer of reinforcement was then modelled as a Von Mises material, but with a stiffness a fraction that of the steel. This is illustrated in Figure B.2-10 . Tensile material data was not obtained for the concrete.

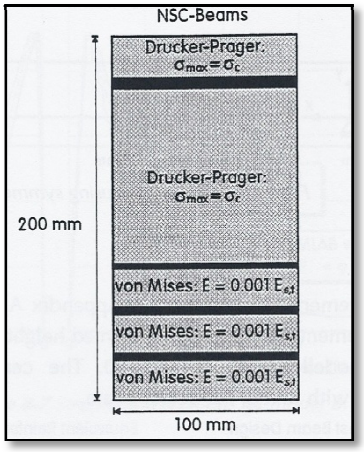

Figure B.2-10 - Cross sectional view of material properties implemented in FEMLAB (Pedersen, et al., 1996).

3 different models were tested, one with the entire concrete portion of the beam modelled as a Drucker-Prager material (Model 1) and two models with concrete modelled as a Drucker Prager material under compression and as a Von Mises material in tension (Models 2 and 3), with one thousandth the stiffness of steel. The difference between the last two models is only the fineness of the mesh (Model 2 having a coarse mesh). The results obtained using FEMLAB on the NSC Size I beam are shown in

Figure B.2-11 (a) for model 1 to show the effect of a change in the value of the dilatancy coefficient, where it is set equal to the coefficient of friction of the concrete (Φ=37°, associative plasticity) and where it is equal to 1 (non associative plasticity). The enhanced ductility due to the enhanced volume change facilitated by associative plasticity is evident. For the other two models, associative plasticity was assumed.

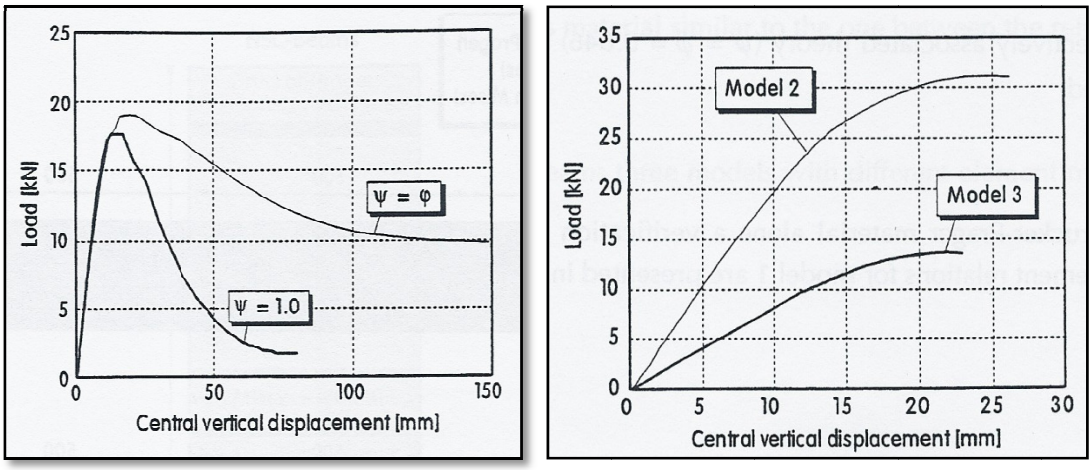

Figure B.2-11 – Load vs. displacement curves for (a) Model 1 and (b) Models 2 and 3 (Pedersen, et al., 1996).

It is evident that the three models do not correlate too well, and the mesh dependence of results where the tension cut-off (Models 2 and 3) was introduced is clear.

The round robin analysis conducted invited several researchers to contribute their analysis results for the problem at hand, with the experimental results, as obtained by Pedersen et al. (1996), kept confidential. Several contributions were made, with many different modelling approaches adopted. All of the contributors did not analyze all of the specimens that were tested, and were free to choose how they would model the structure and the material behaviour. Figure B.2-12 a) shows the variation of the results of the peak loads obtained in comparison to the experimental results, and Figure B.2-12 b) shows the variation of the peak vertical displacements obtained in comparison to the experimental results.

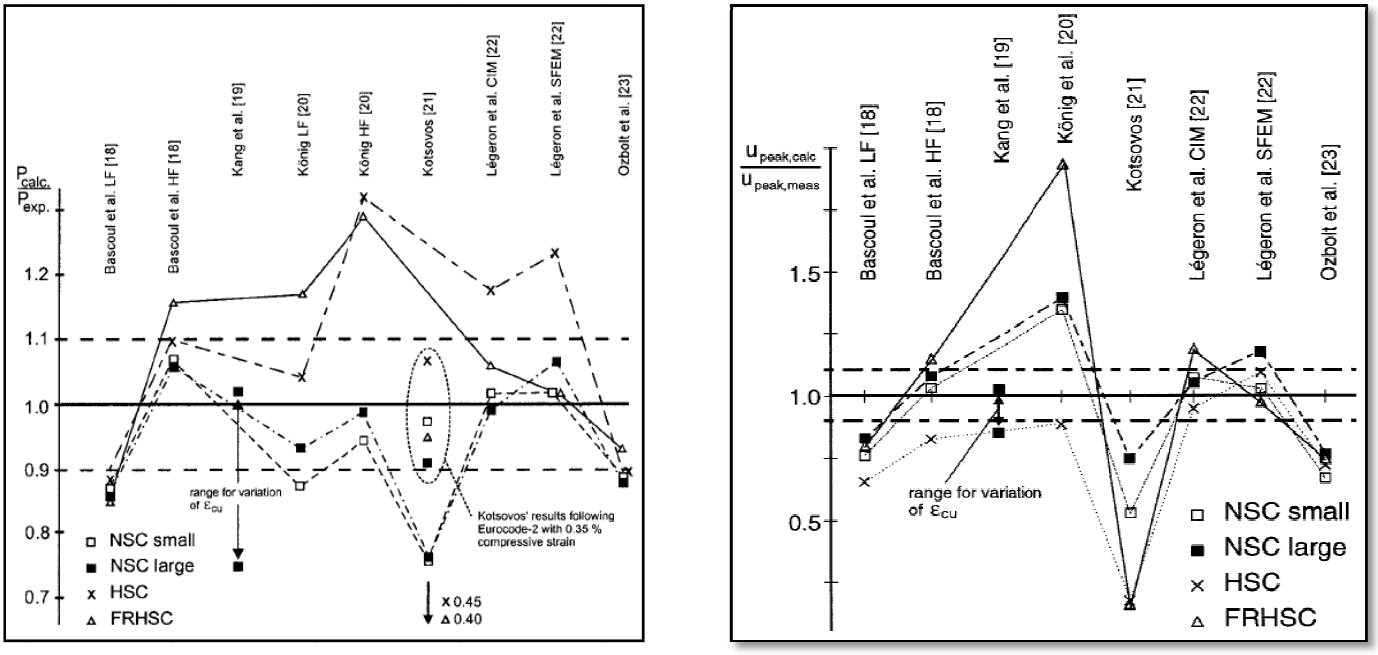

Figure B.2-12 - Comparison of Results obtained in Round Robin analysis for (van Mier, et al., 2000):

a) **Calculated maximum load over experimental maximum load for contributions.**
b) **Calculated maximum deflection over experimental maximum deflection for contributions.**

It is evident that there is significant variation in some instances, indicative of poor modelling practice or incorrect assumptions made regarding material behaviour. However, as limited information is available on the matter, it is difficult to determine the root of the variations. This could be the cause of their overestimation of ultimate strength as evident in Figure B.2-12 a), as failure was postponed to a larger load as the materials' ductility was overestimated and thus redistribution of stresses was more easily accomplished.

B.2.4 Pre-Processing of NLFEA

The over reinforced concrete beams of Pedersen et al. (1996) were analyzed in this project using DIANA and implementing the Rankine-Hill plasticity model as well as the Total Strain based rotating crack model on various mesh sizes. A fixed cracking model was not considered due to it not being physically representative of the experiments.

B.2.4.1 Model Geometry and Boundary conditions

Plane stress analyses were conducted on the simply supported beams subject to four point bending tests. The NSC, HSC and FRHSC small beams were analyzed (Series I). The beam details and boundary constraints are shown in Appendix A. Steel loading platens were implemented as the interaction between the concrete and the support and load points, as was done in the experiments. The dimensions and reinforcement detail of the beam can be seen in Appendix A. The steel reinforcement was modeled as embedded bar elements in DIANA (2009), with the assumption of perfect bond between concrete and reinforcement. The values for the reinforcement material parameters were obtained from tension tests performed by Pedersen et al. (1996). A thickness of 100mm was assigned to beam and plate sections.

B.2.4.2 Material Properties

The compressive concrete material properties were obtained from the uniaxial compressive tests performed by Pedersen et al. (1996). The other parameters were obtained using the parameter estimation relationships in the Model code (2010). The values implemented were the characteristic values, as used by Pedersen et al. (1996) in the analyses conducted in that study and as suggested for analysis and design purposes in the Model Code (2010). The use of the higher mean values as suggested by Hendriks et al. (2009) for ULS investigations, resulted in a more greatly overestimated structural response (the results of which are not considered in this study). The compressive strength data was obtained from the cylinder tests (2:1 aspect ratio) performed by Pedersen et al. (1996) and no adjustments were made to these parameters to incorporate environmental effects due to curing conditions. This was due to the fact that these same compressive strength values were used by Pedersen et al. (1996) in the analyses conducted in that study, thus the expectation of the curing conditions of the cylinders being identical to the beam specimens. The values obtained from the compressive test data along with the Model Code (2010) values were used for the Total Strain rotating crack models for the NSC, FRHSC and HSC beams, shown in Table B.2-2.

Concrete Material Properties for Total Strain Model

Concrete type:		NSC	FRHSC	HSC
Material Models	Rotating	-	-	-
Young's Modulus	E	27 673.6 N/mm²	47 627 N/mm²	52 347 N/mm²
Tension curve	Hordijk*	-	-	-
Tensile Strength	f_{tu}	1.952 N/mm²	8.286 N/mm²	6.09 N/mm²
Tensile Fracture	G_{ft}	0.1294 Nmm/mm²	0.2603 Nmm/mm²	0.1825 Nmm/mm²
Compression Curve	Parabolic*	-	-	-
Compressive Strength	f_{cu}	24.6 N/mm²	125.4 N/mm²	166.5 N/mm²
Comp. Fracture Energy	G_{fc}	4.2 Nmm/mm²	24.6 Nmm/mm²	8 Nmm/mm²

Reinforcing Steel Material Properties

Material model	Von Mises	-
Young's Modulus	E	222 000 N/mm²
Yield Strength	$(f_{ty};\ \varepsilon_y)$	630 N/mm² ; 0.00284
Ultimate Strength	$(f_{tu};\ \varepsilon_u)$	730 N/mm² ; 0.1

Table B.2-2 - Total Strain material parameters, Compressive dominated.

The Model Code (2010) does not account for the superior tensile and ductile properties exhibited by the FRHSC, thus values for the tensile strength and tensile fracture energy were multiplied with 1.5. The adjustment of the fracture energy was done to ensure that the transition from the linear elastic to the nonlinear was more gentle than if the lower value was used (which may cause numerical problems in a Total Strain model if the gradients of the tensile response pre and post peak differ too greatly). Experimental evidence performed by (Van Zijl, et al., 2011) also showed significantly superior tensile response, both ultimate strength and fracture energy for High Performance Fibre Reinforced Concrete. The HSC values were as obtained from the Model Code (2010) and not modified further. The material parameters for the steel reinforcing were obtained from tensile tests performed by Pedersen et al. (1996), and implemented using the pressure independent Von Mises plasticity model.

* Refer to Sections A.3.1.3 and A.3.1.5 for model descriptions.

Fracture energy based models were implemented for the tensile and compressive constitutive models of the concrete, with the values for the tensile fracture energy specified in the Model Code (2010) and the compressive fracture energies as calculated from the uniaxial compressive curves obtained from Pedersen et al. (1996). This was done to ensure regularization of energy dissipation across mesh sizes as well as to incorporate a more realistic behavior of the compressive responses of the material based on observed physical behavior. The compressive fracture energy for HSC could not be established exactly from the uniaxial compressive tests due to lack of post-peak data, thus an approximate value was assumed based on the results and accounting for the rapid rate of energy dissipation typical of such high strength materials.

The parameters implemented for the Rankine Hill plasticity model are shown in Table B.2-3. Isotropic material behavior was assumed for all concrete types, and the values below were used to describe the material properties in both material directions.

Concrete Material Properties for Plasticity Model

Concrete type:		NSC	FRHSC	HSC
Material Models	Rankine-Hill*	-	-	-
Young's Modulus	E	27 673.6 N/mm²	47 627 N/mm²	52 347 N/mm²
Tensile Strength.	f_{tu}	1.952 N/mm²	8.286 N/mm²	6.09 N/mm²
Tensile Fracture Energy	G_{ft}	0.1294 Nmm/mm²	0.2603 Nmm/mm²	0.1825 Nmm/mm²
Shear contribution to tens. failure	α_t	1	1	1
Cracking Viscosity	$m_{x,y}$	0.1	0.1	0.1
Compressive Strength	f_{cu}	24.6 N/mm²	125.4 N/mm²	166.5 N/mm²
Plastic strain at f_{cu}	κ_c	0.0017	0.00071	0.00222
Compressive fracture energy	G_{fc}	4.2 Nmm/mm²	24.6 Nmm/mm²	8 Nmm/mm²
Principal stress relation	β	-1	-1	-1
Shear contribution to comp. failure	γ	3	3	3
Reinforcing Steel Material Properties				
Material model	Von Mises	-		

* Refer to Section A.3.2.3 on page 49 for model material parameter descriptions.

Young's Modulus	E	222 000 N/mm²
Yield Strength	$(f_{ty};\ \varepsilon_y)$	630 N/mm² ; 0.00284
Ultimate Strength	$(f_{tu};\ \varepsilon_u)$	730 N/mm² ; 0.1

Table B.2-3 - Plasticity material parameters for compression critical beams.

A very low cracking rate viscosity was used, and sensitivity analyses on the value showed that there was no significant global influence due to this parameter, as failure was compressive dominated and detailed post peak response curves were not obtained (which would have more clearly shown the influence of this parameter). The use of crack rate dependence was found to be entirely necessary for all plasticity models in this study due to otherwise extensive convergence difficulties. α and γ, the shear stress contribution to tensile and compressive failures, were taken as the default values in DIANA (2009). The rest of the parameters were as established from the uniaxial compressive test data of Pedersen et al. (1996) or using the Model Code (2010).

B.2.4.3 Meshing

Two element types considered in these analyses were the Q8MEM and CQ16M elements (cf. Section B.1.3 on page 63). Three mesh sizes of each type were considered for the Series I beams. The mesh sizes of the quadrilateral elements were of square dimensions 12.5mm, 25mm, 50mm (Mesh sizes I, II and II respectively).

B.2.4.4 Loading and Solution Procedure

Steel loading and support plates were modeled as used experimentally. The loads on the 4 point bending setup were applied at the centre nodes of the steel loading plates. A displacement controlled analysis was performed with a Secant BFGS incremental procedure for all analyses. A regular Newton Raphson method showed divergence at far lower loads, and was thus not used. Step sizes for the Total Strain models varied between 0.005mm and 0.25mm depending on the models. The plasticity models were subjected to time dependant displacement loading corresponding to the loading rate of the experiments and time increments applied.

All analyses were governed by a force and energy convergence criteria with a tolerance of 1% to be satisfied simultaneously. The number of iterations allowed per analysis was 100.

Path following techniques (Updated normal plane and the more complex spherical path arc length methods governed by either regular indirect displacement or crack mouth opening displacement relations) in conjunction with automatically adaptive or energy based step size selection were implemented in attempts to obtain more detailed post peak response curves, but all attempts were futile.

B.2.5 NLFEA Results and Discussion

A summary of the analyses conducted for the compression critical beams are shown in Table B.2-4. Only Rankine Hill plasticity and Total Strain rotating crack models were considered for these beams, as fixed cracking does not describe the physical nature of the experiments. Refer to Table B.2-2 and Table B.2-3 for material parameters.

MESH SENSITIVITY INVESTIGATION – NSC, FRHSC, HSC	
Rankine Hill Plasticity Model	**Total Strain, Rotating Crack**
C-Q8MEM-P-I	C-Q8MEM-TS[R]-I
C-Q8MEM-P-II	C-Q8MEM-TS[R]-II
C-Q8MEM-P-III	C-Q8MEM-TS[R]-III
C-CQ16M-P-I	C-CQ16M-TS[R]-I
C-CQ16M-P-II	C-CQ16M-TS[R]-II
C-CQ16M-P-III	C-CQ16M-TS[R]-III

Table B.2-4 - NLFEA's on Compression critical beams.

B.2.5.1 Plasticity Model

The results obtained for the NSC series I beams using a Rankine Hill plasticity model are shown in Figure B.2-13, along with the experimental average peak load and associated average midspan displacement.

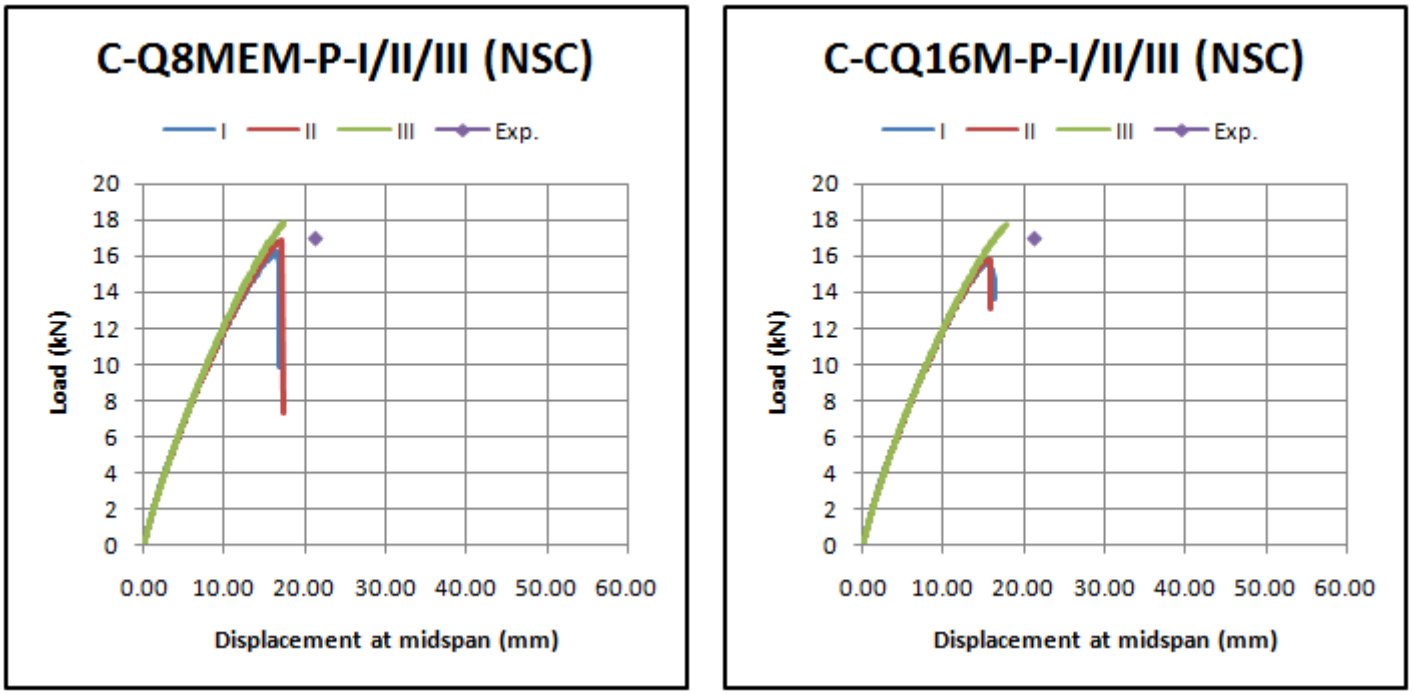

Figure B.2-13 - Load vs. Displacement results for compression critical NSC beams, plasticity model.

The use of cracking rate dependence in the plasticity model yielded good convergence for all analyses, as slight tensile plastic flow was observed numerically before the attainment of peak compressive stress in the model. Without the crack rate dependence, all attempts of attaining a solution diverged upon the first signs of tensile localization. The material imperfection introduced in the constant moment region was also required as the asymmetry in the boundary conditions imposed was not enough to ensure significant enough variation in the stress distribution field to ensure localization occurs and that the solution can continue.

The analyses correlate quite well with the experimental results, with the peak loads attained for most analyses being ‘safe’. The numerical results obtained for the peak loads were within a range of 92% to 105% of the experimental results. However the average experimental loads are underestimated in general. The different mesh sizes show good correlation with one another, as well as between the two mesh types. The C-Q8MEM-P-III and C-CQ16M-P-III analyses showed an increase in strength to some extent past the other peak loads. This may have been due to the choice of iterative procedure (Secant BFGS) and its proclivity of calculating a secant stiffness matrix that is not unique in a system of multiple degrees of freedom. Thus the complexities already inherent in the calculations of

the consistent tangential stiffness matrix relation between the stress and strain rates in a plasticity framework along with some mesh locking due to large element size may have overestimated the strength due to a numerical flaw.

The failure mode observed was also compressive failure, as can be seen by the development of the compressive zone through the load steps and the compressive softening at the top of the beam in Figure B.2-14 illustrating the horizontal stress vs. depth at midspan at various load steps in the analysis. The load steps are shown in steps from 1 to 4, with step 1 being at early stages of the analysis (still linear elastic range) to step 4 being the load step at the peak of the response curve in Figure B.2-13 for the C-Q8MEM-P-II analysis.

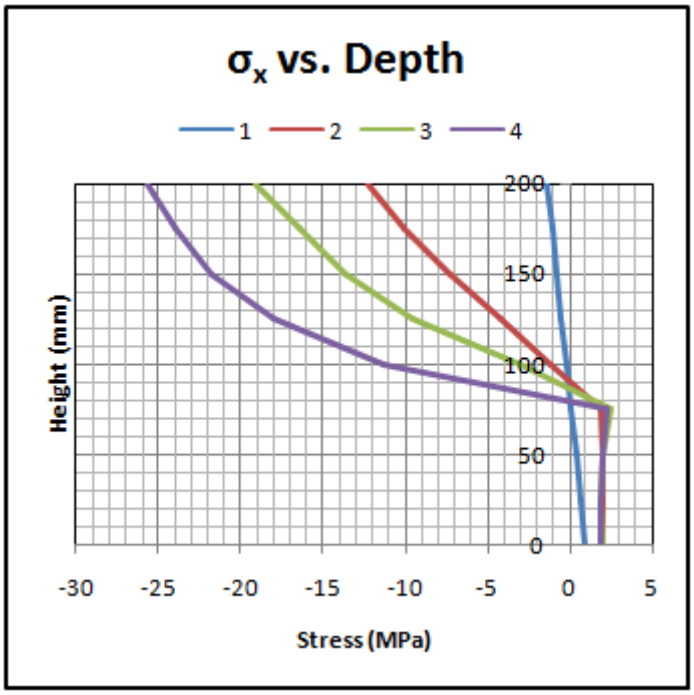

Figure B.2-14 - Development of horizontal stress at midspan over several load steps.

What is of great importance in this particular analysis, is that the use of only the compressive behavior of the concrete in conjunction with the empirical relations given in the Model Code (2010) and relatively simple modeling practice yielded such reasonably accurate results. For the purposes of design based on NLFEA, this is particularly encouraging considering the different and complex mechanisms at work in such a 4 point bending experiment, and that it essentially relates quite closely to the distributed loading anticipated in real beam structures (when considering the similar moment distributions both loading types cause in a

beam). The lack of any significant post-peak response however, other than the rapid drop in resistance, is again discouraging when considering the emulation of physical structures and the other design aspects to be considered.

The response curves obtained for the FRHSC beams modeled with a Rankine Hill plasticity model are shown in Figure B.2-15, along with the experimental average peak load and corresponding displacement at peak load.

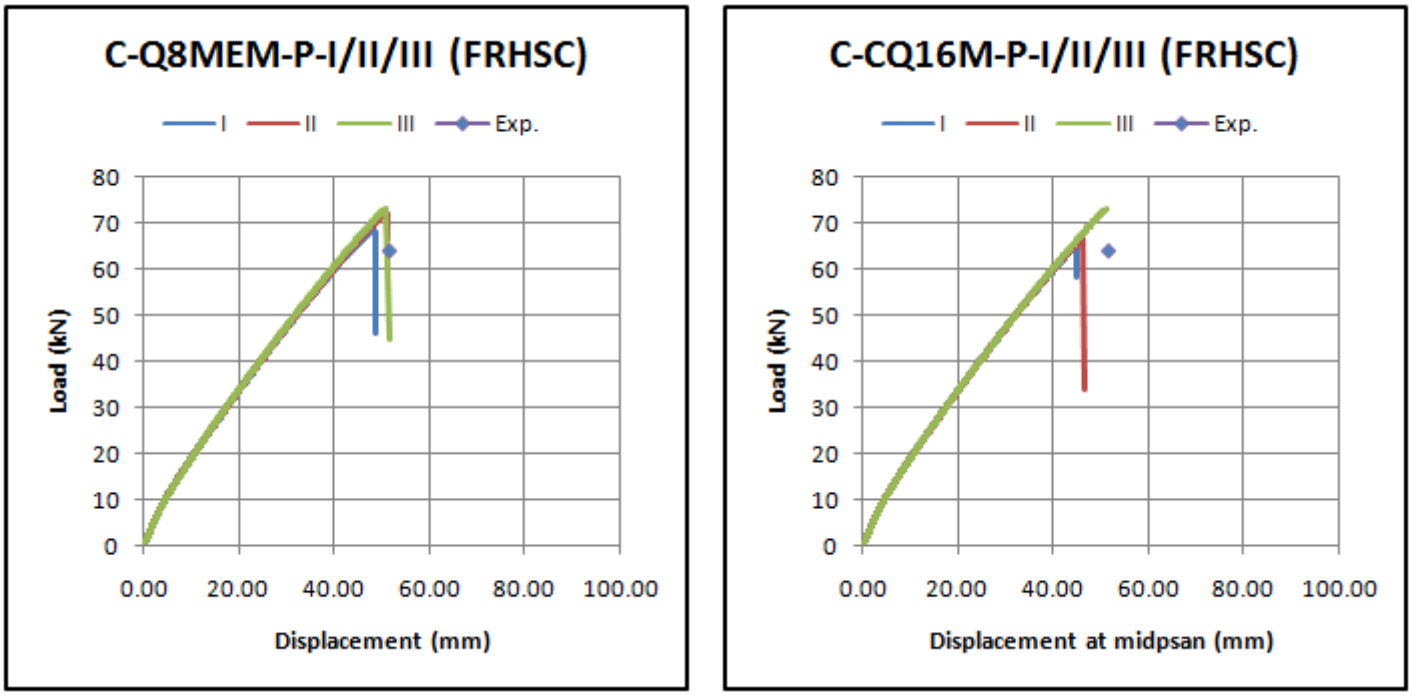

Figure B.2-15 - Load vs. Displacement results for compression critical FRHSC beams, plasticity model.

The experimental peak loads obtained were 60.5, 64 and 67.5 kN, thus variation over a range of 7 kN. Compared to the maximum experimental peak load, the analyses reach a realistic peak, but the average experimental peak load is overestimated by up to 17%. Thus the use of the relations in the Model Code (2010) for the FRHSC provided satisfactory results, as well as the 50% increase on the tensile parameters as obtained from the Model Code (2010), although tension was not a dominant mechanism. Ideally a database of the mechanical properties of fibre reinforced concrete and statistical inferences and extrapolations needs to be created in order for a fibre reinforced concrete specific model code to be established. Only then will any reliability based design practice based on the results of NLFEA be feasible or even possible. One of the

principal advantages of FRHSC is that structural members can be designed with a shallower cross section, due to the superior tensile and ductile characteristics (which will induce a greater compressive stress in the top of the beam at the same loads). Unfortunately beams of varying depths were not tested experimentally, so an investigation on the ability of the Rankine Hill plasticity model to capture any potential difference in behavior for varying beam sizes was not possible.

Good correlation was observed for the different mesh sizes and types, giving further evidence of mesh insensitivity, at least until the peak load was reached. Divergence occurred close to the average experimental peak, except for the C-CQ16M-P-III analysis, which may again be attributed to the Secant BFGS incremental procedure.

The observed mode of failure for these beams was also compressive failure, with compressive softening about to occur, as can be seen in Figure B.2-16, the stress distribution over the height of the beam at midspan at the peak load.

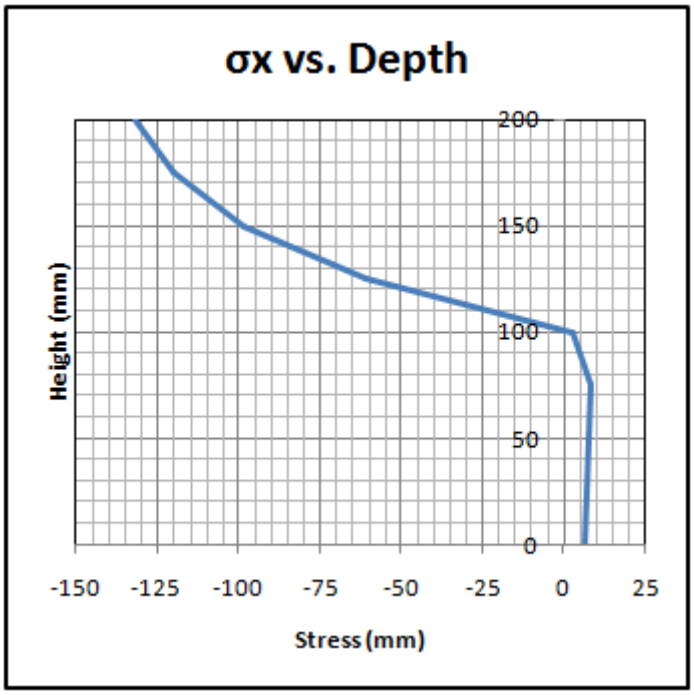

Figure B.2-16 - Horizontal stress through height of FRHSC beam at midspan.

The results obtained for the HSC beams using Rankine-Hill plasticity are shown in Figure B.2-17 along with the average experimental results.

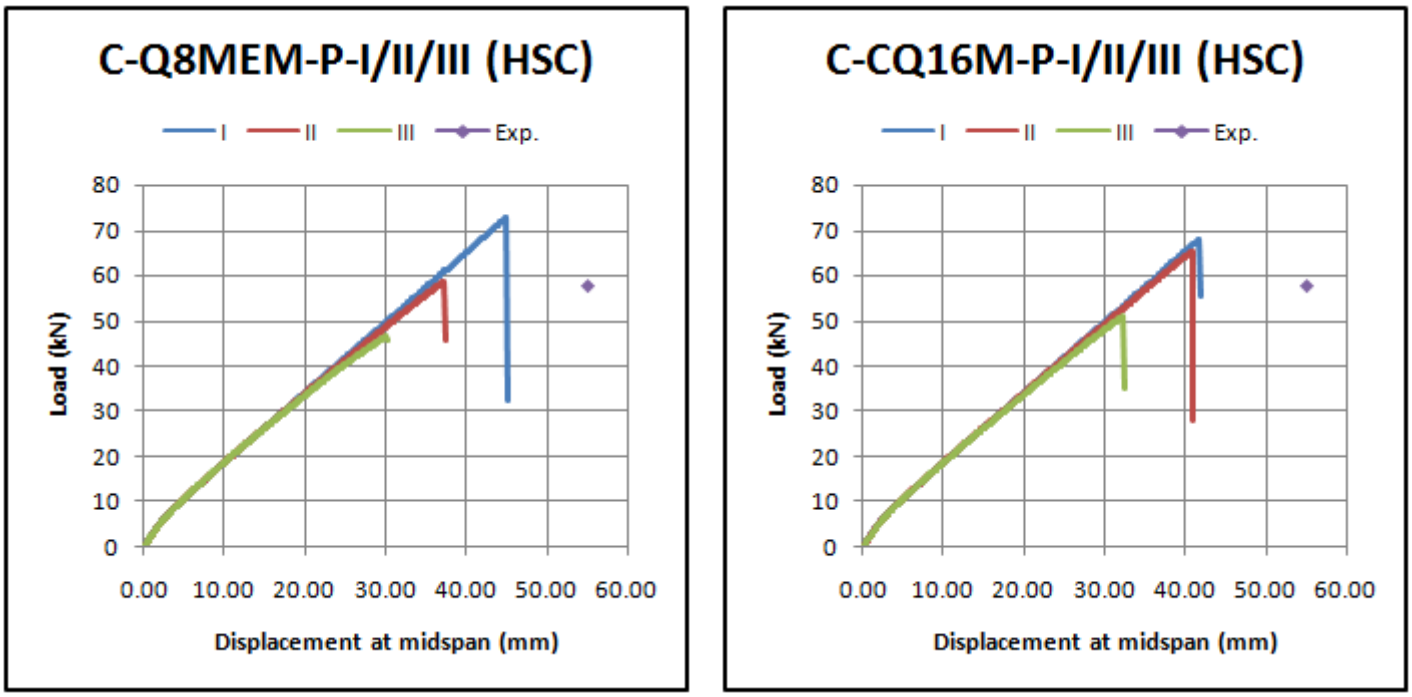

Figure B.2-17 - Load vs. Displacement results for compression critical HSC beam, plasticity model.

None of the analyses on the HSC beam specimens correlated with the experimental results. The use of parameters as established in the Model Code (2010) seems to not be entirely justified. Numerous sensitivity analyses were conducted based on parameter estimation, but due to the interdependence of all the required parameters when the entire model is considered, there was no way of justifying these results. Thus upon scrutiny of the output, it was realized that the choice of the compressive fracture energy G_{fc} (8 Nmm/mm^2), as was calculated for previous analyses done at the early stages of this study based on the criteria of avoiding snap back at a constitutive level, was in fact too low. This was attributed to the fact that those studies involved the use of lower, more conservative values for the compressive strength. Therefore, for the higher compressive strength involved in the new analyses, the intermediate plastic strain value (κ_{mi} cf. eqn.(A.3.95)) was actually too low, resulting in snap back behavior at the constitutive level for the compressive response for the element sizes II and III and thus the early divergence of the solutions. However, the combination of mesh size I and of G_{fc} complied with the limits imposed on κ_{mi}, thus snap back would not have occurred for these models and hence the more detailed response curves. Experience was to suggest that there would have

been more consistency for the analyses if this had been corrected. However, slight compressive softening was observed to have started for analysis C-Q8MEM-P-I (no constitutive snap back) analysis with the incorrect G_{fc} value. Thus it is speculated that with the more appropriate and greater G_{fc} value required, the load that could be attained for this analysis would be higher as higher values of compressive stress would be maintained for longer periods of plastic flow, as the descending branch of the constitutive law governing the compressive response would be less steep. Thus the use of the other material parameters, as established in the Model Code (2010) would still lead to a response curve that overestimates experimental response. This was confirmed with re-analyzing the C-Q8MEM-P-III model, using an appropriate value for G_{fc} (25 Nmm/mm^2) based purely on the requirement of no constitutive snap back. This is shown in Figure B.2-18.

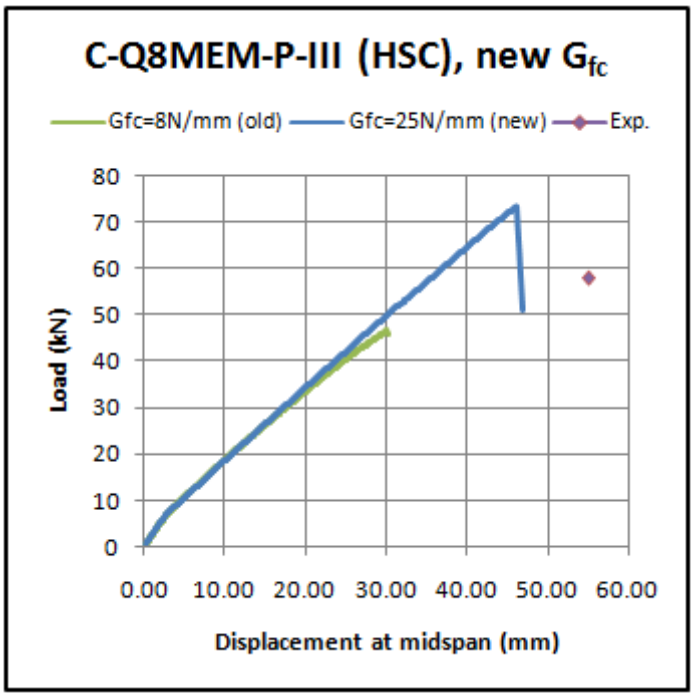

Figure B.2-18 - Load vs. Displacement result using new compressive fracture energy for HSC beam.

The experimental evidence suggests that the HSC showed no compressive 'ductility'. Such explosive failure due to such higher stresses and sudden subsequent energy release, would suggest that there is no softening that takes place thus no gradual decrease of compressive resistance with increasing plastic strain and no concept of inelastic work that can be associated therewith. Thus

HSC materials need some other means of numerically representing their compressive behavior, due to the volatility thereof at such high stresses. For design purposes based on NLFEA results, a fracture energy based approach for modeling compressive behavior does not suffice.

B.2.5.2 Total Strain Rotating crack model

The results obtained for the analyses on the NSC beam using a rotating crack model with parameters as specified in Table B.3-3, are shown in Figure B.2-19 for the various mesh types and sizes along with the average experimental peak load and associated displacement.

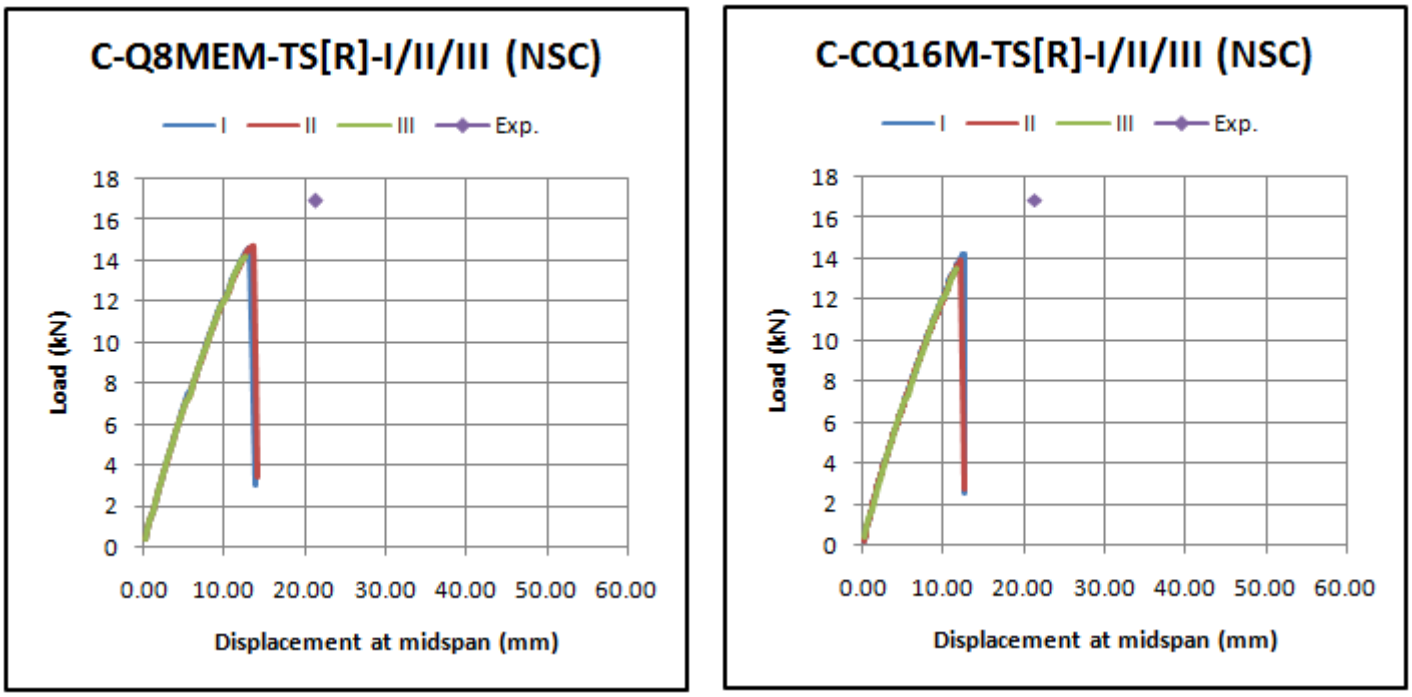

Figure B.2-19 - Load vs. Displacement results for compression critical NSC beams, rotating crack model.

The use of the material parameters established from the Model Code (2010) and the rotating crack model showed peaks for all analyses which were far below (only about 80%) those observed experimentally. There was good correlation between the analyses of varying element types and sizes showing consistency of the constitutive model, the peak values for the Q8MEM meshes were slightly higher than for the CQ16M meshes. The post peak behavior observed was merely a rapid reduction in load carrying capacity followed by divergence of the solution, and not the gradual decrease as observed experimentally. The use of a

parabolic constitutive relation for compression (fracture energy dependant) was found to be necessary as analyses conducted using Thorenfeldt compressive relations (not fracture energy dependant) yielded divergence at an even earlier stage.

Compressive crushing was observed for the elements in the top of the beam in the constant moment region, with the greatest inelastic behavior due to the compressive stresses being observed in the elements at the interior of the loading plates. Several cracks were also formed, with tensile softening taking place before indication of inelastic behavior in compression. The plastic flow can be represented by the normal 'crack' strains at the integration points (ε_{nn}^{cr}) at the peak load, as in Figure B.2-20 showing a vector plot of the crack directions. The plastic flow or rather compressive strength violation is also represented by a 'crack', but with a direction perpendicular to that of the tensile cracks. Thus the direction perpendicular to the cracks seen in the illustration is that of the maximum principal strain vector (ε_1^{cr}).

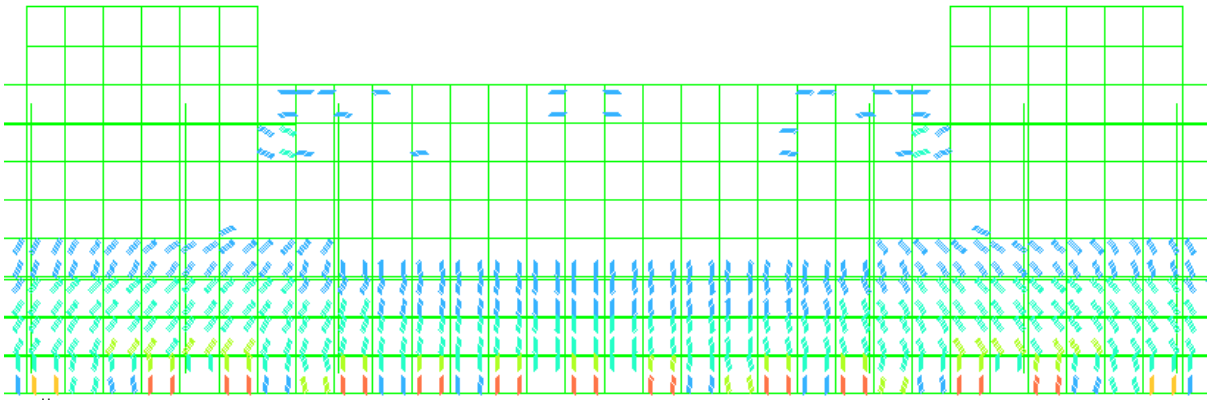

Figure B.2-20 - Cracking at peak load for midspan of NSC beam.

The development of the horizontal stress through the depth of the beam at midspan over a selection of load steps can be seen in Figure B.2-21 (load step 1 at an early stage of the analysis and step 3 at peak load for C-Q8MEM-TS[R]-II model). It is clear that tensile softening has occurred along with some crack propagation, as well as compressive plastic flow having developed through the depth of the beam at the peak load (Curve 3). Such tensile cracking and propagation was not observed experimentally, especially not at these lower load levels. Thus the proclivity of the rotating crack model to exhibit extensive cracking is evident, especially considering the plasticity model more accurately

reflecting reality with no tensile softening being captured at the peak load, consistent with the experiments.

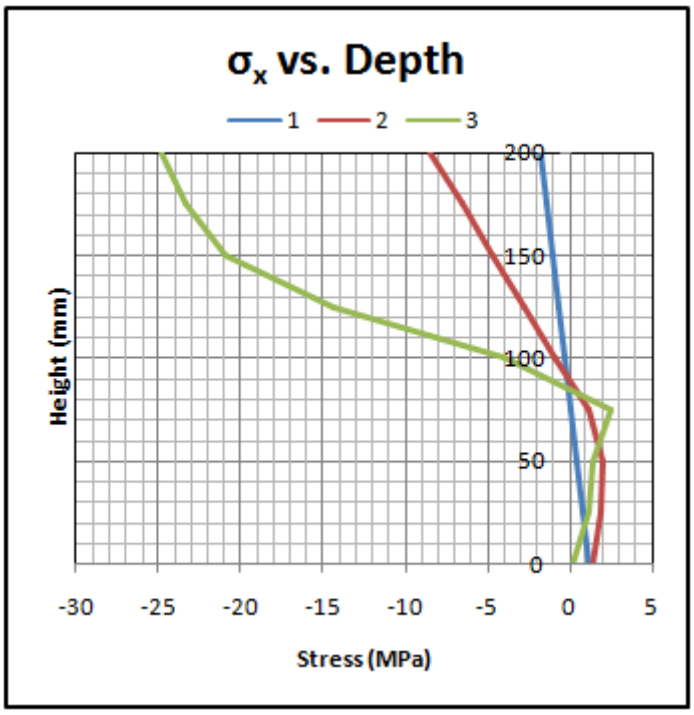

Figure B.2-21 - Variation of horizontal stress at midspan for various load increments.

The results obtained for the FRHSC beam using the rotating crack model are shown in Figure B.2-22.

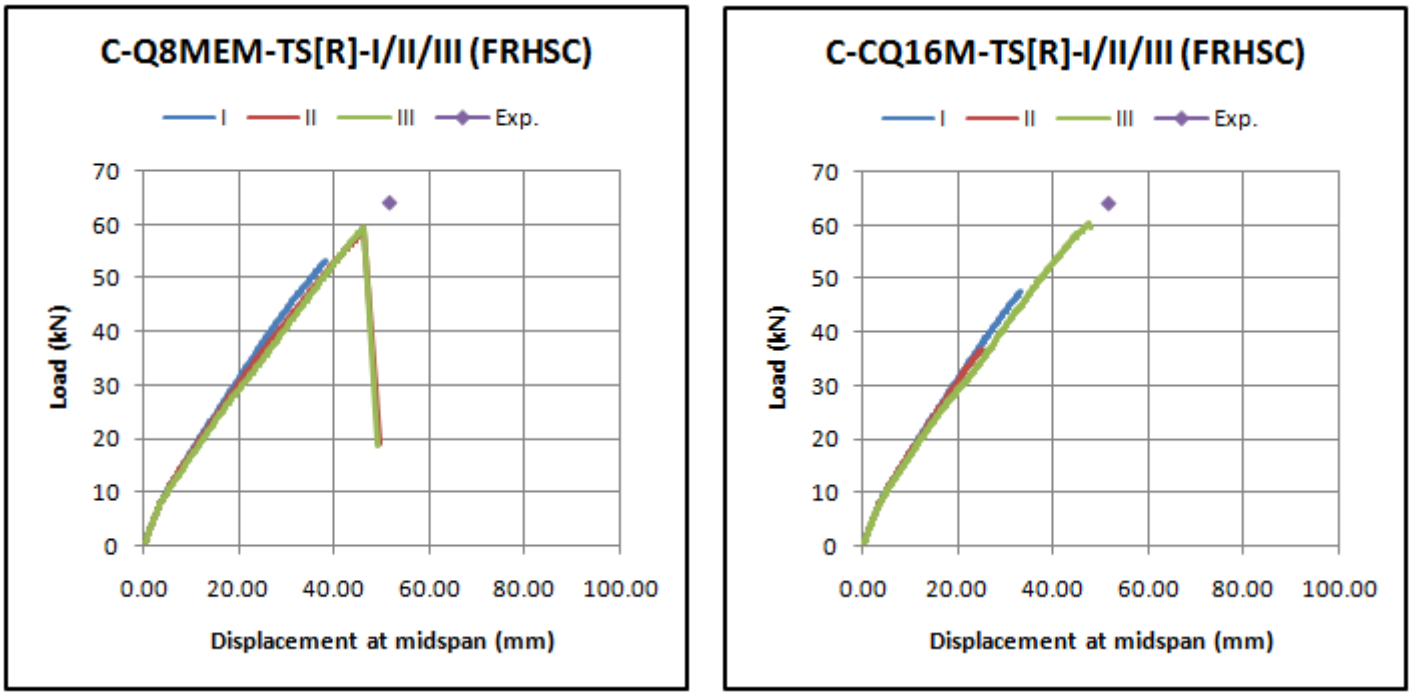

Figure B.2-22 - Load vs. Displacement for compression critical FRHSC beam, rotating crack model.

Only three of the analyses reached a peak (C-Q8MEM-TS[R]-II, C-Q8MEM-TS[R]-III, C-CQ16M-TS[R]-II) and compared relatively well with the experimental values, underestimating the peak position slightly. Very small load increments were used to attain the responses shown in the curves, especially for the smaller mesh sizes but with no additional response captured. It seems that the decision made to increase the tensile parameters for the FRHSC model by 50% of those obtained using the Model Code (2010) relations was again justified, as a decrease in these would lead to a further underestimation of the peak. There is clearly inconsistency between the results for the rotating crack model, not as much in the predicted paths but in the successful convergence rates between the mesh types and sizes.

Compressive failure was observed, as can be seen in Figure B.2-23 for the minimum (maximum compressive) strain contour plot (ε_2) on the deformed shape for the final load step showing the concrete elements at the interior of the supports failing under compressive loads. Figure B.2-24 is a maximum (maximum tensile) strain contour plot (ε_1) for the final load step showing more clearly the crushing failure as the development of cracks in the compressive

zone suggesting the crushing and spalling of the concrete at the top of the beam at midspan.

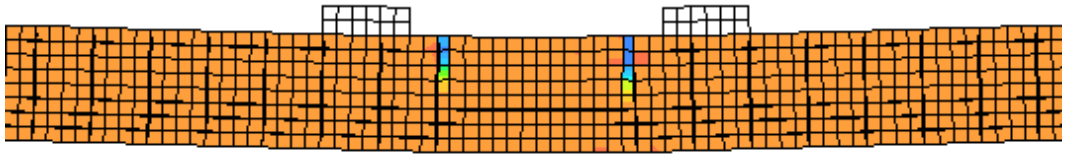

Figure B.2-23 - ε_2 strain contour plot at failure.

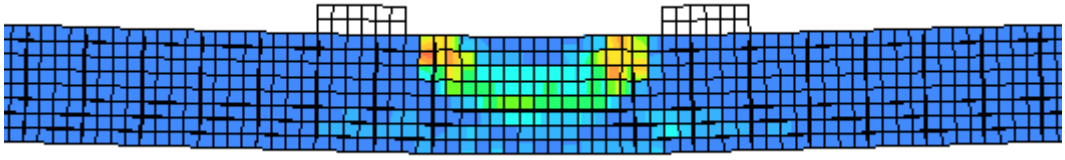

Figure B.2-24 - ε_1 strain contour plot at failure.

The results obtained for the compression critical HSC beams using a total strain rotating crack model are shown in Figure B.2-25.

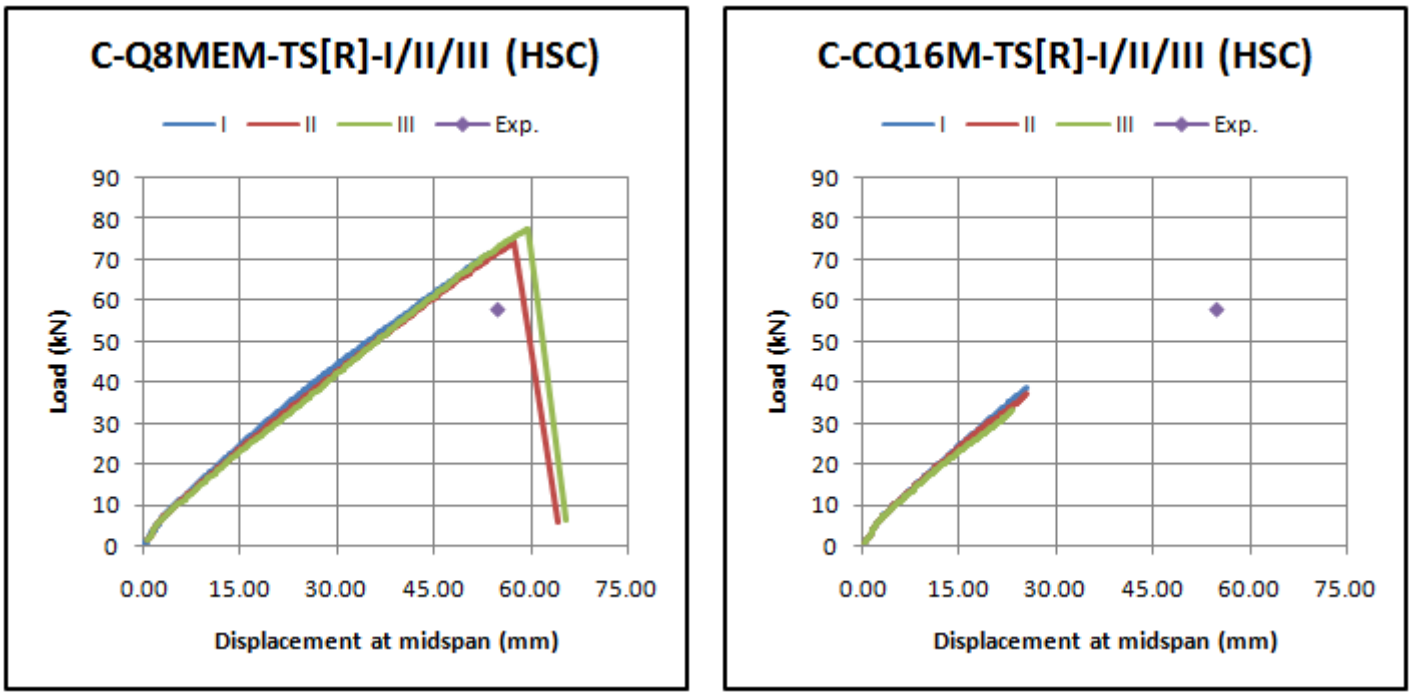

Figure B.2-25 - Load vs. Displacement results for the compression critical HSC beams, rotating crack model.

The Q8MEM models all reached a peak load which exceeded that of the experiments, followed by a sudden drop in resistance which could not be captured experimentally. The CQ16M models all struggled to attain any more detailed responses, regardless of the attempts made. The stiffness of the overall response is less than that obtained with the plasticity models, suggesting that more extensive cracking occurred at early stages of the analysis at the initiation of plastic behavior (non linearity of response curves begin at approximately 4mm), which is typical of a total strain rotating crack model. The system stiffness matrix is reduced more rapidly as cracking is initiated at more integration points.

This more extensive localization leading to a less stiff resistance also changes the location of the compressive failure zone as compared to the other rotating crack models. The compressive failure is focused in the weakened column of elements as opposed to the elements at the interior points relative to the loading plates as for the other analyses. Therefore the failure captured numerically does not represent the 'explosive' failure of the majority of the compressive zone crushing as was observed experimentally. Due to the high compressive capacity of the material and low (relative to the compressive capacity when comparing it to NSC, tensile strength for HSC is 3.65% of compressive strength, ratio for NSC is 7.9%) tensile capacity, the beams deformation and decrease in stiffness (due to cracking) occurred long before it was near compressive failure. Compressive failure was only imminent at a later stage where, considering the geometry of the mesh in the instant configuration prior to compressive localization, the compressive failure and maximum compressive stress localized in the elements at the top of the beam between the supports. Thus the curvature is excessive compared to what happened experimentally as the moment in the midspan is now more focused on the elements of the mesh in the centre of the beam as a result of the extensive cracking. This is explained in Figure B.2-26 for the contour plot of the minimum (maximum compressive) principal strain (ε_2) where the deformation of the element at the top of the beam due to the concentrated curvature is evident.

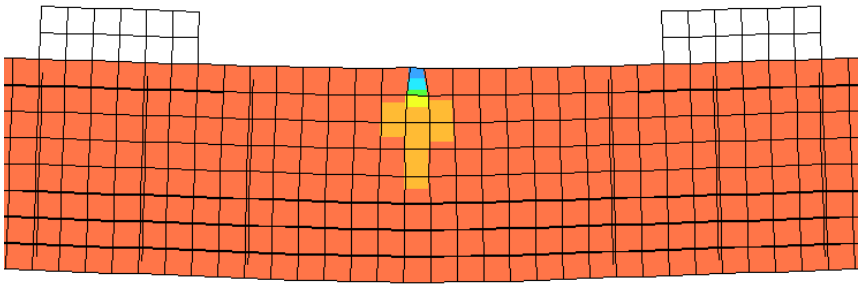

Figure B.2-26 - ε_2 strain contour plot for HSC beam, rotating crack model.

Figure B.2-27 shows the development of stress through the depth of the beam at midspan for model C-Q8MEM-TS[R]-II for various load steps numbered in ascending order according to amount of load applied. It is clear that a complete tensile crack has developed through the section at peak load (curve 5).

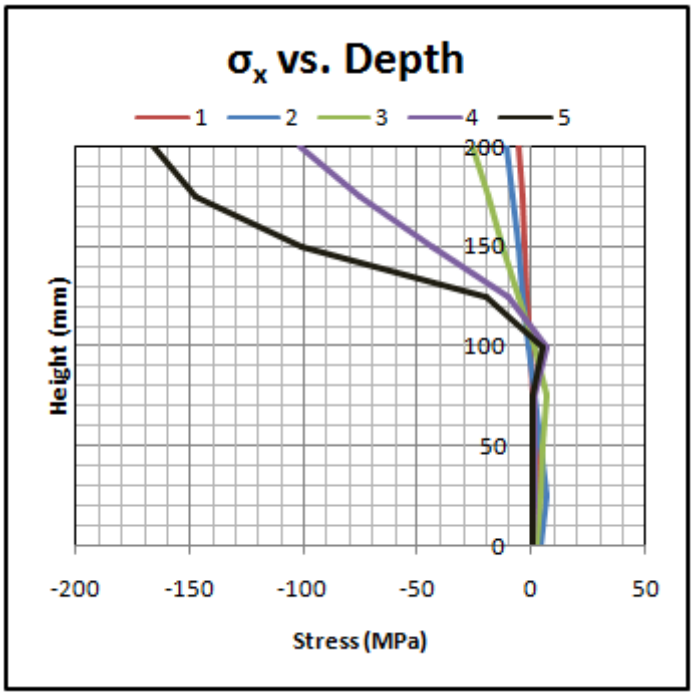

Figure B.2-27 - Horizontal stress variation through depth at midspan, HSC, rotating concrete.

Using the material parameters from the Model Code (2010) in conjunction with the rotating crack model still showed a peak load that far surpassed the experimental peak (for Q8MEM meshes) and that exhibited a different mode of

failure. This suggests that the mechanisms governing physical HSC are vastly different from those captured using these values and numerical tools.

In the next section, the peak loads and corresponding displacements obtained numerically are normalized with respect to the average values obtained experimentally, to provide a summary and a comparison of the analyses for the different material models and mesh types and sizes for the different beams investigated.

B.2.5.3 COMPARISON OF ANALYSES

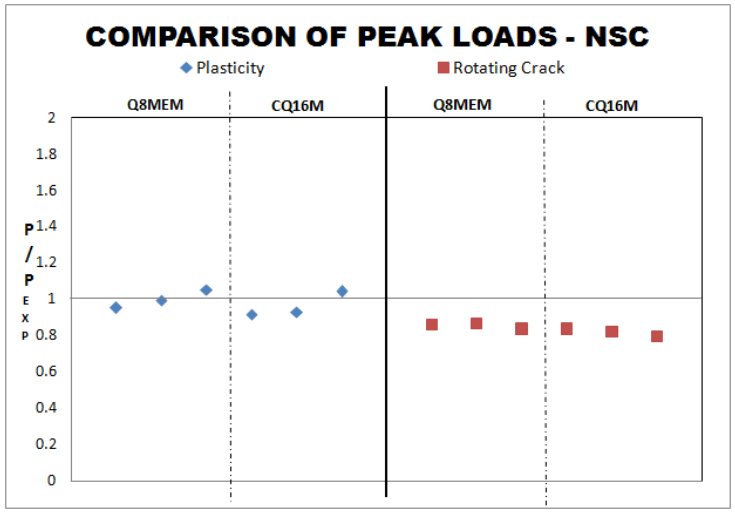

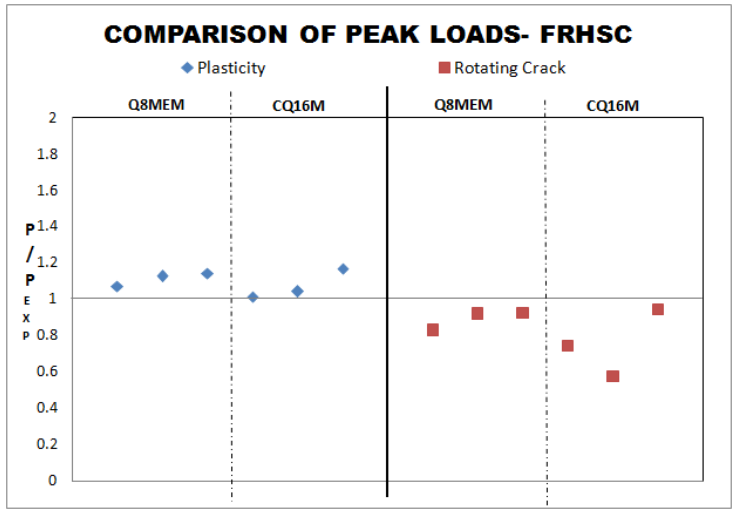

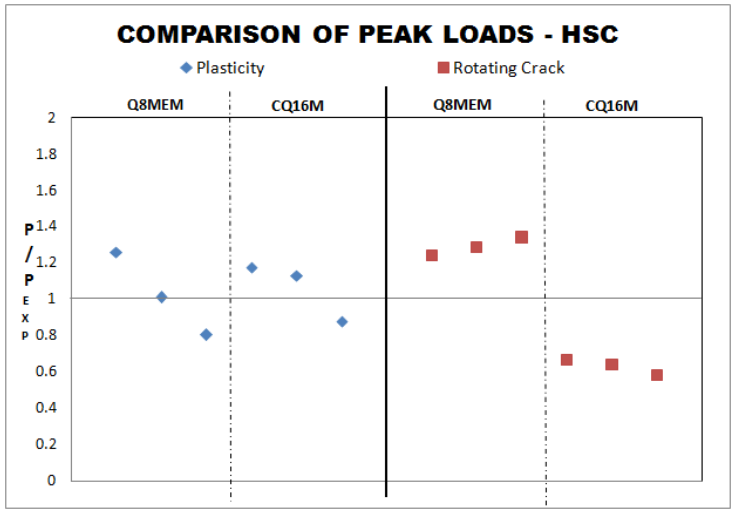

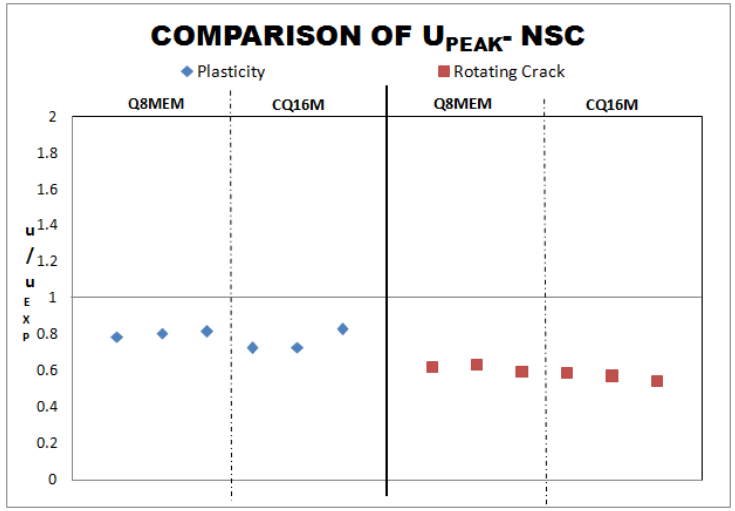

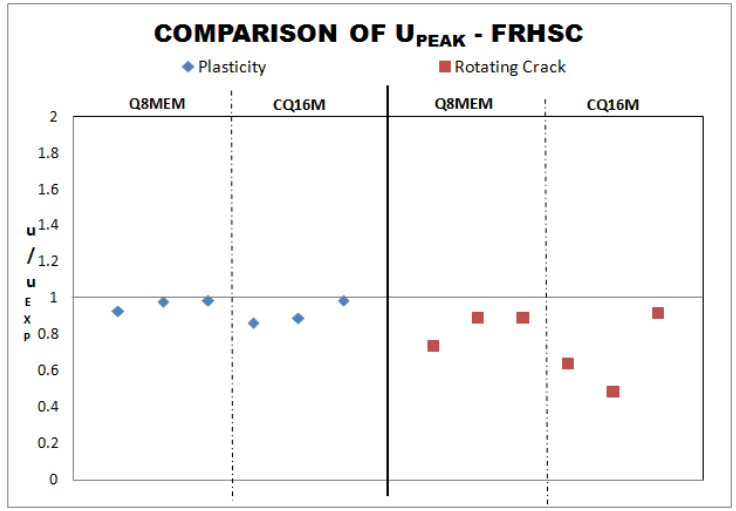

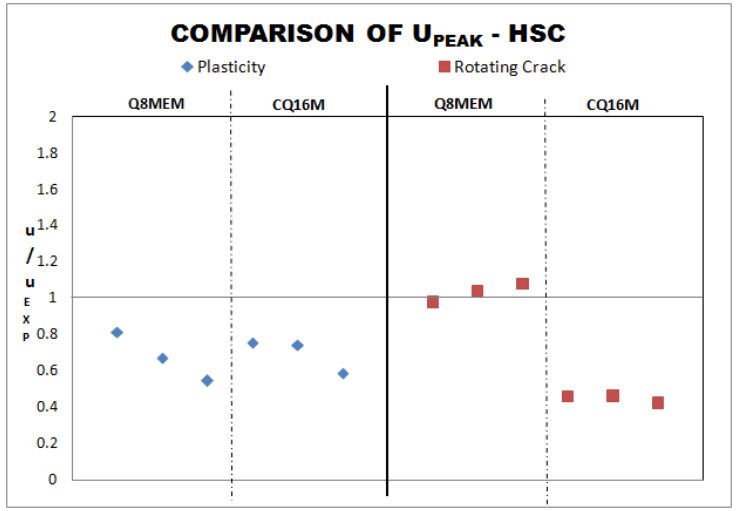

Figure B.2-28 - Comparison of analyses, Compression Dominated Study.

The data points for each mesh type (Q8MEM, CQ16M) are plotted from left to right corresponding to the ascending order of the mesh size (I. II, III) for each material model and beam type investigated in Figure B.2-28.

For the NSC analyses, both material models showed good consistency over the mesh types and sizes. The use of fracture energy dependant constitutive laws for the rotating crack model exhibited mesh independent results effectively. However the peaks were underestimated quite substantially when compared to the plasticity models, due to the poor stress redistribution performance of the rotating crack model and the more tensile dominant failure observed before compressive capacity was attained. The use of the material parameters as obtained in the Model Code (2010) based only on the value of the mean compressive strength of the material, proved to yield good numerical results especially for the plasticity model.

The peak response values of the FRHSC beams were relatively well captured by the plasticity models for all meshes considered. Mesh dependence between the peak values is evident, which may be due to the larger mesh sizes yielding a stronger global response due to either locking or the larger strain increments per element per step, or due to the nature of the Secant BFGS iteration method. The rotating crack model did not exhibit the same consistency between results for various meshes, with differences of 45% to 90% of the experimental average peak values being obtained. The phenomenon of the ‘stress trapping’ and restricted stress redistribution is more pronounced for this stronger material than was the case for the NSC beams, due to the higher stress values attainable.

The HSC analyses poorly reflected reality. In the case of the plasticity models, the rate dependence assumptions provided results where the smaller mesh sizes attained higher peaks than the larger meshes (contrary to the differences for mesh sizes observed for the NSC and FRHSC beams). This was attributed to the use of an incorrect compressive fracture energy, which caused snap back at the constitutive level for the larger mesh sizes and thus premature failure computationally. The snap back is not physically present for this case but rather refers to the steep slope of the descending branch of the softening model and the numerical difficulties associated therewith. This can be seen in Figure B.2-29 showing the comparison between the compressive softening constitutive relations for the Hill criterion and the parabolic compressive relation.

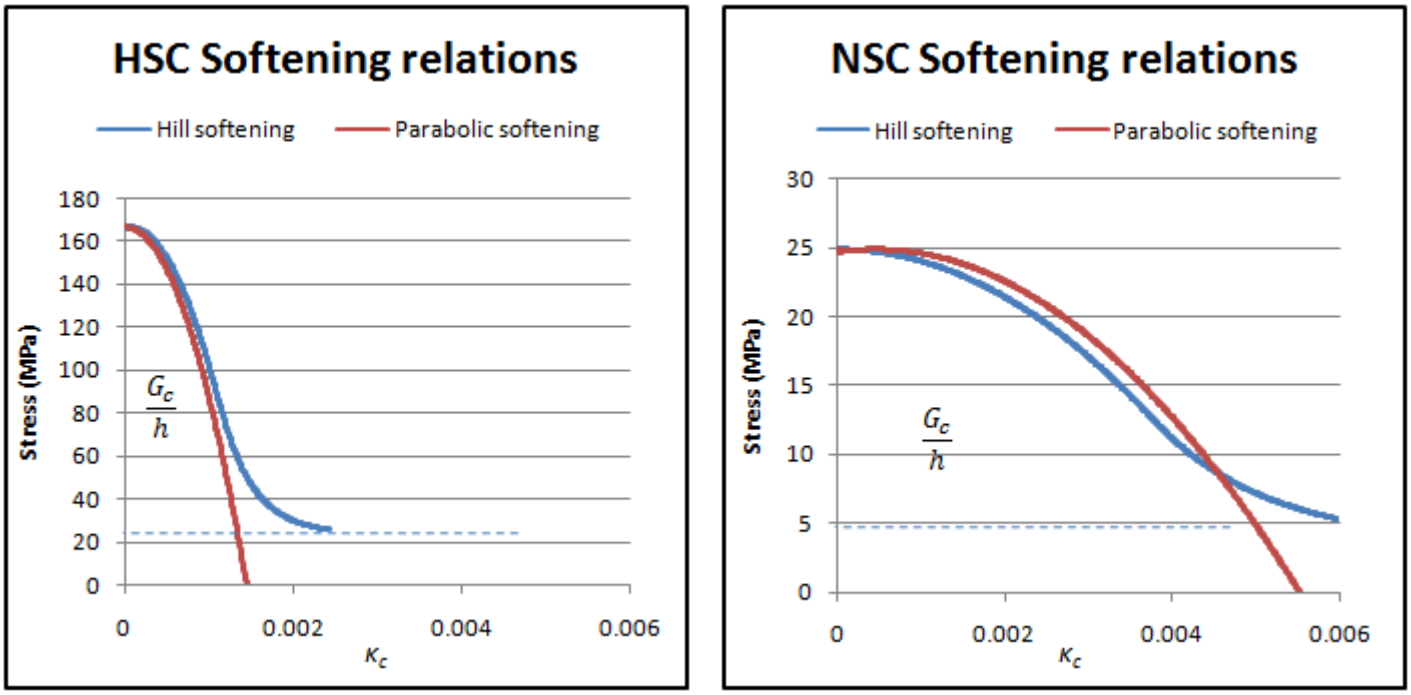

Figure B.2-29 - HSC and NSC Softening relations.

The fracture energy for the Hill softening relation is bounded by the curve and the dashed blue line, and for the parabolic softening relation it is bounded by the red curve and the axes. The compressive softening relation for the NSC material is also shown, with the same scale on the horizontal axis, suggesting a larger fracture energy value for HSC was required. The occurrence of the constitutive 'snap back' is earlier for the larger mesh size, as the intermediate plastic compressive strain is inversely proportional to the representative area of inelastic energy dissipation, which itself depends on the element dimensions. The rotating crack model showed better correlation between mesh sizes of the same type, as constitutive snap back was not present. The post peak softening expressed mathematically by the parabolic constitutive relation, does not require an intermediate plastic compressive strain parameter as there are enough boundary parameters to describe the single parabolic softening function as opposed to the two functions describing the softening slope of the plasticity model. The concept of stress trapping in the elements was evident especially for the Q8MEM meshes where the larger meshes yielded larger peak values as stresses could redistribute more freely. The CQ16M meshes exhibited very limited response curves due to convergence difficulties and attained only roughly 50% of the experimental peak values. The stress trapping is accentuated in these cases due

to the greater number of integration points per element. The plasticity models again showed good consistency between mesh types (not mesh sizes within each mesh type due to the constitutive ‘snap back’) in comparison with the rotating crack model which showed large differences in response between mesh types (under the same, conservative numerical conditions) and some difference between mesh sizes as well.

B.3 Shear Dominated Case Study

B.3.1 Introduction

The shear critical case study considered was an investigation by Slobbe, Hendriks and Rots (2011) into the ability of Sequentially Linear Analysis (SLA) to capture shear dominated failure. The SLA was compared to experimental values obtained from experiments performed at the Delft University of Technology, as well as to those obtained from a NLFEA. The use of SLA as a computational tool eliminates the need for an iteration process and thus avoids convergence difficulties associated therewith. Instead a series of scaled linear analyses are conducted and a damage increment is applied at certain integration points to represent the degradation in stiffness of the material (Slobbe, et al., 2011) The highly non linear material behaviour associated with shear failure, and the potential numerical instabilities involved when considering NLFEA, inspired the use of the more robust SLA.

B.3.2 Experimental Setup and Results

The experimental program consisted of three point static testing of 6 longitudinally reinforced RC beams, without shear reinforcement. The beams were loaded at midspan and simply supported. Refer to Appendix B for drawings illustrating the beam specimen dimensions. The longitudinal reinforcement consisted of a layer of three bars each with a 20mm diameter (Slobbe, et al., 2011).

All of the tested beams showed the same failure mode. The load (N) vs. displacement (mm) response is shown in Figure B.3-1. Figure B.3-2 shows the sequence of the cracking that occurred in the beams through consecutive images taken from a video recording of the experiment (diagonal tension failure due to shear is observed). It is evident that the cracking was quite sudden and propagated through the web quickly, with the crushing at the compressive zone and splitting along the longitudinal reinforcement evident from the last image in Figure B.3-2 (Slobbe, et al., 2011).

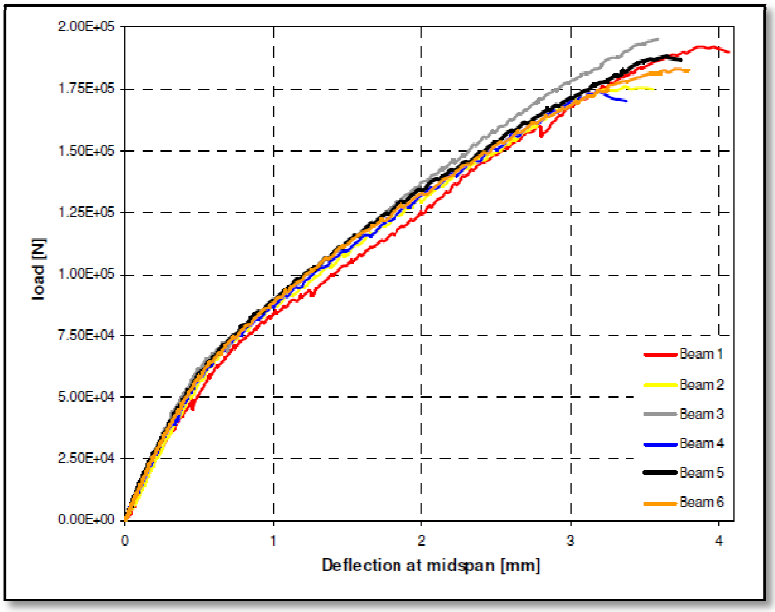

Figure B.3-1 - Load vs. Displacement for the 6 beams (Slobbe, et al., 2011).

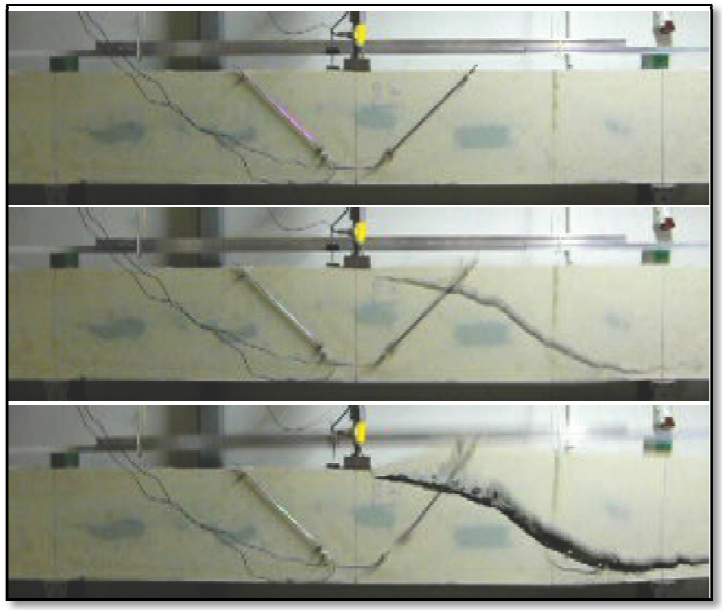

Figure B.3-2 - Cracking observed in experiments (Slobbe, et al., 2011).

B.3.3 Numerical Analyses and Results

The two numerical analyses conducted were a NLFEA and the SLA. The entire beam was modelled by the authors using 25x25mm plane stress, 8 noded elements with a full integration scheme (3x3 Gauss integration) for both analyses. The concrete was modelled using a Total Strain Fixed crack model. In tension, the Hordijk softening relation was used and in compression a linear elastic constitutive relation was assumed. The concrete properties used in this model are shown in Table B.3-1.

Concrete Material Properties		
f_t (N/mm^2)	E_0 (N/mm^2)	G_f (Nmm/mm^2)
3.5	33551	0.0765

Table B.3-1 - Concrete properties (Slobbe, et al., 2011).

In modelling the concrete, a variable shear retention factor ($\beta = f(\tau \; or \; \gamma)$) was implemented, as suggested by Kolmar and Mehlhorn (1984). Thus avoiding the extensive rotation of the principal stresses at the crack interface, this would have arisen otherwise from perpetual shear stress transfer, due to the constant shear

retention factor. The fracture energy was altered by a factor of 1.2 to obtain the final result.

The longitudinal steel reinforcement was modelled with an elastic-plastic relation, the parameters of which are given in Table B.3-2, with a perfect bond being assumed between the reinforcement and the concrete.

Reinforcement Material Properties	
f_y (N/mm^2)	E_0 (N/mm^2)
500	210 000

Table B.3-2 - Reinforcement Properties (Slobbe, et al., 2011).

Displacement controlled analyses were run for The NLFEA using a Secant, BFGS iteration method with a maximum of 25 iterations allowed per displacement step (Slobbe, et al., 2011).

The analyses results for the global load (N) displacement (mm) response are shown in Figure B.3-3, along with a typical experimental result. The fracture energy in the analyses was modified by a factor of 1.2, a change inspired by post-analysis checks. The results clearly correlate well. The convergence rate of the NLFEA was 80% until the peak load was reached, after which no more converged steps were observed (non-converged steps are marked in Figure B.3-3) (Slobbe, et al., 2011).

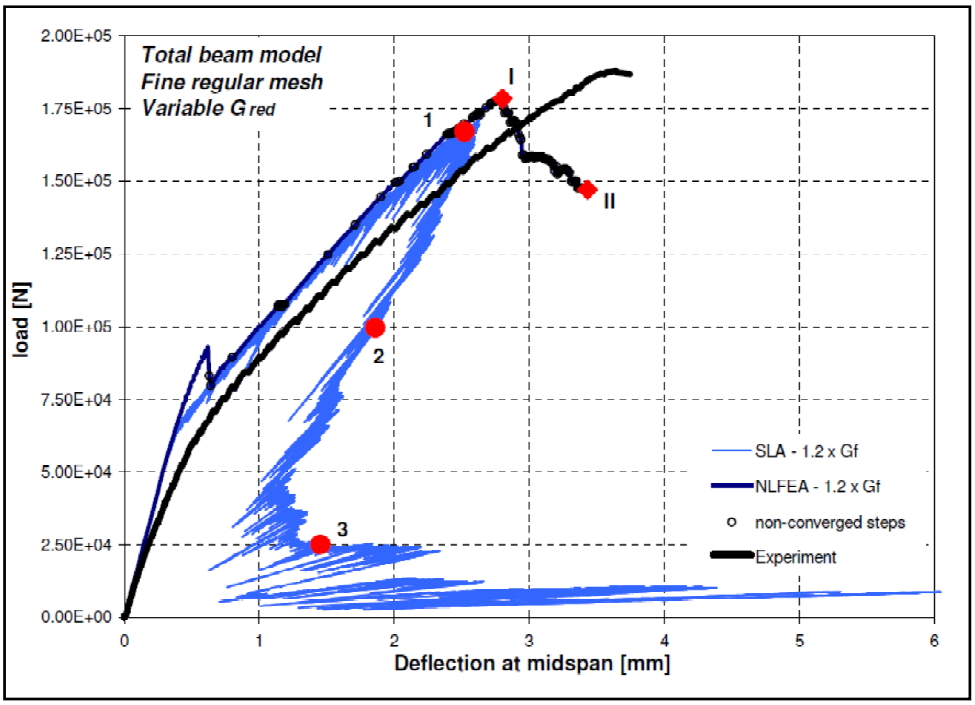

Figure B.3-3 - NLFEA and SLA Load vs. Displacement results. Experimental results for typical beam specimen also shown (Slobbe, et al., 2011)

The ultimate strength of the beams is underestimated by both analyses, but they exhibited the same brittle failure as was observed experimentally. The maximum principal strain (ε_1) contours for the steps highlighted in Figure B.3-3 are illustrated in Figure B.3-4 for both the NLFEA and the SLA. This failure, particularly that of the sudden formation of the dominant diagonal crack through the depth of the beam, correlates well with what was obtained experimentally (cf. Figure B.3-2).

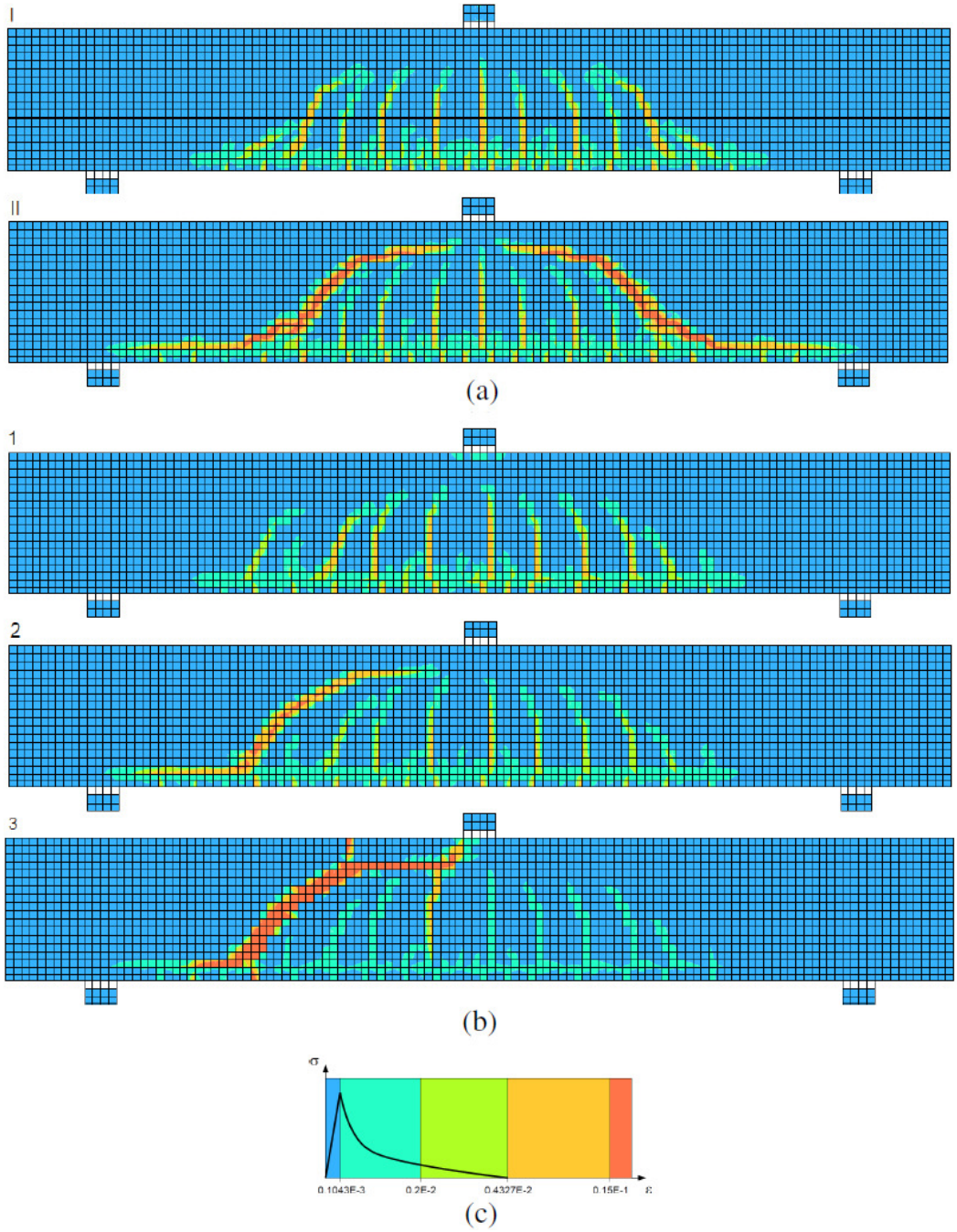

Figure B.3-4 - Maximum principal strain contour plot for a) NLFEA and b) SLA.

B.3.4 PRE-PROCESSING OF NLFEA

The approach adopted for modelling the shear critical beams is similar to that of Slobbe et al. (2011). The beams were modelled and analyzed using standard nonlinear material models as commercially available in DIANA (2009).

B.3.4.1 MODEL GEOMETRY AND BOUNDARY CONDITIONS

A plane stress analysis was conducted on the simply supported beams subjected to three point bending. The beam details and boundary constraints

are shown in Appendix B. The reinforcement was modeled assuming perfect bond between the concrete and reinforcement, using the embedded reinforcement elements available for implementation in DIANA (2009).

Steel loading platens were assumed to be used as the support and loading platens and the constraints were imposed at their centre points for the displacement control and supporting. A thickness of 200mm was given to the concrete and steel plate elements.

B.3.4.2 Material Properties

Beams were modeled using three constitutive relations: Total Strain based rotating and fixed crack models as well as the multi-surface Rankine-Hill plasticity model. The material parameters for the Total Strain based models were taken as those used by Slobbe et al. (2011). The material properties for the total strain analyses (fixed and rotating crack models) are shown in Table B.3-3.

Concrete Material Properties for Total Strain Models

Material Models	Fixed and Rotating	-
Young's Modulus	E	33551 N/mm^2
Tension curve	Hordijk*	-
Tensile Strength	f_{tu}	3.5 N/mm^2
Tensile Fracture Energy	G_{ft}	0.0765 Nmm/mm^2
Shear retention Factor	β ***(Fixed only)***	0.15
Compression Curve	Elastic*	-

Reinforcing Steel Material Properties

Material model	Elastic*	-
Young's Modulus	E	210000 N/mm^2
Steel Area	A_s	942.5 mm^2

Table B.3-3 - Total Strain Material parameters for shear dominated study.

The shear retention factor β was chosen according to the suggestion of a value of 0.2 being commonly applied (de Borst, 2001). A sensitivity analysis for four

* Refer to Sections A.3.1.3 and A.3.1.5 for model descriptions.

values of β was also performed on model S-Q8MEM-TS[F]-II. A variable shear retention factor was also applied to the S-Q8MEM-TS[F]-II model (as suggested by Kolmar and Mehlhorn (1984)) according to the following relation between β and the shear strain, γ (Figure B.3-5).

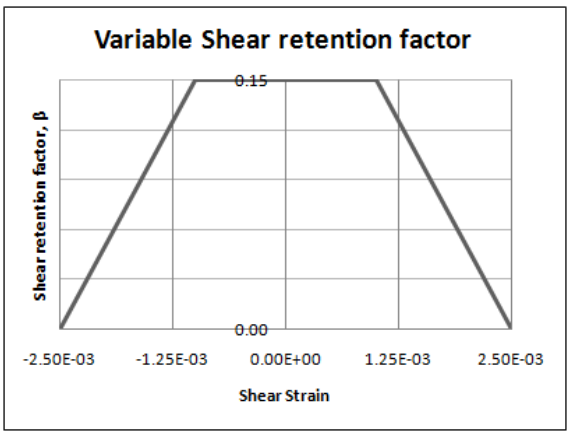

Figure B.3-5 - Variable shear retention factor.

The assumed values for γ in the β-γ relationship implemented were derived from post-analysis checks on the results from the analyses where a constant shear retention factor was used, with the aim of attaining some softening behavior in the global response.

The additional plasticity parameters required (such as compressive behavior properties, which need to be specified in the Rankine-Hill plasticity framework), were derived based on: the Model Code (2010) as a guideline; several post-analysis checks to ensure correlation to results of Slobbe et al. (2011); as well as to avoid snap-back at the constitutive level. The choice of compressive plasticity parameters was also checked against the anticipated compressive response of the concrete from the Total Strain analyses results. The cracking viscosity parameters implemented were obtained from post-analysis checks, with the aim of numerical stability in mind as well as the use of the parameter values that yield the most realistic results. The material properties for the Plasticity analyses are given in Table B.3-4, with isotropic material behavior assumed.

Concrete Material Properties for Plasticity Model		
Material Model	Rankine-Hill Plasticity*	-
Young's Modulus	E	33551 N/mm²
Tensile Strength.	f_{tu}	3.5 N/mm2
Tensile Fracture Energy	G_{ft}	0.0765 Nmm/mm²
Shear cont. to tension failure	α_g	1
Cracking Viscosity	m	100 Ns/mm²
Compressive Strength	f_{cu}	30 N/mm2
Plastic strain at f_{cu}	κ_c	0.002
Compressive fracture energy	G_{fc}	5 Nmm/mm²
Principal stress relation	β	-1
Shear cont. to comp. failure	γ	3
Reinforcing Steel Material Properties		
Material model	Elastic	-
Young's Modulus	E	210000 N/mm²

Table B.3-4 - Plasticity material parameters for Shear dominated study.

The fracture energy per unit area (g_{ft}) was calculated and implemented for each analysis (as required when using a rate dependant plasticity softening relation) using the fracture energy per unit length (G_{ft}) of the material as obtained from the study of Slobbe et al. (2011) and the equivalent length of each mesh size.

A sensitivity analysis was also performed on the plasticity parameters α and γ, representing the shear stress contribution to tensile and compressive failures respectively. Of particular importance is the value of α, which, if not equal to 1 as is commonly the practice, results in a non-associated flow rule for the tensile yield criterion. Thus the overestimated volume change and thus additional ductility typical of associated flow rules and the influence thereof on a shear dominated case can be investigated. The compressive yield surface is merely governed by an associated flow rule and isotropic hardening, so changes in γ are expected to not exhibit much influence on the overall structural response, especially considering the choice of compressive plasticity parameters being

* Refer to Section A.3.2.3 on page 49 for model material parameter descriptions.

such that compressive yielding does not occur (due to the elastic compressive curve implemented by Slobbe et al. (2011)).

For the purpose of ensuring localization will occur and that the stress field is not constant throughout the symmetrical model, a column of elements was weakened with material properties taken as 95% of those specified in Table B.3-4.

B.3.4.3 Meshing

The three element types (cf. Section B.1.3 on page 63) were Q8MEM, CQ16M and T6MEM. Three mesh sizes were considered for Q8MEM and CQ16M to investigate mesh sensitivity. The mesh element sizes were quadrilaterals of dimensions 12.5mm, 25mm and 50mm (Mesh sizes I, II and III respectively). One mesh size was considered for the T6MEM crossed-diagonal mesh, where 4 cross-diagonal elements were meshed within a 50x50mm quadrilateral shape.

B.3.4.4 Loading and Solution Procedure

The loading was applied at midspan at the centre node of the steel loading platen. A displacement controlled analysis was conducted using the Total Strain models, with displacement steps of -0.005mm for each analysis. A Secant BFGS incremental iterative solution procedure was used for the Total Strain based analyses. This combination of step size and procedure showed relatively good convergence rates for all Total Strain based analyses and thus a standard command file was applied to all Total strain models for the sake of analytical consistency. Path following techniques (Arc length methods with energy adapted load steps and automated load steps with force controlled analyses) were applied in order to try and attain a more detailed load deflection response, but all attempts proved futile. A force tolerance convergence of 0.01 was applied and 100 iterations were allowed per increment, as convergence at lower iterations, especially for the smaller mesh sizes, was usually not attained.

Displacement controlled analyses were performed for the Plasticity based models too, but with a Displacement vs. Time relationship monitoring the displacement loads, and time increments being applied in a Secant BFGS incremental iterative procedure. This is due to rate dependence of the softening in the model of Van Zijl (2000) only being active for time incremented analyses. It

was assumed that the experiments were performed in a time of half an hour, and the appropriate Displacement vs. Time relationship based on this assumption was established and implemented. A force tolerance convergence of 0.01 was applied with 100 iterations allowed per step, to facilitate convergence.

B.3.5 NLFEA Results and Discussion

A summary of the NLFEA's conducted on the shear critical beams are categorically shown in Table B.3-5.

MESH SENSITIVITY INVESTIGATION		
Rankine-Hill Plasticity Model	**Total Strain, Rotating Crack**	**Total Strain, Fixed Crack**
S-Q8MEM-P-I	S-Q8MEM-TS[R]-I	S-Q8MEM-TS[F]-I
S-Q8MEM-P-II	S-Q8MEM-TS[R]-II	S-Q8MEM-TS[F]-II
S-Q8MEM-P-III	S-Q8MEM-TS[R]-III	S-Q8MEM-TS[F]-III
S-CQ16M-P-I	S-CQ16M-TS[R]-I	S-CQ16M-TS[F]-I
S-CQ16M-P-II	S-CQ16M-TS[R]-II	S-CQ16M-TS[F]-II
S-CQ16M-P-III	S-CQ16M-TS[R]-III	S-CQ16M-TS[F]-III
S-T6MEM-P-II	S-T6MEM-TS[R]-II	S-T6MEM-TS[F]-II
PARAMETER INVESTIGATION		
Rankine-Hill Plasticity Model		**Total Strain, Fixed Crack**
S-Q8MEM-P-II - α^*		S-Q8MEM-TS[F]-II - β †
S-Q8MEM-P-II - $\gamma^{\ddagger}$		S-Q8MEM-TS[F]-II – $\beta(\gamma)^{\S}$

Table B.3-5 – Summary of NLFEA's conducted on shear critical Beams.

* Sensitivity analysis on α , the shear stress contribution to tensile failure.
† Sensitivity analysis on β, the shear stress retention factor.
‡ Sensitivity analysis on γ , the shear stress contribution to compressive failure.
§ Analysis using a variable shear stress retention factor dependant on the shear strain.

B.3.5.1 PLASTICITY MODEL

The plasticity parameters as specified in Table B.3-4 were implemented in a NLFEA on the shear critical beams for the various mesh sizes and element types and the results obtained are shown in Figure B.3-6.

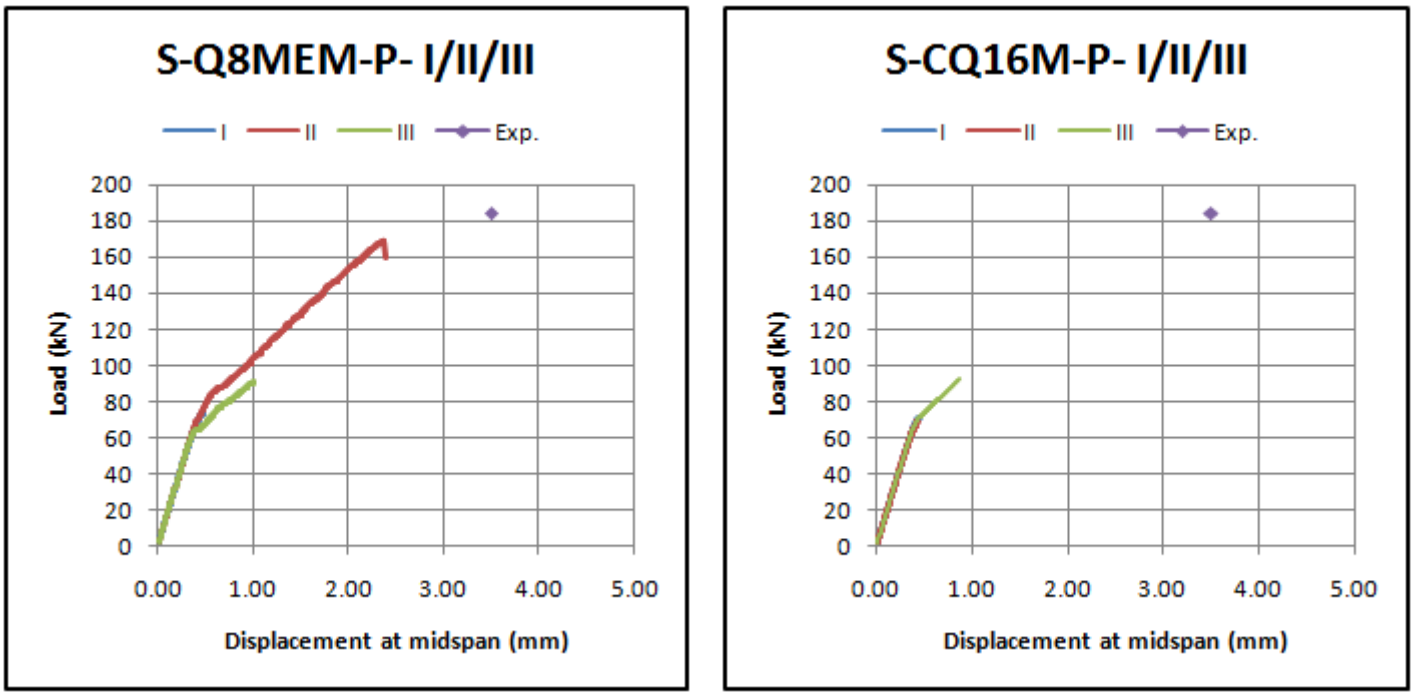

Figure B.3-6 - Load vs. Displacement results for shear critical beam, plasticity model.

The Rankine-Hill plasticity model did not capture the experimental structural response very well for all mesh sizes and types. The S-Q8MEM-P-II analysis provided relatively good response that correlated quite well with the experimental results (91% of the experimental peak load attained). The selective reduced integration of these elements enables them to perform more robustly under shear conditions. The same cannot be said for the other mesh sizes or types. Both of the size I meshes of the Q8MEM and CQ16M analyses yielded no response past the first non linearity encountered in the analyses. Localization difficulties seemed to occur for the small element sizes where a near constant stress field encompassed a large area relative to the element size, thus points of localization were difficult to obtain due to the small variation of stresses within the elements. The size III meshes only showed a slightly more detailed response past the first non linearity, after which the solutions diverged. The cracking viscosity parameter was varied between values of 10 N.s/mm^2 to 10 000 N.s/mm^2 for the mesh types and sizes, but more detailed response curves could

not be attained. Very small time increments were also applied and the number of convergence iterations allowed was increased to 200, but no additional response could be attained.

The development of the cracking started with localization in the column of weakened elements, but stress redistribution due to the rebar and the arch action cause by the compressive force distribution and the associated tensile zone caused major cracks to form away from the zone of initial localization. This can be seen in Figure B.3-7 (ε_1 strain contour plot) for the S-Q8MEM-P-II analysis.

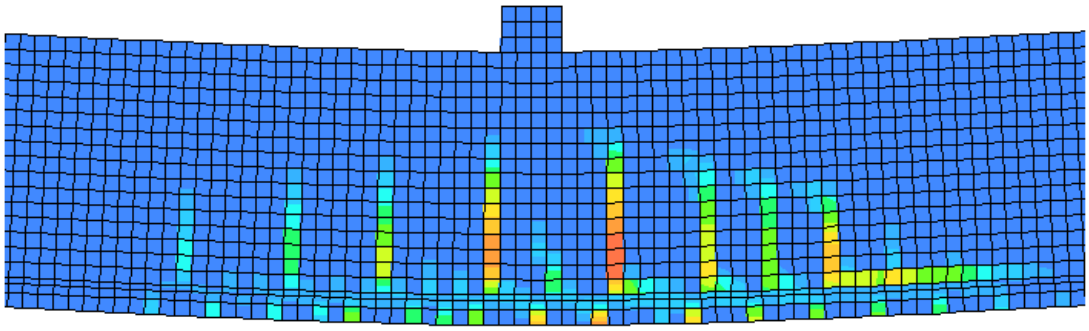

Figure B.3-7 - Cracking observed for plasticity model, shear critical.

The cracking pattern is somewhat similar to that observed by Slobbe et al. (2011) (cf. Figure B.3-4), but with no clear tension diagonal cracking observed numerically as was also done experimentally and no dominant tensile crack observed at midspan. The spacing of the cracks is also similar to that observed by Slobbe et al. (2011) using the Total Strain fixed crack model. The dominant crack observed in Figure B.3-7 was more tension dominated but had more post peak data been obtained, one expects the further softening of this crack to allow for further stress redistribution and potentially the formation of a dominant tension diagonal crack (where the cracking along the reinforcement is already quite developed in Figure B.3-7). The maximum principal strain (ε_1) vector plot is shown in Figure B.3-8 for the S-Q8MEM-P-II analysis. The orientation of the cracks at the integration points is apparent. The dominant crack to the right of the support has an orientation indicating dominance of tensile stresses. The cracks to the right of this show more of a rotation of the principal strains,

indicating shear cracking typical of arch action and the combination of tensile and compressive stresses causing tension diagonal cracking in the elements.

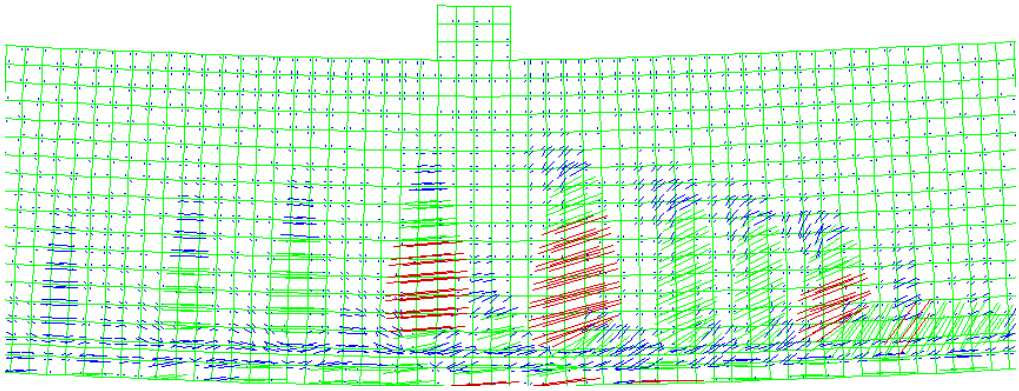

Figure B.3-8 - Maximum principal strain (ε_1) vector plot for plasticity model.

The use of a cracking rate dependant model may not be appropriate for the mechanisms governing shear failure, as it seems that the evolution of cracks at different orientations may occur at different rates. Thus the redistribution of stresses will depend on the rate of softening, which depends on the cracking viscosity parameter. The nature of the tension diagonal cracks as observed experimentally is that they occur quite quickly leading to sudden rupture of the beams, something which may not be captured numerically with a rate dependant plasticity model where tensile cracks evolve relatively slowly and consequently so does the redistribution of stresses through the beam.

The results obtained for the 3 models S-Q8MEM-P-II, S-CQ16M-P-II and the cross-diagonal triangles mesh S-T6MEM-P-II are shown in Figure B.3-9.

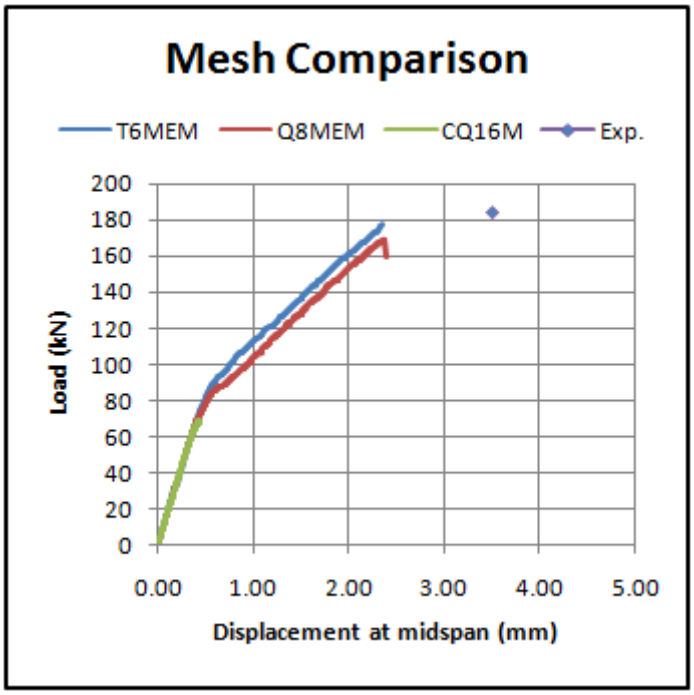

Figure B.3-9 - Mesh comparison for shear critical beam, plasticity model.

The cross-diagonal triangle mesh yielded results that correlate quite well with the S-Q8MEM-P-II analysis. The loading retained by the T6MEM mesh after the first non linearity was slightly higher than the Q8MEM mesh and the tensile softening and redistribution to rebar's effect was not as influential on the global response. A peak load was not reached for the T6MEM analysis, as errors were encountered before this could be obtained. Various techniques were employed to establish a definite peak but none yielded satisfactory results. The maximum principal strain contour plot for the S-T6MEM-P-II analysis is shown in Figure B.3-10.

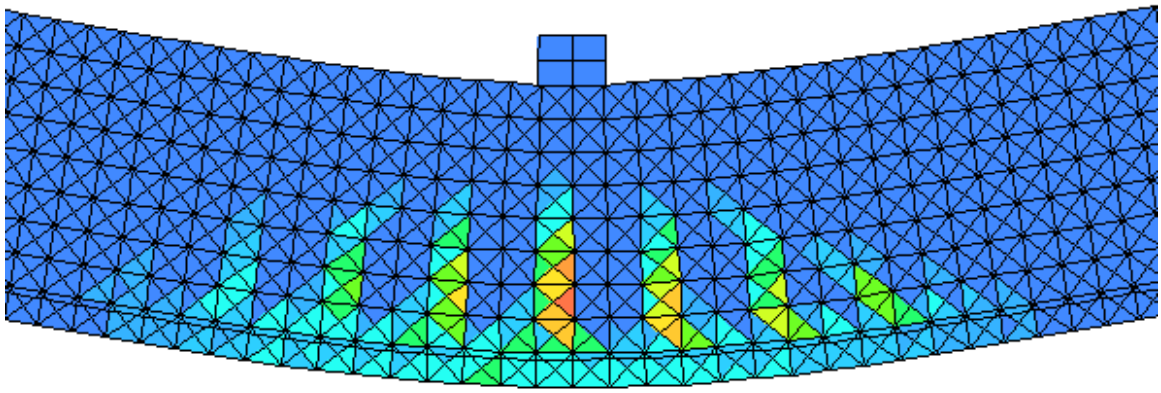

Figure B.3-10 - Maximum principal strain contour plot for S-T6MEM-P-II

It is evident that the tension diagonal cracking is more easily captured by this mesh type (cf. Figure B.3-7 for S-Q8MEM-P-II strain contour plot), due to the presence of the degrees of freedom at the centers of the encapsulating quadrilaterals and the resulting facilitation of stress redistribution in more directions. It is anticipated, had this analysis continued further, that a more prominent tension diagonal crack may have formed.

The results of the investigation of the sensitivity to the plasticity parameters α and γ, which establish the position of the yield surface in the stress space and denote the shear stress contribution to tensile and compressive failure respectively, are shown in Figure B.3-11 for the S-Q8MEM-P-II model.

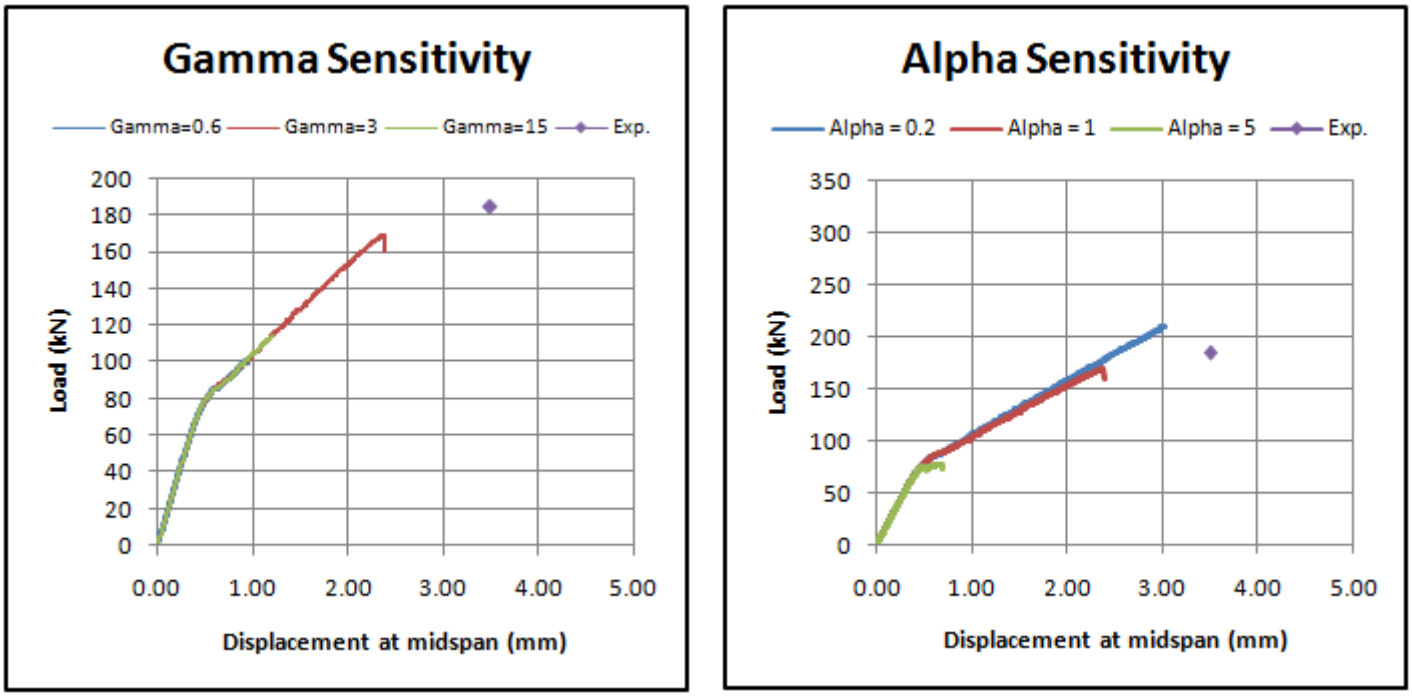

Figure B.3-11 - Sensitivity to Rankine-Hill plasticity parameters α and γ.

The relationship between both α and $\tau_{u,t}$ as well as γ and $\tau_{u,c}$ is inversely proportional (cf. eqns (A.3.72) and (A.3.89)). The values of the parameters were varied by a factor of 5 of the default values in DIANA (2009). The results for the γ sensitivity were inconclusive, as divergence of the solutions occurred so early (approximately 60% of peak load) in the analysis and further response could not be obtained. Similar minimum and maximum principal strain vector plots were attained for all three analyses used to investigate γ sensitivity at the same load steps. γ is proportional to the product of the compressive strength of the material

in both directions (if its value were to calculated explicitly - cf. eqn. (A.3.89)), the values of which were estimated from post analysis checks of the results from the Total Strain models. Thus its influence relies on the accuracy of these estimates and the development of the compressive stress, but to an extent also affirms their correctness when considering the assumption of a linear elastic compressive constitutive relation as done by Slobbe et al. (2011) (no plastic compressive behaviour observed).

The influence of the α parameter is far more pronounced. Decreasing α causes the yield surface to expand (α is inversely proportional to $\tau_{u,t}$) in the stress space in a direction of the axis representing shear stress. Thus the elastic domain of the yield surface has increased slightly, and the influence of the shear stress on the tensile failure is less pronounced as larger shear stress values need to be reached to contribute to tensile failure. For the case of α=5 the opposite is true and the yield surface will shrink slightly with the elastic domain decreasing. The influence of the shear stress on tensile failure is more pronounced as smaller values of shear stress will be needed to contribute to tensile failure. Thus the shear stress limits are reached sooner than for the other α values at the same levels of loading, causing the stress situation to be on the yield surface sooner. This is evident in the result, where for the $\alpha = 0.2$ analysis, the peak response attained is greater than the other analyses, due to the less significant influence of the shear stress contribution to failure. For $\alpha = 5$ failure is observed far sooner at a peak load of 40% of the experimental peak load. Clearly the shear stress contribution to failure is far more significant, as failure occurs at such low values of shear stress.

Due to the limited response available for the $\alpha = 0.2$ analysis and the early failure thereof, the effect of the α parameter cannot be shown illustratively in a comparative manner. Thus, the results for analyses using much larger fracture energy properties for the concrete will be shown. These were also S-Q8MEM-P-II analyses with the α parameter varied by a factor of 5, with the results shown in Figure B.3-12. It is emphasized that this study was purely for comparative purposes to illustrate the influence of α.

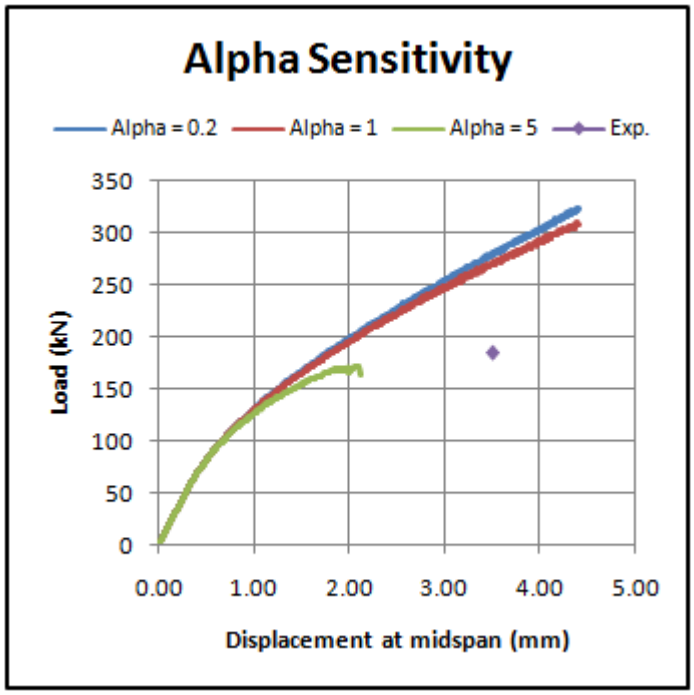

Figure B.3-12 - Alpha sensitivity for S-Q8MEM-P-II, fracture energy increased.

Tensile failure was observed for the analysis using the default value of $\alpha = 1$, with a single dominant tensile crack forming. The high fracture energy implemented allowed this crack to perpetuate, until divergence of the solution. The choice of α parameters gave a similar distribution of results as in Figure B.3-11. The maximum principal strain contour plots are shown in Figure B.3-13 for the same load steps.

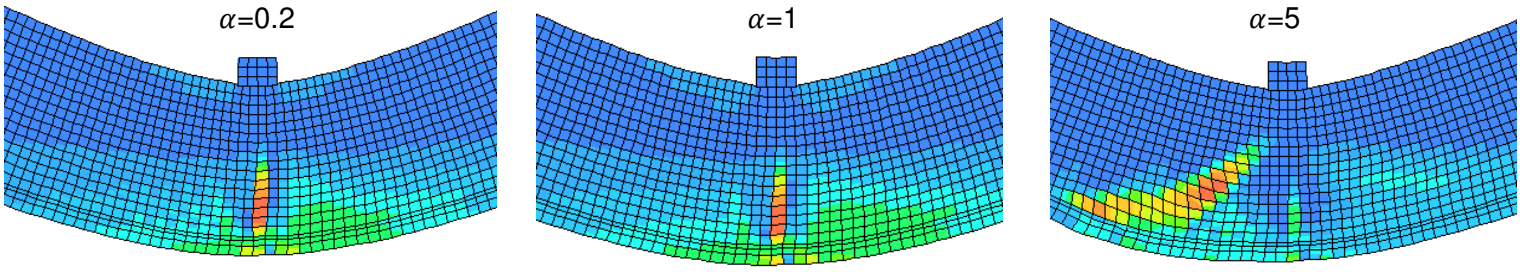

Figure B.3-13 - Maximum principal strain contour plots for various α values.

For $\alpha = 5$, a clear shear crack has formed as opposed to the tension cracks and fixed localization in the tensile zone of the other, smaller α values. The shear

deformation of the elements is also evident at these relatively low shear stress values.

An appropriate choice of α may have yielded better results than those obtained for the analyses of the shear critical beam in Figure B.3-11. The problems encountered with the strain localization due to the distribution of the stress field may have been solved by enabling the influence of the shear stress to be more pronounced. More pronounced tension diagonal cracks would also have been observed as further rotation of the principal stress and strain axes would have been facilitated by the more pronounced shear stress contribution. The attainment of an experimentally determined and exact value for α would be tedious (mainly due to the complexities involved in obtaining τ_u). The use of values that result in correlation with experimental evidence, defeats the purpose of using NLFEA results for design as experimental results will not be available and potential shear failure may not be captured numerically by a plasticity model.

B.3.5.2 Total Strain Fixed crack model

The results for the shear critical beams for the various mesh sizes and analyzed using the Total strain fixed crack model with parameters as in Table B.3-3 are shown in Figure B.3-14 for the investigated mesh types and sizes.

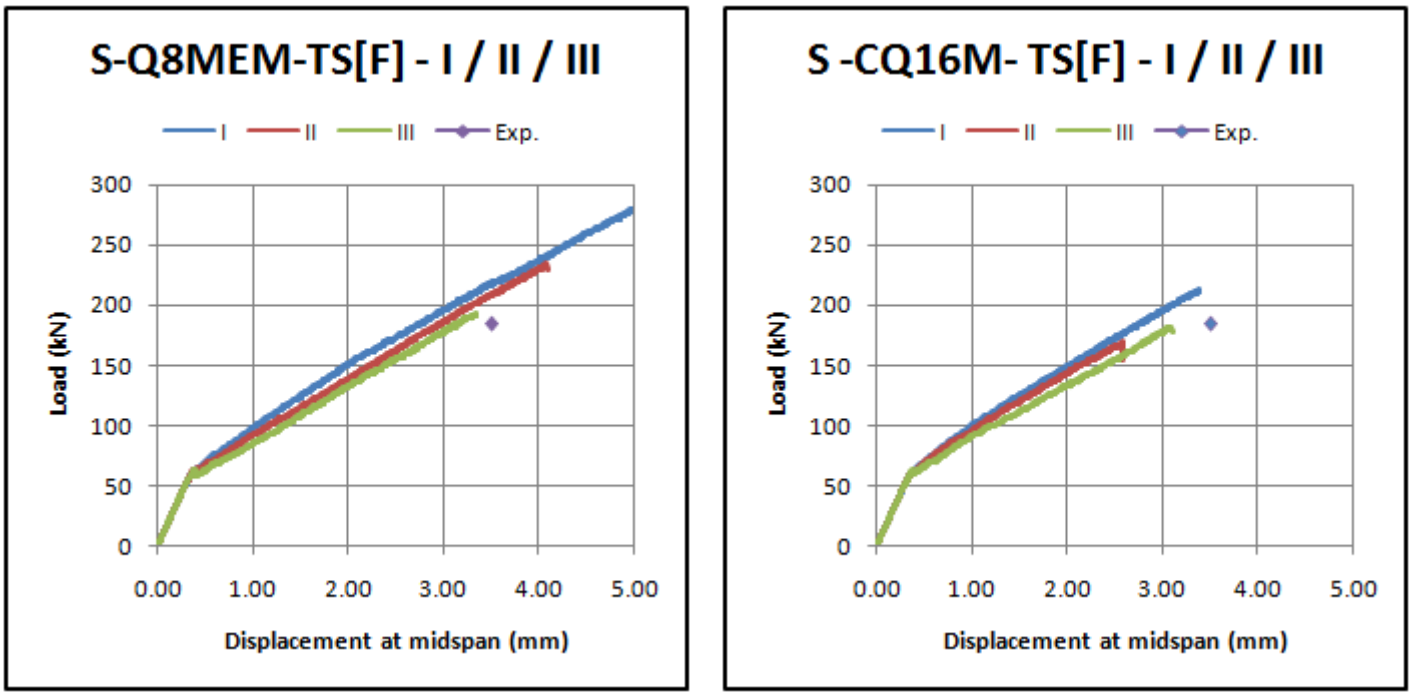

Figure B.3-14 - Load vs. Displacement result for shear critical beam, fixed crack model.

The peak values for load and deflection do not correlate too well with those observed experimentally and numerically by Slobbe et al. (2011) when considering all the analyses. The use of a constant shear retention factor clearly overestimates the strength of the structure, due to the incessant transferral of shear stress over the formed cracks and the neglecting of compensating for the corresponding potential principal stress violation in a direction other than that of the crack. The observed stiffness of the numerical response correlated well with the results of Slobbe et al. (2011) with the responses of all the results obtained following a similar path. The fixed crack models all showed the initial cracking of the beam accurately compared to the NLFEA of Slobbe et al. (2011). This non linearity is evident in the Figures at a deflection between 0 and 1mm, with the tension softening response observed typical of the Total Strain fixed crack model formulated on smeared cracking softening relations. The SLFEA of Slobbe et al. (2011) indicated the more 'natural' response of the experiment (tension stiffening effect). No post peak behaviour could be captured for any of these analyses, despite numerous rigorous attempts.

It is evident that there is a dependence of the shear retention β factor on the mesh element size. This was observed for both element types, where the same β value (0.15) yielded stiffer response curves for the smaller mesh type. This is especially evident in S-Q8MEM-TS[F]-I, where the force increases more rapidly with the displacement, and reaches a higher peak at a higher corresponding displacement. The S-Q8MEM-TS[F]-II and S-Q8MEM-TS[F]-III models showed divergence earlier than S-Q8MEM-TS[F]-I, at much lower loads and deflections. Thus some mesh locking due to the shear retention factor can be seen, due possibly to the assumed strain for the shear stiffness of the Q8MEM elements and reduced integration scheme. The kinematic modes exhibited by the Q8MEM elements in shear are thus limited due to the 1 point integration scheme imposed on them and yielding a constant shear strain over each element. With the smaller element sizes, the combination of the constant strains throughout the elements will actually be able to facilitate a more complex (and unrealistic) deformation, compared to the larger elements which will rather lock. The combined shear strains of the larger elements across the entire model will not be able to describe an as complex deformation as the smaller elements, due to the accumulation of the strains between large elements being done across a larger area as well as the potential discord of shear strain values amongst elements as a result of the

simplified integration scheme. The shear strain increment per small element will also be slightly less, thus once the cracking plane is fixed and the shear stiffness is as determined by β, the shear stresses can be transferred over the cracks for longer resulting in higher shear stresses being able to be obtained and thus higher resistance while accommodating a greater deflection. Thus β being dependant on gamma as suggested by Kolmar and Mehlhorn (1984) is conceivably justified.

The model S-Q8MEM-TS[F]-I showed no signs of diverging and continued to the maximum allowed deflection for the analyses. The CQ16M mesh models all diverged closer to the actual maximum deflection than the Q8MEM models. This was attributed to the selective reduced integration of the Q8MEM elements facilitating shear deformation and the more complex shear strain description of the CQ16M fully integrated elements. The values of maximum deflection for the CQ16M models and the corresponding peak load values are also more closely related to one another than for the Q8MEM models under the same numerical conditions.

The results obtained for the investigation on the shear retention factor β in the Total Strain fixed crack models, are shown in Figure B.3-15 for the S-Q8MEM-TS[F]-II model.

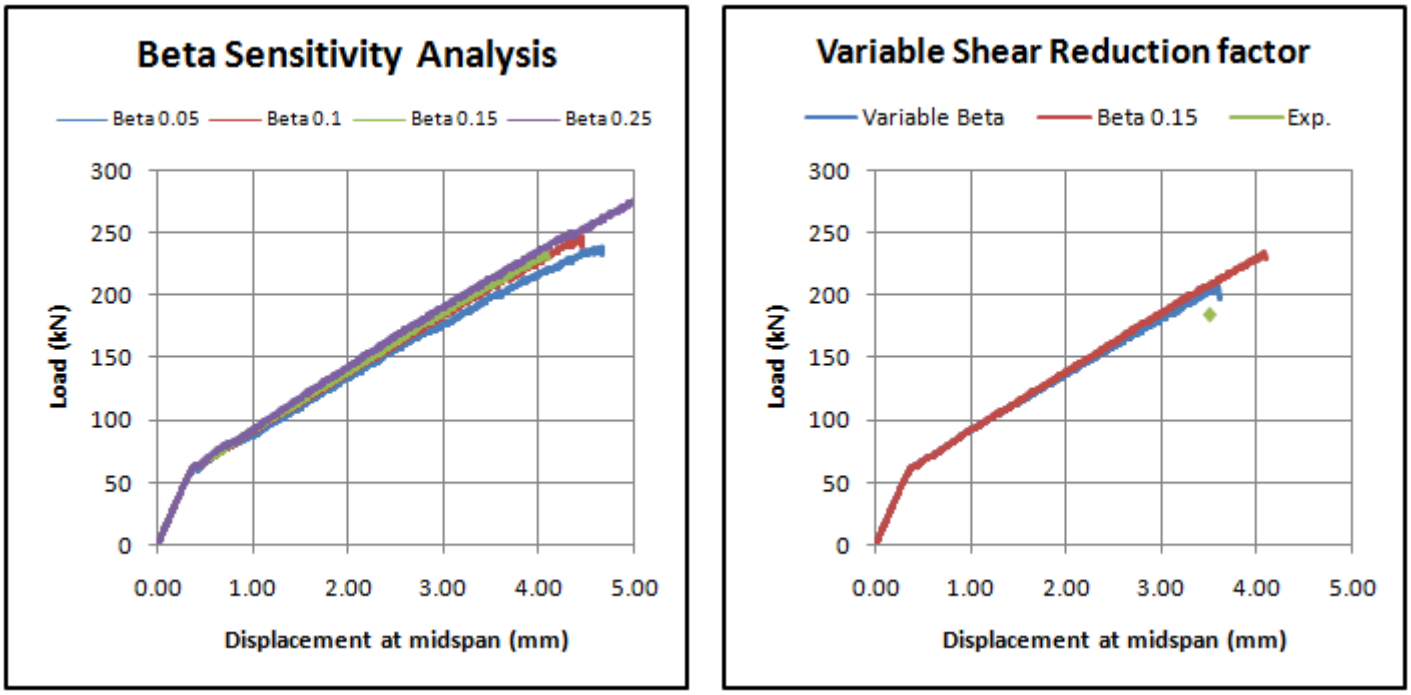

Figure B.3-15 - Shear retention factor investigation.

The sensitivity analysis clearly shows an increase in the stiffness of the response for the entire model. The differences in the results of the analyses for the β values between 0.1 and 0.25 are very similar, thus a value of 0.2 as suggested by (de Borst, 2001) is clearly a good approximation. The smallest β value showed a notably less stiff response after the first crack occurred, and was not compatible for use with the smaller mesh sizes as convergence was not attainable after a deflection of approximately 1.5mm.

The use of a variable shear retention factor, with β a function of the shear strain γ, showed a similar response as using a constant value for β. A simple relation between β and γ was assumed (cf. Figure B.3-5), with the values for the shear strain chosen being much lower than the maximum values anticipated in the analysis, as was confirmed by post-analysis checks on some of the other models implemented. The variable β model does show a deviation from the response path of the constant β model, and seems to approach some peak value as was also observed experimentally. However, for all β values considered, constant or variable, the solution always overestimated the peak load and associated displacement observed experimentally. The variable β analysis yielded a peak load that was 12% greater than the experimental peak loads and at the same corresponding displacement. This encouraging result is overshadowed by the difficulties involved in accurately obtaining a $\beta \sim \gamma$ relationship without relying on post-analysis checks. The difference in cracking behaviour obtained for the variable β and constant β models is shown in Figure B.3-16 and Figure B.3-17 respectively for the peak loads from the response curves.

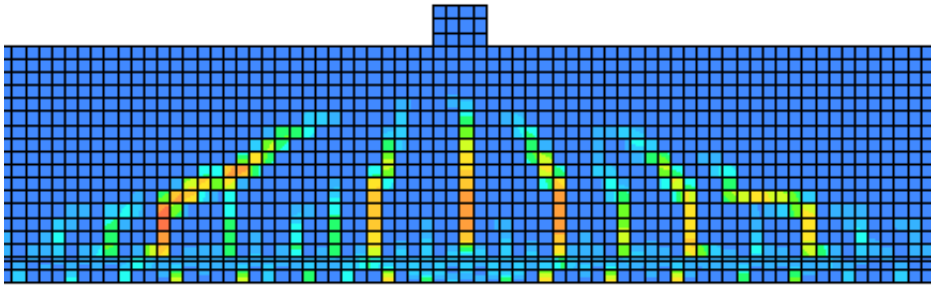

Figure B.3-16 - ε_1 contour plot for variable β model.

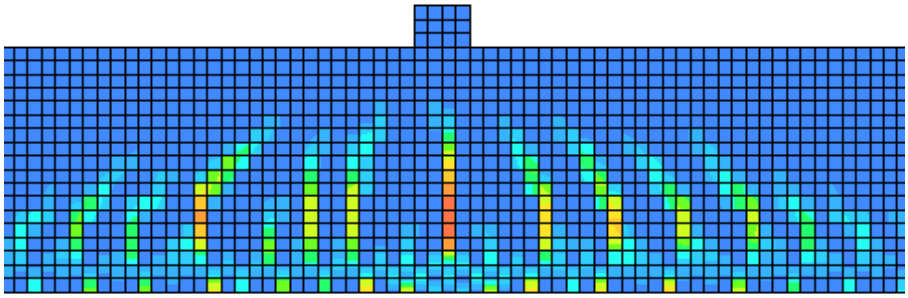

Figure B.3-17 - ε_1 contour plot for constant β model.

It is clear that the variable β model emulates the physical reality of a main tension diagonal crack forming, as cracks in the region of maximum shear coalesce due to the loss of shear transfer capacity (due to β decreasing) and subsequent rotation of the principal stress axes, until one diagonal crack is evident. The constant β model simply retains the initial cracks formed at the integration points and incessantly transfers shear stress across them, so coalition of cracks does not occur even at the higher load at which the crack pattern was obtained. Thus a more pronounced shear crack can be observed for the variable β model which has developed further through the depth. The asymmetry of the crack pattern for the variable β model showing on dominant fixed crack is obviously attributed to the forced asymmetry of the model to ensure initial localization.

Figure B.3-18 shows the response curves of the S-T6MEM-TS[F]-II cross-diagonal mesh, S-Q8MEM-TS[F]-II and S-CQ16M-TS[F]-II analyses.

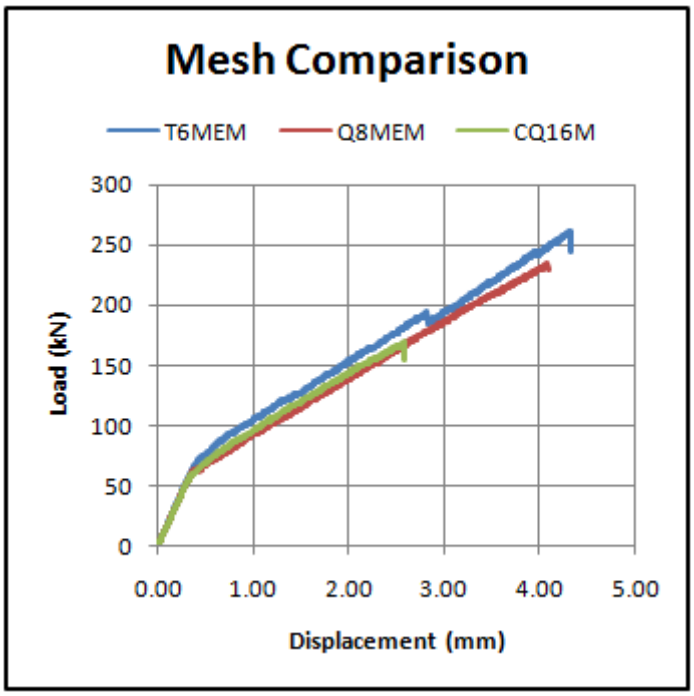

Figure B.3-18 - Mesh comparison for shear critical beams, fixed crack model.

Despite exactly the same boundary conditions and material parameters, the responses are quite different. The stiffness of the T6MEM mesh's response is initially slightly higher than the others until some softening occurs towards the same path as the Q8MEM mesh. The ability of the T6MEM cross-diagonal triangles mesh to capture complex behaviour and deformations in a simplified manner (regarding it consisting of 3 node linearly interpolated triangular elements) is evident, as under the same conditions the CQ16M mesh merely diverges and underestimates the load of the other models and the experimental load, despite its mathematical superiority in describing deformation modes. Figure B.3-19 shows the deformed mesh for the final load step. To the right of the left support, the deformation of the elements is indicative of a tension diagonal shear crack forming, closely resembling the cracking observed experimentally.

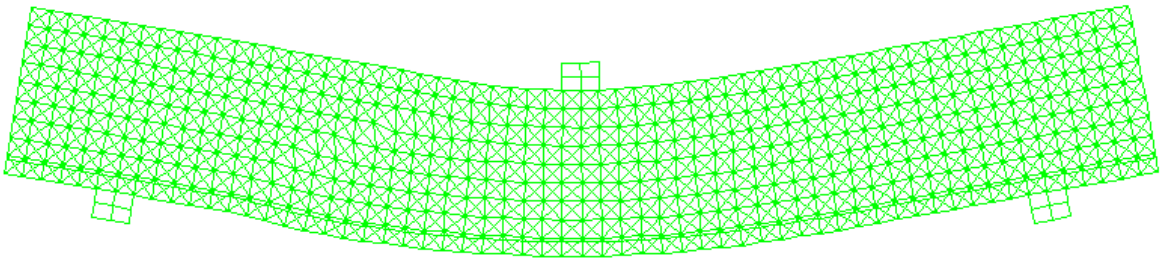

Figure B.3-19 - Deformed T6MEM mesh, fixed crack model.

B.3.5.3 Total Strain Rotating crack model

The results obtained for the load vs. deflection response for the analyses conducted on the shear critical beams using a Total Strain based rotating crack model are shown in Figure B.3-20 for the various mesh types and sizes. The average experimental peak is also shown as a point on the graphs.

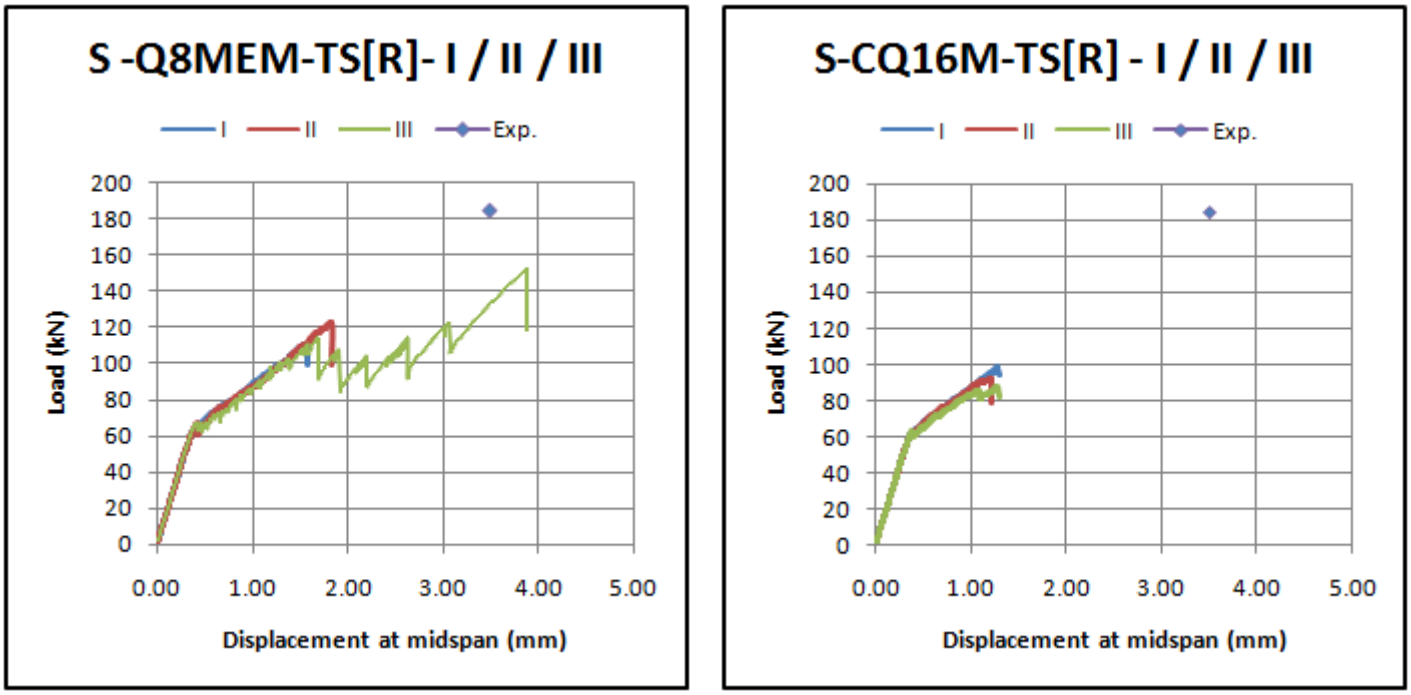

Figure B.3-20 - Results for the shear critical beam, rotating crack model.

Very small step sizes were required to convergence for the Total Strain rotating crack models. None of the models reached or surpassed the experimental average load. The cracking pattern was also very different to those of the NLFEA and SLFEA as obtained by Slobbe et al. (2011), as the rotating crack model is

not an accurate means of describing the actual fixed cracking nature of the experiment, due to the incessant potential rotation of the principal strain axes.

There were much fewer diagonal cracks and a more non symmetric crack pattern was observed, however this is mainly attributed to the forced asymmetric localization than to accurately emulating the experimental evidence. The rotation of the stresses is also evident from the cracking formation observed, as the cracking occurred more favorably in the direction of the rebar indicating pullout due to the rotation of the principal stresses in a direction parallel to the reinforcement, as opposed to commencing in a direction perpendicular to the incipient crack as was the case for the fixed crack model. For the CQ16M models, the diagonal cracks were especially limited, and there is a notable difference in the crack propagation through the depth of the beam for increasing mesh size, as the larger mesh sizes showed cracks propagating further through the beam. The cracking observed for the various CQ16M mesh sizes are shown in Figure B.3-21 (ε_1 contour plots) for the 3 mesh sizes.

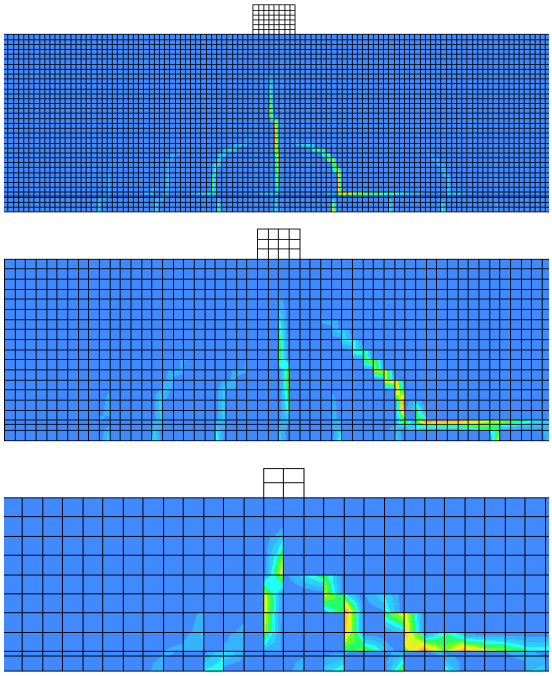

Figure B.3-21 - Cracking for the 3 different mesh sizes, rotating crack.

The strut and tie action typical of shear failure was restricted as the tension zone was not allowed to develop fully to allow for more diagonal cracking, due to the

rotation and alignment of the principal stresses in the direction of the rebar, thus failure due to pull out as a result of combined tensile/ shear failure is more pronounced. The deformation of the CQ16M elements on the crack paths was quite extensive as a result of the stress concentration in these elements as the principal stress directions rotate but remain fixed within the element. Instead of forming a fixed crack plane with reduced shear stress transfer across it, which then allows the stress to still develop and propagate through the rest of the beam, the stress is more focused in specific places which encounter high stresses at initial stages of the analysis, so softening is concentrated and stress is not allowed to develop throughout the rest of the beam, hence the main 'shear cracking' (not a typical diagonal tension shear crack, but combined tension/ shear crack) being so far from and remaining far from the support (especially the case for the small meshes). This then causes a stress locking between load steps as the stresses remain in the element, rotating only slightly upon each increment and due to the more fine discretization, the principal stresses still occur in only those elements and only redistribute through the rest of the beam once the combined rotation and softening of the element is exhausted for the initially cracked element. For the Q8MEM-III analysis, the stresses were not 'trapped' as severely, as due to the element size, larger stresses could develop quicker due to the larger strains per load step, and thus the combined rotating and softening in the elements could finish and stress transferred to the next elements. Therefore there is a much more detailed response for this model, as the stresses are transferred to the reinforcement and the appropriate tension softening is more freely accommodated. The mechanism of shear failure is captured to a certain extent, but not correctly or accurately.

The Q8MEM models again exhibited a more elaborate response than the CQ16M models due to the simplification of the shear strain in these elements.

Figure B.3-22 shows the response curves of the S-T6MEM-TS[R]-II cross-diagonal triangle mesh, S-Q8MEM-TS[R]-II and S-CQ16M-TS[R]-II analyses.

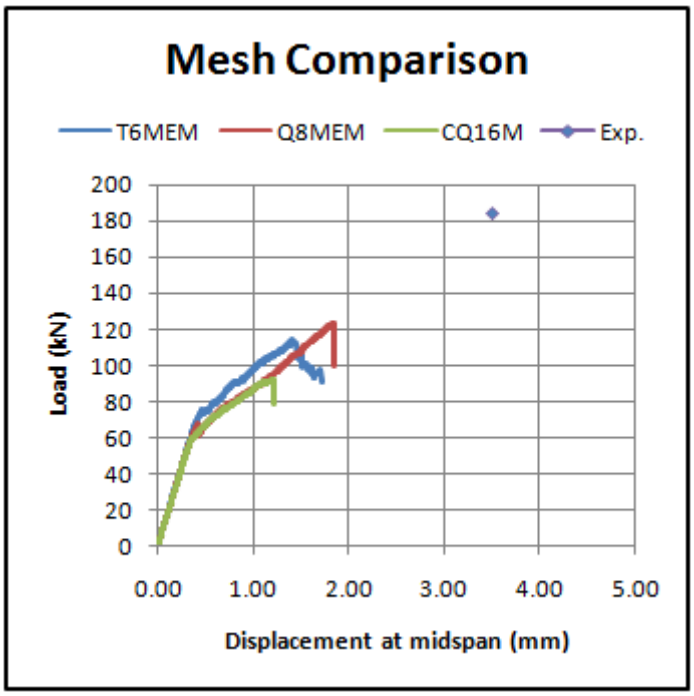

Figure B.3-22 - Mesh comparison for shear critical beams, rotating crack model.

All three models grossly underestimate the experimental average load and corresponding deflection. This has been attributed to the more rapid failure of the models (especially the finer meshes) due to the rotating crack model 'trapping' the stresses within the elements focussed around the zone of maximum tension and not facilitating stress redistribution effectively. The T6MEM again shows the ability to capture a detailed response curve, despite the simplicity of the constitutive elements. Reinforcement pullout was also the observed form of failure, with indications of a shear crack forming but the alignment of the principal strain directions with that of the reinforcement occurred before this developed further. The deformed mesh at the final load step can be seen in Figure B.3-23. It is clear by the deformation of the elements, that the straining was concentrated in the region of maximum tensile stress; a redistribution of the stress is not as pronounced as what was observed for and allowed by the fixed cracking model. The deformation of the elements parallel to the reinforcement is evident, and the indication of a slight diagonal crack propagating from the reinforcement to the support is evident. The absence of a clear tension diagonal shear crack as in Figure B.3-19 is evident.

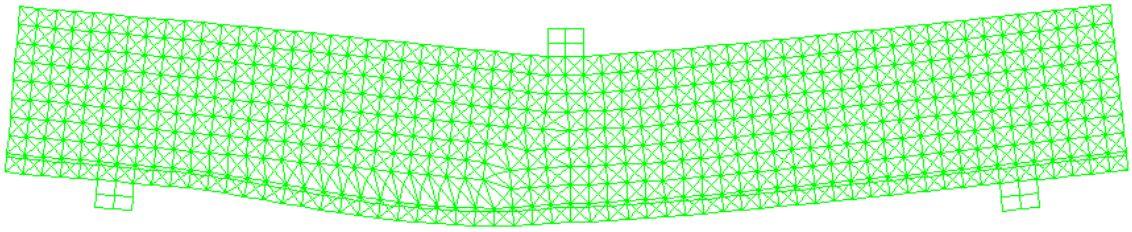

Figure B.3-23 - Deformed T6MEM mesh, rotating crack model.

In the next section, the peak loads and corresponding displacements obtained numerically are normalized with respect to the average values obtained experimentally, to provide a summary and a comparison of the analyses for the different material models and mesh types and sizes for the beam investigated.

B.3.5.4 Comparison of analyses

The data points for each mesh type (Q8MEM, CQ16M) are plotted from left to right corresponding to the ascending order of the mesh size (I. II, III) for each material model and beam type investigated in Figure B.3-24.

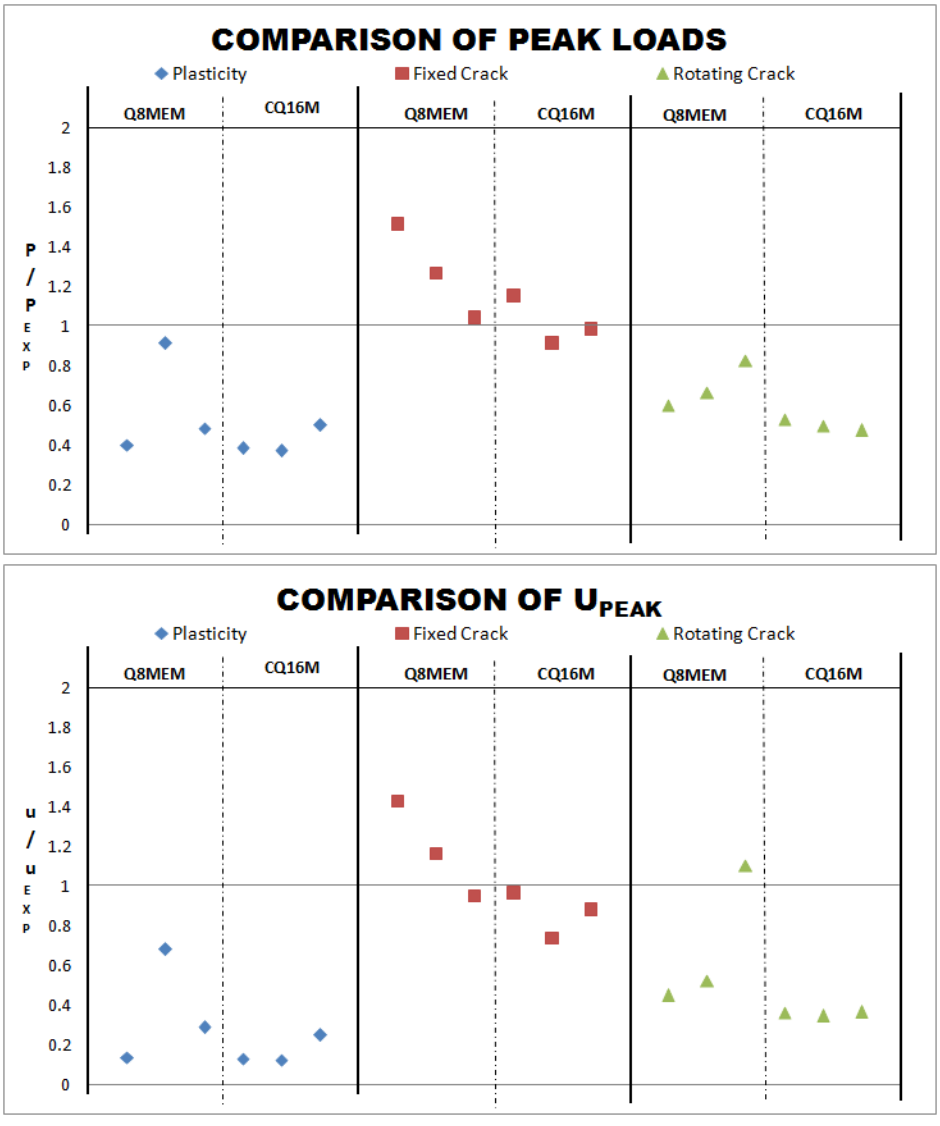

Figure B.3-24 - Comparison of analyses, Shear Dominated Study.

The plasticity model showed poor correlation with the experimental results, due to divergence of most of the solutions at the first non linearity encountered in the structural response curve due to localization difficulties at points in the mesh where the stress field was either constant or tending towards the formation of diagonal cracks. The S-Q8MEM-P-II model performed quite well attaining a peak load 91% that of the experimental peak. This gives evidence of the superior behavior of the Q8MEM elements when subjected to shear deformation, especially considering that none of the CQ16M analyses attained detailed responses. The cracking of the S-Q8MEM-P-II analysis showed indications of forming tension diagonal cracks as observed experimentally, but no such cracks could be explicitly identified. The influence of the model parameter α was investigated, and showed that shear deformation and definite shear cracking could be observed. The current implementation of the Rankine-Hill deformation based plasticity model, with a single isotropic softening parameter with the two fracture energies in each material direction to represent anisotropy works well for most applications, but clearly not this particular and potentially some other shear dominated situations. The development of a plasticity model incorporating two kinematic scalar softening parameters that control the movement of the yield surface in the stress space should be considered, which gives a flexible response in shear (Lourenco, et al., 1997). This would require a formulation of the Rankine criterion in a principal stress space, as well as a combined yield surface, one for each principal direction within this Rankine criterion. Establishing the principal stress space and the conversions between the ‘normal’ stress space and principal one can become very complex. Solutions to these problems have been considered, such as using strain based formulation of plasticity theory (as opposed to deformation based).With the strains being established in a principal strain space, the establishing of the principal stress values can be done relatively simply (Feenstra, 1993). Further complexities will include establishing the relationships at the intersections of the 3 intersecting yield surfaces now defined in a principal stress space, all within a more ‘dynamic’ system where each of the surfaces can independently soften.

The fixed crack model, with a constant shear retention factor, also exhibited great variance among analyses. The S-Q8MEM-TS[F]-I model showed no signs of diverging and continued far past the experimental peak before the analysis was stopped, due to the smaller strain increments per element per load step, and

thus the retention of higher stresses for longer coupled with the ongoing transferral of stresses across the cracks. Under the same numerical conditions, the other fixed crack analyses diverged much sooner. The dependence of the shear retention factor on mesh size is evident from the Q8MEM fixed crack investigations. The selective reduced integration inherent in the mathematical representation of the Q8MEM elements in DIANA (2009) enabled them to perform better under the shear conditions, and convergence was more easily attained as compared to the CQ16M models. The CQ16M models did generally show good accuracy and relatively good precision, with the peaks attained being within 25% of the experimental values. Despite being the one model that best captured the shear failure of the beam, it was also the model that exhibited the most inconsistency of results for the various mesh types and sizes.

The rotating crack model underestimated the peak loads for all the mesh types and sizes. The larger Q8MEM mesh models performed better (as did, contrarily, the smaller meshes of the fixed crack models) as the relatively large strain increments per load step allowed for more pronounced rotation of the cracking axes per load step, leading to better stress redistribution through the beam and more closely resembling shear failure (especially the S-Q8MEM-TS[R]-III model). The other rotating crack analyses showed regions of localized stresses that were ‘trapped’ in these elements and stress redistribution was not easily facilitated, thus shear dominant failure was not as well captured as for the fixed crack models, where stress redistribution is more easily accommodated.

In general, the variation of the results obtained as well as the inability of the models to adequately capture a correct response in a shear dominant investigation, does not inspire confidence regarding the use of NLFEA results as a basis for design. The development of a plasticity model which incorporates two independent hardening parameters for each yield surface for each material direction could help overcome the shortfalls of the currently available Rankine-Hill plasticity model regarding capturing shear failure. Thus any potential designer would need to establish absolutely that shear failure is not imminent.

B.4 Tension Dominated Case Study

B.4.1 Introduction

The tension critical beams that were analyzed were those tested by Victor (2011), cast of an SHCC mix design at the University of Stellenbosch. The SHCC beams were loaded until failure, and the force vs. displacement response was obtained. The experimental programme encountered several problems, ranging from incorrect casting of the specimens to inaccurate measurements of the basic concrete properties. Thus there exists no record of the mechanical properties of the concrete used in these tests. However, previous SHCC data as obtained by Molapo (2010) for the same mix design was used, along with the one parameter SHCC constitutive model as developed by Van Zijl (2000) and implemented in DIANA as a user supplied subroutine. The effects of shrinkage and creep were not included in the analysis. Calibrated material parameters were also obtained as suggested by the procedure available in Van Zijl (2009), where the values for the 3 parameter model of Bazant and Oh (1983) were calculated from previous tensile loading tests at several loading rates (obtained from Adendorff's (2009) results for SHCC of the same mix), and the one parameter model's viscosity was estimated by inverse analysis and post-analysis checks. These attempts proved futile to the largest extent, the futility of which will be elucidated.

B.4.2 Experimental Setup and Results

The experimental procedure consisted of the three point bending tests of three longitudinally and shear reinforced SHCC of dimension 3000x300x300mm. The beam specimens and different cross sections are shown in Appendix C. The various beam properties are summarised in Table B.4-1.

	BEAM 1		BEAM 2		BEAM 3	
Type	**1a**	**1b**	**2a**	**2b**	**3a**	**3b**
Length (m)	3.0	3.0	3.0	3.0	3.0	3.4
Width (m)	0.3	0.325	0.3	0.295	0.31	0.302
Depth (m)	0.28	0.28	0.275	0.275	0.28	0.275
As	2 Y 10		3 Y 20		2Y32 + 1Y16	

As’	2 Y 10	2 Y 10	2Y10
Shear rebar	R8 @ 300mm c/c	R8 @ 300mm c/c	R8 @ 300mm c/c
%Reinforcement	0.175%	1.05%	2%

Table B.4-1 – SHCC Beam Properties Victor (2011)

Altogether 6 beams were tested, different beams with 3 different ratios of reinforcement and 2 of each type. It is clear that the beams were not geometrically consistent, but this was not accounted for in the analyses and one FEM model was created for all beams, with the intended geometry considered (dimensions of 3000x300x300mm).

The testing was conducted using an hydraulic jack, at a rate of 10mm/min at the midspan of the beams. The displacement measuring devices were not connected directly at the point of maximum deflection, to avoid any potential damage to them. Thus a fourth order polynomial was used to calculate the midspan deflection from other measured deflections on the beams. Unfortunately cracking was not recorded adequately in this testing session (Victor, 2011).

In the testing of the more longitudinally reinforced beams, early compression failure of the compressive steel reinforcement was observed, causing spalling of the concrete at the top of the beams. This was attributed to the spacing of the shear reinforcement being too large. This failure was only observed in the tests of beams 2 and 3 (cf. Table B.4-1). Thus the resistance afforded by the compressive steel was of no more consequence to the beams, and the more heavily reinforced beams more closely resembled shear failure as opposed to the intended tensile failure, due to the disturbance imposed on and subsequent breaking of the shear reinforcement as a result of the failure and buckling of the compressive reinforcement.

The experimental load (kN) vs. displacement (mm) results as obtained by Victor (2011) are shown in Figure B.4-1, Figure B.4-2 and Figure B.4-3 for beams 1 (a and b), 2 (a and b) and 3 (a and b) respectively. Also shown in these results are those obtained by Victor (2011) based on the model she considered, which is not considered in this study.

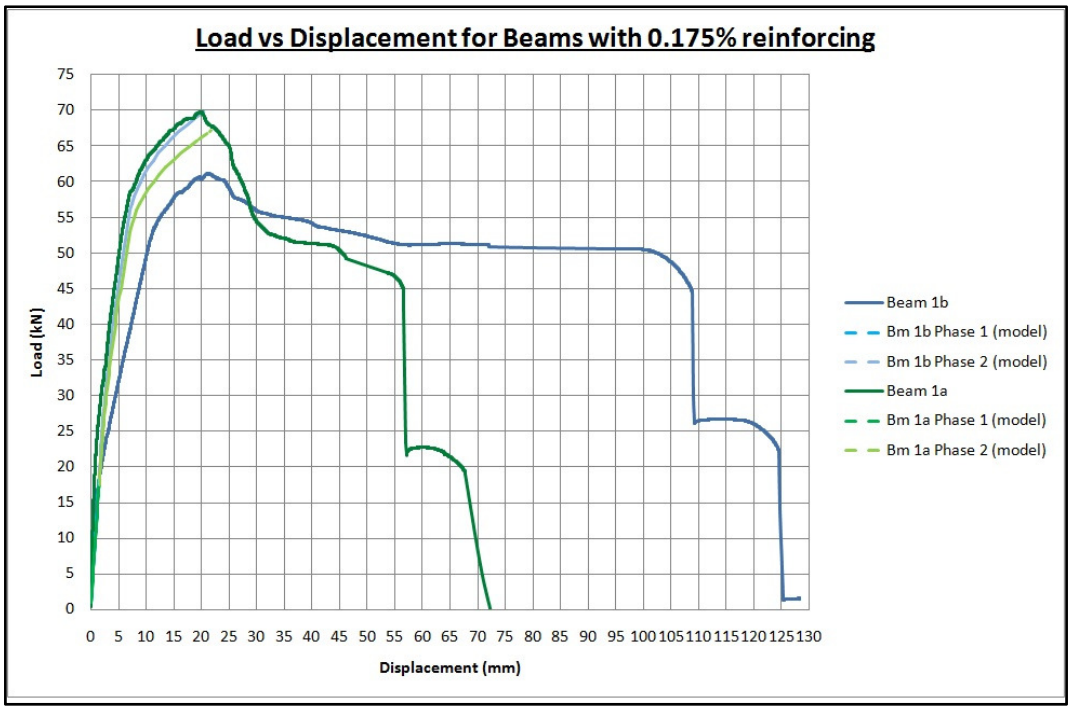

Figure B.4-1 - Load vs. Displacement for Beams 1a and 1b (Victor, 2011)

The sudden drops in resistance evident in Figure B.4-1 were observed to be due to the failure of one of the tensile reinforcing bars. This behaviour was only observed for the second beam at a much larger deflection. Beam 1a also showed an increased flexural resistance and inferior ductility to that of Beam1b. Beam 1a was not observed to exhibit a large number of cracks spread across the length of the beam as would be expected of the material, but rather had one major localised crack at midspan which almost propagated through the entire depth of the beam, with but a few more dispersed cracks. Beam 1b exhibited this characteristic material property, hence its superior ductility. No shear cracking was observed on these beams. It is clear that there wasn't significant consistency in the experiments.

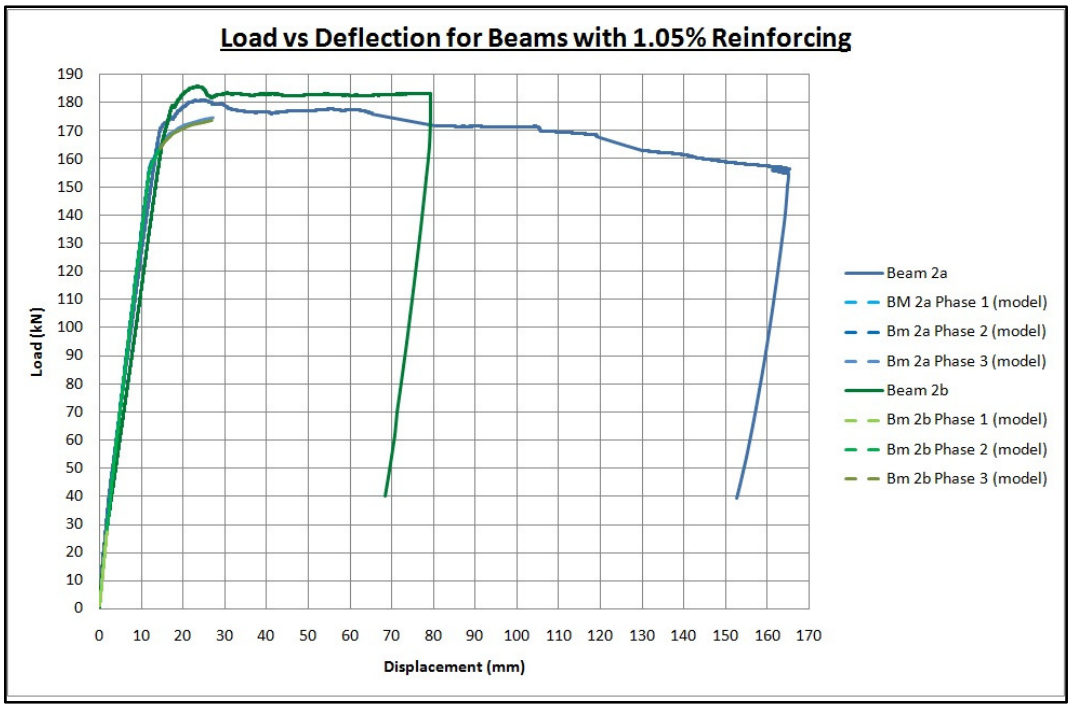

Figure B.4-2 - Load vs. Displacement for Beams 2a and 2b (Victor, 2011)

The beams in Figure B.4-2 showed better correlation between the results, and failure of the compressive reinforcement was observed for both, soon after crack localization. Both beams also exhibited numerous cracks along their length.

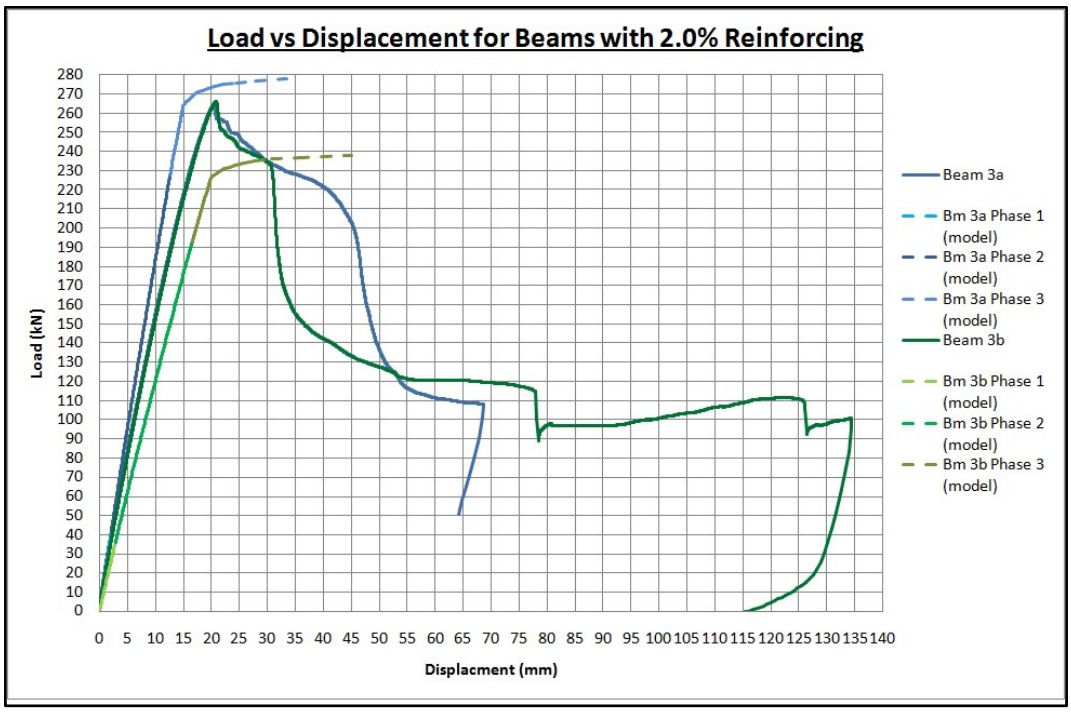

Figure B.4-3 - Load vs. Displacement for Beams 3a and 3b (Victor, 2011)

Beams 3a and 3b were observed to not fail entirely in flexure. The compressive reinforcement failure and spalling of the concrete at the top of the beams was prominent, and shear cracks developed through the beams' depth. As a result some of the shear stirrups were bent open. Beam 3b seemed to have been more ductile than 3a, this was attributed to it being slightly longer (by 300mm) (Victor, 2011).

B.4.3 Pre-Processing of NLFEA

The beams from the experimental investigation of Victor (2011) were analyzed using DIANA (2009) in conjunction with a user supplied subroutine for the modelling of SHCC materials as formulated by Van Zijl (2000). Uncertainty prevailed regarding the choices for the material parameters to be implemented, as no set database for the material strength properties for the mix design used in the experiments was established. Thus various options regarding material property choices were investigated, and the best fit option was applied to the analyses of the three beam types.

B.4.3.1 Model Geometry and Boundary conditions

A plane stress analysis was conducted on the 3 different simply supported beams subjected to three point bending. The standard beam dimensions of 3000x300x300mm were modeled. The details of the beams and boundary constraints imposed on the beams are shown in Appendix C, along with the longitudinal and shear reinforcement. A perfect bond was assumed between the concrete and reinforcement, with the reinforcement modeled using the embedded reinforcement elements available for implementation in DIANA. The reinforcement was placed at the same locations as in the experiments, with the equivalent combined area of the reinforcing bars in the same horizontal plane input as the reinforcements cross sectional property.

Steel loading platens were modeled at the supports and the area of loading, with the constraints imposed at the centre points of these platens. A thickness of 300mm was assigned to the concrete beam and steel plates.

B.4.3.2 Material Properties

Beams were modeled using two constitutive relations: Total Strain based rotating crack models as well as the multi-surface SHCC material model as developed by

Van Zijl (2000). The rotating crack model was considered as suggested by Hendriks et al. (2009) as well as the anticipation of a large amount of stress redistribution in the analyses due to the ductility and extensive cracking observed experimentally and as is characteristic of the material Thus the fixed crack model was anticipated to merely reflect its own downfall, that of excessive stress locking at the cracked locations due to principal stress rotations and was thus not considered, as well as due to difficulties establishing a shear retention factor. The SHCC material model was provided by Van Zijl (2000) in the form of a DIANA subroutine, and implemented accordingly.

The Total Strain models do not have the ability to reflect the loading/strain rate dependant (in both hardening and softening) nature of the SHCC material. However, it was considered to implement these models due to their tendency of simulating extensive cracking, a property also exhibited by SHCC materials. Due to the failure of Victor (2011) to obtain adequate material data, the material input used was obtained from experimental data done by Molapo (2010), as was suggested by Victor (2011). The data for the Total Strain rotating crack model is shown in Table B.4-2. This data was found to correlate reasonably well when implemented in a Total Strain formulation, regardless of the strain rate at which the data was obtained or the strain rate to which the concrete was exposed to within the analysis. A multi-linear tension curve was used in this model to reflect the initial tensile strain hardening and the subsequent softening, which does not depend on the fracture energy. However, in calculating the softening curve, fracture energy was required to emulate the anticipated material tensile response. The tensile fracture energy parameter used was as is typical of the material, and obtained from Van Zijl (2009). Thus the fracture energy per unit area was known for a specific mesh size ($g_{ft}, \frac{N}{mm^2}$) and was used to calculate the softening portion of the multi-linear tensile model for the other mesh sizes (which was taken as softening linearly to a point close to 0 stress, but allowed an ‘infinite’ asymptotic strain increase with decreasing stress, to avoid numerical complications at 0 stress). A Thorenfeldt compression curve (DIANA, 2009) was used to model the compressive behavior, due to suggestion by Hendriks et al. (2009). The use of a parabolic compressive curve to model the compressive response such that it was fracture energy dependent was considered, but observation of the results obtained from the plasticity models showed

compressive failure to not be of importance, thus the fracture energy independent Thorenfeldt compressive curve was considered in conjunction with the fracture energy independent multi-linear tensile curve.

Concrete Material Properties for Total Strain Models		
Material Models	Rotating	-
Young's Modulus	E	7780 N/mm^2
Poisson's Ration	ν	0.3
Tension curve	Multi linear*	-
Yielding Tensile strength	f_{t1}	2.529 N/mm^2
Strain at yield	ε_{t1}	0.00033
Ultimate Tensile Strength	f_{tu}	3.054 N/mm^2
Ultimate strain	ε_{tu}	0.01617
Tensile Fracture Energy	g_{ft}	0.01 N/mm^2
Compression Curve	Thorenfeldt*	-
Ult. Compressive strength	f_{cu}	30 N/mm^2

Table B.4-2 - SHCC Properties for Total Strain model (Molapo, 2010).

The creep and shrinkage aspects developed and implemented in the SHCC plasticity model were not considered. The SHCC DIANA subroutine affords the user the ability to implement the model using the 1 parameter cracking rate dependant formulation of Van Zijl (2000) or the 3 parameter cracking rate dependant model of Wu and Bazant (1993). The plasticity material model used for the mesh sensitivity investigation for the different material models was also based on values obtained by Molapo (2010) as suggested and used by Victor (2011), in conjunction with the 1 parameter crack rate dependence model developed by Van Zijl (2000) and using some material values suggested by Van Zijl (2009) (specifically fracture energy values). The cracking rate viscosity parameter used was established via several post analysis checks, with convergence for most mesh sizes in mind, as well as correlation with the experimental results. The material parameter values used are shown in Table B.4-3, with isotropic material behavior assumed.

* Refer to Sections A.3.1.3 and A.3.1.5 for model descriptions.

Concrete Material Properties for Plasticity Model		
Material Model	Rankine-Rankine Plasticity*	
Young's Modulus	E	7780 N/mm²
Yielding Tensile Strength	f_t	2.529 N/mm²
Ultimate Tensile Strength.	f_{tu}	3.054 N/mm²
Equivalent ult. Tensile strain	κ_{tu}	0.01584
Tensile Fracture Energy	g_{ft}	0.01 N/mm²
Shear cont. to tensile failure	α_t	1
Cracking Viscosity	m	500 Ns/mm²
Yielding Compressive Strength	f_c	20 N/mm²
Ultimate Compressive Strength	f_{cu}	30 N/mm²
Equivalent strain at Ult. Comp.	κ_{cu}	0.02
Compressive fracture energy	g_{fc}	5 N/mm²
Shear cont. to comp. failure	γ	3

Table B.4-3 - SHCC Plasticity Material Parameters (Molapo, 2010)

An attempt was also made to attain more accurate plasticity parameters for input. This was done by calibrating values obtained by Adendorff (2009) for tensile tests performed at various rates for SHCC dog bone specimens of the same mix design as used by Victor (2011). The calibration procedure can be found in (Van Zijl, 2009) for obtaining the values for the 3 parameter model of Wu and Bazant (1993). These values were implemented in the models for one of Victor's (2011) tests. The 1 parameter model's crack rate viscosity parameter was determined from the 3 parameter model values, based on correlation with analyses done on one element under pure tension. The anticipated loading rate on an element in the zone of localization in the physical beams was calculated. The material response was determined by using the 3 parameter model on the single element by imposing the calculated loading/strain rate. The value for the one parameter model which, when implemented on the same single element test and yielded the same response as the 3 parameter model, was then also used in

* Refer to Section A.3.2.4 for material model and parameter descriptions.

an analysis of Beam 1. Refer to Table B.4-4 for the results of the calibration and the parameters used.

Calibrated Material Properties for Rate dependant Plasticity Models

Material Model	**3 Parameter model**	
Yield strength	f_{t1}	2.2 N/mm²
Ultimate tensile strength	f_{tu}	3.97 N/mm²
Strain at ult. Tens. strength	κ_{tu}	0.051
1st parameter	c_1	0.0071145
2nd parameter	c_2	0.001
Reference strain rate	$\dot{\kappa_r}$	10^{-5}
Material Model	**1 Parameter Model**	
Yield strength	f_{t1}	2.2 N/mm²
Ultimate tensile strength	f_{tu}	3.97 N/mm²
Strain at ult. Tens. strength	κ_{tu}	0.051
Cracking viscosity parameter	m	500; 1000; 10000 Ns/mm²

Table B.4-4 - Calibrated values for SHCC plasticity model.

Thus due to insufficient experimental data for the concrete used in Victor's (2011) experiments, the assumption of using Molapo's (2010) values in the Total Strain and plasticity frameworks (which ended up correlating well with experimental results) would deem to be a feasible assumption, especially considering that the one parameter rate dependent model of Van Zijl (2000) depends only on some 'instantaneous' rate (specific to the analysis); as opposed to the rate-dependant (at the tensile test strain rate level) crack rate dependant (at the numerical level) 3 parameter model of Wu and Bazant (1993). Thus correct (to an extent) material response can be numerically reflected upon an appropriate estimation of m (through inverse analysis) despite the tensile strength values of the material used numerically having been obtained at a strain rate (from a tensile test) that does not represent that which the actual experiment encountered, and will only suffice as the choice of parameters for that specific combination of parameters and m won't be a consistent material property. m is specific for a specific rate and specific tensile strength values, not consistently specific for a wide range of strain rates and tensile properties.

Despite lack of steel reinforcing properties, typical values were assumed and controlled by a Von Mises pressure independent yield criterion. The values assumed for the steel reinforcing are typical values and are based on tests done previously (Van Zijl, 2009). The reinforcing steel parameters used are shown in Table B.4-5.

Longitudinal Reinforcing Steel Material Properties		
Material model	**Von Mises**	-
Young's Modulus	**E**	200 000 N/mm²
Poisson's Ration	ν	0.3
Yield Strength	f_y	550 N/mm²
Ultimate Strength	f_u	650 N/mm²
Ultimate Plastic Strain	ε_u	0.08
Steel Area Beam 1	A_s	157.08 mm²
Steel Area Beam 2	A_s	942.5 mm²
Steel Area Beam 3	A_s	1809.55 mm²
Transverse Reinforcing Steel Material Properties		
Material model	**Von Mises**	-
Young's Modulus	**E**	200 000 N/mm²
Poisson's Ration	ν	0.3
Yield Strength	f_y	350 N/mm²
Ultimate Strength	f_u	550 N/mm²
Ultimate Plastic Strain	ε_u	0.05
Steel Area Shear Rebar	$A_{s,shear}$	100.5 mm²
Spacing		300 mm c/c

Table B.4-5 - Reinforcement properties for tension critical beams (Van Zijl, 2009).

B.4.3.3 MESHING

The three element types used in analyses (cf. Section B.1.3 on page 63) were Q8MEM, CQ16M and T6MEM. Three mesh sizes were considered for Q8MEM and CQ16M to investigate mesh sensitivity. The mesh element sizes were quadrilaterals of dimensions 12.5mm, 25mm and 50mm (Mesh sizes I, II and III respectively). One mesh size was considered for the T6MEM crossed-diagonal

mesh, where 4 cross-diagonal elements were meshed within a 50x50mm quadrilateral shape.

B.4.3.4 Loading and Solution Procedure

The loading was applied at midspan at the centre node of the steel loading platen for all the beams. A displacement controlled analysis was conducted for the Total Strain based models with displacement steps of -0.25mm. A secant BFGS incremental iterative solution procedure was used for the Total Strain based analyses. Again, Arc length methods were used to attain any more structural response, but with no success. A force and energy based convergence tolerance of 1% was applied to the analyses to be satisfied simultaneously, and 100 iterations were allowed per displacement increment.

For the SHCC Plasticity model analyses, displacement controlled analyses were also conducted using a displacement vs. time relationship controlling the displacement increments in order to incorporate the rate dependence parameters. The displacement vs. time relationship was according to the experimental loading rate of 10mm/ min. A force and energy convergence criteria was imposed on the model, to be satisfied simultaneously.

B.4.4 NLFEA Results and Discussion

The material parameters used in the NLFEA's of the tension critical reinforced SHCC beams are listed in Table B.4-3. In Table B.4-6 a summary of the analyses that were conducted is shown. Only the Total strain rotating crack model was considered for these experiments, due to the material having the propensity of forming numerous cracks as well as per suggestion by Hendriks et al. (2009).

MESH SENSITIVITY INVESTIGATION - BEAMS 1,2 and 3	
SHCC Plasticity Model	**Total Strain, Rotating Crack**
T-Q8MEM-P-I	T-Q8MEM-TS[R]-I
T-Q8MEM-P-II	T-Q8MEM-TS[R]-II
T-Q8MEM-P-III	T-Q8MEM-TS[R]-III
T-CQ16M-P-I	T-CQ16M-TS[R]-I
T-CQ16M-P-II	T-CQ16M-TS[R]-II
T-CQ16M-P-III	T-CQ16M-TS[R]-III
T-T6MEM-P-II	T-T6MEM-TS[R]-II
SHCC PLASTICITY PARAMETER CALIBRATION INVESTIGATION,BEAM1.	
1 Parameter model	**3 Parameter model**
T-Q8MEM-P(A)-II*	T-Q8MEM-P(A)-II*

Table B.4-6 - NLFEA's conducted for tension critical beams

* **P(A)** in the model description refers to the plasticity parameters as calibrated from Adendorff's (2009) results.

B.4.4.1 Plasticity Model

The SHCC plasticity material model developed by Van Zijl (2000) as a subroutine for implementation in DIANA was used to model the SHCC beams tested in 3 point bending by Victor (2011). All three beam types (with varying amounts of reinforcement) were tested for the various mesh sizes and element types. The results for the beams will be discussed in ascending order of reinforcement ratio, thus starting with Beam 1's results, as shown in Figure B.4-4.

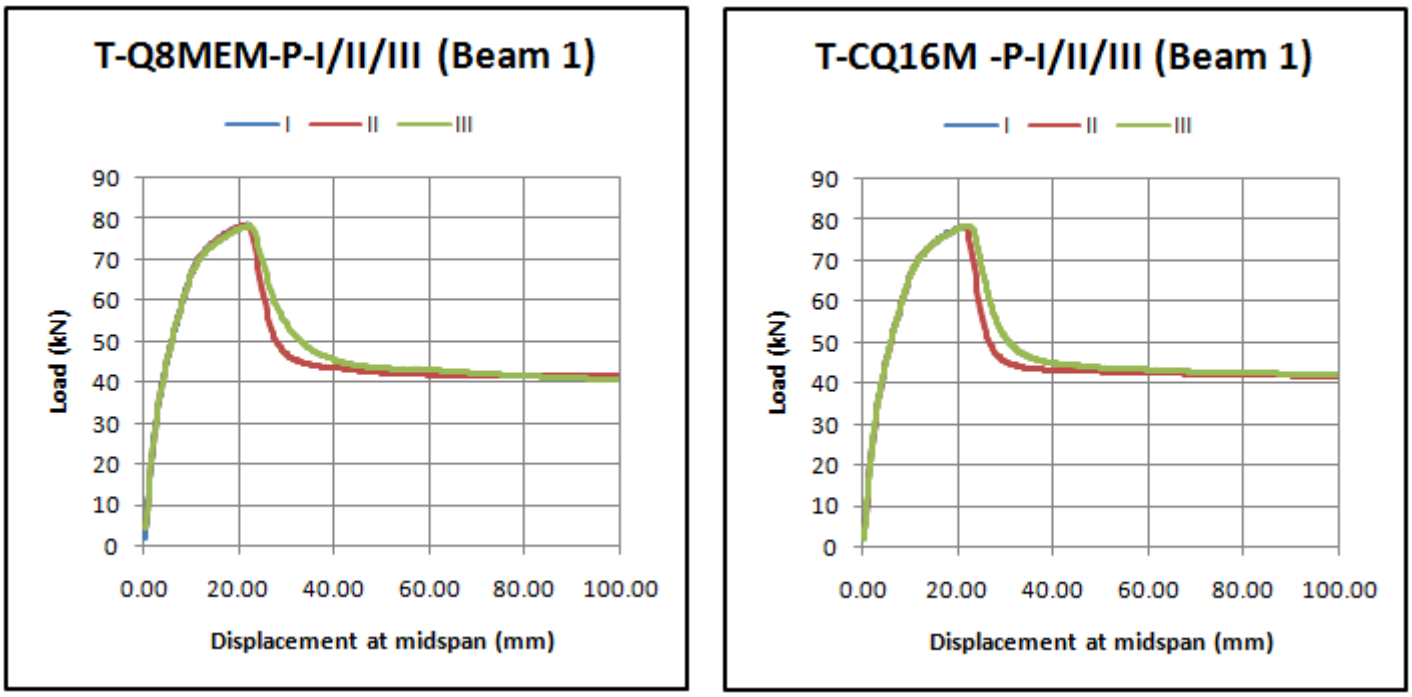

Figure B.4-4 - Load vs. Displacement results for tension critical Beam 1, plasticity model.

The results of the NLFEA's for Beam 1 showed good correlation with those obtained experimentally, despite the complications and errors involved in the experimental procedure. The ultimate load of the beams was overestimated in the analyses, but considering that the experimental beam dimensions were not exact and that the concrete mixing was not performed properly, one could safely expect a more superior experimental response if a more appropriate scientific approach were to be taken. The use of Molapo's (2010) material parameters in conjunction with the chosen cracking rate viscosity yielded satisfactory results. A sensitivity analysis on the cracking viscosity parameter showed that the peak load and corresponding displacement increased with increasing cracking

viscosity, which is as intuitively expected. Thus a value was chosen which provided the response most closely representing the experimental results, as well as providing a detailed (regarding post peak data) response curve. The softening branch obtained numerically is steeper and occurs more abruptly than was observed experimentally, this can be attributed to the uncertainty surrounding the exact material parameters of the material used experimentally and the potential for the cracking viscosity to actually be higher for a slower softening response. There was also no evidence in the analysis of the tension reinforcement failing, which was observed experimentally for both beams tested. The steel reinforcement material properties were estimated based on characteristic material data obtained from Van Zijl (2009), as no such data was obtained experimentally. Mention was also made by Victor (2011) that the specimens may have been loaded slightly asymmetrically, which would have induced asymmetric tensile reinforcement failure. The post peak response showed a residual strength plateau at approximately that obtained by Victor (2011), but for a much larger deflection range as tensile reinforcement failure was not observed numerically.

The plasticity model yields consistent results for all the quadrilateral mesh sizes and types considered and analyzed, and especially the pre peak response was shown to be mesh unbiased. The T-Q8MEM-P-I and T-CQ16M-P-I models diverged once the peak load was obtained, and post peak convergence for these models could only be obtained when very high values for the cracking viscosity parameter were used, which yielded incorrect peak values. However, all meshes and element types reached the same peak load at the same displacement, as is evident in Figure B.4-4. The difference in post peak response between the II and III mesh sizes is evident in Figure B.4-4, where the descending branch is slightly less steep for the larger mesh size. Similar observations were made by Van Zijl (2009) for varying mesh sizes and constant cracking rate viscosity value. This was thought to be due to the dependence of the cracking rate viscosity on the equivalent strain rate in the mesh area prone to cracking in the analysis. Due to the larger element size, the anticipated equivalent strain rate would develop slightly slower than for smaller elements. Thus imposing the same viscosity on these slower strain rates would yield a stiffer ductile response for the mesh containing the larger elements. Imposing the same viscosity on the slightly faster

strain rates anticipated in the smaller mesh sizes would yield a less stiff ductile response.

The results for the analyses on the Beam 2 specimens are shown in Figure B.4-5 for the mesh types and sizes.

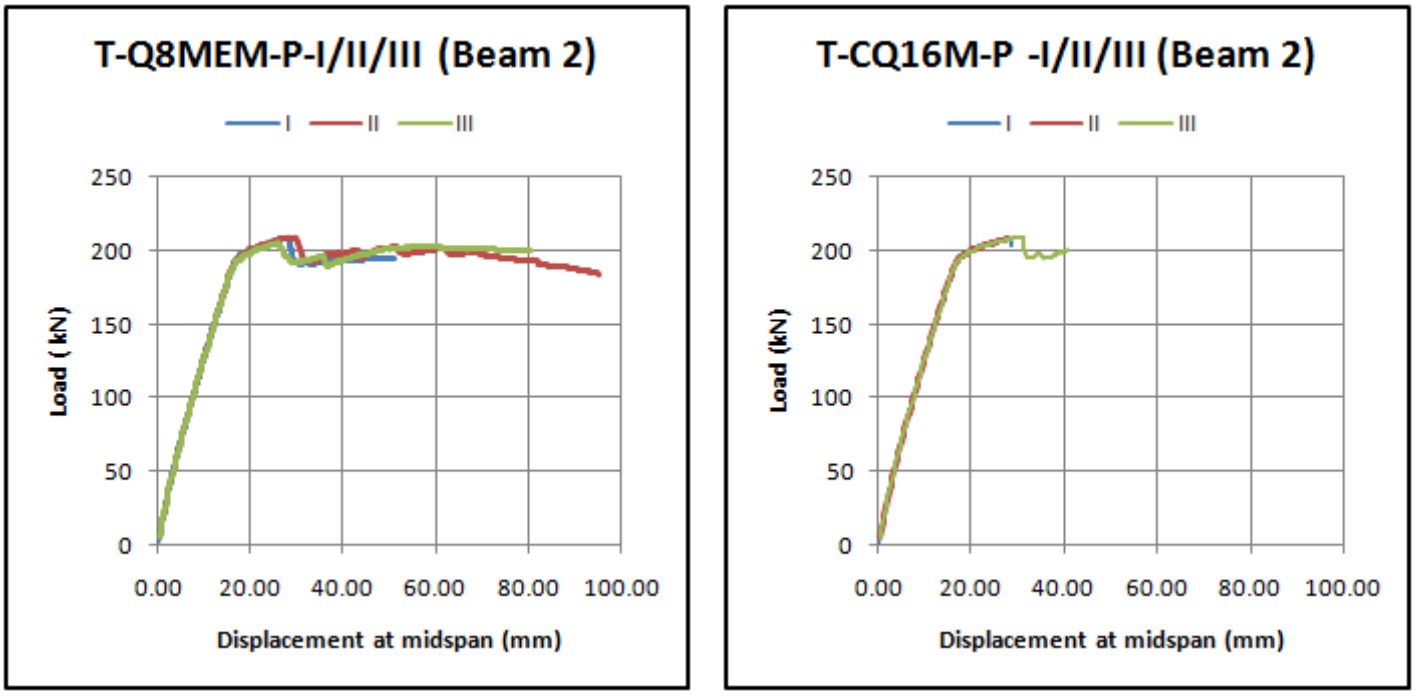

Figure B.4-5 - Load vs. Displacement results for tension critical Beam 2, plasticity model.

It is clear that there is generally very good correlation between the results regardless of mesh type or size. A more detailed post peak response was obtained for the Q8MEM models, something which has been observed throughout this study. The benefits of the higher order elements, in that they can describe more complex displacement fields and deformation modes and subsequently more accurate results due to their more complex mathematical descriptions, seems to also lead to their downfall in non linear analyses where the additional mathematical intricacies they introduce yield convergence difficulties in the numerical solution process.

The peak load and associated displacement reached in the analyses was consistent with the experimental values, with the peak load being slightly overestimated due to the material and experimental specimen uncertainties. The retention of the peak load for a large range of deflection was also observed numerically, especially so for the T-Q8MEM-P-II and III models, where

divergence occurred at an appropriate deflection when compared to the experimental results. Divergence for these models occurred after the tensile reinforcement had reached its ultimate stress. The T-Q8MEM-P-II model continued past this point until failure in the compressive rebar also occurred. Thus the failure of compressive buckling of the compressive reinforcement and subsequent spalling of the concrete observed experimentally is conceivable, especially considering the large spacing of the stirrups. This failure could not be observed numerically due to embedded reinforcement elements' strain development being dependant purely on the displacement of the elements within which they are embedded. The cracking pattern exhibits tensile failure as can be seen in Figure B.4-6 showing the ε_1 contour plot at the final load step. The use of an associative flow rule governing the tensile yield regime is evident due to the large volume change of the elements.

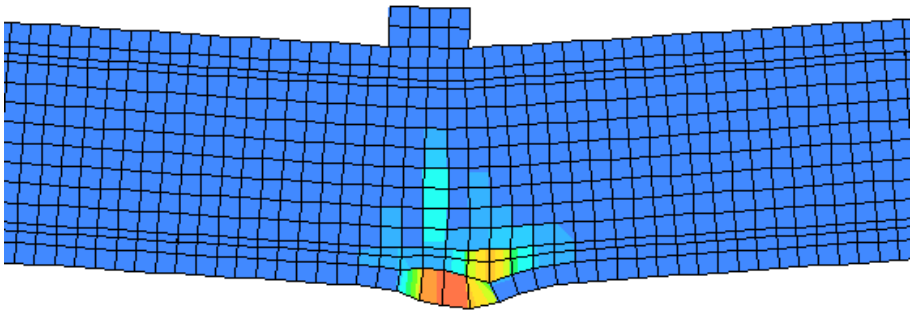

Figure B.4-6 - Principal strain contour plot at failure.

The results for the Beam 3 specimens are shown in Figure B.4-7 for the mesh types and sizes.

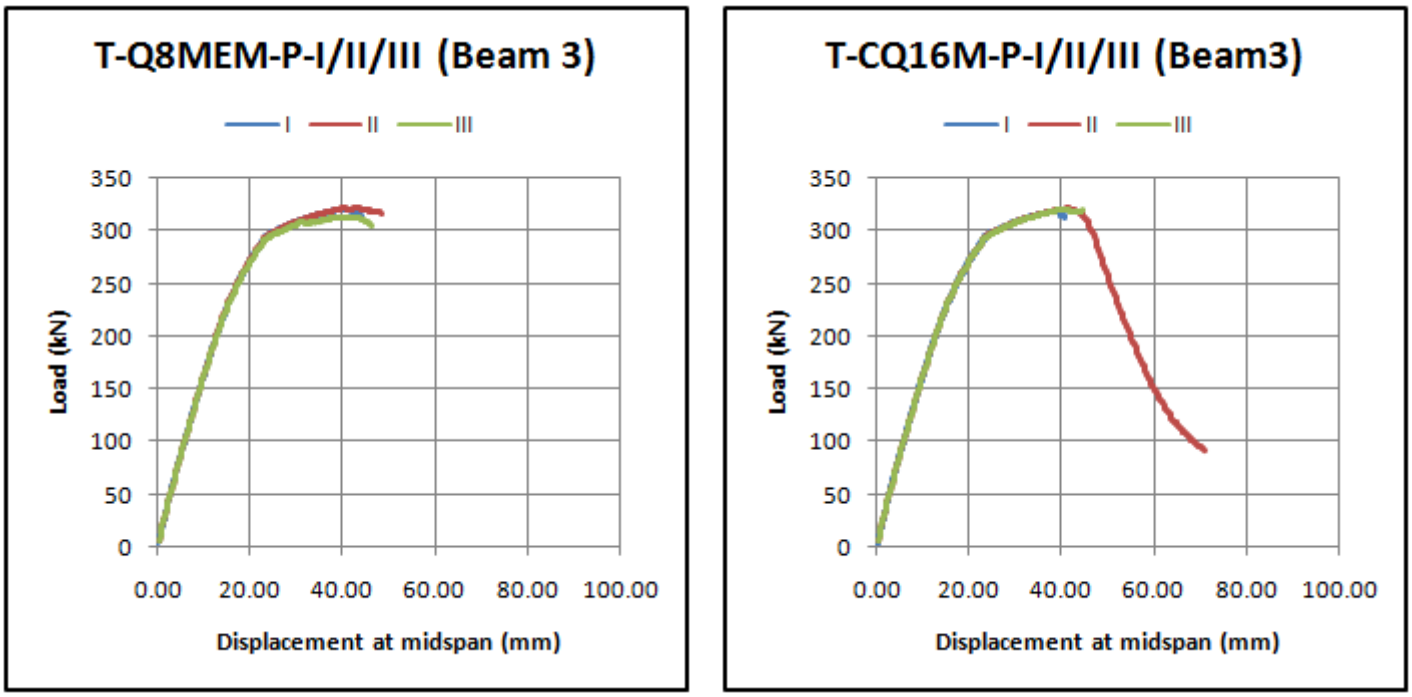

Figure B.4-7 - Load vs. Displacement results for tension critical Beam 3, plasticity model.

Again tensile failure was observed in the analyses, but the compressive stress in the top of the beam was close to reaching maximum compressive stress and compressive plastic flow was evident through part of the depth of the beam, as can be seen in Figure B.4-8 taken from the analysis T-CQ16M-P-II at the peak load step.

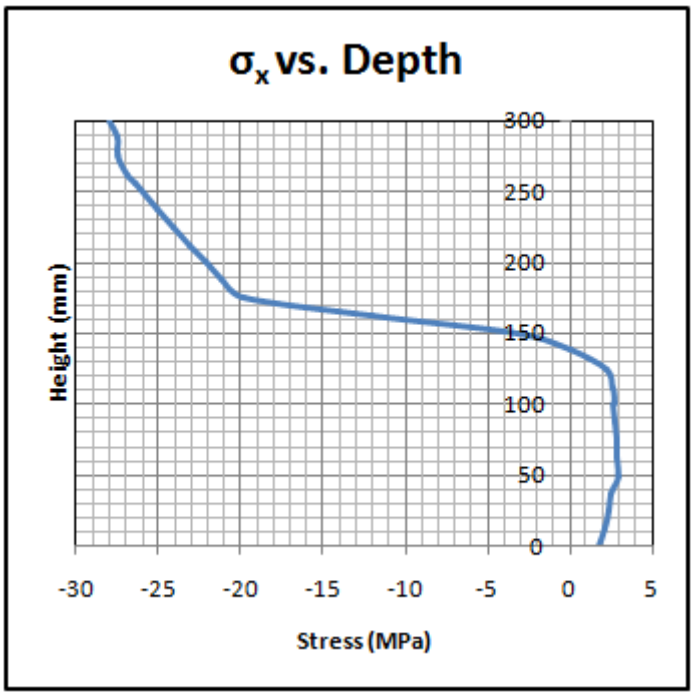

Figure B.4-8 - Horizontal stress distribution through depth of Beam 3.

Clearly the concrete has lost some tensile capacity and has softened in tension, contrary to the experimental observation of compressive reinforcement buckling and spalling of the concrete and some indications of shear failure.

Consistency between analyses is again observed, however only the T-CQ16M-P-II analysis exhibited post peak response. All other models diverged either at or shortly after attaining the peak response and the associated tensile localization. The reinforcement showed no signs of exceeding its capacity in neither tension nor compression, contrary to the experimental observation of compressive reinforcement failure and spalling of concrete.

Figure B.4-9 illustrates the different response curves obtained for Beam 1 with the cross-diagonal and quadrilateral mesh types using the one parameter plasticity model.

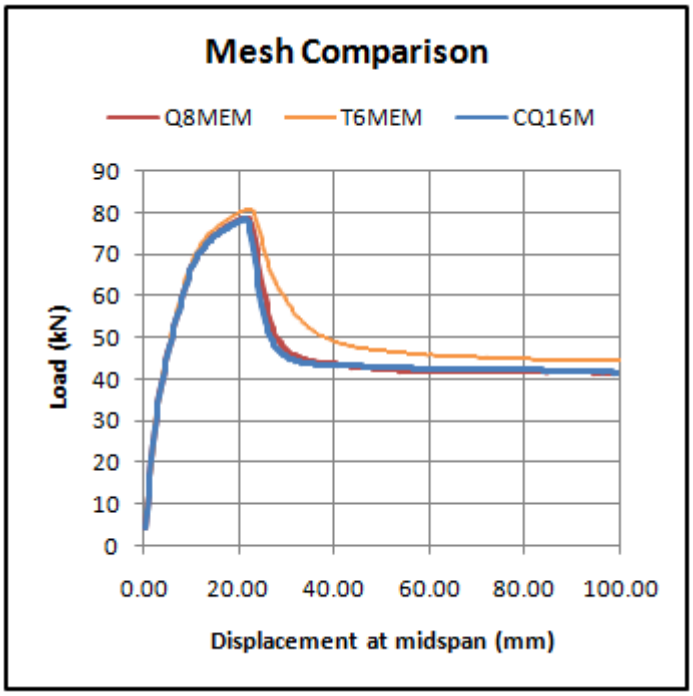

Figure B.4-9 - Mesh comparison for Beam 1, plasticity model.

The response of the T6MEM cross-diagonal mesh shows the attainment of a slightly larger peak, as well as a more gradual descending post peak branch. The attainment of the peak and the corresponding higher displacement has been attributed to the superior deformation behaviour of the cross-diagonal mesh type, due to the additional displacement degrees of freedom available at the centre of the quadrilateral containing the triangular elements. This superiority is further facilitated when used in conjunction with an associated flow rule governing tensile behaviour, as was done for these models, as plastic volume change is more easily accommodated by this mesh type (despite an associated flow rule not reflecting the physical nature of quasi brittle materials correctly).

The post peak response shows the mesh dependence of the one parameter model. With the same cracking viscosity used in this tension dominated case for all three models, the softening of the cross-diagonal mesh occurs more slowly. This is due to the size of the individual mesh elements being used to establish the length of the fracture process zone and subsequently the strain rate at which tensile softening develops. The slightly faster strain rate development in the smaller triangular elements occurs over the same equivalent length as with the quadrilateral meshes (crack-band width), which yields an overall slower softening strain rate. This slower (relative to the quad meshes) softening rate acting

against the same viscosity will yield the more gradual softening response observed. The strain hardening that takes place at the lower strain rate means that the higher stress resistance values are retained for longer, which could account for the greater peak load attained as well as the slightly higher residual strength in the beam once the inelastic work is almost entirely dissipated in the dominant crack.

Similar observations could not be made for the other beams due to lack of post peak behaviour for the cross-diagonal mesh, but it is anticipated (had a more detailed response been obtained) that the influence on the softening of the response would be less pronounced, as the reinforcement in these more heavily reinforced beams would have the greater influence on the mechanics of the structure.

The results obtained using the calibrated values as determined from Adendorff's (2009) experimental results according to the procedures described in Van Zijl (2009), are shown in Figure B.4-10. The calibrated parameters were only implemented using the T-Q8MEM-P-II model for Beam 1.

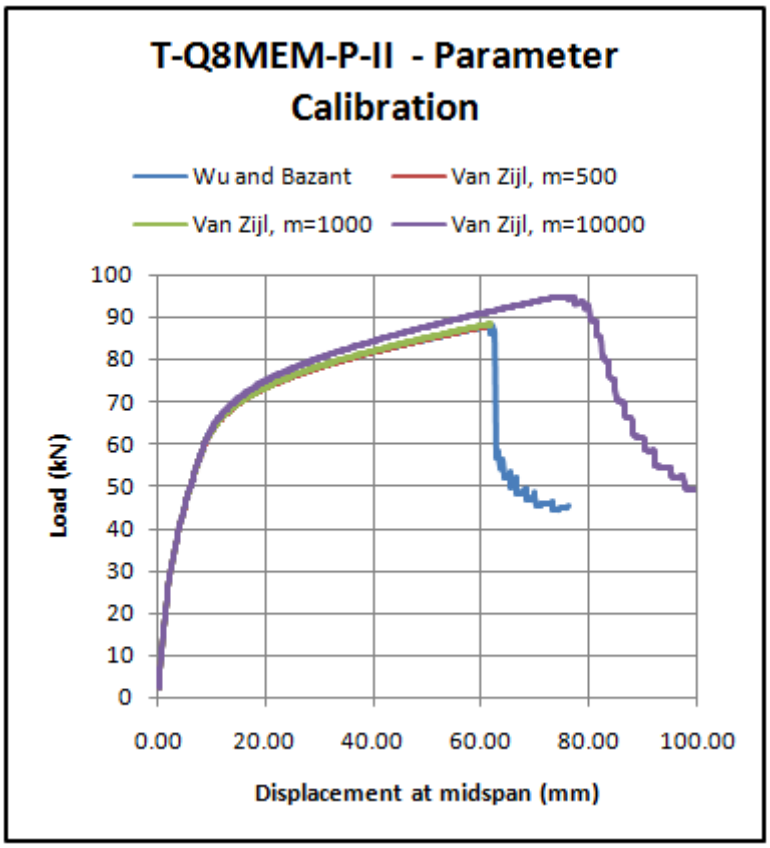

Figure B.4-10 - Load vs. Displacement results using calibrated values for SHCC model for Beam 1.

The calibrated values clearly showed a very unrealistic response, as the peak response for Beam 1a was at (70kN; 20mm). This may be attributed to the various problems encountered in Victor's (2011) experiments as well as the uncertainties revolving around the exact material parameters for these experiments, regardless of the fact that the same mix design as Adendorff (2009) was used.

It was found that the anticipated tensile plastic strain rate in the experiment was close to the value of the reference rate of the 3 parameter model. Thus the one element tests performed at the anticipated loading rate of an element in the zone of localization in the experiment yielded the 'base line' response of the Wu and Bazant (1993) 3 parameter model and thus the loading rate independent tensile response curve, with the values obtained for the first and ultimate tensile strengths being the input values. Therefore the calibration of the 1 parameter model of Van Zijl (2000) yielded a range of cracking viscosity parameters that were suitable for implementation and matched the response of the 3 parameter

model, as it doesn't depend on any reference rate itself. This can be seen for the responses in Figure B.4-10 for the model using cracking viscosity parameters of 500 and 1000 (Ns/mm^2), which yielded exactly the same results as one another as well as the 3 parameter model but exhibited no post peak behaviour. There would be a suitable choice for m which is just high enough to allow for the post peak response to be obtained. The independence of m from the other material parameters is illustrated through the use of a very high value of 10 000 Ns/mm^2 on the model. This value shows a much higher peak load and corresponding displacement, as the low strain rate develops against a high viscosity, causing stronger hardening of the material as the high stress values are retained for longer. Thus there exists a value for m between 1000 and 10 000 Ns/mm^2 which will provide the appropriate response that is approximately equal to the 3 parameter model's response for this element size.

The cracking viscosity parameter is also clearly dependant on the strain rate of an analysis in the region of maximum tensile straining. The fact that a specific value for m cannot be attained, that is specific for a specific mix design, and is applicable over for implementation over a myriad of strain rates is problematic. For design based on the results of NLFEA, various structural elements, their various geometrical properties and their interconnectivity may be analyzed to obtain a response and anticipated ultimate loads. Different strain rates may be present in these various structural elements, meaning various m values may need to be determined which are specific to each element. Thus there exists the need for the development of some strain rate dependant cracking viscosity parameter, a formulation which does not have the singularity problems or severe mesh dependence of the 3 parameter model.

B.4.4.2 Total Strain Rotating crack model

The results obtained for the tension critical Beam 1 modeled using a Total Strain rotating crack model, are shown in Figure B.4-11.

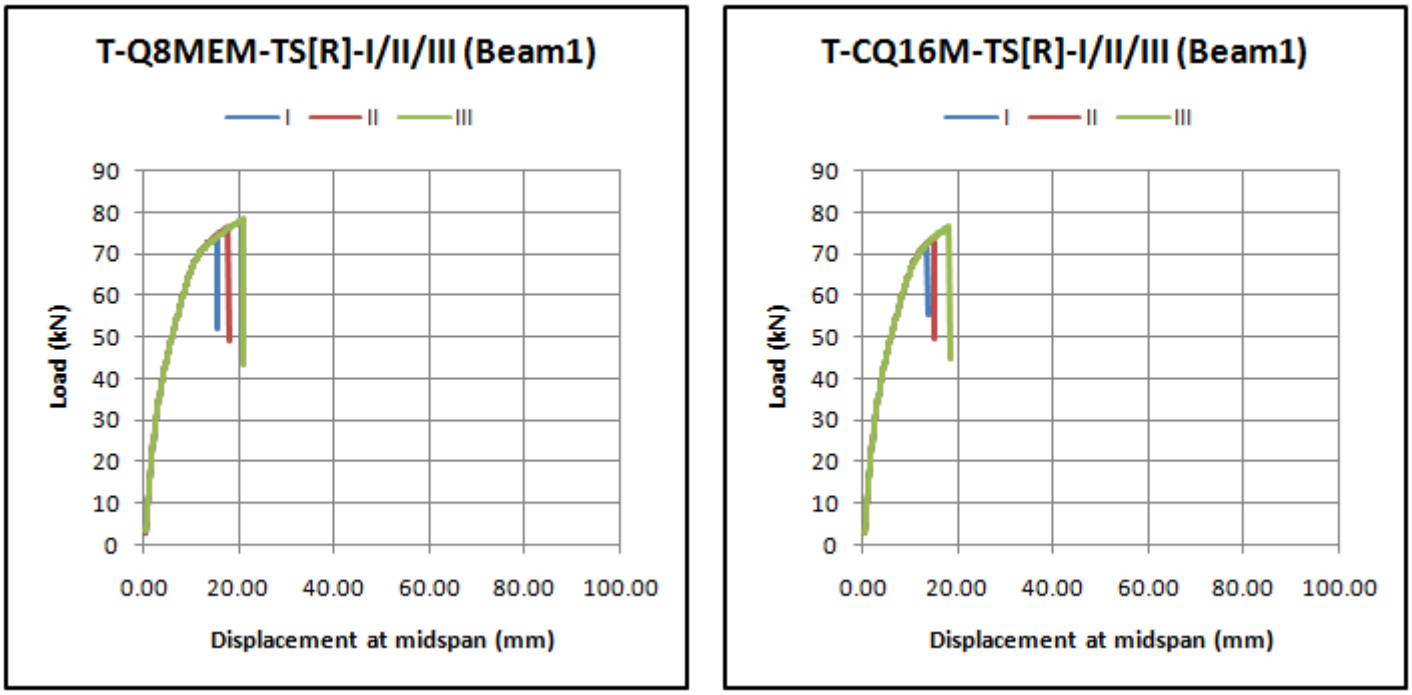

Figure B.4-11 - Load vs. Displacement results for tension critical Beam1, rotating crack model.

The rotating crack model results showed reasonably good correlation with the experimental results, with an overestimation of the peak load of approximately 10kN but at a similar corresponding displacement. Tensile failure was observed for all models, with the solution procedure diverging soon after localization and the formation of one dominant tensile crack.

The results for the rotating crack model also correlated very well with the plasticity model's peak values for all the analyses considered but did not provide as detailed post peak data. This correlation was observed regardless of the lack of any rate dependence in the rotating crack model, thus the material parameters as obtained from the experiments of Molapo (2010), were performed at a sufficiently low loading rate, so as to yield a rate independent response. The use of a multi-linear curve to model the tensile response of the SHCC in the Total Strain framework seems to have been a suitable choice, as well as the use of the Thorenfeldt compressive curve. However, the use of fracture energy dependent

models may have been able to describe the tensile softening more appropriately, but the tensile constitutive models available in DIANA are unable to incorporate the strain hardening nature of SHCC in conjunction with a fracture energy based softening model.

The larger mesh sizes were observed to attain a larger peak load and associated displacement, which was again attributed to the better performance of the larger elements in a rotating crack framework, due to the larger strain increments per element and subsequent larger rotation of the crack axes per load step. As can be seen in Figure B.4-12 for the cracks developed at the final load step for the meshes of the Q8MEM analyses, the cracks are 'trapped' in the smaller mesh and redistribution of stresses throughout the beam is more difficult due to the small strain increments and small rotation of principal axes per load increment. The cracks propagate further for the larger mesh sizes due to their easier facilitation of stress redistribution. Thus the length of the fracture process zone at the localization of the cracks differs for the mesh sizes, and tensile softening can occur through a greater depth of the beam for the larger meshes. For the size I mesh, the strains are focused lower in the beam at the integration points closer to the embedded reinforcement. Thus the variation of strain through the concrete beam is more severe, leading to the comparatively earlier failure of the concrete elements close to the reinforcement due to their large strains. The redistribution of the stresses and subsequent strain or crack propagation for the larger mesh sizes is more easily accommodated. This results in more uniformly distributed crack intensity as compared to the small mesh. The range of the magnitude of the strain vectors plotted in Figure B.4-12 is specific for each mesh type.

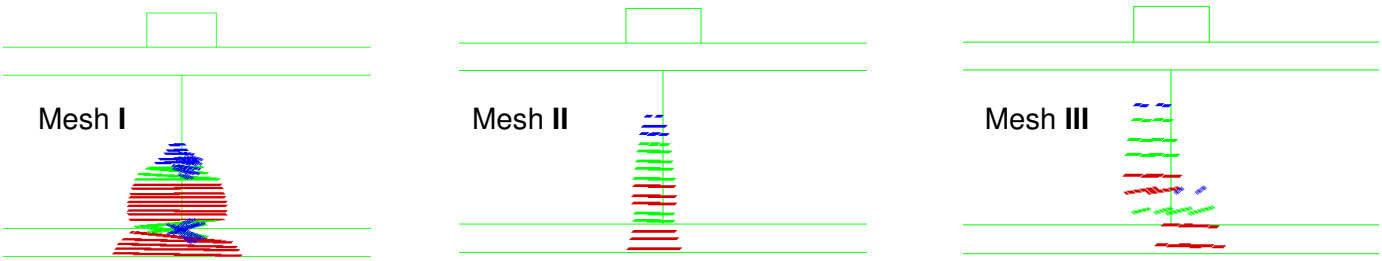

Figure B.4-12 - Comparison of cracking for meshes I to III.

The results for the Beam 2 analyses using the Total Strain rotating crack model are shown in Figure B.4-13.

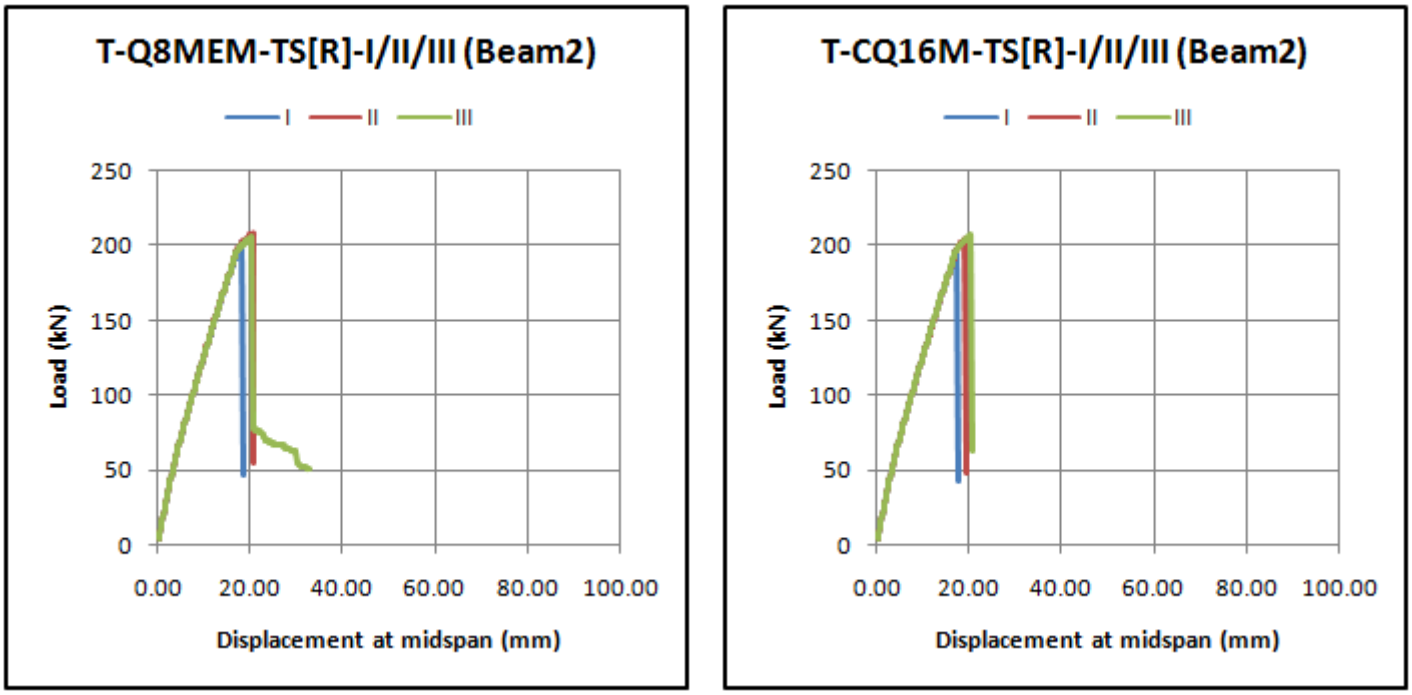

Figure B.4-13 - Load vs. Displacement results for tension critical Beam 2, rotating crack model.

Reasonably good correlation was found with the plasticity models for some of the responses for the peak values attained. The experimental peak is again overestimated and for the smaller mesh sizes, the corresponding displacement at peak load is underestimated. The failure was observed to be slightly more compressive dominated than was found for the plasticity models of the beams, with the peak compressive stress being reached in the top of the beam prior to divergence for all the analyses. This can be seen in Figure B.4-14 for the stress distribution through the depth of the beam at midspan at the peak load for the T-CQ16M-TS[R]-II-Beam 2 model. Compressive softening is clearly imminent as inelastic compressive behavior is observed in the top of the beam.

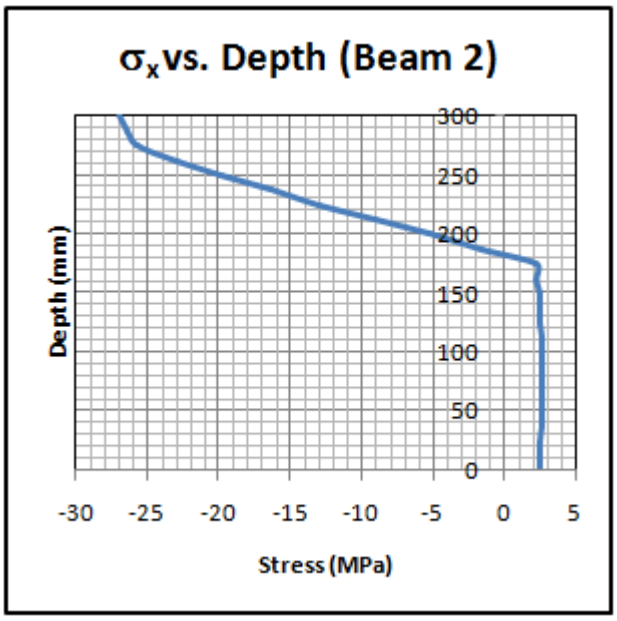

Figure B.4-14 - Horizontal stress distribution through depth, Beam 2.

Experimentally the failure at the top of the beam was due to buckling of the compressive reinforcement, and not attributed to concrete crushing. The reinforcement in these analyses was not observed to be near the ultimate strength.

The rate dependence of the plasticity model allowed the tensile stress to develop depending on the cracking viscosity of the material, thus also establishing the rate of curvature of the beam and indirectly the rate of compressive stress development in the top of the beam. As the multi-linear tensile constitutive model is rate independent, the tensile response for the rotating crack model was still in the hardening phase as the compressive peak was reached. Thus the 'rate' at which the tensile strain developed in the rotating crack model was slower than that of the plasticity model, due to the choice of viscosity parameter facilitating faster tensile strain rate development and therefore tensile failure preceded compressive failure for the plasticity model.

The difference in results between the mesh types is not too pronounced, with the CQ16M models showing failure slightly sooner than the Q8MEM models. No post peak residual strength was observed for the total strain analyses, as was done in the experiments and plasticity models. This can be attributed to the rate independent models used in compression and tension, where the energy dissipation upon softening occurs more rapidly and suddenly than for rate

dependant models. The use of a fracture energy dependant compressive model may have been more appropriate to ensure a more, and in order to achieve regularization of energy dissipation over the mesh sizes. However, based on the experience in this study, the attainment of significant post peak data using any of the elementary constitutive models available for implementation in DIANA is extremely difficult and seemingly impossible, regardless of solution procedures considered.

The results obtained for the analyses on Beam 3 for the various mesh sizes and types are shown in Figure B.4-15.

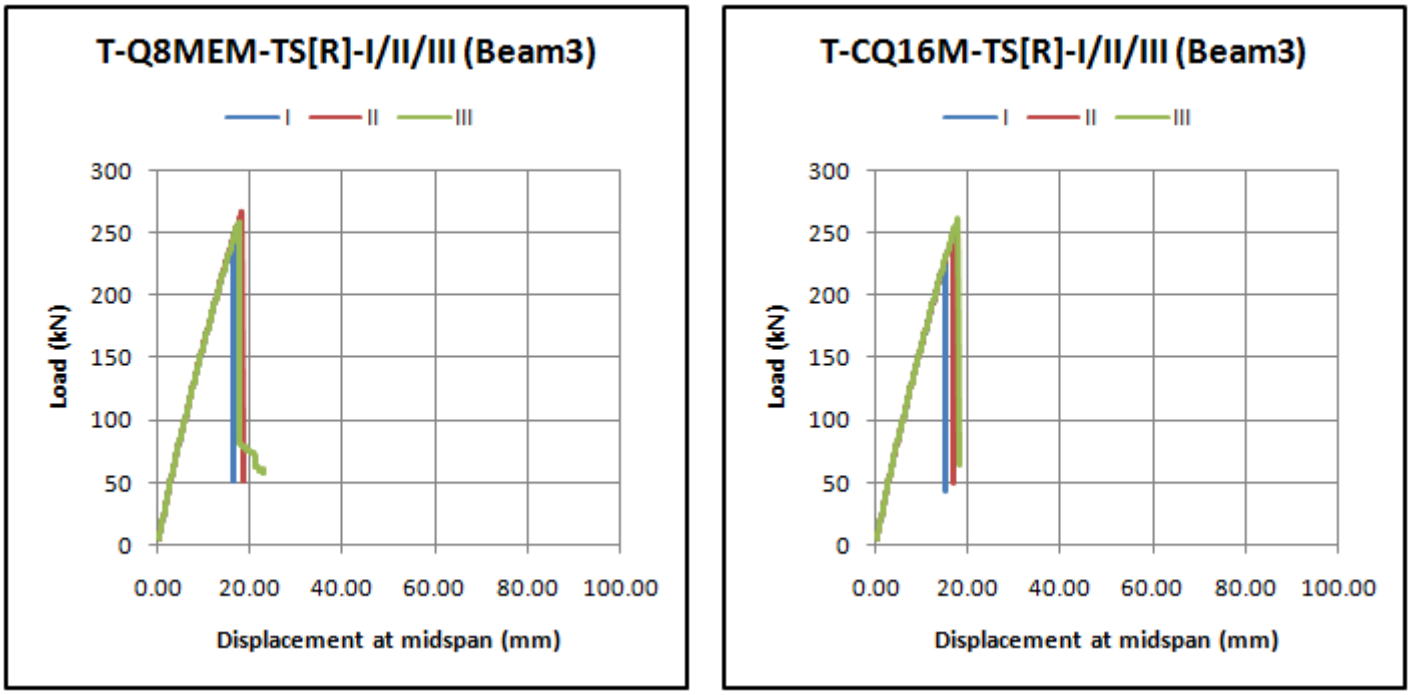

Figure B.4-15 - Load vs. Displacement results for Beam 3, rotating crack model.

The analyses for Beam 3 showed premature failure compared to the experimental results and those obtained from the plasticity model. The amount of tensile reinforcement caused the development of a deep compressive zone, leading to the build of large compressive stresses. Failure was also attributed to compressive failure of the concrete, with inelastic compressive behavior occurring and accompanied by divergence of the solution. This compressive failure for the rotating crack model is again due to the rate independence of the energy build up and release, which is not characteristic of the material. The inelastic compressive behavior at the peak load can be seen in Figure B.4-16 for the T-CQ16M-TS[R]-I model for a cross section at midspan, after which the

solution diverged. The compressive limit had been exceeded and softening is imminent, while the tensile region showed no evidence of cracking. At a height of 40mm a slight deviation from the constant tensile stress from near uniform tensile stress is evident due to the proximity of the reinforcement. The compressive zone has also clearly developed through a larger depth of the beam as compared to Beam 2 (Figure B.4-14).

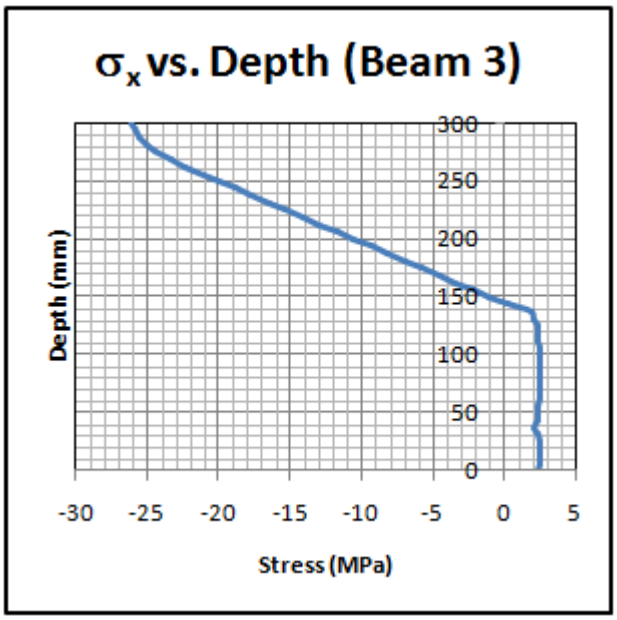

Figure B.4-16 - Horizontal stress vs. depth Beam 3, rotating crack model.

Again, the use of a fracture energy based compressive curve may have been more suitable; however use thereof would not have benefited the accuracy of the results as premature compressive failure would still have been observed.

Figure B.4-17 shows the results obtained for the cross-diagonal triangle mesh (T6MEM) along with the results of the C-Q8MEM-TS[R]-II and C-CQ16M-TS[R]-models for Beam 1.

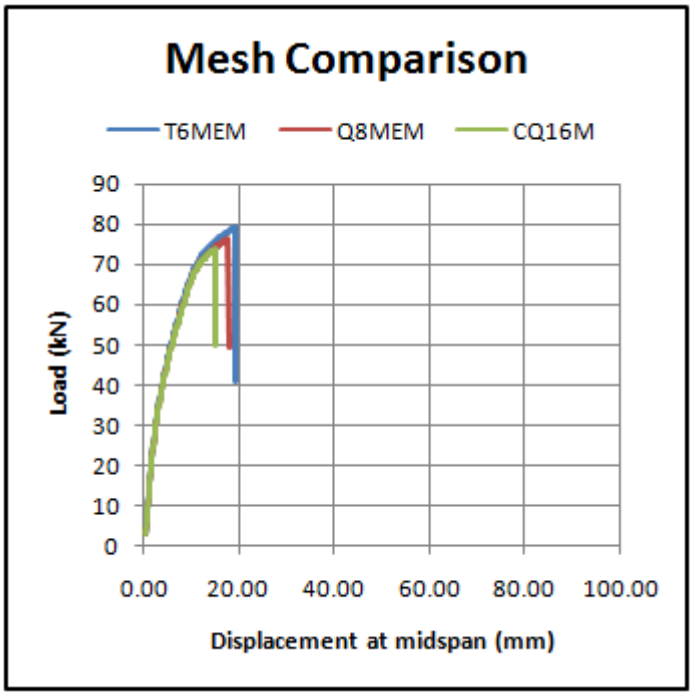

Figure B.4-17 - Mesh Comparison tension critical Beam 1, rotating crack model.

No significant difference was observed between the cross-diagonal triangle mesh and the quadrilateral meshes. A slightly larger peak load and corresponding displacement were obtained, due to the superior deformation capacity of the mesh.

In the next section, the peak loads and corresponding displacements obtained numerically are normalized with respect to the values obtained experimentally for Beam 1a, to provide a summary and a comparison of the analyses for the different material models and mesh types and sizes.

B.4.4.3 Comparison of analyses

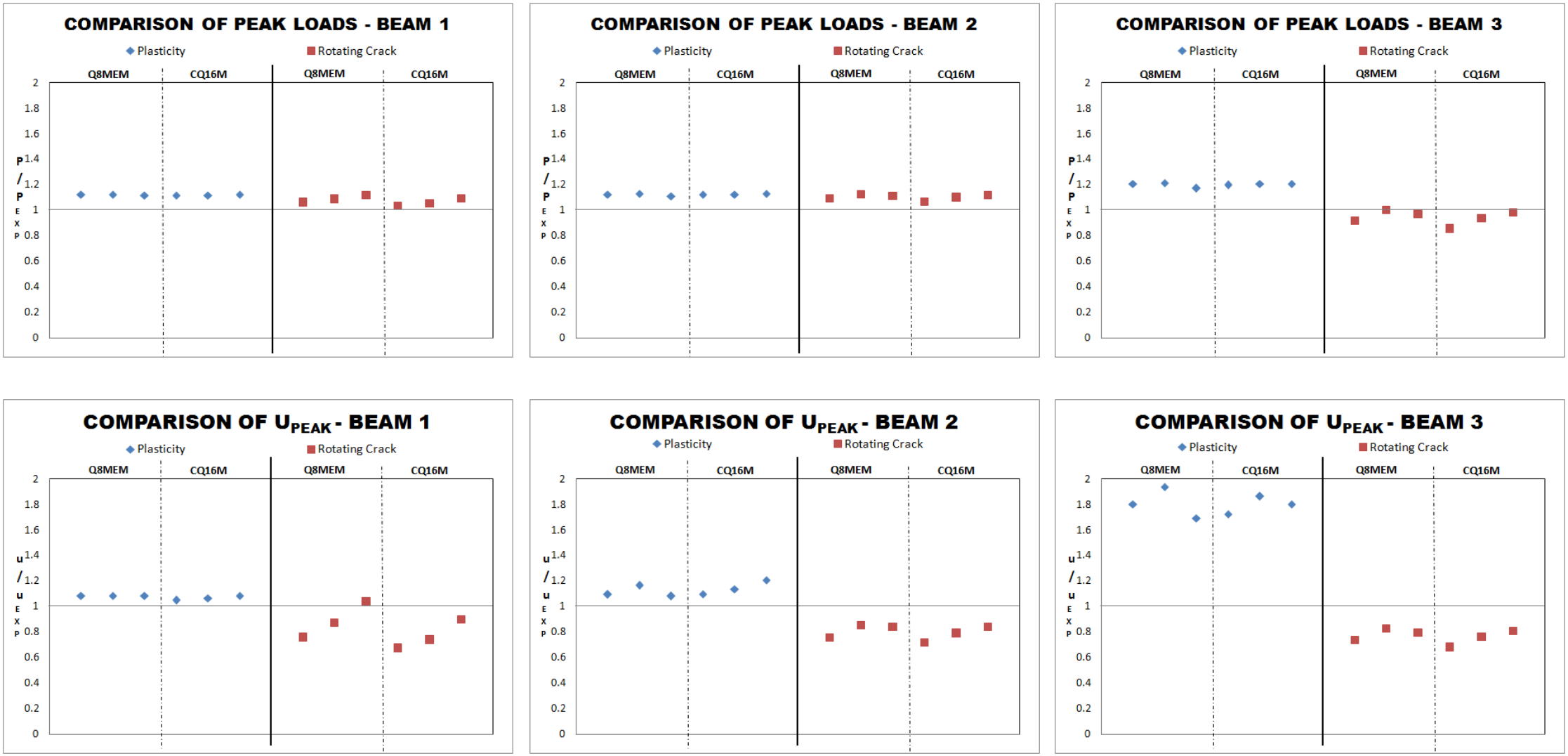

Figure B.4-18 - Comparison of analyses, Tension Dominated Study.

The data points for each mesh type (Q8MEM, CQ16M) are plotted from left to right corresponding to the ascending order of the mesh size (I. II, III) for each material model and beam type investigated in Figure B.4-18.

The peak load and corresponding displacement was very well captured by the SHCC plasticity model of Van Zijl (2009) for the plasticity analyses of Beam 1. The peak loads were overestimated by only 12% and the corresponding displacements by 8%. The results were also consistent across mesh types and sizes. The rotating crack model also yielded peak values within 12% of the experimental peaks, but less consistency across meshes was attained than the plasticity model. This inconsistency is also evident for the corresponding displacement at peak load, where the results range from 74% to 104% of the peak values obtained. This inconsistency is attributed to the use of fracture energy independent and rate independent constitutive models for the rotating crack analyses. The meshes with the larger element size exhibited larger peak values, which was attributed to the superior stress redistribution capacity of these mesh sizes.

The plasticity model again yielded peak load values that were consistent and within 12% of the experimental values obtained for Beam 2, with good consistency between mesh types and sizes. The corresponding peak load values all fell within 120% of the experimental values and showed slight variation between mesh types and sizes. This slight variation was considered to be due to the influence of the large amount of tensile reinforcement and the associated retention of peak loads for such large displacements. The difference in the strain rate in the elements but with the use of the same viscosities had a more pronounced effect on the displacement results due to the larger reinforcement ratio and the differences inherent in stress transfer to the reinforcement for the different mesh sizes (thus the mesh dependence of the cracking viscosity parameter is more pronounced). The peak loads for the rotating crack model were also within 120% of the experimental values and only slight mesh dependence of these results was observed. The results for the corresponding displacements underestimated the peak values by up to 70%. This was due to the premature imminent compressive failure observed for the total strain analyses due to the ‘stress trapping’ caused by the rotating crack model. The plasticity models seem to favour exhibiting tension dominated failure, due to the

formation and perpetuation of a major crack upon initial localization in which the effects of the rate dependence of the model and the use of only one strain hardening parameter more easily facilitate tensile failure. Redistribution of stresses throughout the rest of the beam is then more easily accommodated. The dissipation of energy in one dominant crack yields satisfactory numerical results, but does not necessarily reflect the physical cracking nature of SHCC.

The differences between the plasticity models results and those obtained experimentally are more pronounced for the Beam 3 specimen, especially considering the values of the displacement at peak loads where values up to 195% of the experimental values were obtained. Tensile failure was again observed for these analyses compared to the compressive spalling and shear failure observed experimentally. It is difficult to establish whether the large difference in the results is due to the favouring of tension dominated failure of the plasticity models or the lack of good scientific practice in the experimental study. The experimental results showed very sudden failure due to the spalling of the concrete and loss of the compression zone (cf. Figure B.4-3) as compared to the more gradual tensile failure observed numerically (cf. Figure B.4-7). The rotating crack model exhibited a compression dominated failure, with the peak loads obtained numerically being between 85% to 100.3% of the experimental values. The corresponding displacements were within 68% to 83% of the experimental values, again typical of the limited displacement facilitated by the rotating crack model due to the limited stress redistribution. No conclusive evidence can suggest that the rotating crack model more accurately describes reality for this specimen, as the complications involved in the experimental programme do not inspire one with confidence regarding its use in establishing a definitive benchmark with which to compare numerical results. Furthermore, both numerical constitutive models captured near satisfactory results for the other two specimens (the plasticity model more so than the rotating crack model), thus no extrapolations from the other analyses can be used to deduce which numerical model more accurately captures reality for the Beam 3 specimen.

C. Conclusion and Summary

C.1 Conclusion

Generally, the structural response of the beams investigated was not consistently well captured by the constitutive models considered. Some models favoured certain failure modes, but also only provided acceptable results for certain mesh sizes and types. The need for precise material parameters is of great importance and the sensitivity of the analyses to the choice of parameters as well as the interdependence of parameters was observed. When considering reliability based design, one would require an extensive database of the mechanical properties of the concrete considered as well make a statistical inference about the distribution of the material parameters and also establish relationships between them (to incorporate interdependence of parameters) in order to provide a probability distribution of resistance of the structure considered. Firstly, the use of specific parameters as obtained from the statistical distribution of mechanical properties could easily yield an incorrect structural response due to the sensitivity of the models to these chosen parameters and the potentially large variance of the statistical distribution obtained. The interdependence of certain parameters on one another and on structural response can potentially trigger different failure mechanisms, as was seen for the C-Q8MEM-TS[R]-HSC analyses where the excessive curvature (due to the dependence of the structural response on the ratio of the compressive and tensile properties) of the beams resulted in the incorrect failure mechanism. For advanced cementitious materials to be exploited and used widely in practice, extensive experimental testing is required to formulate documents similar to the Model Code (2010) for normal strength concrete. Only then can sufficient 'trust' in the results of the computational modelling of these materials be established, once the constitutive material parameters can be determined easily and reliably.

The various failure modes could not be consistently well captured for all the cases considered. In the compressive dominated study, the uncertainty of the material parameters for the HSC and FRHSC beams yielded inconsistent results. The response of the NSC beams was relatively well simulated. The shear

dominated study inspired no significant confidence in the capacity of the available models to capture such failure. Various numerical difficulties were encountered and often detailed response curves were not obtained. It was found, however; that the Q8MEM mesh types performed better than the CQ16M meshes under shear. These mesh types were more robust and convergence was more easily attained, due to the selective reduced integration of the elements. It seems the tension dominated study yielded some good results for both constitutive model types, despite the uncertainties governing the exact material properties of the concrete used in the experimental investigations. Some of the experimental results obtained showed different failure mechanisms than some of the comparative computational studies, which may either be attributed to poor experimental practice or the material properties being slightly different at the higher loads experienced in these experiments. The results seem to be indicative of the nature of the development of the constitutive models, where tensile response simulation is of greatest importance and the other failure mechanisms are considered as an afterthought.

The plasticity models simulated the physical behaviour of concrete in the compression and tension critical cases sufficiently well and on average, good consistency across mesh sizes and types was found. Thus these models were found to not have severe mesh compatibility issues. The model performed poorly when simulating shear failure. Convergence was not easily attained for the shear study and failed to be attained for most meshes. The investigation of the parameter that represents the shear stress contribution to failure, did exhibit more definitive shear failure. The rate dependence of the cracking viscosity parameter of the one parameter model needs to be considered, and a rate dependant parameter that can be established from experimental data needs to be formulated. The development of a strain based plasticity model with two kinematic hardening parameters should be investigated, with the aim of effectively capturing shear failure. It could also be considered that it be made possible for the user to change the dilatancy angle of the plastic potential function, to control the strain rate evolution. Thus the volume change of the elements could be controlled, which may enable better shear behaviour.

The total strain models showed some good results, but often with peak load values obtained being close to those observed experimentally but at a much

lower corresponding displacement (for the compression and tension critical studies). The phenomenon of stress trapping in the zones of localization was observed for the rotating crack model, where stress redistribution through the beams was inhibited due to the small and incessant rotations of the axes of orthotropy. More extensive tensile cracking was observed for these models in the compression dominated study, where the governing failure mechanism was actually found to be tension dominated in some instances due to the excessive development of cracks. Greater variation across the mesh types and sizes was also observed in these models, especially in the tension dominated study, where fracture energy independent constitutive models were used. In the shear dominated study, the fixed crack model yielded the most accurate result, but was also the most inconsistent across mesh types and sizes. The Q8MEM elements more easily accommodated the shear deformations, but the smaller mesh sizes for the fixed crack models could redistribute the stresses far easier and for longer due to the smaller strain increments per step. Thus with no reduction in the shear retention factor, these small mesh sizes could carry far larger loads than observed experimentally. The use of a variable shear retention factor showed promising results, but experimentally obtaining such a relationship for a material without the luxury of post analysis checks, would be tedious.

Generally, the fully integrated CQ16M mesh types performed quite poorly, especially in the shear dominated study. The solutions for these elements also required the use of the less strict numerical conditions (which were also applied to the other mesh types). It seems the mathematical complexity of these elements in conjunction with the additional complexities inherent in non linear mechanics is not really compatible. The combination of a CQ16M mesh and a rotating crack model exacerbates the concept of stress trapping, where localization is able to occur at more integration points per element and the rotation of the principal strain axes being even less per integration point. The Q8MEM mesh types were found to be more robust and convergence difficulties were far less widespread. The T6MEM cross diagonal triangle mesh yielded some very good results due to its mathematical simplicity and the fact that it affords the additional internal degrees of freedom. The incorporation of a meshing algorithm to easily create a cross diagonal triangle mesh in DIANA should be considered.

Overall, the results are not encouraging when considering using non linear finite element results for design purposes with the models considered; due to either inconsistency across mesh types and sizes, inaccuracies of results or even the simulation of incorrect failure modes. The goal should be to develop a constitutive model that can consistently and accurately simulate realistic structural response for all failure mechanisms in a computationally robust manner. It appears the complexity of such a model will be extensive, and considering the fact that there was no significant attainment of post peak data for most of the analyses in this study, such a model will require more advanced solution techniques and a superior computational platform. Another consideration is that the end designer will have to, regardless of the ease of implementation or the 'user friendliness' of any non linear finite element analysis program, be very familiar with the entire system governing these analyses (not only the non linear models but also the structure of the program and structural mechanics etc).

C.2 Summary

In summary, the following can be concluded from this thesis work:

- **Failure modes**

  The failure modes were generally not consistently accurately captured computationally. Convergence was not easily (if at all) attained for most analyses, despite the imposition of relatively lenient numerical constraints. The tensile failure of the SHCC beams was sufficiently well captured for most instances considered. Shear failure was especially poorly simulated and the potential of such failure occurring needs to be correctly emulated.

- **Computational models**

  The plasticity models showed better consistency across mesh types and sizes as compared to the total strain models. The total strain rotating crack model exhibited stress trapping in the zones of localization, resulting in poor stress redistribution and associated potential premature failure or even simulation of the incorrect failure mode. The SHCC plasticity model developed by Van Zijl (2009) yielded some good results for the tension critical SHCC beams. An effort should

be made to develop a model that consistently accurately captures the correct structural response. The development of one such model that is widely accepted and proven to simulate structural response for various modes of failure, would enable the development of reliability based design codes based on the results of non linear finite element analyses using such a model. The existing models are limited in their capacity to represent real structural response, and some are more specifically suited for the modelling of certain failure modes.

- **Model parameters**

  Significant sensitivity to model parameters was observed for all computational models, the effect of which is more pronounced in a plasticity framework where a greater number of, and more complex parameters are involved. In the compressive dominated study, the models generally performed well for the NSC beams, the parameters of which were determined from the Model Code (2010) based on the compressive strength. This was not observed for the other concrete types in the compressive critical study especially the HSC beams, thus either the model representation of the material is flawed or the correct material parameters were not reflected by the Model Code (2010) relations. The latter suggests the need of such a document specific to certain concrete types. The chosen parameters for the SHCC tension critical investigation yielded acceptable results for both models considered, as the strain rate dependence of the material was not a critical factor in the analyses.

- **Choice of element type**

  The Q8MEM meshes mostly outperformed the CQ16M meshes. This was attributed to the mathematical simplicity as well as the selective reduced integration of the shear stiffness terms in the formulation of the element matrix of these elements, which more easily facilitated numerical convergence. The stress trapping observed from the total strain rotating crack model was exacerbated for the CQ16M meshes due to the additional integration points per element.

- **Expertise of analyst**

  It is imperative for the analyst undertaking any non linear finite element analyses to be extensively familiar with the intricacies and theories of the computational model at hand as well as with the interdependencies and origins of the material parameters; and with the finite element mathematical framework and the finite

element software proposed for use. Extensive training is thus required to ensure the attainment of reliable and accurate results, and to ensure that the results obtained are sufficiently well scrutinized based on the underlying theory to ascertain their accurate representation of reality.

D. References

Adendorff CJ The time-dependant cracking behaviour of strain hardening cement-based composites, MScEng-thesis [Report]. - [s.l.] : Stellenbosch University, 2009.

Bazant Z P and Oh B H Crack Band theory for fracture of Concrete. [Article] // RILEM Mat. Struct.. - 1983. - 16.

Bazant Z P Instability, Ductility and size effect in strain softening concrete. [Journal]. - [s.l.] : ASCE J Engng Mech, 1976. - 102.

Cope R J [et al.] Modelling of reinforced concrete behaviour for finite element analysis of bridge slabs. [Article] // Numerical Methods for non-linear problems.. - Swansea : Pineridge Press, 1980.

de Borst R and Sluys L J Computational Methods in Non-Linear Solid Mechanics [Book]. - Delft : Delft University of Technology, 2002.

de Borst R Fracture in quasi-brittle materials: a review of continuum damage-based approaches. [Journal] // Engineering Fracture Mechanics 69. - 2001. - pp. 95-112.

DIANA TNO DIANA User's Manual - Material Library, Release 9.4 [Electronic Help Files]. - [s.l.] : TNO DIANA, 2009.

Feenstra P H and de Borst R A Plasticity Model and Algorithm for Mode I cracking in concrete. [Journal] // Int. J. Numer. Meth. - 1995. - pp. 2059-2529.

Feenstra P H Computational Aspects of Biaxial Stress in Plain and Reinforced Concrete. [Report] : PhD Thesis. - [s.l.] : Delft University of Technology, 1993.

Feenstra P.H, Belletti B. and Hendriks M.A.N Guidelines for non-linear finite element analysis of concrete structures [Report]. - Delft : Delft University of Technology, 2011.

Hendriks M.A.N, Feenstra P.H and Rots J.G Guidelines for Non-linear Finite Element Analysis of Concrete Structures [Report]. - Delft : Delft University of Technology, 2009.

Hillerborg A, Modeer M and Petersson P E Analysis of crack formation and crack growth in concrete by means of fracture mechanics and Finite Elements. [Article] // Cement Concrete Res.. - 1976. - 6.

Koiter W T Stress-strain realtions, uniqueness and variational theorems for elastic-plastic materials with a singular yield surface. [Journal] // Quart Appl. Math. - 1953. - pp. 350-354.

Kolmar W and Mehlhorn G Comparison of shear stiffness formulations for crakced reinforced concrete elements. [Conference] // Proceedings of the International Conference on Computer Aided Analysis and Design of Concrete Structures.. - [s.l.] : Pineridge Press., 1984.

Lourenco Paulo B, De Borst Rene and Rots Jan G A Plane Stress Softening Plasticity Model for Orthotropic Materials. [Journal] // International Journal for Numerical Methods in Engineering. - TUDelft : John Wiley & Sons, Ltd, 1997. - pp. 4033-4057.

Molapo KT The behaviour of strain-hardening cement composites under biaxial compression, MScEng-thesis [Report]. - [s.l.] : Stellenbosch University, 2010.

Nagtegaal J.C, Parks D.M and Rice J.R On numerically accurate finite element solutions in the fully plastic range. [Article] // Comp. Meth. Appl. Mech. Eng.. - 1974. - 4.

Pedersen L.H, Bundgaard K. and Morch T. Numerical and Experimental Invastigations of Compression Failure of Concrete Beams. [Report]. - Aalborg : Aalborg University, Department of Building Teschnology and Structural Engineering, 1996.

Pedersen Lone Hogholm, Bundgaard Kim and Torben Morch Compression Failure of Concrete Beams [Report]. - [s.l.] : Aalborg University, 1996.

Rashid Y.R. Analysis of Prestressed concrete pressure vessels. [Journal]. - 1968. - 7.

Rots J G [et al.] Smeared Crack approach and Fracture localization in Concrete. [Article] // Heron. - Delft : CUR-VB, 1985. - 1 : Vol. 30.

Rots J.G Computational Modelling of Concrete Fracture [Report] : Ph.D. - [s.l.] : Delft University of Technology, 1988.

Slobbe A T, Hendriks M.A.N and Rots J.G Capturing Brittle failure behaviour of shear critical RC Beams using sequentially linear analysis. [Conference] // fib Symposium. - Prague : [s.n.], 2011.

Suidan M and Schnobrich W C Finite element analysis of reinforced concrete. [Journal]. - [s.l.] : ASCE J. Struct. Div., 1973. - Vol. 99.

van Mier J.G.M and Ulfkjaer J.P Round Robin Analysis of over-reinforced concrete beams - Comparison of results. [Report]. - Delft : [s.n.], 2000.

Van Zijl G.P.A.G Computational Modelling of Masonry creep and shrinkage. // Dissertation. - Delft : [s.n.], 2000.

Van Zijl G.P.A.G Cracking Concepts. [Book Section] // Advanced Mechanics of Materials and Modeling.. - 2010.

Van Zijl G.P.A.G, de Borst R and Rots J G A numerical model for the time-dependant cracking of cementitious materials. [Article] // Int. J. Numer. Meth. in Engng. - 2001. - 52.

Van Zijl GPAG and Zeranka S The impact of rheology on the mechanical performance of steel fibre reinforced concrete [Conference] // HPFRCC 6. - Ann Arbor, Michigan, USA : [s.n.], 2011.

Van Zijl GPAG Computational Modeling of SHCC [Report]. - Stellenbosch University : ISE Report 2009-20, 2009.

Victor S Unpublished results. [Report]. - 2011.

Walraven et al. fib Model Code Draft [Report]. - Lausanne, Switzerland : International Federation for Structural Concrete, 2010.

Wu Z S and Bazant Z P Finite element modelling of rate effect in concrete fracture with influence of creep [Article] // Creep and Shrinkage of concrete.. - London : E.&F.N.Spon, 1993.

Appendix A

SYMMETRICAL VIEW OF COMPRESSION CRITICAL BEAM.

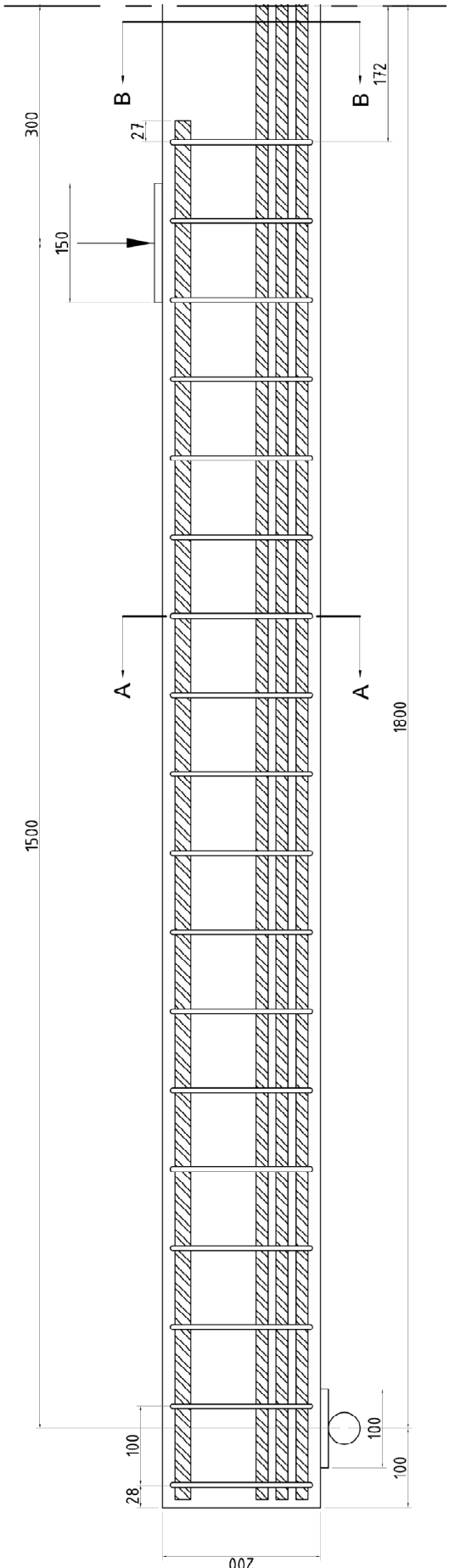

CROSS SECTION OF COMPRESSION CRITICAL BEAM:

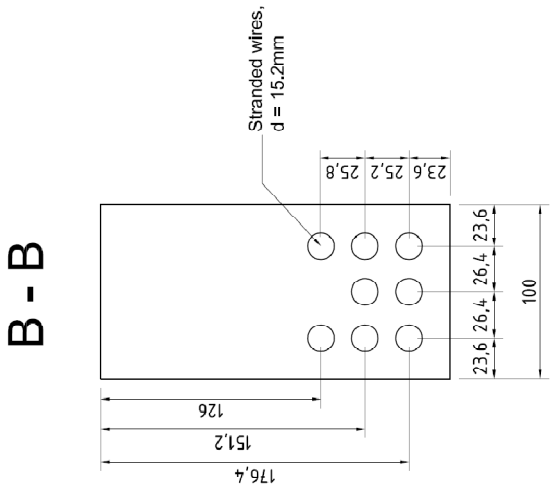

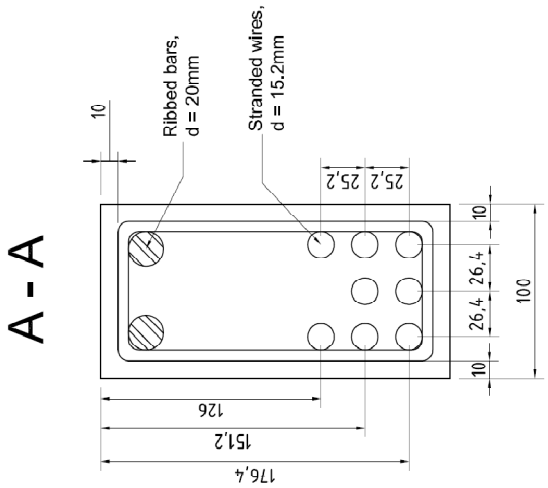

Appendix B

SHEAR CRITICAL BEAM DETAIL:

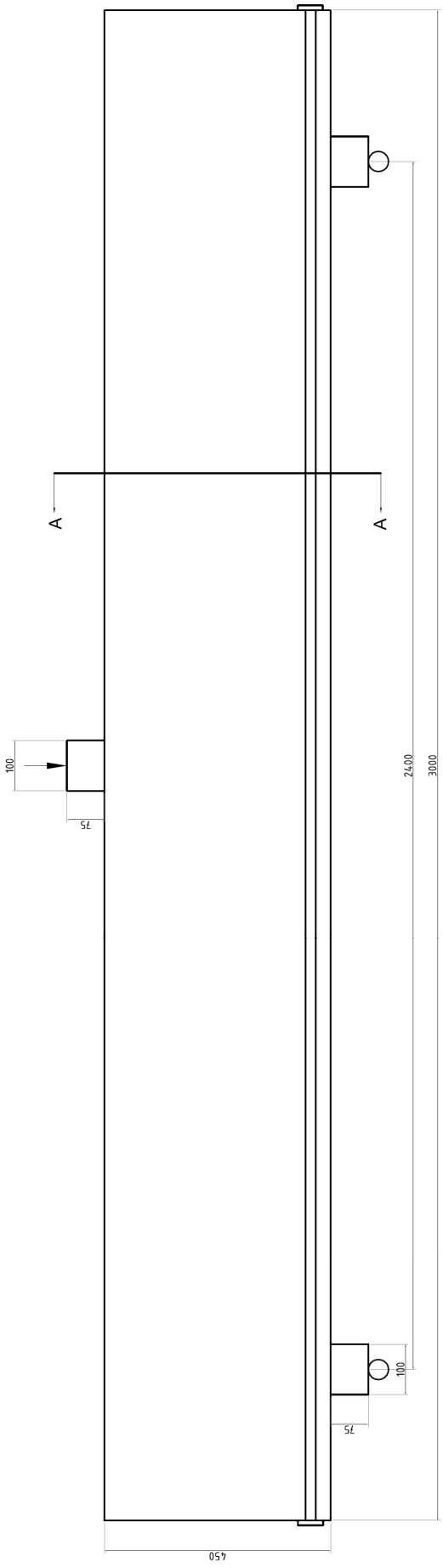

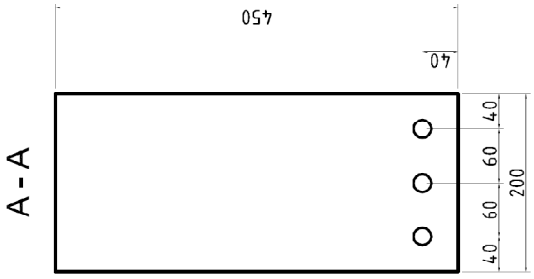

Appendix C

TENSION CRITICAL BEAM DETAILS